



Inhibition studies of metalloproteins by means of electrochemistry and spectroscopy

Anton Nikolaev

► To cite this version:

Anton Nikolaev. Inhibition studies of metalloproteins by means of electrochemistry and spectroscopy. Other. Université de Strasbourg, 2018. English. NNT : 2018STRAF053 . tel-02146028

HAL Id: tel-02146028

<https://theses.hal.science/tel-02146028>

Submitted on 3 Jun 2019

HAL is a multi-disciplinary open access archive for the deposit and dissemination of scientific research documents, whether they are published or not. The documents may come from teaching and research institutions in France or abroad, or from public or private research centers.

L'archive ouverte pluridisciplinaire **HAL**, est destinée au dépôt et à la diffusion de documents scientifiques de niveau recherche, publiés ou non, émanant des établissements d'enseignement et de recherche français ou étrangers, des laboratoires publics ou privés.

ÉCOLE DOCTORALE DES SCIENCES CHIMIQUE
UMR7140, Chimie de la matière complexe

THÈSE présentée par :

Anton Nikolaev

soutenue le : **29 octobre 2018**

pour obtenir le grade de : **Docteur de l'université de Strasbourg**

Discipline/ Spécialité : Chimie

**Etudes d'inhibition de métalloprotéines
par électrochimie et spectroscopie**

Inhibition studies of metalloproteins by means of electrochemistry and
spectroscopy

THÈSE dirigée par :

Pr HELLWIG Petra, Université de Strasbourg, Strasbourg, France

RAPPORTEURS :

Pr MIOMANDRE Fabien, Ecole normale supérieure de Cachan, Paris, France

Dr LOJOU Elisabeth, BIP CNRS AMU, Marseille, France

AUTRES MEMBRES DU JURY :

Dr KIEFFER Bruno, Université de Strasbourg, Strasbourg, France

Content

Content	2
Acknowledgments	6
Abbreviations and acronyms	7
Resumé en français.....	9
<i>Préface</i>	<i>9</i>
<i>Partie A. Cytochrome bd-oxydase.....</i>	<i>9</i>
<i>Partie B. La protéine mitoNEET.....</i>	<i>16</i>
List of the communications	18
List of the publications	18
Preface.....	19
Part A. Cytochrome bd-oxidase.....	20
<i>Introduction.....</i>	<i>20</i>
I. The place of complex IV in the respiratory chain.....	21
1. Bioenergetic membranes.....	21
2. Components of respiratory chain.....	22
Eukaryotic respiratory chain	22
Cytochrome proteins and heme cofactors.....	24
Prokaryotic respiratory chains.....	25
ROS	25
Quinolns.....	26
3. Cytochrome bd is a prokaryotic complex IV.....	27
Classification of complex IV.....	28
Structure of complex IV.....	29
A-type oxidases	29
B- and C-type oxidases, NORs.....	31
bd-oxidases	32
Catalytic cycle.....	35
aa ₃ -oxidase.....	35
bd-oxidase	37
Function	38
II. Inhibitors: role in the protein characterisation	39
1. Kinetic parameters of enzyme catalysis.....	39
2. Influence of the inhibitors on enzyme kinetics Inhibitor classification	41
3. Inhibition measurements.....	43
III. bd-oxidase and inhibitors.....	45
IV. Development of electrochemical biosensor for the detection of inhibitors.....	49
1. Biosensors.....	49

2. Protein film voltammetry	50
Practical aspects.....	50
Choice of the surface modification	50
Gold electrode modified with GNPs covered with SAM	54
Comparison of immobilised and solubilised complex IV.....	54
The aims of the project.....	56
Results.....	57
I. Optimisation of the cyt bd immobilisation.	58
1. Influence of concentration	58
2. Stability of the signal	59
Influence of the lipids.....	60
Desorption or loss of the activity?	61
Mutual influence of the surface charge of the SAM and lipid type	61
Influence of the thiol spacer length.....	63
Detergent variations	64
3. Improvement of the preparation procedure	65
GNPs deposition	65
Thiol incubation	67
The protein incubation at the surface	69
4. Control experiments with HQNO.....	69
5. Conclusions.....	71
II. The compound examination.	72
1. Aurachin D derivatives examination.....	72
2. Various compound sets	74
3. Conclusions.....	81
III. Cytochrome bd from <i>G. thermodenitrificans</i>	82
1. Comparison with <i>E. coli</i> at pH7	82
UV/Vis-spectroscopy.....	82
Spectroelectrochemistry.....	83
UV/Vis titration	83
Redox-induced differential FTIR spectroscopy.....	87
Resonance Raman spectroscopy	90
Electrochemistry	92
2. The influence of the heme d on cyt bd properties.....	95
3. Dependency on pH and T.....	96
Influence of T	96
Influence of pH.....	97
Mutual influence of pH and T	98
4. Preliminary inhibition experiments	101
5. Conclusions.....	103

Part B. mitoNEET	104
Introduction	104
I. Structure.....	105
II. Biophysical properties and mechanism	106
III. Biological role	107
IV. Influence of addition of compounds.....	107
Aim of the PhD project.....	108
Results and discussion.....	109
I. Preliminary studies	110
1. Cyclic voltammetry	110
2. Resonance Raman spectroscopy.....	111
3. Redox-induced differential FTIR spectroscopy.....	113
II. Influence of phosphate ions.....	114
1. Cyclic voltammetry	114
2. Resonance Raman spectroscopy.....	115
III. Influence of pH.....	115
1. Resonance Raman spectroscopy.....	115
2. Redox-induced differential FTIR spectroscopy.....	116
IV. Influence of the ligands	118
1. Cyclic voltammetry	118
2. Resonance Raman spectroscopy.....	119
3. Redox-induced differential FTIR spectroscopy.....	120
Conclusions	121
General conclusions and perspectives	122
Experimental part	123
Methods	124
I. Electrochemistry	124
1. Cyclic voltammetry of adsorbed species.....	124
2. Stationary electrochemistry	126
II. Spectroscopy	128
1. Absorption spectroscopy.....	128
UV/Vis spectroscopy and its application towards proteins and cofactors.....	130
Mid-infrared spectroscopy of proteins.....	132
2. Raman spectroscopy. Application for the study of protein cofactors.....	135
Instrumentation	139
I. Electrochemical equipment.....	139
II. UV/Vis spectrometer	139
Thin-layer electrochemical cell.....	140
III. FTIR spectrometer	141
Transmission cell.....	142

IV. Raman spectrometer	143
V. Clark-electrode	144
Experimental protocols	145
I. Protein preparations	145
1. Purification	145
<i>bd</i> -oxidase from <i>E. coli</i>	145
<i>bd</i> -oxidase from <i>G. thermodenitrificans</i>	145
mitoNEET	145
2. Pretreatment of the samples	145
PFV	145
Differential FTIR spectroscopy	147
Raman spectroscopy	147
Electrochemical titrations	147
FTIR transmission measurements	147
Catalytic activity measurements in solution	147
II. Electrode pretreatment and modification	147
III. FTIR parameters	148
IV. Raman spectroscopy measurements	149
V. Redox titration experiments	149
VI. IR transmission	149
VII. Catalytic activity in solution	150
Materials	151
I. Compounds	151
II. Gold nanoparticles preparation and validation	151
III. Gold grid modification	151
IV. Mediators	152
V. Inhibitor addition	153
Software	153
Annexes	154
References	163
List of figures	179
List of tables	183
List of annexes	185

Acknowledgments

I would like to express my endless thanks to my supervisors Pr. Hellwig and Dr. Melin for their kind attitude regardless my performance in the laboratory. In particular, I would like to express my gratitude to Pr. Hellwig for granting me the opportunity to enter electrochemistry even if my background did not correspond at that time, and for encouraging in the time of frustrating experiments. It was a pleasure to discuss the ongoing experimental issues and result interpretations with Dr. Melin. Also I would like to thank Pr. Friedrich for receiving me in his laboratory in Freiburg and Alex Thesseling for his excellent protein purifications.

I would like to make my acknowledgments to all collaborators contributing to my PhD project and members of the thesis committee accepting the proposition to be in the jury and dedicate their time for this.

I am grateful to our engineer Dr. Boubegtiten for her not only scientific but personal help and care. Especially, I will never forget that you did not leave me alone face-to-face with bureaucratic system. Due to this I also would like to make an acknowledgement to Ms Hnini with whom it was warm to speak every time. At the same time, I would like express my appreciation to Dr. El Khoury.

All PhD and master students I met in the laboratory were not less important for me. I will remember hilarious discussions with Sinan Sabunku and Natalia Grytsyk, Filipa Santos who could rescue almost every minute even if you was not in need, and Katherine Mezic who endured my linguistic jokes in English with comprehension.

I also would like to thanks my friends Guli Trukhmanova, Paul Jamme, Aleksandra Kostuk who spent their immense quantity of time for and with me. Special thanks I would address to Kathia Chernova carrying a piece of home with her and maintaining adventurous spirit in us.

I am grateful to many other of my acquaintances, to my teachers and to my alma mater Saint-Petersburg State University.

And the last but not the least, they are my dear parents Marina and Igor Nikolaevyi who are happy about my presence in spite of everything.

Abbreviations and acronyms

Adx	—	adrenoxine
AOXs	—	alternative oxidase
ATP	—	adenosine triphosphate
BNC	—	binuclear centre
CcO	—	cyt <i>c</i> oxidase
CE	—	counter electrode
CIO	—	cyanide-insensitive oxidase
CNSs	—	carbon nanospheres
CV	—	cyclic voltammetry
cyt	—	cytochrome
DDM	—	n-Dodecyl β -D-maltoside
DET	—	direct electron transfer
(DM)PE	—	1,2-dimyristoyl-sn-glycero-3-phosphoethanolamine
DMQ	—	2-polyprenyl-3-methyl-6-methoxy-1,4-benzoquinone
DMSO	—	dimethyl sulfoxide
(DO)PG	—	1,2-dioleoyl-sn-glycero-3-phosphoglycerol
FAD	—	flavin adenine dinucleotide
FAR	—	far infrared
Fdx	—	ferredoxin
FMN	—	flavin mononucleotide
FTIR	—	Fourier-transform infrared spectroscopy
GCE	—	glassy carbon electrode
GNPs	—	gold nanoparticles
Grx	—	glutaredoxin
HCOs	—	heme-copper oxidases
HQNO	—	2-heptyl-4-hydroxyquinoline N-oxide
HT	—	hexanthiol-1
HTS	—	high-throughput screening
IC₅₀	—	half-inhibition concentration
IMAC	—	immobilized metal affinity chromatography
IMM	—	inner mitochondrial membrane
IMS	—	intermembrane space
IC	—	internal conversion
IR	—	infrared
IRP-1	—	iron regulatory protein 1
MCH	—	6-mercapto-1-hexanol
MCT	—	mercury cadmium telluride
MEA	—	mercaptoethylamine
MHA	—	6-mercaptophexanoic acid
MIR	—	middle IR
MLCT	—	metall-ligand charge transfer

MNG	—	maltose-neopentyl glycol
mNT	—	mitoNEET
MO	—	molecular orbital
MOPS	—	3-(N-morpholino)propanesulfonic acid
MPA	—	3-mercaptopropionic acid
MQ or MK	—	menaquinone
MUA	—	11-mercaptoundecanoic acid
MWCNTs	—	multi wall carbon nanotubes
NAD(P)H	—	nicotinamide adenine dinucleotide (phosphate)
NDH	—	NADH dehydrogenase
NIR	—	near infrared
NOR	—	NO reductase
PCET	—	proton coupled electron transfer
PFV	—	protein film voltammetry
PGE	—	pyrolytic graphite electrode
pio	—	pioglitazone
<i>pmf</i>	—	proton motive force
PQ	—	plastoquinol
RDE	—	rotating disk electrode
RE	—	reference electrode
RHE	—	reversible hydrogen electrode
RNS	—	reactive nitrogen species
ROS	—	reactive oxygen species
RR	—	resonance Raman
rsv3S	—	resviratrol-3-sulfate
SAM	—	self-assembled monolayer
SHE	—	standard hydrogen electrode
SQR	—	succinate-ubiquinone reductase
SWCNTs	—	single wall carbon nanotubes
tBLM	—	tethered bilayer membrane
TMPD	—	tetramethyl-p-phenylenediamine
TZD	—	thiazolidinedione
UHDBT	—	undecylhydroxydioxobenzothiazole
UQ	—	ubiquinone
UV/Vis	—	ultraviolet/visible
VR	—	vibrational relaxation
WE	—	working electrode

For the list of amino acid and their pK and pI values see Annex 1.

Values of the physical constants mentioned in the thesis:

- $R=8.31$ – universal gas constant, $\text{J}\cdot\text{mol}^{-1}\cdot\text{K}^{-1}$
- $F=96485.33$ – Faraday constant, $\text{C}\cdot\text{mol}^{-1}$
- $c=3\cdot 10^8$ – light velocity in vacuum, $\text{m}\cdot\text{s}^{-1}$
- $h=6.63\cdot 10^{-34}$ – Planck constant, $\text{m}^2\cdot\text{kg}\cdot\text{s}^{-1}$

Resumé en français

Préface

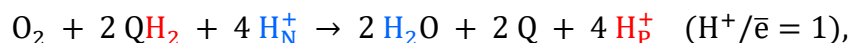
Les études d'interaction protéine-ligand permettent d'élucider la structure, le mécanisme catalytique des protéines et d'identifier les inhibiteurs. Les méthodes spectroscopiques et électrochimiques sont très efficaces pour la caractérisation des paramètres structuraux et fonctionnels des protéines et du complexe protéine-ligand¹.

Dans notre travail, nous avons étudié deux types de métalloprotéines : l'hème contenant le cytochrome *bd*-oxydase et le FeS-cluster contenant la mitoNEET.

Partie A. Cytochrome *bd*-oxydase

Les mécanismes de conversion de l'énergie dans la cellule biologiques sont basés sur le gradient de protons électrochimique et aussi appelés la force motrice du proton, *pmf*. Le groupe des protéines donnant à la cellule la capacité de former un gradient essentiel est appelé chaîne respiratoire et il est localisé dans la membrane mitochondriale interne (dans le cas des eucaryotes) ou dans la membrane cellulaire (dans le cas des procaryotes). Toutes ces protéines, ou complexes, sont des métalloprotéines capables de transférer des électrons. Les électrons viennent des agents réduits (NADH, succinate) à travers la chaîne respiratoire des protéines, et au niveau du complexe IV sont ensuite transférés à l'accepteur terminal oxydatif qui est habituellement l'oxygène². Le complexe IV a été classé en 3 familles: l'oxydase hème-cuivre, les *bd*-oxydases et les oxydases alternatives³. Dans nos études, nous nous sommes concentrés sur les *bd*-oxydases de type I exprimées chez *Escherichia coli* et chez le thermophile *Geobacillus thermodenitrificans*. Les *bd*-oxydases sont exprimées dans la cellule procaryote seulement et exclusivement dans des conditions microaérobiques sous lesquelles les agents pathogènes virulents peuvent se développer comme *E. coli*, *M. tuberculosis*, *L. monocytogenes*, *K. pneumonia*⁴. Une telle spécificité et une telle importance bioénergétique font du cytochrome *bd* une cible potentielle de nouveaux antibiotiques.

L'enzyme oxyde une molécule de quinol (UQ et MQ pour *E. coli*, MQ pour *G. thermodenitficans*) et réduit l'oxygène en eau. Au cours d'un cycle catalytique, deux protons sont libérés dans périplasme, dans le cas de bactéries Gram-négatives en formant le gradient de protons. La réaction totale est la suivante :



ou H_N^+ – protons dans le cytoplasme, H_P^+ – protons dans l'espace externe⁴.

Les études récentes aux rayons X⁵ ont confirmé que la protéine est composée de 3 sous-unités (CydA, CydB, CydX) et contient 3 hèmes comme cofacteurs : hème b_{558} (hexacoordiné à bas spin), b_{595} (hexacoordiné à haut spin) et l'hème d (pentacoordiné à haut spin). La partie de la protéine liée au quinol est appelée une boucle Q. Les *bd*-oxydases montrent une variation de la longueur de la séquence de la boucle Q: une boucle Q longue (*E. coli*) et une boucle Q courte (*G. thermodenitrificans*)⁶.

Plusieurs groupes de ligands interagissant avec le cytochrome *bd* et modulant sa fonction peuvent être définis en fonction de la localisation de leur site de liaison. Néanmoins, les ligands ciblés pour une liaison avec la quinone sont les plus spécifiques en raison de l'interaction sélective du substrat de la quinone avec le cytochrome *bd*. De ce fait, dans ce projet, nous avons examiné des composés structurellement apparentés à la quinone et à la ménaquinone : quinolones, quinones, hydroxyl- et bromo-naphtoquinones, quinazolines, coumarines, flavanones, naphtofuran/pyranes, etc. Nous avons comparé l'influence des ligands sur le fonctionnement des *bd*-oxydases.

Résultats et discussion

1) Développement d'une méthode de détection bioélectrochimique.

La voltampérométrie cyclique a été appliquée récemment pour la caractérisation des protéines de la chaîne respiratoire⁷. Dans ce projet, nous avons optimisé la méthode pour la *bd*-oxydase. La procédure de modification de l'électrode en or à disque tournant est la suivante : la surface d'or de l'électrode est augmentée par l'addition en goutte à goutte de nanoparticules d'or préparées par la méthode de Turkevich et Frens⁸. L'étape suivante est l'incubation dans une solution de thiol (par exemple : 1-hexanethiol 'HT' et 6-mercaptohexanol 'MCH') qui permet de former une monocouche auto-assemblée. Dès que la monocouche est formée, la protéine est déposée.

Pour stabiliser le film de protéine, nous avons essayé de modifier les paramètres expérimentaux. Le facteur le plus crucial pour la stabilité des protéines a été l'ajout de lipides. Pour le lot de protéine qui a subi une procédure de purification plus drastique et contenant ainsi moins de lipides, nous avons déterminé qu'une quantité de 22% de lipides (phosphatidylethanolamine/phosphatidylglycerol PE/PG=1/1) est optimale pour la stabilisation des film (Fig 1, tableau 1).

Tableau 1. Influence de la quantité de lipides sur la stabilité des films de protéine. i_1 - courant mesuré au 1^{er} balayage, i_2 - courant mesuré au 2^{ème} balayage. La surface est non chargée (HT / MCH, 1/1).

lipides, %	$di/i=(i_1-i_2)/i_1$
0	0.39
5	0.26
15	0.13
22	0.07
30	0.08
44	0.40

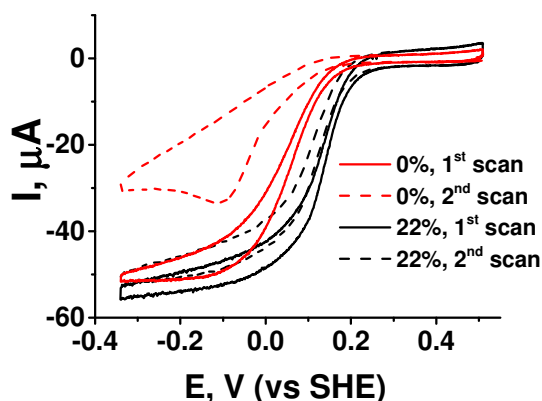


Fig. 1. Effet de la quantité de lipides sur la stabilité des voltamogrammes cycliques du cytochrome bd immobilisé sur l'électrode d'or modifiée avec HT/MCH (1/1).

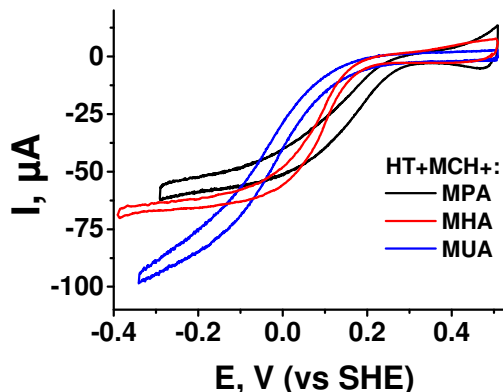


Fig. 2. Dépendance des voltamogrammes cycliques du cytochrome bd en la longueur du thiol : MPA vs MHA vs MUA.

La stabilité dépend également du type de thiol et de lipide. Deux types de surfaces ont été comparées : chargée (HT, MCH et acide 6-mercaptophexanoïque 'MHA') et non chargée (HT, MCH). L'influence mutuelle a été observée. Les films les plus stables ont été obtenus en utilisant les combinaisons surface de thiols chargée et du lipide PE, ou de surface de thiols non chargée et du lipide PG. L'estimation de l'influence du type de charge a été effectuée. Deux mélanges HT/MCH/cystéamine MEA et HT/MCH/acide mercaptopropionique MPA ont été comparés. Comme il ressort des résultats (tableau 2), une surface chargée négativement conduit à un film légèrement plus stable qu'une surface chargée positivement. Pour les deux types de surfaces, on peut remarquer une forte pente du voltamogramme cyclique qui peut être expliquée par l'orientation nonhomogène des molécules de protéine. Ensuite, l'influence de la longueur du thiol a été étudiée. Trois types de thiols chargés ont été ajoutés au mélange de HT et MCH: MPA, MHA ou 11-mercaptoundécanoïque acide MUA.

Tableau 2. Influence du type de lipide et du type de surface sur les paramètres des voltamogrammes de la bd-oxydase.

conditions d'immobilisation		surpotentiel E_{cat}	pente	stabilité di/i
type de lipides	type de thiol	V (vs SHE)	$\Delta i/\Delta E$, $\mu A \cdot mV^{-1}$	-
PG	HT/MCH (1/1)	+ 0.13	0.012	0.06
PE	HT/MCH (1/1)	+ 0.08	0.052	0.15
PE	HT/MCH/MPA (1/1/1)	+ 0.16	0.028	0.04
PE	HT/MCH/MHA (1/1/1)	+ 0.11	0.010	0.07
PE	HT/MCH/MUA (1/1/1)	- 0.01	0.023	0.10
PE	HT/MCH/MEA (1/1/1)	+ 0.20	0.019	0.08

Les thiols courts ainsi que les thiols longs (MUA) ont conduit à une pente plus élevée, probablement, en raison d'une contribution accrue des défauts dans la monocouche.

Nous avons ensuite optimisé la procédure de modification de l'électrode. Ces séries d'expériences ont été réalisées sur le lot de protéines contenant du MNG comme détergent qui est plus proche structurellement de l'environnement naturel de la protéine, les lipides. Néanmoins, la méthode de modification appliquée précédemment n'a pas révélé une stabilité élevée des voltamogrammes. Le volume de nanoparticules d'or déposé s'est avéré crucial pour la stabilité du film protéique. De plus, nous avons diminué les temps d'incubation dans les thiols et les solutions de protéines (3 heures en tout). De tels paramètres de modification nous ont fourni des données robustes sur la stabilité (di/i est d'environ 0.03), et des caractéristiques satisfaisantes de la courbe du voltamogramme ($E_{cat} = -0.05$ V, pente $0.015 \mu A/mV$).

2) Etude des ligands

Plusieurs groupes de ligands ont été testés à une concentration de $10 \mu M$. Les changements du courant catalytique à -0.3 V après addition du ligand ont été pris comme mesure de l'efficacité de l'inhibition (tableau 3). Les inhibiteurs les plus efficaces ont été trouvés dans les familles des quinolones et des quinazoline. En particulier, dans la famille des quinolones, les dérivés de l'aurachine D ont été éliminés puisqu'ils sont supposés être de puissants inhibiteurs^{9,10}. La CI_{50} et la constante d'inhibition K_I^{app} ont été déterminées pour les ligands avec l'activité d'inhibition la plus élevée en faisant varier la concentration. L'activité d'inhibition la plus élevée a été observée lorsqu'un substituant hydrophobe était situé à proximité de l'hétéroatome (O ou N). En particulier, le substituant phényléthylamine a permis au composé QN-1Br de démontrer l'efficacité la plus élevée avec une constante d'inhibition apparente de 430 nM. La structure déterminée de l'inhibiteur le plus efficace peut servir de modèle utile pour synthétiser des composés encore plus efficaces.

Tableau 3. Diminution du courant (di/i) mesuré pour les composés ayant une activité d'inhibition la plus marquée (concentration finale de 10 μ M).

groupe	composé	di/i, %	CI ₅₀ , μ M	K _I ^{app} , μ M
DMSO 100 μ M/control 1		1	n.d.	n.d.
quinolones	HQNO/control 2	28	n.d.	n.d.
	aurachin D derivatives	SB1	32	1.5
		SB2	21	n.d.
		SB3	6	n.d.
		SB4	9	n.d.
		SB5	16	n.d.
		SB6	11	n.d.
	Qo-5	25	1.0	1.32
	Qo-7	43	8.1	8.35
quinazoline	QN-1	24	2.5	2.79
	QN-1Br	35	0.7	0.43
	QN-2	26	1.7	0.78
	QN-3	19	n.d.	n.d.
	RK-04	18	n.d.	n.d.

2) Caractérisation de la *bd*-oxydase de *G. thermodenitrificans*

La spectroscopie FTIR différentielle induite par la réaction redox a été réalisée avec l'utilisation de la cellule ultra-mince à trois électrodes¹¹. Lorsque l'on compare les spectres IR du cytochrome *bd* provenant de *E. coli* et de *G. thermodenitrificans* (Fig. 3), il est clair que la teneur en quinone n'est pas la même: la bande à 1296 cm⁻¹ provient des vibrations C-C/C=C de la ménaquinone tandis que la bande à 1264 cm⁻¹ est attribuée aux vibrations de la chaîne latérale méthoxy CO de l'ubiquinone. Les différences dans la région de l'amide I (1680-1630 cm⁻¹) pourraient également être dues à un excès de ménaquinone dans l'échantillon de *G. thermodenitrificans*. La comparaison de positions des signaux attribués aux acides aminés à chaîne latérale acide (> 1720 cm⁻¹) a permis de conclure qu'ils sont situés dans des environnements différents dans les deux protéines.

Complémentaire à la spectroscopie IR, la technique de la résonance Raman permet d'étudier les cofacteurs et leur environnement. L'excitation laser à 514 nm (dans la région de la bande Q des hèmes *b*) conduit à des bandes de RR impliquant diverses vibrations de squelette dans le plan des hèmes *b* uniquement. L'analyse des spectres des *bd*-oxydases provenant des deux espèces n'a pas montré de différences marquées entre les deux protéines (Fig. 4).

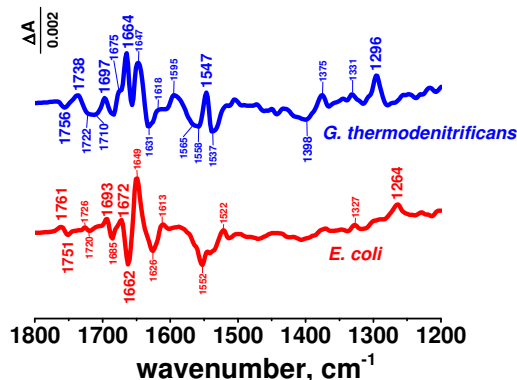


Fig. 3. Spectre FTIR différentiel induit par la réaction redox du cytochrome bd provenant de *G. thermodenitrificans* et d'*E. coli*. 5°C, pH7.

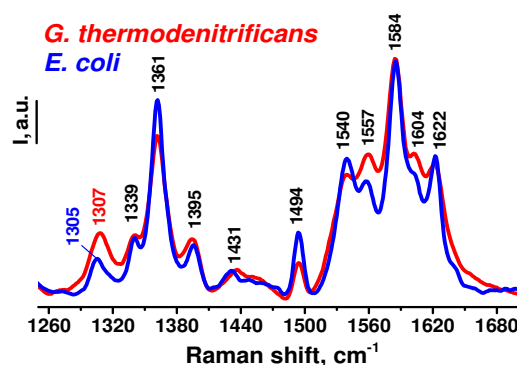


Fig. 4. Spectre de Raman de résonance du cytochrome bd de *G. thermodenitrificans* et d'*E. coli*. Films secs. Excitation laser de 514 nm.

Des titrations par spectroscopie UV/Vis ont été effectuées pour déterminer les potentiels redox des cofacteurs. Les spectres (Fig. 5) ont montré que la bande à 630 nm (*E. coli*) attribuée à transition de l'hème *d* est décalée hypsochromiquement à 620 nm dans l'enzyme thermophile. Les changements d'absorbance UV-Visible induits par la réaction redox ont été tracés en fonction du potentiel pour les bandes à 430 (tous les trois hèmes), 560 (hèmes *b*), et 620 (hème *d*) nm et un fit avec une équation de Nernst modifiée a été effectué (Fig. 6). Les valeurs des potentiels médians obtenues étaient les suivantes : -43 mV pour l'hème *d*, +30 et +137 mV pour les hemes *b*. Dans les autres organismes^{4,12}, l'hème *d* est habituellement le composant de potentiel le plus élevé. Cependant, pour *G. thermodenitrificans* l'hème *d* semble être l'hème de potentiel le plus bas, ce qui devrait inverser le flux d'électrons des hemes *b* vers l'hème *d*. Cela pourrait être lié au fait que le cytochrome *bd* de *G. thermodenitrificans* démontre la plus faible affinité pour l'O₂ entre divers organismes^{6,13}.

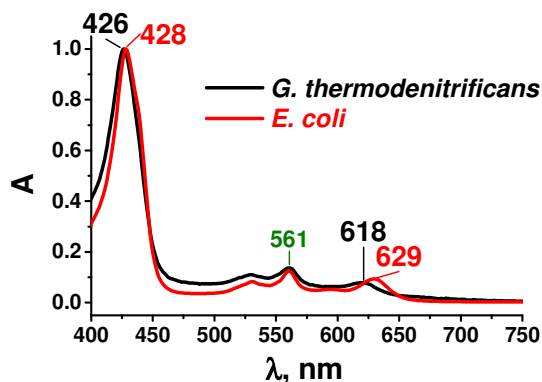


Fig. 5. Spectres d'absorption UV/Vis pour les bd-oxydases de *G. thermodenitrificans* et d'*E. coli*.

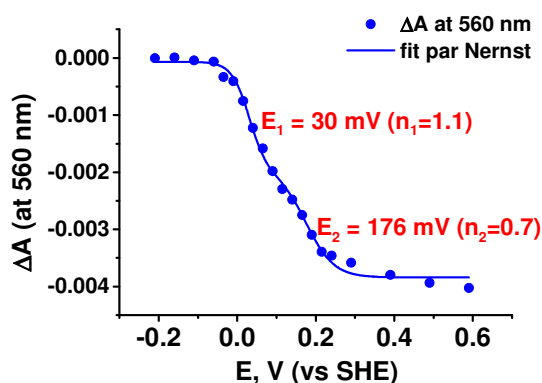


Fig. 6. Exemple de la détermination des potentiels médians des cofacteurs par le fit avec l'équation de Nernst modifiée. Les transitions à 560 nm sont montrés.

Enfin, les voltamogrammes cycliques (Fig. 7) du cytochrome *bd* immobilisé de *G. thermodenitrificans* ont également confirmé que les deux oxydases *bd* ne se ressemblent pas. A pH7 et température ambiante, la *bd*-oxydase provenant des bactéries thermophiles a montré une très faible activité catalytique. En augmentant la température jusqu'à 45°C, la protéine devient de plus en plus active ; néanmoins, le voltamogramme ne montre pas de forme sigmoïdale triviale (auto-croisement). Un tel comportement pourrait être expliqué par l'inhibition avec un substrat¹³, ou l'activation reductive réversible¹⁴. En augmentant à la fois la température et le pH, on observe un comportement catalytique conventionnel. L'explication la plus probable est qu'une acide aminé protonable contribue à la fonction de la protéine.

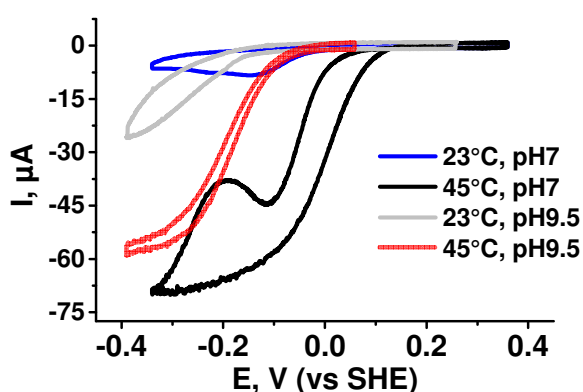


Fig. 7. Voltamogrammes cycliques du cytochrome *bd* de *G. thermodenitrificans* dans différentes conditions.

Conclusions

Le capteur bioélectrochimique pour l'inhibition du cytochrome *bd* a été créé. La méthode d'immobilisation a été optimisée et accélérée. Il a été montré que la présence de lipides dans le film est cruciale pour la fonction de la *bd*-oxydase. De plus, une certaine influence synergique mutuelle du type de surface et du type de lipide a été observée.

Les études d'inhibition ont montré l'efficacité supérieure des composés des familles quinolone et quinazoline et en particulier ceux ayant un substituant plus hydrophobe.

Le cytochrome *bd* de *G. thermodenitrificans* (sous-famille de boucle Q courte) a été caractérisé par spectro-électrochimie et comparé au cytochrome *bd* provenant d'*E. coli* (sous-famille de boucle Q longue).

La protéine de l'organisme thermophile contient de la menaquinone; son hème *d* est situé dans un environnement plus hydrophobe que son homologue provenant d'*E. coli* et montre un

potentiel médian inférieur. En électrochimie, les conditions optimales pour le fonctionnement de la *bd*-oxydase de *G. thermodenitrificans* sont également de 45°C et pH 9.5.

Des expériences supplémentaires devraient être menées pour caractériser l'interaction protéine-inhibiteur et l'influence des ligands sur l'activité du cyt *bd* de *G. thermodenitrificans*.

Partie B. La protéine mitoNEET

Récemment, une protéine soluble 'mitoNEET' a été découverte. La protéine est ancrée avec la queue hydrophobe dans la membrane mitochondriale externe et est considérée comme une cible dans le traitement du cancer, du diabète et d'autres maladies. Sa structure dimérique comprend deux clusters FeS de type $[\text{Fe}_2\text{S}_2]$ coordonnés à 1His et 3Cys. Vraisemblablement, la protéine peut passer un de ces clusters à son partenaire (par exemple : aconitase, Fdx), régulant ainsi le métabolisme du fer dans la cellule eucaryote. La protéine est très stable à l'état réduit, mais à l'état oxydé, le cluster FeS devient instable et, de plus, à un pH plus acide, sa labilité augmente. L'influence sur sa stabilité et sa labilité peut être modulée par la pioglitazone et le resvératrole-3-sulfate^{15,16}. Toutes ces propriétés font de la protéine mitoNEET un système intéressant pour l'étude.

Résultats et discussion

Par le moyen de la bioélectrochimie directe, l'estimation du potentiel médian a été effectuée. Pour l'immobilisation sur monocouche MHA, une valeur du potentiel d'environ +10 mV (vs SHE) a été obtenue. Des expériences de spectroscopie FTIR différentielle induite par la réaction redox (Fig. 8) ont été effectuées dans l'intervalle de pH de 4.6 à 8.0. Avec une diminution du pH, des altérations dans la région de l'amide I ont été observées. À pH 5.4, l'intensité des spectres différentiels était assez faible, probablement en raison de la perte du cluster FeS. À pH 4.6, les spectres différentiels n'ont pas pu être obtenus. L'influence des ions phosphates a également été étudiée. Cependant, la comparaison des tampons avec et sans ions phosphates n'a pas montré d'influence sur les changements conformationnels.

Des études en diffusion Raman de résonance (Fig. 9) ont confirmé les observations IR. Tous les spectres ont été obtenus pour l'état réduit du mitoNEET. Dans la gamme de pH 5.4–8.0, l'intensité et les positions des bandes n'ont pas changé. Ainsi, le cluster était dans le même environnement. À pH 4.8, l'élargissement des bandes et des déplacements ont été observés, ce qui pourrait être dû aux changements dans la liaison du cluster FeS.

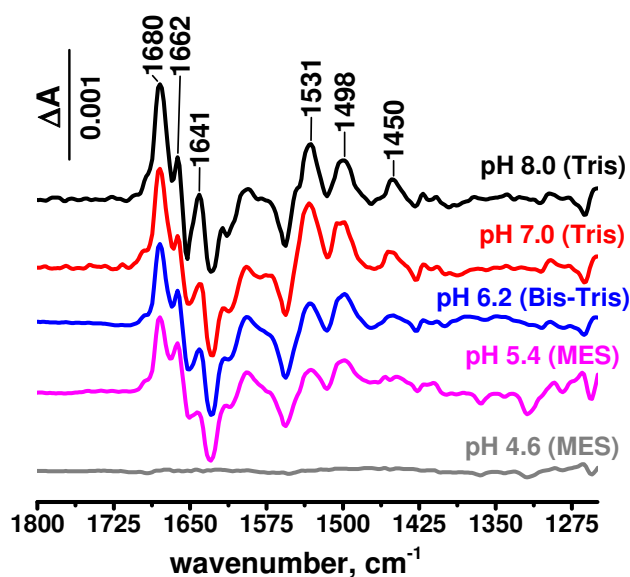


Fig. 8. Spectres FTIR différentiels induits par la réaction redox du mitoNEET dépendant du pH dans le tampon dépourvu des ions phosphates.

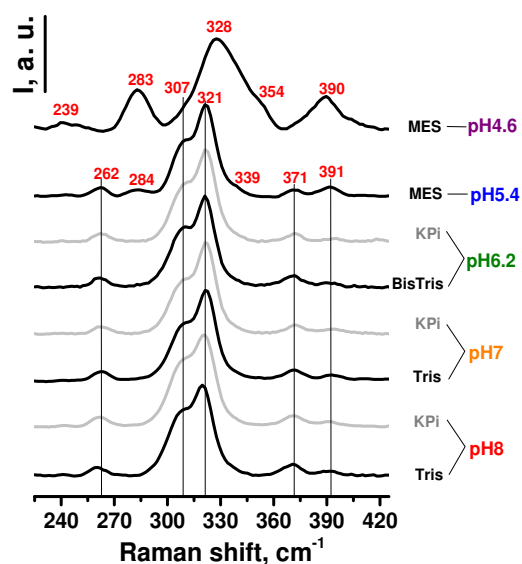


Fig. 9. Spectres de résonance Raman de mitoNEET dépendant de la présence d'ions phosphates et du pH. Films secs. Excitation laser de 514 nm.

Dans l'étape suivante, l'influence des ligands (pioglitazone, resvératrol-3-sulfate, DMSO) a été étudiée. Les spectroscopies IRTF et RR n'ont pas révélé de changements considérables dans de conformations des protéines et la symétrie du cluster. Dans les expériences électrochimiques, seule l'influence du DMSO a montré une diminution de la cinétique du transfert d'électrons.

Conclusions

La protéine mitoNEET n'était plus redox active à faible pH, et les propriétés du cluster FeS étaient modifiées après acidification. Cependant, sa structure est assez conservée dans une vaste gamme de pH. L'influence des ions phosphates n'a pas été observée comme dans le cas des ligands pioglitazone et resvératrol.

List of the communications

Anton Nikolaev, Eugenie Fournier, Hamid Nasiri, Petra Hellwig, Frederic Melin, Hartmut Michel, Schara Safarian. Spectroelectrochemical investigation of *bd*-oxidase inhibition, 19ème Congrès du Groupe Français de Bioénergétique, Lacanau, 20-24 septembre 2017 (oral communication)

Anton Nikolaev. A comparative study on *bd* oxidases, le workshop à collège doctoral binational "Enzyme reactivities and their applications", Strasbourg, 30 november 2017 (oral communication)

Anton Nikolaev. Inhibition studies of cytochrome *bd*-oxidase by means of electrochemistry and spectroscopy, Journée doctorant et master, Strasbourg, 17 avril 2018 (oral communication)

Anton Nikolaev, Alexander Thesseling, Laura Stief, Schara Safarian, Hamid Nasiri, Andreas Speicher, Thorsten Friedrich, Hartmut Michel, Frédéric Melin, Petra Hellwig. Development of a Bioelectrochemical Sensor Based on Cytochrome *bd* Oxidase for Identification of New Antibiotics, 69th Annual Meeting of the International Society of Electrochemistry, Bologna (Italy), 2-7 september 2018 (poster)

List of the publications

Fournier E., Nikolaev A., Nasiri H. R., Hoeser J., Friedrich T., Hellwig P., Melin F. Creation of a gold nanoparticle based electrochemical assay for the detection of inhibitors of bacterial cytochrome *bd* oxidases. *Bioelectrochemistry*. **2016**, 111:109-14.

Melin F., Nikolaev A., Hellwig P. Redox Activity of Cytochromes from the Respiratory Chain. In: Wandelt, K., (Ed.) Encyclopedia of Interfacial Chemistry: Surface Science and Electrochemistry, **2018**, vol. 7, pp 451–469.

Mons C., Botzanowski Th., Nikolaev A., Hellwig P., Cianféroni S., Lescop E., Bouton C., Golinelli-Cohen M.-P. The H₂O₂ -Resistant Fe–S Redox Switch MitoNEET Acts as a pH Sensor To Repair Stress-Damaged Fe–S Protein. *Biochemistry* (2018) (accepted: August 22, 2018).

Anton Nikolaev, Alexander Thesseling, Thorsten Friedrich, Frederic Melin, Petra Hellwig Stabilization of the highly hydrophobic membrane protein cytochrome *bd* oxidase for direct electrochemical studies (in preparation).

Preface

The studies of the protein-ligand interaction help elucidate the structure and the catalytic mechanism of proteins and identify inhibitors. Spectroscopic and electrochemical methods are very efficient for the characterisation of the structural and functional parameters of the protein and protein-ligand complex¹. In this work two types of metalloproteins were studied: heme containing cytochrome *bd* (cyt *bd*) and FeS-cluster containing mitoNEET (mNT).

Cytochrome *bd*-oxidase is a component of the respiratory chain in prokaryotic cells. It is a one of the key components supporting bioenergetical function of the cell. As a terminal oxidase this protein oxidises quinol and reduces oxygen and it conserves the energy in the form of a proton gradient. However, the mechanism of function of cyt *bd* is still not fully understood^{5, 17}. This type of protein constitutes a separate family of oxidases that is expressed only in microaerobic conditions in the prokaryotic cell. It can be considered as a factor of virulence of such pathogens as *Mycobacterium tuberculosis*, *Klebsiella pneumoniae*, etc⁴.

Recently the crystallographic structure was obtained for cyt *bd* from *G. thermodenitrificans*⁵. Nonetheless, it is still unclear how the quinol binding site is organised. It is known that the so-called Q-loop, a hydrophilic periplasmic part of this highly hydrophobic membrane protein, participates in the substrate binding^{18,19}. Two subfamilies can be distinguished including the long or the short Q-loop^{6,20}. Thereby, it is interesting to develop highly specific antibiotics of new generation towards bioenergetics of the various pathogens with low rates of the drug resistance development²¹. Moreover, the examination of the potential inhibitors will allow us to better understand the organisation of the quinol binding site and its function.

In our studies we compare two cyt *bd*-oxidases, one from *E. coli* (long Q-loop) and the other from thermophile *G. thermodenitrificans* (short Q-loop). We optimise the bioelectrochemical sensor modification based on the rotating gold electrode and monitor the influence of different ligands on catalytic function of the protein.

The second project deals with mitochondrial protein mNT. The protein is suggested to contribute to the bioenergetics of the cell²². The malfunction of mNT is associated with several diseases (e. g., diabetes, cancer)^{23,24}. The protein is characterised with high stability in the reduced state but being oxidised it releases FeS-cluster at low pH^{15,25,26}. It is interesting to understand the role of the protein and the reasons of the high stability of the reduced state. Thereby, spectroscopic and electrochemical studies are conducted with pH variation. Some ligands which are supposed to interact and stabilise the protein are investigated as well.

Part A. Cytochrome *bd*-oxidase

Introduction

I. The place of complex IV in the respiratory chain

1. Bioenergetic membranes

The performance of various biological functions demands various energy sources. Depending on the localisation of energy conversion process the different so-called “energetic currencies” are put into process: at the membrane they are electrochemical gradients of proton and/or sodium ($\overrightarrow{\Delta\mu H^+}$ or $\overrightarrow{\Delta\mu Na^+}$), in the non-membrane compartments they are high-energetic compounds as ATP, for instance. The conserved energy in the form of the gradient ($\overrightarrow{\Delta\mu H^+}$ or $\overrightarrow{\Delta\mu Na^+}$) or in the form of macroergic compounds can be converted to mechanical work, osmotic work (passive transport) or heat. One of the key points in bioenergetics is conversion process: for example, the production of ATP through the utilisation of $\overrightarrow{\Delta\mu H^+}$ (oxidative phosphorylation). This phenomenon demands the presence of a membrane that allows separating charges and that is not permeable to ions. This kind of membrane can be found in eukaryotic (e. g., inner membrane of mitochondria) and prokaryotic (e. g., cell membrane) cells. The proteins dedicated to separate charges belong to, for instance, the “respiratory/electron-transport chain”. Electron-transport chains relay the electrons from electron donors (H_2 , lactate, NADH, Fe^{2+} , etc.) to acceptors (O_2 , NO_3^- , NO_2^- , NO, N_2O , N_2 , CO_2 , Fe^{3+} , etc.). In aerobic conditions the most common respiratory chain, which can be found in eukaryotic and prokaryotic cell, consists of dehydrogenases and terminal oxidase, and intermediate complexes/molecules. The formers receive the electrons from NADH (and succinate, in case of *Eucaria*) and relay them to the terminal oxidases which reduce oxygen. The energy accumulation through $\overrightarrow{\Delta\mu H^+}$ formation can be described as:

$$\overrightarrow{\Delta\mu H^+} = nF\Delta\varphi + RT\ln\left(\frac{[H^+]_p}{[H^+]_n}\right) \quad (1)$$

where F – Faraday’s constant, $\Delta\varphi$ – transmembrane potential difference, R – universal gas constant, T – temperature, $[H^+]_p$ – the proton concentration in the more positive/acidic side, $[H^+]_n$ – the proton concentration in the more negative/alkaline compartments, n – charge of the proton. To convert J/mol into mV one should divide $\overrightarrow{\Delta\mu H^+}$ by Faraday constant ($T = 298 K$):

$$\frac{\overrightarrow{\Delta\mu H^+}}{F} = \Delta p = \Delta\varphi - 0.06\Delta pH \quad (2)$$

where Δp – proton motive force (*pmf*); at 25°C proton gradient of 1 *kJ/mol* corresponds to 10.4 mV of *pmf*. *Pmf* was defined in analogy to electromotive force. It takes into account electrical $\Delta\phi$ and chemical ΔpH components contributing to the free energy which can be spent on the proton gradient work (thus, one mole of protons releases around 24 *kJ*). The $\Delta\phi$ is usually ≤ 200 mV since higher values lead to disruption of the lipid bilayer, hence, preventing the proton-coupled electron transport PCET^{2,27}.

2. Components of respiratory chain

Eukaryotic respiratory chain

The respiratory chain of the eukaryotic mitochondria includes the 4 so-called complexes with corresponding acceptor/donor substrates (Fig. 10, table 1).

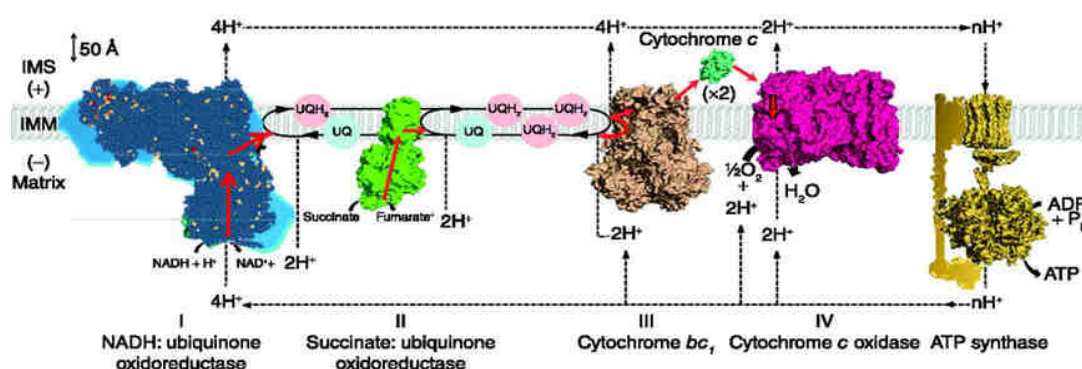
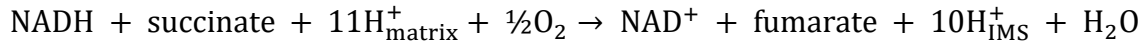
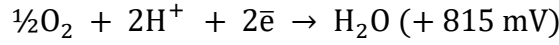
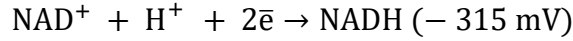


Fig. 10. Electron transport chain in inner mitochondria membrane (IMM)²⁸.

The complex V is ATPase that consumes the energy of the proton gradient (e. g., for ATP synthesis). In mitochondria reduced NADH and succinate produced during Krebs's cycle are oxidised by complex I and complex II, respectively. They are the entrance for electrons into the respiratory chain. Then, the electrons are dropped to UQ-pool which consists of UQ-10. UQ-10 reduces complex III, which, in turn, reduces cyt *c*. Cyt *c* shuttles electrons between complex III and complex IV. Finally, complex IV catalyses the reaction of oxygen reduction to water. All the complexes and lipophilic UQ-10 are localised in the inner membrane of mitochondria (IMM). Cyt *c* is a membrane (IMM) associated soluble protein that occupies intermembrane space (IMS). The protons are pumped by complexes I ($4H^+$), III ($4H^+$) and IV ($2H^+$) from the matrix/negative site of the IMM/ to the IMS/positive site. The total equation of the respiration chain cycle is:



For the redox reactions:



we have $\Delta E^0 = +1130 \text{ mV}$ or $\Delta G^0(\text{NADH}/\frac{1}{2}\text{O}_2) = -nF\Delta E = -218 \text{ kJ/mol}$ ($n = 2$).

For example, the resting potential at the mitochondrial membrane is around $\Delta\varphi = +168 \text{ mV}$ with $\Delta\text{pH} = \text{pH}_{\text{out}} - \text{pH}_{\text{in}} = 0.75$. Therefore, under physiological conditions (37°C) the energy consumed for single proton pumping against the gradient is:

$$\Delta G^0(\text{pumping}) = nF\Delta\varphi + RT\Delta\text{pH} = 20.5 \text{ kJ/mol} \quad (3)$$

where $n = 1$ for 1 proton. Thus, two molecules of NADH passing 4 electrons to one molecule of O_2 should induce pumping of $\frac{\Delta G^0(\text{NADH}/\frac{1}{2}\text{O}_2)}{\Delta G^0(\text{pumping})} = 21$ protons. However, a natural protein could not perform this process in one cycle. Due to this the respiratory chain contains several proteins that couple several redox reactions with a lesser ΔE^0 (table 4)^{2,29}.

Table 4. Characteristics of the redox processes occurring in the complexes (c.) of mitochondrial respiratory chain. The route of electron flow within the protein and quantity of pumped proton per electron are also mentioned^{2,28}.

c.	electron donor (E_{m7} , vs SHE)	cofactors (E_{m7} , vs SHE)	electron acceptor (E_{m7} , vs SHE)	ΔE^0 , mV	ΔG^0 , kJ/mol	$\frac{\text{H}^+}{\bar{e}}$
1	NADH (-315 mV)	FMN (-340 mV), FeS-clusters: N3, N1b, N4, N5, N6a, N6b, N2 (-250/-30 mV)	UQ (+45 mV)	360	-70	2
2	succinate (+30 mV)	FAD (-65 mV), Fe_2S_2 (+10 mV), Fe_4S_4 (+175 mV), Fe_3S_4 (+65 mV), heme <i>b</i> (+36 mV)	UQ (+45 mV)	15	-3	0
3	UQH_2 (+45 mV)	heme <i>b_L</i> (-40 mV), heme <i>b_H</i> (+40 mV), FeS (+280 mV), cyt <i>c_I</i> (+220 mV)	cyt <i>c</i> Fe(III) (+235 mV)	190	-37	1
4	cyt <i>c</i> Fe(II) (+235 mV)	Cu_A (+240 mV), heme <i>a</i> and heme <i>a₃</i> (+220 and +380 mV), Cu_B (+340 mV)	O_2 (+815 mV)	580	-110	2

It was proposed³⁰ that the optimal potential difference for redox reactions occurring in the cell is $\Delta E^0 = 150 - 200 \text{ mV}$.

In the natural conditions some complexes (II, V) work as dimers and all the complexes in general are gathered together in proximity. This arrangement is supposed to increase the efficiency of the respiratory chain. Several models were proposed to describe the structural types of such respirasomes^{31,32}.

Cytochrome proteins and heme cofactors

The complexes III and IV and cyt *c* are included in the group of the proteins called cytochromes. The cytochrome is the heme containing protein which principal function is to support electron transfer. The cytochrome classification is based on spectroscopic properties and the utilized names are usually trivial³³.

Heme is a tetrapyrrolic macrocycle chelate (porphyrin, 22 π -electrons) of an iron atom that can be reversibly reoxidised. The metal can be found in Fe(II) (ferroheme), Fe(III) (ferriheme) and Fe(IV) oxidation states^{33,34}. The mid-point potential of the heme can be tuned by type of core structure (Fig. 11), type of axial ligands (determining spin-state) and environmental parameters such as pH, solvent exposure/accessibility, ion strength, etc.^{35–37}

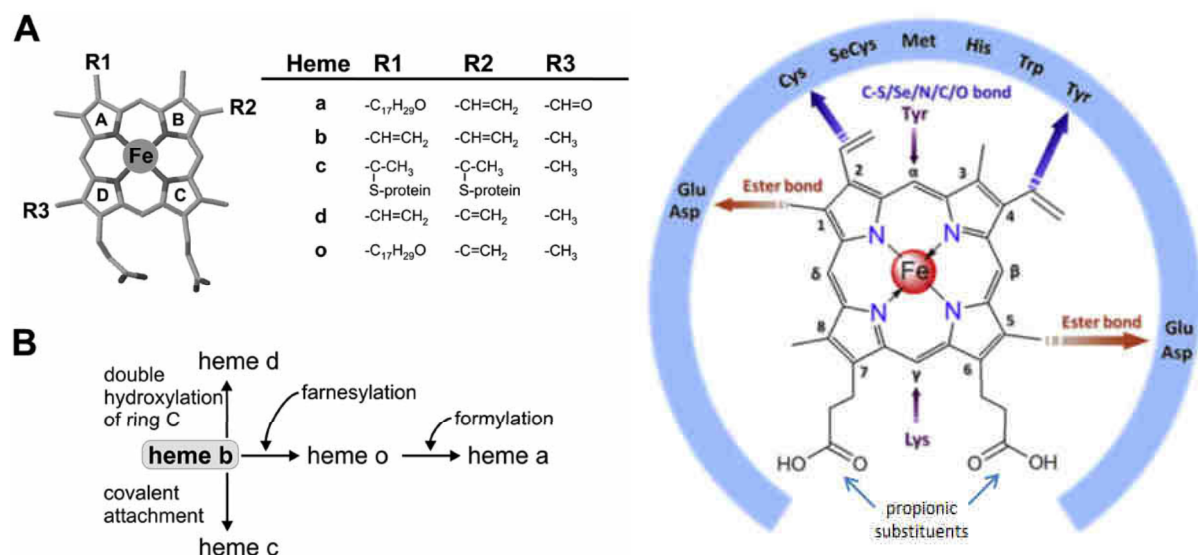


Fig. 11. Left: natural heme structures (A) and a scheme of biosynthesis (B)³⁸. Right: possible heme covalent bonding with protein scaffold encountering in the nature.

The core structures are based on the heme *b* (protoheme IX) which is attached to the protein only through axial ligands. Heme *o* is derived from heme *b* through addition of long farnesyl tail. Oxidation of the heme *o* leads to the formation of heme *a*. Additionally, heme *b* can be a precursor of heme *d* which possess the chlorin structure (20 π -electrons). In heme *d* the presence of the propionate group in the 6th position leads to the formation of γ -spirolactone. The 5th and 6th positions are additionally hydroxylated. All four hemes *b*, *o*, *a*, *d* are not covalently attached to the protein, but the heme *c* which is also originated from heme *b* is covalently tethered to the protein through thioester bonds of vinyl side chains and Cys protein residues³⁸.

Prokaryotic respiratory chains

Since prokaryotes preceded eukaryotes in evolution, different strategies to develop the optimal respiratory chain were observed^{39–42}. Due to this, a great diversity of prokaryotic electron transport chain types can be found in Nature. For aerobic conditions and proton gradient formation the main differences (compared to *Eucaria*) are as follows:

- NADH dehydrogenases: NDH-1 and NDH-2. If NDH-1 is homologue to the mitochondrial complex I, then NDH-2 can be expressed only in prokaryotic cell under microaerophilic conditions and function with lower efficiency.
- complex IV. Some types of the terminal oxidases can employ UQH₂ and/or MQH₂ as a substrate. Some can be expressed at microaerophilic conditions and show differences in the structure (*vide infra*). Only bd-oxidases do not have homologues in eukaryotic cell.
- complex III. Since some prokaryotic complex IV can utilize quinol as substrate complex III is not required in some prokaryotic respiratory chains. Additionally, it can form *pmf* or function as regular complex III.
- The mediating molecules can include different types of quinones (UQ, DMQ, MQ, PQ, etc.) and some species do not hold cyt *c*.
- The electron injection into respiratory chain can be done through: complex I (or other dehydrogenase, in general), quinone, or cyt *c*.

The energetic efficiency of the prokaryotic respiratory chain is usually low. This is due to substitution of the canonical complexes I, III, IV with noncoupled or partially coupled electron transfer pathways².

For example, the respiratory chain in the cell of *E. coli* contains in high aerobic conditions NDH-1, SQR (complex II), UQ-8, *bo*₃-oxidase (complex IV). When the oxygen decreases in the environment the bacteria switches its respiratory chain to a chain containing NDH-2, MQ and DMQ, *bd*-oxidase (complex IV)⁴². This transition induces the decrease of the respiration efficiency: 1H⁺/ē instead of mitochondrial 4H⁺/ē are pumped. Due to this it is possible to continue process of respiration in almost anoxic conditions^{4,41,42}.

ROS

The unspecific leakage of electrons to oxygen provokes the generation of reactive oxygen species (ROS). The main sources of the ROS production are semiquinones, flavins, FeS-

clusters of nonheme proteins with a redox potential close to O_2/O_2^- (-330 mV). Around 1-2% of the consumed oxygen is involved in ROS formation at the level of complex I, complex III and with a lesser extent at complex II.^{2,43}

Quinols

Quinones are low-weight electron mediating molecules with polar head-group and isoprenoid chain. Depending on the organism the type of head-group and the length of the tail can vary. Moreover, upon different conditions a prokaryotic cell can express different sets of quinones, which are suitable for the corresponding redox couples (table 5). The most widespread quinones are benzoquinone derivatives, ubiquinones. However, the naphthoquinone derivatives, menaquinones MQs, were created evolutionary earlier. MQs were employed in a more reduced atmosphere with a lesser oxygen concentration⁴⁴. Thereby, the reduced MQ can react with oxygen providing non-catalytic reduction. Due to this the prokaryotes switch from UQ to MQ in microaerobic or anoxic conditions³⁹.

The isoprenoid side chain of quinone consists usually of 6-10 prenyl units which are unsaturated in most of the cases. The extent of the isoprenoid chain saturation depends on the growth temperature of the prokaryotic culture^{30,41}. Nonetheless, the difference in the mid-point potentials comes from modification of the head-group with various substituents and tail length.

Table 5. Reductive potentials of the some quinole/quinone pairs in water/ethanol solution^{45,46}.

redox couple	E_{m7} , mV (vs SHE)
UQH ₂ -8/UQ-8	+ 60
MQH ₂ -8/MQ-8	- 80
UQH ₂ -10/UQ-10	+ 70
UQH [•] -10/UQ-10	- 54
UQ [•] -10/UQ-10	- 230
UQH [•] -10/UQH [•] -10	+ 190

Since the process of the oxidation of the quinol is proton coupled (PCET), a pH dependency of the mid-point potential of the quinol is expected (Fig. 12). It should be noticed that quinol oxidation is performed in several steps with intermediate semiquinone radical (Fig. 13). The semiquinone radical can be stabilised when interacting with protein^{47,48} but is almost undetectable in protic solution (e.g., only 0.5% MQ-7 in *Mycobacterium phlei*). The reduced quinol is more polar than oxidised quinone which probably leads to its preferred location on the break of hydrophobic and hydrophilic phases.

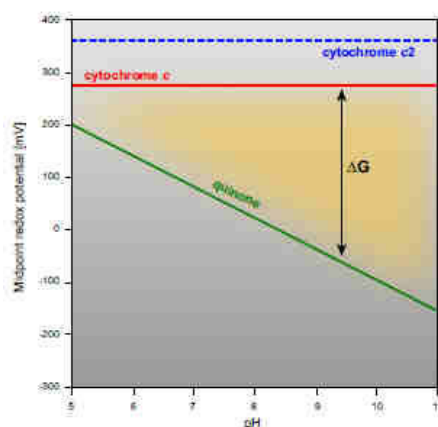


Fig. 12. Comparison of the pH dependency of the midpoint potential of the prokaryotic cyt c_2 - , mitochondrial cyt c - and Q -pools⁴⁰.

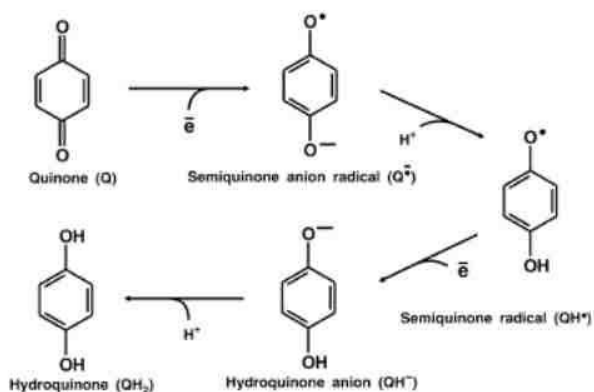
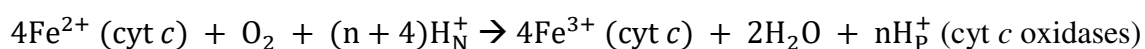


Fig. 13. Stages of the quinone core reduction to quinol. The process involves two protonation and two reduction events: $Q + 2e^- + 2H^+ \rightarrow QH_2$.

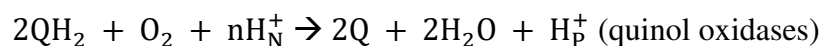
3. Cytochrome *bd* is a prokaryotic complex IV

The main system studied in this thesis is a prokaryotic complex IV, cyt *bd*-oxidase. It is, however, helpful to describe the variety of the complex IV and their mechanism of function for better understanding of cyt *bd* itself.

Complex IV is a terminal oxidase in the electron transport chain. It catalyses the reaction of oxidation of the electron donor (cyt *c* or Q) and reduction of acceptor (O_2). As the result, it couples electron transfer with proton translocation forming proton gradient through proton pumping or Q -loop mechanism. The complexes IV can be classified as cytochrome *c* (CcO) and quinone oxidases, depending on their electron donor. The catalytic reaction can be written as follows:



or



where H_N^+ – protons in the negatively charged aqueous phase (cytoplasm of prokaryote or matrix of mitochondria), H_P^+ – protons in the positively charged aqueous phase (periplasm or outer space in case of Gram-negative or - positive prokaryotes, respectively, or IMS of the mitochondria).

Classification of complex IV

Phylogenetical classification approach results in three superfamilies of the oxygen reductases/complexes IV: heme-copper oxygen reductases (HCOs), *bd*-oxidases and cyanide-insensitive oxidases (CIOs)/alternative oxidases (AOXs)³.

The attribution of the terminal oxidase to the HCOs superfamily is based on the homology of central subunit I. Four types of the HCOs can be distinguished: A- (A1 and A2), B-, C-types and nitric oxide reductases (NOR). All HCOs bear a copper ion and high-spin heme as cofactors in the active site; all HCOs possess proton channels differing in their quantity and amino acid residues types. In particular, A-type HCOs contain D- and K-channels (named according specific amino acid residues) and can be split into A1- and A2-subtypes (A2-type does not contain GluI-278, but possesses conservative YS motif). Also, there are B-type (the residues constituting the channels are not conserved) and C-type (contains just a part of K-channel). NORs demonstrate homology in the subunit I, but they have neither K- nor D-channel and, therefore, do not generate proton gradient. Moreover, NORs utilize protons from positive side of the membrane for their functioning.

To speak in general, all HCOs:

- incorporate at least two hemes in the structure. The high-spin heme, together with copper ion, form a binuclear center (BNC) for oxygen reduction. The second heme is used for transferring of the electrons to this catalytic site. It should be mentioned that copper ion is coordinated with three His-ligands (so-called Cu_B center), one of which is linked to aromatic amino acid residue (Tyr). The last participates in the catalytic reaction, probably, through proton and/or electron donation.
- possess channel(s) for proton uptake and delivery to catalytic site and/or proton pumping.^{2,3,49,50}

The second superfamily of *bd*-oxidases encompasses oxidases that are not homological to HCOs and contain the third heme group instead of copper ion. *bd*-oxidases form the $\Delta\mu\text{H}^+$ gradient through Q-loop mechanism (proton gradient forms through oxidation of the quinol and not through proton pumping) and, hence, in contrast to HCOs, do not represent true pumps.

In spite of possession of BNC (two iron ions) and ability to reduce oxygen (but not to form proton gradient) as complex IV the third group of AOXs does not have any hemes^{51–53}. Therefore, we will not further describe the properties of these enzymes.

Structure of complex IV

Complex IV of the eukaryotic cell in mitochondria, which is *aa*₃-oxydase, comprises 13 subunits (200 kDa in average). The first three subunits are hydrophobic and mainly perform catalytic function since they accommodate all essential cofactors. At the same time, the construction of prokaryotic complex IV is based just on these three pivotal subunits (with total mean mass around 100 kDa); however, auxiliary subunit(s) can be also identified and their presence can be crucial for enzyme stability and function^{2,54,55}. For the convenience, we summarised the structural information in the table 6.

A-type oxidases

The structure of *aa*₃-oxidase (A1-type HCO) from *P. denitrificans* comprises 4 subunits (I, II, III, IV). The second subunit houses archetypal cupredoxin domain Cu_A (two bound copper ions coordinated with His-ligands), the first subunit houses hemes *a* and *a*₃ and Cu_B-centre. The electrons are donated with cyt *c* to Cu_A site through Trp121 residue. Then, the electrons are passed to heme *a* (ls6c, His/His) and, finally, reach BNC that consists heme *a*₃ (hs5c, His) and Cu_B-centre. The distance between Fe and Cu ions in BNC is about 5 Å. The electron transfer between hemes *a* and *a*₃ is conducted through DET or amino acid residues mediation⁵⁶. It is worth mentioning that the presence of the lipids is crucial for (1) heme *a*₃ stabilisation (the farnesyl group interacts with the lipids), and (2) enhancement of proton uptake through D-channel which is under control of subunit III that binds the lipids, and (3) several other functions^{57,58,59}.

*bo*₃-oxidases (A1-type of HCO) are also composed of the 4 subunits, but these enzymes lack Cu_A-centre and use quinol as electron donor to heme *b* (ls6c, 2 axial His) and then flow to BNC. The BNC consists of heme *o*₃ (hs5c, His) and Cu_B. There might exist two sites for quinone binding, the role of the second Q-site could be in the stabilization of semiquinone radical that mediates electron transfer from quinone to heme *b*^{60–62}. However, according to the last report there might be only one Q-site.

The two subunit (I/III, II/c) containing *caa*₃-oxidase is included in A2-type HCOs. The electron pathway starts from Cu_A-site, continues with heme *a* (ls6c, 2 axial His) and

terminates at the BNC: Cu_B and heme *a*₃ (hs5c, His). The proton channels are characteristic to A2-type (*vide supra*)^{63,64}.

Table 6. Structural characteristics of the terminal oxidases and the description of electron pathways. BNC – binuclear centre or its analogue (catalytic site); hs or ls – high or low spin; Nc – coordinated with N ligands.

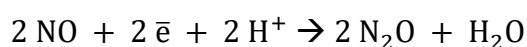
classification			complex IV	organism	subunits (main+auxiliary)	redox active cofactors (properties), BNC	natural electron donor	electron pathway	proton channels	ref.
HCOs	A-type	A1	<i>aa</i> ₃	mitochondria (bovine)	3+10	Cu _A , heme <i>a</i> , <u>heme <i>a</i>₃</u> , Cu _B	cyt <i>c</i>	cyt <i>c</i> → heme <i>a</i> → BNC → O ₂	D, K, ±H/E	65,66
				<i>P. denitrificans</i>	3+1		cyt <i>c</i> ₅₅₂ , cyt <i>c</i> ₅₅₀			56,67
		A2	<i>bo</i> ₃	<i>E. coli</i>	4	heme <i>b</i> (ls6c, 2 His), <u>heme <i>a</i>₃</u> (hs5c, His), Cu _B	UQ-8	UQ-8 → (Q _L →) Q _H → heme <i>b</i> → BNC → O ₂		60–62
			<i>caa</i> ₃	<i>R. marinus</i>	2	Cu _A , heme <i>a</i> (ls6c, 2 His), <u>heme <i>a</i>₃</u> (hs5c, His), Cu _B	HiPIP [53]	HiPIP → Cu _A → heme <i>a</i> → BNC → O ₂		63
	B	<i>ba</i> ₃	<i>T. thermophilus</i>	2+1	heme <i>b</i> (ls6c, 2 His), <u>heme <i>a</i>₃</u> (hs5c, 1 His), Cu _B	cyt <i>c</i> ₅₅₂ [31]	cyt <i>c</i> → Cu _A → heme <i>b</i> → BNC → O ₂	K	68–70	
	C	<i>cbb</i> ₃	<i>P. stutzeri</i>	3+1	3 heme <i>c</i> (ls6c, 2 His/His, His/Met), heme <i>b</i> (ls6c, 2 His), <u>heme <i>b</i>₃</u> (hs5c, His), <u>Fe_B</u> (3c, 3 His)	cyt <i>c</i> ₄	cyt <i>c</i> ₄ → heme <i>c</i> → heme <i>b</i> → BNC → O ₂	K	71	
	NOR	cNOR	<i>P. denitrificans</i>	2	heme <i>c</i> (ls6c, His/Met), heme <i>b</i> (ls6c, 2 His), <u>heme <i>b</i>₃</u> (hs5c, His), <u>Fe_B</u> (3c, 3 His)	cyt <i>c</i> ₅₅₁ , azurin	cyt <i>c</i> ₅₅₁ → heme <i>c</i> → heme <i>b</i> → BNC → NO	E	72, 73	
<i>bd</i>			<i>bdI</i>	<i>E. coli</i>	2+1	heme <i>b</i> ₅₅₈ (ls6c, His/Met), <u>heme <i>b</i>₅₉₅</u> (hs5/6c, His, Glu), <u>heme <i>d</i></u> (hs5c, Glu)	UQ-8, MQ-7	Q → heme <i>b</i> ₅₅₈ → BNC → O ₂ or Q → heme <i>b</i> ₅₅₈ → heme <i>b</i> ₅₉₅ → heme <i>d</i> → O ₂	CydA, CydB	6,54

B- and C-type oxidases, NORs

B-type ba_3 -oxydase is the smallest CcO and it contains three subunits. Electron flow as follows: cyt $c \rightarrow Cu_A \rightarrow$ heme b (ls6c, 2 His) \rightarrow BNC: Cu_B and heme a_3 (hs5c, 1 His $\rightarrow O_2$)
The D-pathway in ba_3 -oxidase was lost in the course of evolution but remaining K-like-channel is much larger at the expense of proton translocation efficiency ($0.5H^+/e^-$).^{63,68–70,74–77}

C-type cbb_3 -oxidases are the four subunit (N, O, P, M) proteins. The electrons pass from cyt c to hemes c , and then through heme b to BNC (heme b_3 and Cu_B)^{71,75,78,79}.

NO-reductases (NOR) are evolutionary close to cbb_3 -oxidases³. However, NOR use NO as acceptor and cyt c (cNOR) or quinone (qNOR) as a donor of the electrons:



cNOR is a two subunit protein with electron flow: cyt $c_{551} \rightarrow$ heme c (ls6c, His and Met) \rightarrow heme b (ls6c, 2 His) \rightarrow BNC: heme b_3 (hs5c, His) and Fe_B (Fe ion with 3 His coordination)^{72,80}.

Table 7. Comparison of the efficiency of the terminal oxidases and affinity to the oxygen.

classification			c. IV	organism	H _{transferred} /O ₂	H ⁺ /e ⁻ ratio	K _m (O ₂)
HCOs	A-type	A1	<i>aa</i> ₃	<i>P. denitrificans</i>	4	2	0.1 - 1 μM [9,10]
			<i>bo</i> ₃	<i>E. coli</i>	4	2	0.15– 0.35 μM ^{4,81} [7,8,]
	B-type		<i>ba</i> ₃	<i>T. thermophilus</i>	3	0.4-0.5 ^{63,75}	nM range ⁸²
	C-type		<i>cbb</i> ₃	<i>P. stutzeri</i>	2	0.2-0.5 ⁷⁸	for <i>B. japonicum</i> 7-40 nM ^{65,83,84}
<i>bd</i> -oxidases			<i>bd</i>	<i>E. coli</i>	2	1 ^{4,12}	3-8 nM ^{81,82}

Usually, HCO terminal oxidases bear inside supplementary cofactors like Mg^{2+} , Mn^{2+} and/or Ca^{2+} but they are not redox active. It is also important to note that the oxygen affinity is varied: B, C-type oxidases possess lower constants of dissociation in comparison to A-type

(table 7), and, thus, predominate in the cells cultivated in microaerobic conditions. Moreover, in the environment with decreased oxygen pressure it is oxidases of *bd* superfamily that can be produced by prokaryotic cells.

bd-oxidases

The crystallographic structure of cyt *bd* from *Geobacillus thermodenitrificans* with resolution of 3.6 Å was obtained recently⁵. *bd*-oxidases have three subunits (I/A, II/B, X/S), and three cofactors (hemes *b*₅₅₈, *b*₅₉₅, *d*) (Fig. 14-16).

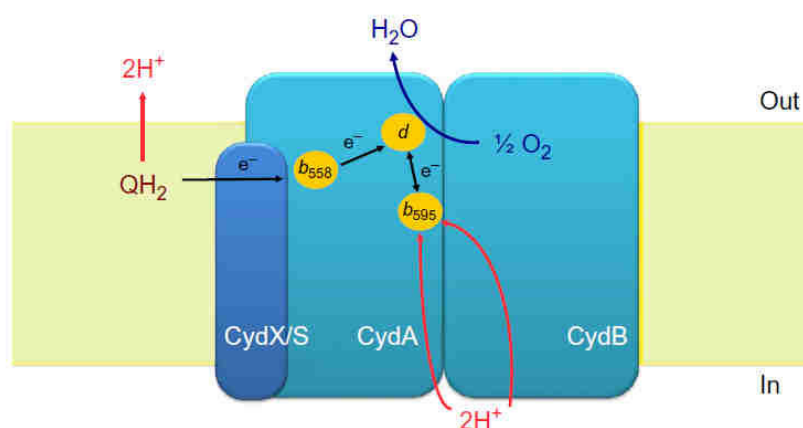


Fig. 14. Probable organisation of the electron transport in cyt *bd* (from *G. thermodenitrificans*)¹⁷.

Two major subunits CydA and CydB are characterized with the same fold: nine transmembrane helices grouped in four-helix bundles with one peripheral helix. Such heterodimerisation could result from gene duplication. The difference between these two subunits is a hydrophilic Q-loop localized in CydA which is believed to bind the quinol substrate. Hydrophobic interactions stabilise the dimer. The third auxiliary subunit CydX is a single α -helix and was shown to stabilise the protein upon changes of the redox-state (probably heme *b*₅₅₈ stabilisation), increase sensitivity to H_2O_2 and inhibitors^{54,55,85,86}. This subunit is also necessary for the assembly of cyt *bd*⁵⁴. The general secondary structure of the protein is α (~70%), β (~4%), turns (~10%), and disordered structure (~16%). The alignment of the amino acid sequences of cyt *bd* from *G. thermodenitrificans* and *E. coli*⁵ is shown in Annex 2.

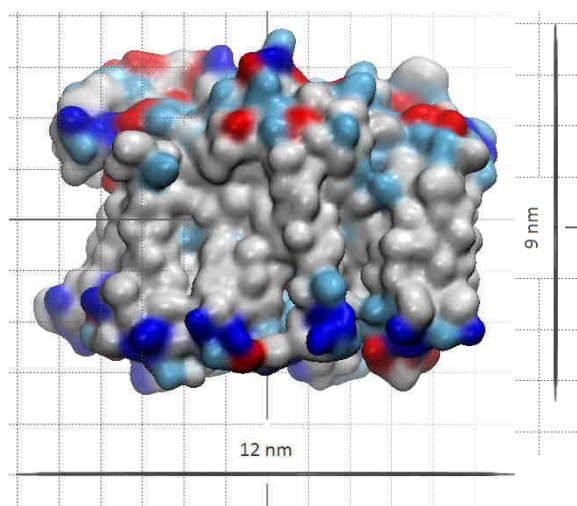


Fig. 15. Crystal structure of cyt *bd* from *G. thermodenitrificans* with resolution 3.6 Å. The charges at the surface are shown (red – negative, blue – positive, navy blue – polar). [pdb 5IR6]⁵

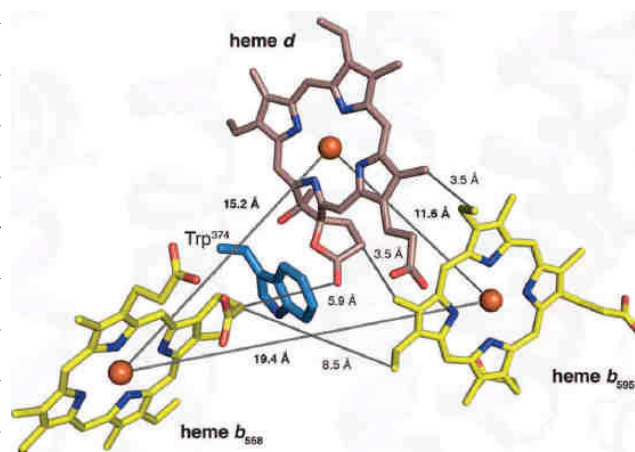


Fig. 16. Relative localisation of the hemes in cyt *bd* from *G. thermodenitrificans*. The distances Fe-to-Fe (15.2 vs 19.4 Å) and edge-to-edge (5.9 vs 8.5 Å) are provided. Trp residue between hemes *d* and *b*₅₅₈ is shown. [pdb 5IR6]⁵

The prosthetic groups - heme *b*₅₅₈, heme *b*₅₉₅, heme *d* - are all located in CydA subunit and form a triangle (Fig. 16) close to periplasmic side of the protein. Heme *b*₅₅₈ is in proximity to the Q-loop and it is the primary electron acceptor. Heme *b*₅₅₈ is a six-coordinated (His/Met) low-spin heme. Analysis of the distances between the hemes (Fig. 16) allows us to propose that the electrons flow to heme *d* directly. It is in line with observation that electron flow from heme *b*₅₅₈ to hemes *b*₅₉₅ and *d* is not slower than the one between heme *d* and *b*₅₉₅²⁰. Nonetheless, it was suggested earlier that *b*₅₉₅/*d* forms a BNC in analogy to HCOs. The Fe-to-Fe and edge-to-edge distances are both shorter in case of *b*₅₅₈/*d* hemes relatively to *b*₅₉₅/*d* hemes. The role of the hexacoordinated (His/Glu) high-spin heme *b*₅₉₅ is, thus, not clear. It could be that heme *b*₅₉₅ pools an electron (in analogy with heme cofactor in complex II)⁸⁷, serves as a proton donor or secondary oxygen-binding site^{4,12}. The main site of the oxygen reduction reaction, the heme *d*, is a pentacoordinated high-spin heme with a Glu residue as axial ligand. The highly conserved Trp374 is supposed to play a role of electron transporter between *b*₅₅₈ and *d* hemes, which is also found in HCOs (Trp as a mediator between).

In the structure there are several access points to the cofactors for different ligands¹⁷. Two of them lead to heme *b*₅₉₅ and are hydrophobic. Heme *b*₅₅₈ is reachable from the large access point from the membrane side close to Q-loop, it is hydrophobic and bears one charged (Asp) residue. The access point to heme *d* probably serves for direct interaction with oxygen, since

no special O₂ channel was discovered. This may be the reason for the high O₂ affinities in this protein superfamily. Based on the X-ray structure for cyt *bd* from *G. thermodenitrificans* this access point was found as more charged than the others, which raises some question concerning delivery of the apolar oxygen molecule. There are two proton transfer pathways (CydA and CydB) leading from cytoplasm to active site of the *bd*-oxidase^{4,5,12,20,81,88}.

The main structure of the quinone-binding site is the so-called Q-loop: periplasmic hydrophilic disordered amino acid sequence with short α -stretch and antiparallel β -sheet located near heme *b*₅₈₅^{5,88}. It is proposed that Q-loop participate in the first step of recognition, binding and electron transfer to heme *b*₅₈₅. Depending on the length of the sequence cyt *bd* can be classified into long (e.g., *E. coli*) and short Q-loop (e. g., *G. thermodenitrificans*)^{6,20}. The long Q-loop possesses a 65 amino acid insertion when compared to the short one; and it is possible that CydX interacts with it in case of the long Q-loop cyt *bd*. The highly conservative sequence **GWXXXEXGRQPW** was revealed through sequence alignment of this hydrophilic region⁸⁹. It was shown that residues Arg391⁸⁸, Arg298, Tyr290, Lys252 and Glu257⁹⁰ in Q-loop determine the quinol oxidation ability of cyt *bd*, and, in particular, Glu280 interacts with 2- and 3-methoxy group of UQ⁹¹. There are also several Pro, Gly, Phe and Trp residues that could maintain the quinol-binding pocket structure. Cyt *bd* possesses only one Q-binding site and does not have tightly bound quinol (in contrast to cyt *bo*₃). The process of quinol oxidation (2QH₂) is strongly coupled to the 4 \bar{e} oxygen reduction (1O₂) and the semiquinone radical was observed in one work⁹². It was also proposed that electron transfer could circumvent quinol-binding site⁹³ and this additional electron pathway is not connected with Q-loop mechanism. It was assumed⁹⁴ that the large hydrophobic pocket is located near the Q-oxidation site. The dimensions of the pocket could be quite vast since the protein can accommodate various types of the natural quinols (MQ, DMQ, UQ, PQ)^{30,95}.

For *E. coli* two types of *bd*-oxidases were characterised: *bd*-I and *bd*-II. There are some physiological differences between them: cyt *bd*-II has lower affinity to oxygen and more sensitive to gaseous inhibitors (CO, NO). However, it is cyt *bd*-I that was more well-studied.

Catalytic cycle

aa₃-oxidase

The catalytic cycle of complex IV was much studied in the case of mitochondria-like *aa₃*-oxidase. One turnover encompasses several intermediates. Here we will describe the main stages of the cycle (Fig. 17, table 8). Under natural aerobic conditions, the enzyme undergoes a 2e⁻-reduction. Oxidized *aa₃*-oxydase (or so-called fully oxidized/as prepared/natural oxidized/O-state) obtains two electrons from two cytochromes *c* successively (E- and R-states). The electrons reach binuclear site and reduce Cu(II) to Cu(I) in the Cu_B centre (E-state), and then Fe(III) is reduced to Fe(II) in heme *a₃* (R-state). Reduction of the copper ion leads to the opening of the oxygen channel. At first, an O₂ molecule weakly binds to CuI and then to heme *a₃* (FeII) with formation of ferric (FeIII)-superoxide complex (A-state). If heme *a* is oxidized the reaction proceeds through Tyr residue oxidation, which donates proton as well and forms radical (P_M-state). P_M-intermediate is reduced that leads to F compound with Tyr anion. The successive reduction regenerates the initial O-state of the enzyme.

Thus, to break the O-O bonding 4 electrons are utilized (2 from heme *a₃*, 1 from Cu_B, 1 from Tyr). The cleavage of this bond O-O may be a cause of the proton translocation. On the other hand, the proton pumping may be caused due to negative charge compensation at heme groups upon oxidase reduction. The backflow (to N-side) of the protons is thermodynamically unfavorable⁹⁶. It maintains proceeding of the proton translocation through Grotthuss mechanism to the P-side of the membrane, against the electrochemical gradient⁹⁷⁻¹⁰³.

For the B-type oxidases the cycle is, in general, the same. The exception is at O → E, P → F transitions where there is no proton pumping. That is due to the absence of a proton transfer to binuclear centre for F-state formation where the protons are taken from the nearby located protonable group^{75,104}. The mechanism of C-type oxidases is less well-studied¹⁰⁵.

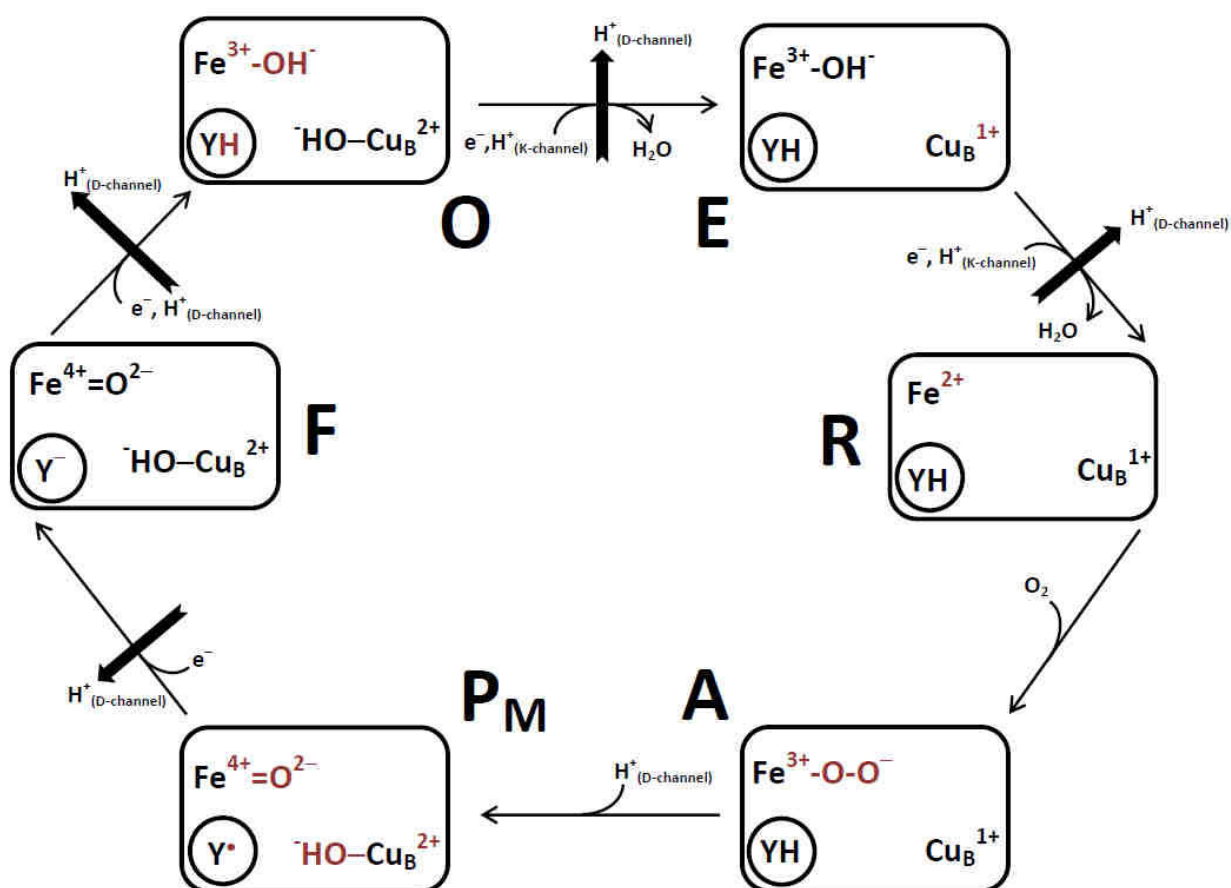


Fig. 17. Proposed catalytic cycle of aa_3 cytochrome c oxidase. In the frame there is a schematic drawing of BNC of the enzyme. To simplify, the heme a_3 is depicted as Fe^{3+} and aromatic (Tyr) residue as Y. The changes in the BNC during catalysis are highlighted in red.

Table 8. Intermediates of the catalytic cycle of the aa_3 -oxidase with precision of the oxidation state and ligation of the redox active cofactors.

state	Oxidation and ligand binding state				
O	$Fe(III)_{a3}-OH^-$	$Cu(II)_B-OH^-$	TyrOH	$Cu(III)_A$	$Fe(III)_{a3}$
E	$Fe(III)_{a3}-OH^-$	$Cu(I)_B$	TyrOH	$Cu(II)_A$	$Fe(III)_{a3}$
R	$Fe(II)_{a3}$	$Cu(I)_B$	TyrOH	$Cu(II)_A$	$Fe(III)_{a3}$
A	$Fe(III)_{a3}-O_2^-$	$Cu(I)_B$	TyrOH	$Cu(II)_A$	$Fe(III)_{a3}$
P_M	$Fe(IV)_{a3}=O^{2-}$	$Cu(II)_B-OH^-$	TyrO $^\bullet$	$Cu(III)_A$	$Fe(III)_{a3}$
F	$Fe(IV)_{a3}=O^{2-}$	$Cu(II)_B-OH^-$	TyrO $^-$	$Cu(III)_A$	$Fe(III)_{a3}$

bd-oxidase

Interestingly, the catalytic cycle of cyt *bd* oxidase is relatively similar to the one of HCOs^{106–109}. It was initially proposed that *b*₅₉₅/*d* play the role of BNC as in HCOs, but the recent structure and identified intermediates do not confirm this hypothesis.

Cyt *bd* binds oxygen in fully reduced state R^1 , so-called mixed valence state (Fig. 18). The ferrous-oxy heme *d* adduct A^1 , one-electron reduced oxygen bound state, is highly stable. One quinol molecule donates 2 electrons to cyt *bd* transforming A^1 to A^3 adduct. This transition does not lead to a proton gradient. Two protons from the cytoplasm enter the protein and bind to one oxygen atom, resulting in the formation of one molecule H_2O . Then, the ferryl-intermediate radical F^* forms. In order to enter this state, heme *b*₅₉₅ ($Fe^{2+} \rightarrow Fe^{3+}$), heme *d* ($Fe^{2+} \rightarrow Fe^{4+}$) and the heme *d* porphyrin ring deliver 4 electrons to the O-atom. Thus, an uncoupled electron is left on the heme *d* porphyrin ring. Earlier it was supposed¹¹⁰ that this state is a peroxy-complex of heme *d* (Fe-O-OH) and the F^* was, thus, called P-state. In the next stage of the cycle, one electron migrates from heme *b*₅₅₈ to stabilise the porphyrin π -cation radical with formation of the F-intermediate. The F-state interacts with the second quinol molecule which leads to regeneration of the R^1 -state and electric potential generation ($2H^+$ goes to the P-site of the membrane).

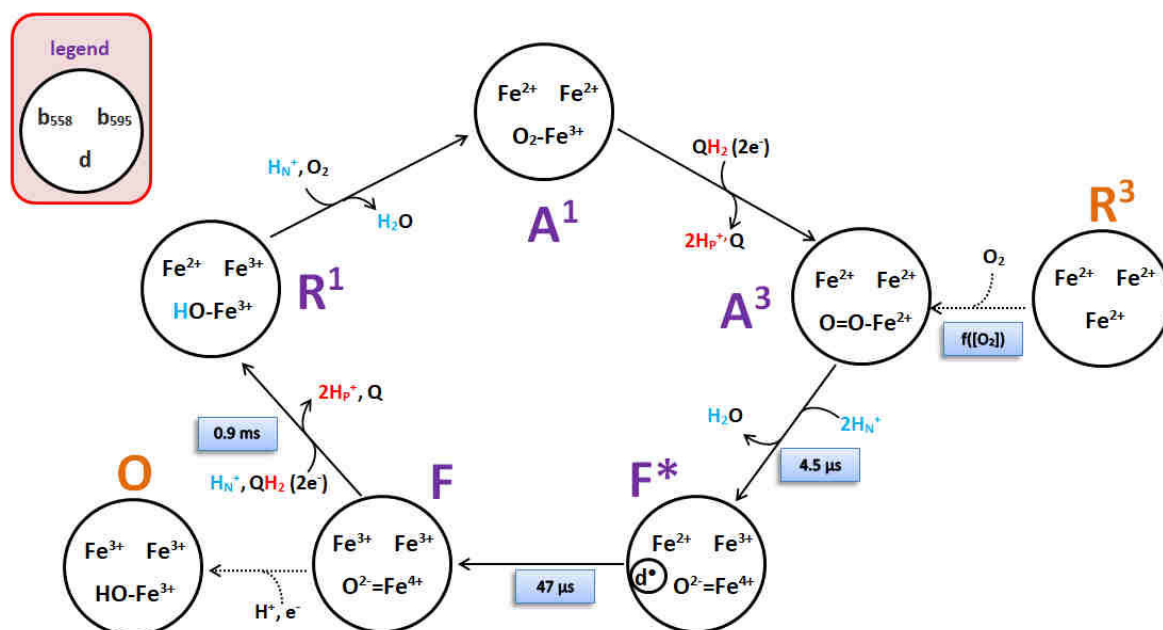


Fig. 18. Catalytic cycle of cyt *bd*. The superscripts of the state labels correspond to electron quantity injected in the system. $R^3 \rightarrow A^3$: 1.4 μs for 365 μM O_2 ; 0.9: 0.6–1.1.

Under steady-state equilibrium conditions, the protein stays most of the time in the A¹ (40%) and F (40%) states. In other words, the hemes *b*₅₅₈ and *b*₅₉₅ are mostly oxidised (>70 and >90%, respectively) and heme *d* (80%) is equally reduced (in A¹ state) and oxidised (in F-state).

Several concomitant intermediates were observed. The O-state can be formed in case of the bound quinol can donate only 1 electron. As compared to the single-electron state R¹, the three-electron reduced R³ species are characterised with lower affinity to O₂ and other heme *d* ligands (NO, CO) suggesting that the binding constant is in dependence of the redox-state of the hemes. It was also shown that R¹ state cyt *bd* can exist in two forms: opened (accessible to O₂) and closed (inaccessible to O₂).

The pH-dependent activity of the protein does not show a volcano-like optimum curve: it starts to rise from pH5.5 reaching a plateau at pH7.5. The activity also depends on the nature and amount of detergent and lipids^{12,37}.

Function

The principal function of complex IV is to generate the *pmf*. However, it is not the sole opportunity as far as *bd*-oxidase is concerned. Cyt *bd* being expressed under microaerophilic conditions and characterised with high affinity for oxygen can play the role of a scavenger: protection of O₂-sensitive enzymes. It can also be regarded as an electron sink for ROS and RNS¹¹¹. Furthermore, the peroxidation reaction ($\text{H}_2\text{O}_2 + 2\text{e}^- + 2\text{H}^+ \rightarrow 2\text{H}_2\text{O}$) was also observed and the catalase ($2\text{H}_2\text{O}_2 + 2\text{e}^- + 2\text{H}^+ \rightarrow 2\text{H}_2\text{O} + \text{O}_2$) reaction was absent¹¹². The production of the H₂O₂ is the side effect of anaerobic fumarate dehydrogenase. Thus, cyt *bd* could serve as a scavenger of peroxide. Finally, a low inhibition effect was shown for KCN and such gasotransmitters as H₂S, CO and NO which are produced by eukaryotic organism to struggle with pathogens¹⁷. All these allows the prokaryotes to maintain bioenergetics processes (*pmf* generation) in the niches lacking oxygen and to circumvent hostile environment conditions such as the presence of toxic sulphide¹¹³, oxidative (O₂, ROS, H₂O₂) and nitrosative (RNS, NO) stress¹⁰⁸. Cyt *bd* is expressed under unfavourable conditions as alkaline pH, high temperature, etc. Thus, cyt *bd* is important component of the respiratory chain of many pathogens such as *Mycobacterium tuberculosis*, *Staphylococcus aureus*, *Shewanella oneidensis*, *Shigella flexneri*, *Enterococcus faecalis*, *Salmonella enterica*, *Brucella spp.*, *Clostridia spp.*, *Listeria sp.*, *Bacillus subtilis*, *Klebsiella pneumoniae*, and many others. Cyt *bd* plays a role in the adaptability and virulence of these pathogens⁴².

II. Inhibitors: role in the protein characterisation

Inhibition studies help to understand the mechanism of protein function and structure of active site. The determined parameters in the experiment are usually associated with the theory of enzyme kinetics^{27,114–116}. Based on them several types of catalysis and inhibition modes were defined.

1. Kinetic parameters of enzyme catalysis

The kinetics of the reaction of the enzyme (total concentration $[E]_0$) and substrate S with formation of a transient enzyme-substrate complex which then yields the product P :



can be described with Michaelis-Menten equation:

$$v_0 = k_2 \frac{[E]_0[S]}{K_M + [S]} = \frac{v_{max}[S]}{K_M + [S]}, \text{ where } K_M = \frac{k_{-1} + k_2}{k_1} \quad (5)$$

The *Michaelis-Menten constant* K_M is equal to substrate concentration when half of enzyme active sites are bound to the substrate and, thus, the reaction rate reaches the half-maximal value. K_M is identical to *substrate dissociation constant* K_S if the condition of $k_2 \ll k_{-1}$ is fulfilled, that is, $K_M \approx K_S = \frac{k_{-1}}{k_1}$. And therefore, K_M^{-1} - can be interpreted as the affinity of the enzyme for the substrate. The constant shows dependency on pH, temperature, ion strength, substrate type and so on. Thus, it is a characteristic of a specific system in specific conditions. In most cases, the values of the constant are found in the range of $[10^{-1}; 10^{-7}]$ M.

Knowing $[E]_0$ and v_{max} , one can determine the so-called *turnover number/catalytic constant* k_{cat} , since $v_{max} = k_2[E]_0$. k_{cat} (k_2 in the eq. 5) is the quantity of substrate molecules (or moles of substrates) utilised by protein to produce product per unit of time with the condition that all enzyme molecules are involved in the reaction. k_{cat} usually shows values from 1 to 10^5 s^{-1} . However, if the purity of the enzyme and/or the active site quantity is unknown the turnover number is substituted with *specific activity* (which is defined as the enzyme quantity needed to produce 1 μmol of the product per unit of time). In physiological conditions $[S]/K_M < 1$ and, thus, $v_0 = \frac{k_{cat}}{K_M} [E]_0[S]$. This leads to the definition of the *enzyme efficiency*

as k_{cat}/K_M . Thus, the highest efficiency of the enzyme can be reached with high catalytic rate k_{cat} together with the high affinity to substrate $1/K_M$.

The multisubstrate catalysis can be classified in several mechanisms (Fig. 19) depending on the order of the substrate binding and the product release:

- a) *Ternary-complex mechanism*. The first stage includes enzyme binding with several substrates and the second stage product release.
 - a. *Ordered*. The binding order of the substrate depends on substrate type
 - b. *Random*. The enzyme binds substrate in random order.
- b) *Ping-pong mechanism*. The enzyme turns over the first product and only then turns over the second one.

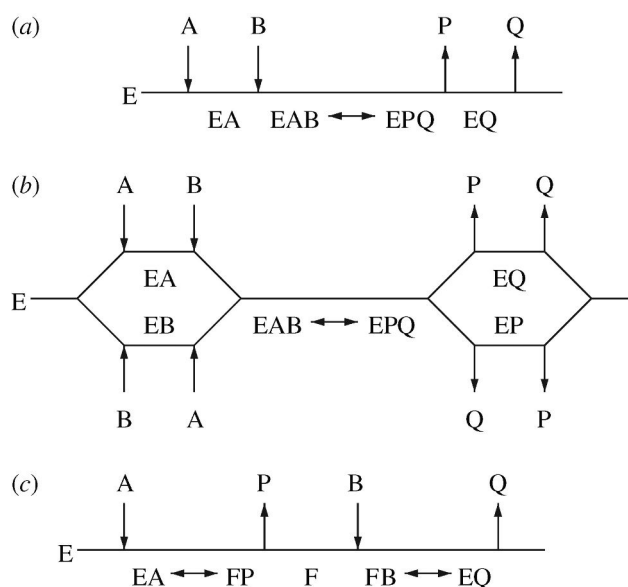


Fig. 19. Diagram of the two substrate and two product (bi-bi) catalysis. a) ordered mechanism, b) random mechanism, c) ping-pong mechanism. The A is a leading substrate, B is following substrate¹¹⁷.

Therefore, the interaction of the macromolecule can be accomplished with several ligands due to possession of several binding sites. This so-called *allosteric* type of interaction is connected with (*anti*)*cooperative effect* when the binding of molecule $n - 1$ influence the binding constant of molecule n . The ligand that forms the complex with the macromolecule and that changes the binding constant for the next binding ligand is named *effector*. The interaction with different effectors induces *heterotropic effect*. When the ligands are identical the *homotropic effect* takes place. The cooperative effects can be described through the Hill equation (not shown) and Hill coefficient n ($n = 1$ – not any cooperativity, $n > 1$ - cooperativity, $n < 1$ - anticooperativity; in ideal situation n reflects the quantity of binding

sites). Hill equation is an empirical description of the process and does not explain the mechanism of interaction. Several models were proposed for allosteric interaction (Concerted, Sequential, linlog kinetics model, etc.).

2. Influence of the inhibitors on enzyme kinetics

Inhibitor classification

A inhibitor is a low-weight molecule that reduces or completely inhibits enzyme activity.

The inhibitor binding can be *reversible* or irreversible. In the former case, the equilibrated system can demonstrate three modes of behaviour: competitive, uncompetitive and mixed inhibition, - with corresponding kinetic parameters changes (table 9)^{27,114–116,118–120}.

- A. The *competitive* inhibition model includes binding of the inhibitor I and substrate S in the same site of the enzyme. Complex EI already cannot bind substrate molecule. In this situation, the inhibitor has to resemble the substrate. The reaction rate is described as:

$$v_0 = \frac{v_{max}[S]}{K_M(1 + \frac{[I]}{K_I}) + [S]} \quad (6)$$

where $K_I = \frac{[E][I]}{[EI]}$ – inhibition constant (M), $K_M(1 + \frac{[I]}{K_I}) = K_M\alpha = K_M^{app.}$ is apparent (substrate) affinity. As one can see, the lower the K_I the more effective the inhibitor. Upon competitive inhibition, the substrate behaves as if it was too diluted. Since the system is reversible then the effect of the competitive inhibitor can be diminished through substrate concentration increase. From the mathematical point of view, the $v_0 \rightarrow v_{max}$ when $[S] \rightarrow +\infty$ leads. Thus, the inhibitor does not affect turnover number of the enzyme.

- B. The second inhibition type is *uncompetitive/anti-competitive* inhibition during which the inhibitor can bind enzyme-substrate complex only. Therefore, the inhibitor does not necessarily resemble substrate and if it binds before the substrate it does not distort the active site. In general, the inhibitor does not affect substrate affinity, but the catalytic function is diminished:

$$v_0 = \frac{v_{max}[S]}{K_M + (1 + \frac{[I]}{K_I'})[S]} \quad (7)$$

where $K_I' = \frac{[ES][I]}{[ESI]}$ – inhibition/dissociation constant, $[S](1 + \frac{[I]}{K_I'}) = [S]\alpha'$ is apparent (substrate) concentration. Uncompetitive inhibition lowers maximal rate by the factor α' (apparent rate: $v_{max}^{app.} = v_{max}/\alpha'$) and, as compared to competitive inhibition, it cannot be restored to initial values just by addition of the higher substrate quantity. When $[S] \ll K_M$ the effect of the inhibitor is almost absent.

C. *Mixed* inhibition supposes that the inhibitor can bind to both the free enzyme and enzyme-substrate complex. It is presumed that inhibitor has allosteric binding site, that is, different from the active site. However, the interaction with allosteric site induces changes in active site and catalysis. The reaction rate obeys the equation:

$$v_0 = \frac{v_{max}[S]}{\alpha K_M + \alpha'[S]} \quad (8)$$

Due to the inhibition factors α and α' before K_M and $[S]$ as in competitive and uncompetitive inhibition, respectively, the mixed inhibitors are effective both at low and at high concentrations. The case when $K_I' = K_I$ and, thus, $\alpha' = \alpha$ is called *noncompetitive* inhibition which is associated with equal affinity of the inhibitor to enzyme and enzyme-substrate complex.

Table 9. Kinetic parameter changes in the dependence on the inhibition type¹¹⁶.

	without inhibitor	competitive	uncompetitive	mixed (noncompetitive)
$v_{max}^{app.}$	v_{max}	v_{max}	v_{max}/α'	v_{max}/α'
$K_M^{app.}$	K_M	αK_M	K_M/α'	$\alpha K_M/\alpha'$
complex with inhibitor	-	EI	ESI	EI, ESI
substrate affinity	K_S	$\downarrow K_S$	K_S	$\downarrow K_S$
catalysis function	k_{cat}	k_{cat}	$\downarrow k_{cat}$	$\downarrow k_{cat}$
to remove effect	-	$\uparrow [S]$	$\downarrow [S]$	inhibitor is effective at any $[S]$

Upon *irreversible* inhibition, the effectiveness of the inhibitor (or, here, inactivator) is not defined through equilibrium constants, but through the rate of binding. The so-called Michaelis-Menten plot obtained in the experiments with irreversible inhibitor resembles the one obtained in case of mixed inhibitor. However, the irreversible inhibitors only alter the apparent maximal rate, but not the Michaelis-Menten constant. The inhibition rises with time and the complete inhibition can be reached when $[I] \geq [E]$. During irreversible inhibition a covalent bond may form between inhibitor and enzyme^{118,120}.

In some situations the dissociation constant of the EI-complex is so low that the reversible process resembles irreversible inhibition. This kind of inhibitor is called *tight-binding inhibitors*^{120–122}.

Additionally, the *complete/linear inhibition* occurs if the inhibition effect can be described with simple multiplication by $1 + \frac{[I]}{K_I}$ factor. The *partial inhibition* is a type of non-linear inhibition and corresponds to a situation when the rate does not reach 0. The complex ESI upon partial inhibition still possesses reduced catalytic activity. Moreover, *time-dependent inhibition* can be misinterpreted as partial inhibition when the incubation time is too low^{120,123}.

There are different other ways to describe enzyme inhibition types (substrate, product inhibition, etc.). For the rational drug design it is important to develop compounds that could structurally resemble substrate. However, it is necessary that the product of such substrate could form irreversible complex EI. This so-called suicide inhibition is associated with very high specific ligand. This ligand is not active as inhibitor before the interaction with target, but undergoes the paracatalytic reaction with formation of transient compound which inactivates the enzyme instead of the product generation¹²⁴.

3. Inhibition measurements

The inhibition can be characterised through inhibition constant K_I , half-inhibition concentration IC_{50} , or $(I/S)_{50}$. According to Cheng-Prusoff equation¹²⁵, in case of competitive inhibition the IC_{50} can be converted to K_I :

$$IC_{50} = \left(1 + \frac{[S]}{K_M}\right) K_I \quad (9)$$

The IC_{50} depends on the substrate concentration. Thus, it is more useful to compare the results in the form: $(I/S)_{50}$, where I is a half-inhibition concentration and S is the substrate concentration.

For both, uncompetitive and mixed inhibitions, in the excess of substrate ($S \gg K_M$) it can be shown¹²⁵ that IC_{50} is equal to K'_I .

The Cheng-Prusoff IC_{50} - K_I relation is adequate for the situation of classical inhibitors. When one study tight-binding inhibitors the assumption that free inhibitor concentration is no

longer equal to the total inhibitor concentration should be taken into account since Michaelis-Menten kinetics no longer applies. For the classical inhibitors the concentration of the enzyme greatly exceeds the concentration of inhibitor ($K_I \gg [E]_0$). For tight binding inhibitors the inhibition occurs at the inhibitor concentration equal or even less than concentration of the enzyme ($K_I \ll [E]_0$)^{121,122,126}. For the tight-binding inhibitors Cha introduced¹²⁷ the additional member $[E]_0/2$:

$$IC_{50} = K_I^{app} + \frac{[E]_0}{2} \quad (10)$$

where

$$K_I^{app} = K_I \left(1 + \frac{[S]}{K_M} \right) - \text{competitive}$$

$$K_I^{app} = K_I \left(1 + \frac{K_M}{[S]} \right) - \text{uncompetitive}$$

$$K_I^{app} = \frac{[S] + K_M}{\frac{[S]}{\alpha K_I} + \frac{K_M}{K_I}} - \text{mixed } (K_I^{app} = K_I - \text{noncompetitive})$$

Nevertheless, “IC₅₀ wall” issue¹²⁸ takes place: the IC₅₀ value of the inhibitors that are active at picomolar concentrations cannot be determined lower than half-enzyme concentration which is in the range, e.g. of nanomolar concentrations. Moreover, the term “tight-binding” should be correlated with conditions and not inhibitor, since the enzyme concentration determines the IC₅₀. Albeit most of the studies (including pharmaceutical companies) utilise IC₅₀ as a standard inhibition characterisation, it is more correct to use inhibition constant K_I . In case of tight-binding inhibitors K_I is not equal to IC₅₀ and it does not depend on $[E]$. To get K_I values the Morrison equation can be employed:

$$v = v_0 \frac{[E] - [I] - K_I^{app} + \sqrt{([E] - [I] - K_I^{app})^2 + 4[I][E]}}{2[E]} \quad (11)$$

where v_0 is a control rate at $[I] = 0$, v – initial reaction rate (Y), $[I]$ – inhibitor concentration (X), $[E]$ – enzyme concentration, K_I^{app} – apparent inhibition constant.

The mathematical simplification of the Morrison approach can be conducted with Henderson or Dixon models¹²⁹. Both models are intended to linearize the plot. Henderson linearization includes plotting of fractional velocity as a function of inhibitor concentration; however, it can be not reliable enough for classical inhibitors when $K_I \gg [E]$. On the contrary, the Dixon approach with plotting of the reciprocal velocity against the inhibitor concentration

permits to avoid such problem, but it is sensitive to the noisy data that can be obtained at low-concentration region when measuring tight-binding inhibitors¹²².

III. *bd*-oxidase and inhibitors

Inhibitors of cyt *bd* can target:

- oxygen-binding heme-group;
- quinone-binding site;
- H-channels;
- annular lipids;
- other unspecific site binding (allosteric inhibitors) are possible, but not identified yet.

The heme-binding inhibitors are represented by strong ligands (CO, NO, azide N_3^- , cyanide CN^-) which interact with the iron atom(s) in the active site^{4,12,17,37,130}. However, they demonstrate lesser inhibition effectiveness as compared to other types of complex IV (e. g., *bo*₃-oxidase)^{17,37}. This can be due to two reasons. The heme *d* macrocycle conjugation is lower (20 π -e) than the one of the other hemes (22 π -e), this leads to elevated electron density at the iron atom. On the other hand, the oxygen-binding pocket could be more hydrophobic in the case of cyt *bd*. The neutral O₂, CO, NO preferably bind to the reduced state of the enzyme whereas the anionic CN^- more readily binds to oxidised state¹⁷. The heme *d* was shown to interact with cyanide leading to a shift of the midpoint potential, the UV/Vis spectrum bands and a lower catalytic activity. Nonetheless, all the changes are less prominent as compared to high-spin hemes of HCOs. Heme *b*₅₉₅ located near heme *d* and characterised with a high-spin state could be also a target for cyanide; however, it was shown^{17,130} that it almost does not form Fe-CN complex. The heme *b*₅₅₈ is six-coordinated and in the low-spin state, but it can form some small fraction of the Fe-CN complex due to the lability of the Met coordination. These ligands are very helpful to trap of the intermediates of the catalytic cycle^{108,110,131}. However, they are not specific and potent inhibitors. In summary, they are less effective for inhibition of cyt *bd* (table 10).

On the contrary, the quinone-binding site is much more specific. Pauling (1946)¹²⁴ postulated that the ligand would possess a higher affinity to an enzyme if its configuration is close to that of substrate in the transition state presented during the catalysis. It was proposed that ring part is critical for the interaction of the substrate with the protein and for providing of electron transfer. It is thus important to know or to have some hints concerning the Q-binding site organisation to predict the structure of effective inhibitors (*vide supra*).

a) Oxidised *UQ*-2 shows weak noncompetitive inhibition⁹⁴. Its uncompetitive inhibitor analogues with azido- and ethoxy-substituents at the position of the methoxy-groups revealed modified bi-bi ping-pong mechanism provoking the formation of inactive binary and ternary complexes. The formation of the ternary complex suggests that albeit there is just one quinone-binding site several substrate molecules can bind simultaneously. It was suggested that 6-diprenyl and 2/3-ethoxy/methoxy/azido groups contribute to substrate inhibition. The 3-methoxy group of *UQ* is less well-recognisable by the protein than that at the 2 position.

UQ-2, analogues of *UQ*-2, and decylbenzoquinol inhibit at high concentration suggesting that they are classical inhibitors.

Additionally, the comparison of the substrate and product structures can be helpful since the product has lower affinity to the enzyme than the substrate. The oxidised quinol (product) is less polar than the reduced form (substrate) (Fig. 20).

Table 10. Inhibition and Michaelis constants for the discussed compounds. For *KCN*, *NO*, *CO* the *UQH*₂-oxidation reaction was monitored.

compound	K_M or K_I
<i>UQH</i>₂-1⁹⁴	$K_M=0.04-0.28$ mM (<i>E. coli</i>)
<i>UQH</i>₂-2⁹⁴	$K_M=0.05-0.08$ mM (<i>E. coli</i>)
Antymicin A ⁹³	$K_I=11$ μ M (<i>A. vinelandii</i>)
UHBDT ⁹³	$K_I=20$ μ M (<i>A. vinelandii</i>)
aurachin D ¹³²	$K_I=13$ nM (<i>A. vinelandii</i>), $=10$ nM (<i>E. coli</i>)
aurachin C	n.d.
HQNO ¹³³	$K_I=1-20$ μ M
KCN ¹³³	$K_I=2$ mM
NO ¹⁷	$K_I=100$ nM
CO	n.d.

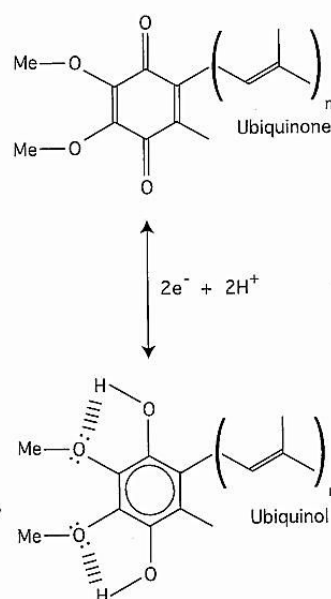


Fig. 20. Difference in the substrate (*UQH*₂) and product (*UQ*) structures utilised by *cyt bd*¹³⁴.

The substrate inhibition is not a rare phenomenon in the respiratory chain. For example, the *bc*₁ complex is substrate-inhibited with 2,3-dimethoxy-6-decyl-1,4-benzoquinone. SQH is substrate inhibited with mono/diethoxy analogues of DecUQ. However, *bo*₃ oxidase does not show the substrate inhibition effect with *UQ*₂⁹⁴. All these also confirm that the quinol binding site is specific in each protein even if they use the same substrate for catalysis.

b) *Quinolone* is an example of compounds that can show significant effect on *cyt bd* catalysis^{9,132,135}. Quinolones can be synthesized by bacteria and serve as quorum quenching signal^{136,137}. The natural compounds such as HQNO, aurachin A, C, D and synthetic analogues (e. g., nalidixic acid) were already tested for *cyt bd* inhibition activity⁴.

HQNO (2-heptylhydroxyquinoline-N-oxide) resembles naphthoquinone (e.g., MQ) scaffold and was shown to act as competitive inhibitor. The other benzoquinone-like antibiotic Piericidin A was twice as less effective at 15 μM ¹¹¹. These types of inhibitors are very unspecific and can influence complexes I, II, III of the eukaryotes, prokaryotic complex *bc_L*, etc^{138–141}.

Aurachins are natural antibiotics produced by *Stigmatella aurantiaca*¹⁴². Aurachins C and D (Fig. 21) specifically bind to *bd*-oxidase⁹. The N-oxide of aurachin D, aurachin C, is less effective (4 times less), but still more inhibiting than other mentioned compounds. The aurachin D studies⁹ revealed that the inhibition does not show dependency on the UQ substrate concentration and, thus, is proposed to be noncompetitive¹³². The interaction with the protein leads to redshift of heme *b*₅₅₈ in UV/Vis spectra and the redox potentials of the heme *b*₅₅₈ and *b*₅₉₅ were up- and downshifted, respectively. However, the internal electron flow was not perturbed¹³². Aurachin C and its analogues, with different length and saturation of the isoprenoid chain, showed that the presence of C=C bonds in the tail is not important, but that the type of the substituents in the ring is crucial⁹. Thereby, aurachin C derivatives were less effective as compared to aurachin D. For both aurachins C and¹⁴³ D it was shown that CH₃-group in the 2- or 3-position is necessary for inhibition. Additionally, the bulkiness of the substituent at 3-position is not important as well as the presence of OH-group in 1-position (aurachin C vs D)⁹. All these suggest that the quinone-binding pocket in *cyt bd* is quite large.

Interestingly, in contrast, *cyt bo₃* was sensitive only to aurachin C (importance of 1-OH-group) and the bulky substituents in the 3-position decreased the inhibition potency. The vulnerability to aurachin derivatives was also demonstrated in case of mitochondrial complex I and complex III, plant *cyt b_{6/f}* and photosystem II, prokaryotic *cyt bc_L*^{144,145}.

c) The group of *antibiotics specifically binding to bc_L complex*: Antymicin A, UHDBT, myxothiazol, - were also examined⁹³. Antymicin A noncompetitively inhibits reduction

of heme b_{558} , but hemes d and b_{595} are still reduced with UQ. Additional experiments with TMPD (one-electron donor for cyt bd) revealed the reduction of heme b_{558} . It was proposed that Antymycin A blocks the electron transfer from $UQ \rightarrow$ heme b_{558} but not from $UQ \rightarrow$ heme b_{595}/d . This bifurcation of electron transfer could solve the issue of oxidising of two electron donors UQH_2 by one electron acceptor O_2 . UHDBT can also lead to cyt bd inhibition but without spectral band shifts. Probably, UHDBT binds to the same site as Antymycin A. Myxothiazol did not influence protein catalysis.

Potential inhibitors can be found in the families of the heterocycle compounds (quinolones, coumarins, quinazolines, quinoxalines, indoles, acridones, etc.). However, the ring substituents should be customised to enhance the inhibition of cyt bd and to avoid inhibition of the other enzymes, and especially the components of the eukaryotic respiratory chain. Finally, the inhibitors of quinone-binding enzymes exclusively expressed in prokaryotic cell (NDH-II, formate dehydrogenase, hydrogenases and some others) could also be interesting to test on the bd -oxidase. For example, the vulnerability in submicromolar concentrations of NDH-II to phenothiazine analogues, platanetin, quinolinyl pyrimidines, scopafungin, trifluoperazine was observed¹⁴⁶.

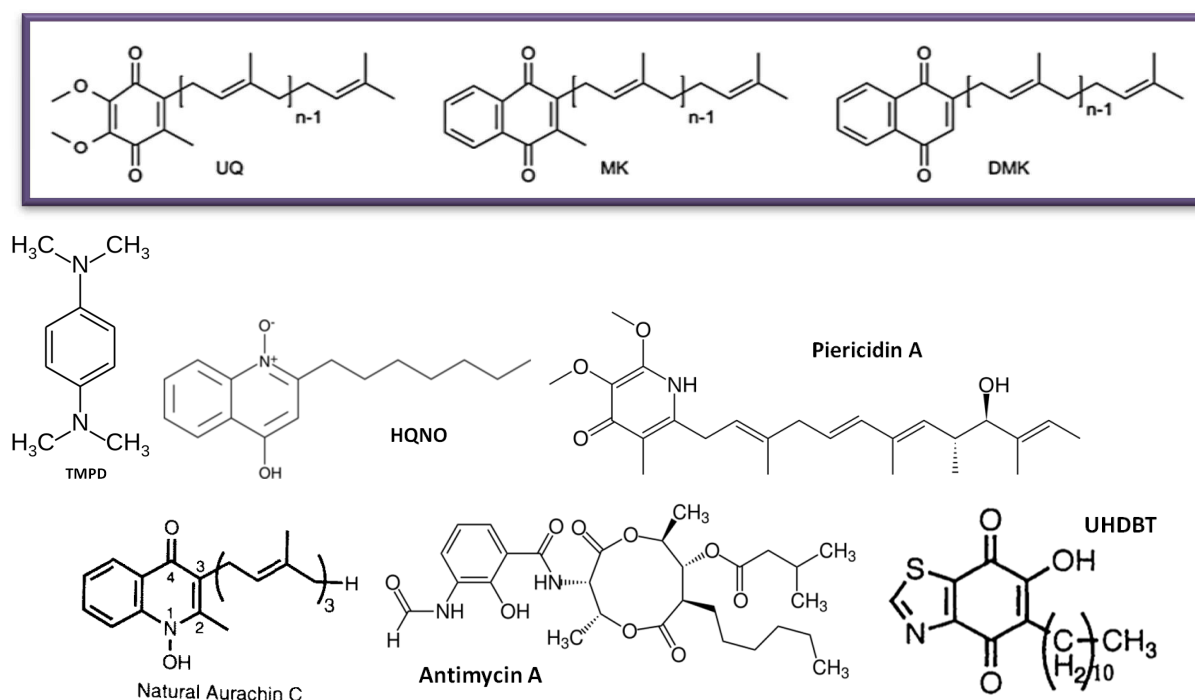


Fig. 21. Structures of the natural electron donors of cyt bd (UQ, MQ, DMQ), TMPD and the structures of the several inhibitors (HQNO, Piericidin A, aurachin C (aurachin D lacks 1-OH group); Antimycin A, UHDBT).

The H-channels of complex IV and other membrane protein were found to be a target for Zn(II) ions^{147,148}. Nonetheless, there was a weak inhibition of cyt *bd* when ZnSO₄ was used (IC₅₀=60 mM compared to, e. g., K_I=1 μM for cyt *bo₃*)³⁷.

Lipids are known to be crucial for membrane protein structure. For example, *aa₃*-oxidase is deactivated in the absence of cardiolipin which interacts with farnesyl tail of the heme *a₃*¹⁴⁹. In case of cyt *bd* there were not any detailed studies of the influence of the lipids. However, it was mentioned³⁷ that protein devoid of phospholipids (<0.5 nmol/mg of cyt *bd*) had slowed down oxidation activity. Thus, antibiotics like Gramisidin S¹⁵⁰ could inhibit cyt *bd* through removal of annular lipids and interaction with hydrophobic surface of the protein. Additionally, some detergents such as Triton X-100, cholate, octylglucoside were shown to interact with cyt *bd* and to induce a loss of function^{36,133}.

IV. Development of electrochemical biosensor for the detection of inhibitors

1. Biosensors

Since the X-ray structure of *E. coli* cyt *bd* oxidase is unknown the conduction of rational drug design (e. g., molecular docking) is not possible. Thus, pharmacophore-based set of ligands have to be tested on the system *in vitro*. High-throughput screening HTS can be realised through biosensor development.

Biosensors^{151–154} allow us to convert biological data directly to electrical signal and to conduct specific (semi-)quantitative analysis. The two main elements of a biosensor are the bioreceptor and transducer. Bioreceptor is an immobilised biological element sensitive to analyte. The role of bioreceptor can be played by oligonucleotides, antibodies, or enzymes. The transducer is dedicated to convert biological signal to electronic data.

Biosensors can be classified by the transducing elements: electrochemical, optical, piezoelectric, and thermal¹⁵². The electrochemical biosensors offer several advantages^{152,155}:

- low required quantity of the sample (in picomolar range);
 - rapid and continuous control;
 - short time of response
- (fast preparation of the sensor, one sensor can be used for several data points and conditions);

- easy variation of the experimental conditions (pH, t° , ion composition, etc.);
- thermodynamic and kinetic data can be obtained;
- several modes of measurements possible: amperometric, potentiometric, conductometric detection;
- difficulties of diffusion (especially for the macromolecules, since $D = f\left(\frac{1}{r}\right) = \frac{RT}{N_A} \frac{1}{6\pi\eta r}$) are avoided due to immobilisation of the bioreceptor.

There are also several drawbacks such as:

- degradation of bioreceptor;
- low intensity signal;
- difficulties in the choice of the immobilisation method (to provide quasi-natural environment for biological macromolecule);
- shortening of the distance between redox-active centre and electrode in order to provide direct electron transfer DET.

2. Protein film voltammetry

Electrochemical biosensors can utilise protein film voltammetry PFV. This requires immobilisation of the protein onto the electrode. The immobilisation approach should respond to several requirements. The most important ones are providing direct electron transfer DET and maintaining the protein in native conformation as detailed further^{156,157}.

Practical aspects

Choice of the surface modification

The protein immobilisation includes several approaches¹⁵⁷:

1. Physisorption

The direct deposition of protein on electrode surfaces leads to unspecific noncovalent interaction (Fig. 22). The passive adsorption involves noncovalent bonds (mostly electrostatic and hydrophobic)¹⁵⁸. The OH-groups of Ser and Thr residues interact with gold surface.

Only a few proteins can be successfully immobilised through physisorption. The disadvantages include denaturation, multiorientation and large distance between cofactor and electrode. Thus, the results can represent properties of the system in non-native state.

Carbon electrodes (glassy carbon electrode GCE, pyrolytic graphite electrode PGE) serve as a better template than metallic electrode. It is possible to control the fractions of surface groups such as hydroxyl, carbonyl, carboxylate, lactone, phenolic on the carbon electrode by varying electrode polishing procedure and, thus, the C/O ratio¹⁵⁹. Therefore, milder conditions for the immobilised protein take place. However, the diversity of the surface chemical groups leads to decrease in the interfacial electron transfer rate and in its homogeneity.

An obvious advantage of this method is the short time required for electrode preparation since samples are just placed on the surface.

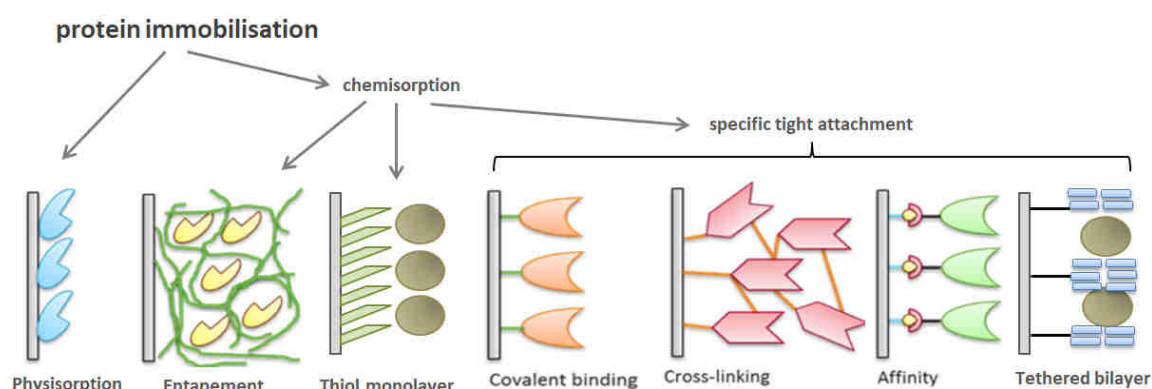


Fig. 22. Schematic representation of some immobilisation approaches (adapted from ¹⁶⁰).

2. Chemisorption

a. Specific tight attachment

The covalent, coordination or biological high affinity attachment of the protein to the metallic surface can be accomplished through linkers (Fig. 22)¹⁵⁷. The role of the linker can be performed by a:

- Cys-group located at the protein surface. In this situation the specific Au-S-Cys link formation is performed, which results in well-orientated protein monolayer devoid of kinetical issues due to existing DET at the short distance electrode-cofactor. However, this immobilisation can usually lead to protein denaturation.
- copper- or nickel-chelating nitrile-triacetic acid, or imidodiacetic acid (Cu/NiNTA/IDA) to which the protein is attached through His-tag (protein-His-Cu/Ni-NTA/IDA-Au_{electrode});

- linker-modified lipids that form bilayer at electrode surface (so-called tethered bilayer lipid membrane tBLM);
- modified thiol with a corresponding protein substrate as a head-group (e. g., complex I can be attached through NADH-NCO-thiol-Au_{electrode}). Additionally, the membrane can be reconstituted via lipid mixing with protein and detergent removal (forming also tBLM)^{161,162}.
- cross-linker. Tight artificial binding between two proteins permits to form a strong bonding with the surface. The enzyme deactivation is a frequent side effect.
- biological linker. Biological affinity based protein anchoring can be achieved through interaction between: 1. (strept)avidin-biotin. 2. antigen-antibody interaction. 3. lectin-carbohydrate.

The linker-based protein attachment provides a well-orientated protein film, and in case of membrane protein lipids allow the creation of native environment. However, the electrode-cofactor distance should be controlled in order not to exceed 14-20 Å¹⁶³ and, thus, to fulfil the DET conditions. The fabrication of the sensor demands special preparation and, thus, can take several hours..

Additionally, the protein NH₂, -COOH and -SH groups can be modified to provoke bond formation with correspondingly modified electrode surface.

b. Attachment through self-assembled monolayers (SAM)

The thiols or silanes functionalise the gold surface via the formation of strong covalent bonds. Densely packed and organised monolayers can be obtained. The strength and orientation of protein adsorption can be controlled through the choice of the head-group. The variation of the length of the spacer of the SAM allows reaching the optimal conditions for DET.

The disadvantages of the attachment via SAM are:

- the defects in the monolayer (Fig. 23) prevent completely homogenous orientation of the adsorbed molecules (pinholes, metal film and surface impurities, defects at gold step edges, etc.). The quantity of the defects can be increased with the decrease of the length of the alkyl-chain spacer and increase quantity of charged head-groups.

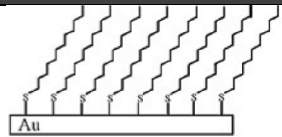
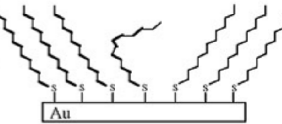
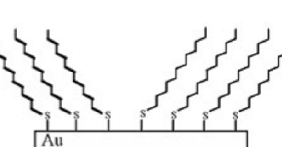
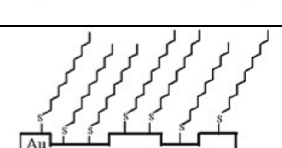
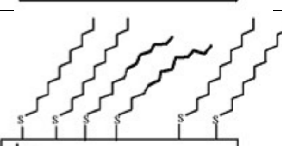
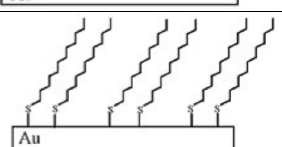
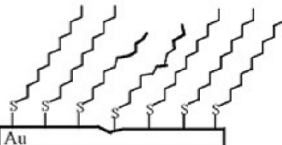
structure group	structure	description	visualisation
denseness	compactness	Regions of the SAMs are well-organized crystalline, SAMs have same molecular conformation	
defect	grain boundary	Regions of the SAMs formed on the adjacent grain of the same phase with different orientations	
	domain boundary	Domain boundaries include tilt boundaries, stacking faults, rotational boundaries, and antiphase boundaries, which are caused by the low symmetry of the molecular lattice and are typically 0.2-0.3 nm in width.	
	vacancy island	Regions of the SAMs offset in height by one gold atomic diameter from the surrounding regions	
	collapse	Locally thin regions of the SAMs resulting from the large oriented angle of thiol molecules near defects or different tilted angles at the boundaries of differently oriented domains	
	pinhole	The exposures of the gold surface in SAMs, they behave as an array of extremely small microelectrodes, possibly in the size range 5-10 nm	
	structural defect of gold	Defects in SAMs caused by variations in the surface of the gold	

Fig. 23. Defects found in SAM formed on gold surface. Moreover, the tightly attached impurities can cause additional disorder.¹⁶⁴

- limited electrode potential window (the monolayer can be destroyed upon application of extreme potentials, e. g., reductive desorption);
- the protein affinity depends on presence of detergent, lipids, impurities competing for interaction sites with head-groups of SAM;
- the biosensors based on the SAM usually do not have a long life span (thiol partial desorption and oxidation).

3. Entrapment

The protein can be incorporated in polymer matrices deposited on electrode surface. Amphiphilic and clay coating polymers are the most biocompatible materials. The approach leads to films of proteins preserving native conformation but with a high degree of inhomogeneity in the orientation.

Signal enhancement approaches.

The utilisation of nanomaterials (carbon nanostructures or metal nanoparticles) allows increasing signal intensity. The carbon nanomaterials - single-wall or multi-wall carbon nanotubes (SWCNTs or MWCNTs), carbon nanospheres (CNSs) - are characterised with high surface area, high conductivity, and presence of the polar groups on surface. The signal is enhanced due to the increased surface at which the protein can be adsorbed, and DET is facilitated. The other carbon materials such as carbon black and graphene also allow the signal to be improved^{157,165–167}.

The most well-studied metal nanoparticles are based on gold. The choice of gold is dictated by the simplicity and variety of preparation, chemical inertness, strong binding of thiol, and biocompatibility. In case of SAM formation, the high affinity to thiols allows manipulating in not sterile conditions since thiols can substitute the impurities¹⁶⁸. The nanoparticles increase the catalytic activity of the enzymes and improve the electron transfer to the occluded redox active sites¹⁶⁹. When deposited at the electrode surface they drastically increase the surface area and, thereby, the adsorbed protein quantity which increases the signal intensity. The intriguing nanoparticles properties are due to quantum effects and the quantity of the atoms at the surface in comparison to total atom number in the colloid (>10 nm) or cluster (<10 nm)^{168,170,171}.

Gold electrode modified with GNPs covered with SAM

Recently^{7,172,173} the successful immobilisation of complexes IV from different origins was demonstrated. The immobilisation was conducted on gold electrode modified with gold nanoparticles (GNPs) and monolayer of thiols (1-hexanthiol and 6-mercaptophexanol). It was shown that 15 nm in diameter GNPs lead to the highest current enhancement⁷. For the 15 nm nanoparticles about 7% of gold atoms constitute the surface¹⁶⁸.

Comparison of immobilised and solubilised complex IV

1. Catalytic activity

Catalytical studies in the presence of substrate (oxygen) in the solution provide us with turnover numbers in, approximately, ten times higher than the values ($1\text{--}30\text{ s}^{-1}$) obtained for immobilised on the electrode proteins (table 11). It was proposed that only small fraction of immobilised protein molecules are in the active state and the transition from inactive to active state is supposed to be a limiting parameter. This could explain the lowered k_{cat} values of the immobilised protein¹⁷⁴.

Table 11. Electrochemical and catalytical properties of terminal oxidases from various organisms.

classification			complex IV	organism	k _{cat} , s ⁻¹ (solution)	k _{cat} , s ⁻¹ (immobilised)	
HCOs	A-type	A1	aa ₃	<i>P. denitrificans</i>	91,136 ¹⁷⁵	21 ¹⁷⁶	
			bo ₃	<i>E. coli</i>	375 ⁶²	27 ⁷	
	B-type		ba ₃	<i>T. thermophilus</i>	75 ¹⁷⁷	180 ¹⁷⁶	
	C-type		cbb ₃	<i>P. stutzeri</i>	63 ¹⁷⁸	10 ¹⁷⁶	
bd-oxidases			bd	<i>E. coli</i>	650 ³⁶	10 ¹⁷⁹	

Mostly, the immobilised enzymes show relatively low E_{cat} and turnover number. The exception is ba_3 -oxidase from *T. thermophilus* with a $k_{cat} = 180 \text{ s}^{-1}$ and $E_{cat} = +220 \text{ mV}^{176}$. Thus, the overpotential is low and k_{cat} values are relatively high. Therefore, the modification of the surface for ba_3 -oxidase is the most suitable. This could be connected with differences in the lipid environment in the thermophiles where lipids are mostly saturated and protein are conferred with specific properties^{181–185}.

The rate of electron transfer varies from 7 to 180 electrons per second. Nonetheless, it was demonstrated as well that even at high electron transfer rates (1000 s^{-1}) the catalytical potential of immobilised at the electrode aa_3 -oxydase reaches -190 mV .

2. Protein film properties in the absence of the substrate

The determination of the mid-point potentials of the cofactors is also not straightforward. The peaks at cyclic voltammograms are not well-resolved and can have contribution from quinol species. Most of the peak current position values are lower than the ones obtained during titration. However, when interpreting the data one should consider parameters of the measurements (pH, detergent and lipids composition, ion strength, surface modification, quinone presence, etc.)^{36,186,187}. Additionally, in some cytochromes the effect of cooperativity is presented which originates from^{188–191}:

- Bohr effect which predicts the mutual dependence of reduction potential $E_{1/2}$ of the cofactor(s) and pK of protonated group(s);
- interaction between cofactors which can be measured as an interaction potential which corresponds to the difference between potential of the cofactor in the absence and presence of the interacting partner that alters the mid-point potential of the former.

It should be emphasize that in titration experiment the system is at equilibrium whereas PFV measures the system parameters in non-equilibrated state.

When the substrate is absent the CVs of cyt *bd*-oxidase are characterised with a cathodic and anodic peaks at – 120 (with concomitant low-potential shoulder) and – 60 mV, respectively; these values are lower than the ones obtained in the anaerobic solution¹⁷⁹.

The aims of the project

This PhD project follows several goals:

1. Development of biosensor and its surface characterisation (**Optimisation**)

The PFV of cyt *bd* from *E. coli* was shown to be a powerful tool for examination of the potential inhibitors. The optimisation of the cyt *bd* immobilisation, the understanding of the interfacial chemical processes underlying the observed signal and surface characterisation should be conducted. It is crucial to obtain a stable signal and to control the orientation of cyt *bd* molecules in the protein film at the electrode.

Additionally, it is important to decrease the time of the modification steps in order to be able carry out fast screening of a wide range of the compounds. This would help to define the method not only for cyt *bd*, but also for other membrane proteins.

2. High-throughput screening, to reveal the most potent inhibitors (**HTS**)

Some inhibitors were already tested before towards cyt *bd*. Nonetheless, there is no systematic screening reported so far. The discovery of the potent inhibitors would help to:

- launch the design of the powerful inhibitors in order to develop antibiotics of new generation with novel mode of action (**practical aspect of screening**)
- elucidate the Q-binding site, organisation which is still not clear (**fundamental aspect of screening**)

3. Comparison of cyt *bd* from two different organisms (**Comparison**)

Albeit cyt *bd* of different organisms belongs to one superfamily, the similarity of their properties does not seem clear. The *bd*-oxidases differ in structure features (Q-loop) and biophysical properties ($K_M(O_2)$, mid-point potentials). To understand the heterogeneity of cyt *bd*, two *bd*-oxidases are compared: cyt *bd* from *E. coli* (long Q-loop) and cyt *bd* from thermophilic *G. thermodenitrificans* (short Q-loop). If cyt *bd* from *E. coli* is quite well-known, then our knowledge about cyt *bd* from *G. thermodenitrificans* is poor and need to be elaborated.

Part A. Cytochrome *bd*-oxidase

Results

I. Optimisation of the cyt *bd* immobilisation.

Previously in the laboratory the immobilisation on gold nanoparticles was successfully probed for various terminal oxidases *aa*₃, *ba*₃, *bo*₃, and *cbb*₃^{192,7,176}. Furthermore, preliminary studies of the immobilisation of cytochrome *bd*-oxidase from *E. coli* were conducted. The optimal pH (pH7) was determined and the absence of the quinol influence was demonstrated¹⁷⁹. In all experiments the modification procedure was carried out employing 15 nm GNPs with formed multicomponent monolayer (1-hexanethiols and 6-mercaptophexanol). However, further experiments are required for the optimisation of the biosensor.

In order to allow a rational comparison of the data we utilised the following parameters for catalytic voltammogram description:

- E_{cat} - the half-wave potential of the catalytic sigmoidal curve. It is related to the kinetic efficiency of the oxygen reaction. The lower E_{cat} , the higher the overpotential for O₂ reduction¹⁹³. Estimated error for E_{cat} is 0.02 V.
- di/dE - the slope of the catalytic curve in the region of limiting current. It could be associated with the inhomogeneity of the protein molecules orientations on the electrode surface, which leads to a distribution of interfacial electron transfer rate¹⁹⁴. Estimated error for di/dE is 0.003 $\mu\text{A}/\text{mV}$.
- $\frac{di}{i} = \frac{i_n - i_{n+1}}{i_n}, \%$ - the variability of the limiting current value between two successive scans that allows one to evaluate the stability of the protein films; n – number of scan. Estimated error for $\frac{di}{i}$ is 0.02.
- transition zone – the potential range from the beginning of the catalysis to the region of the limiting current plateau

1. Influence of concentration

In order to determine the optimal protein surface coverage cyt *bd* samples in the concentration range of 1 to 200 μM were tested (Fig. 24). In general, the catalytic curves resembled recently obtained voltammograms for cyt *bd* in the laboratory¹⁷⁹: the mean half-wave potential was approximately -50 mV (vs SHE). The limiting current values increased with dilution of the sample from 200 μM to 6 μM . Further decrease in the protein concentration from 6 μM to 1 μM induced a drop in the signal. The di/dE parameter of the

plateau in the region of the limiting current also varied: the lowest values were observed for the 10 μM sample. Therefore, an optimal concentration of 10 μM (that is 1 mg/ml) was chosen for further studies. This concentration corresponds to the coverage of $\Gamma=0.1 \text{ pmol}\cdot\text{cm}^{-2}$ estimated from integration of the cathodic peak of non-turnover voltammogram.

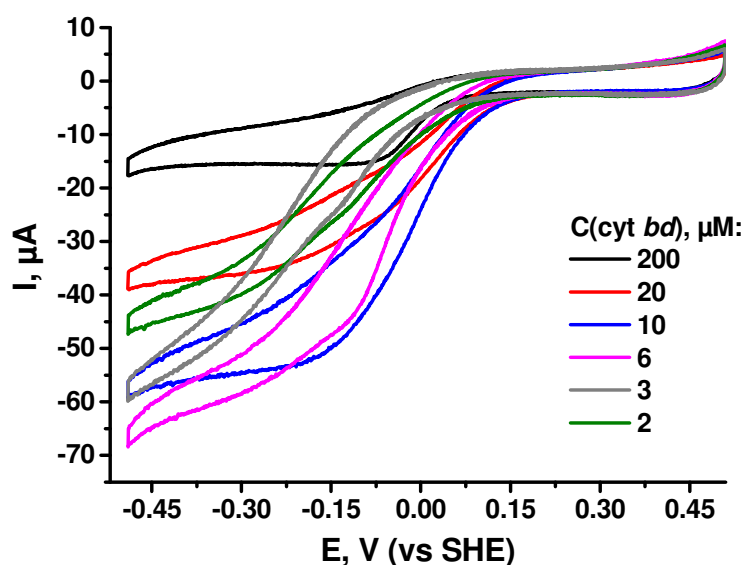


Fig. 24. Catalytic voltammograms of cyt bd in presence of O_2 . 1000 rpm, 0.02 V/s, pH7, KPi 0.1 M.

Such a dependence of the voltammogram parameters on the protein concentration could be explained by several factors. Deposition of high concentrated sample could lead to the formation of protein multilayers or monolayer with very high packing density¹⁹⁵. In either way, the catalytic current decrease could arise from transport limitation through the protein layer¹⁹⁵ and/or from lateral steric effect¹⁶⁸. At low concentration the signal intensity decreases due to insufficient coverage. The differences in overpotential values could be caused with different protein environment (e.g., due to protein multilayer formation or detergent adsorption at the electrode surface). Biphasic process in case of much diluted samples could be as a result of quinone and protein cofactor contributions.

2. Stability of the signal

The main requirement for the biosensor development is the stability of the signal. However, in the course of several measurements it was observed that the limiting current decreased upon successive scanning.

Influence of the lipids

To understand more thoroughly the role of the lipids in cyt *bd* adsorption at the SAM, the lipid and thiol mixtures were varied.

Since lipids PE and PG constitute the main fraction of the *E. coli* lipid membrane (70 and 16%, respectively^{196,197}) cyt *bd* sample containing the lowest lipid quantity (purification №2) were mixed with the protein before immobilisation with 0, 5, 15, 22, 30 and 44% of a 1/1 composition of PG and PE lipids.

The initial sample with only small traces of lipids showed a low stability ($di/i=39\%$). Increase in the lipid fraction up to 22% induced stabilisation of the films (table 12, Fig. 25): two consecutive voltammograms were characterised with closer values of maximal limiting current. Interestingly, upon further addition of the lipids, the stability of the films decreased. At 22% of lipids the di/i parameter is comparable to the one observed in the absence of the lipids.

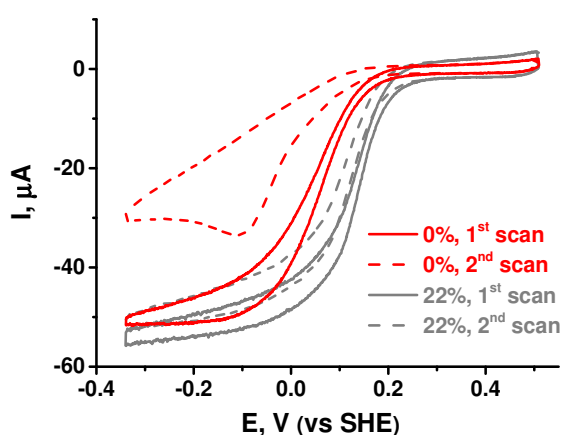


Fig. 25. Stabilisation of the cyt *bd* protein films upon addition of the PE/PG (1/1) lipid mixture. The 22% lipid concentration (grey line) led to the optimal results.

Table 12. Parameters of the voltammograms of cyt *bd* oxidase in dependence on the concentration of added lipid mixture (PE/PG 1/1).

added lipid concentration %	E_{cat} V (vs SHE)	di/dE $\mu A/mV$	di/i %
0	0.06	0.007	39
5	0.16	0.017	26
15	0.16	0.020	13
22	0.16	0.008	7
30	0.16	0.020	8
44	0.11	0.009	40

Additionally, the optimal lipid mixture of 22% led to the lowest slope in the limiting current region and the largest E_{cat} value. This indicates that the optimal lipid concentration supports the orientation homogeneity and protein catalytic activity.

It is known that the membrane protein function depends on the presence of the lipids^{197,65,198,199}. It was also shown that cyt *bd* from *E. coli* (with lipid concentration <0.5 nmol/mg) needs phospholipids to enhance catalytic activity 30-fold³⁷. A smaller effect was observed in case of cyt *bd* from *A. vinelandii*²⁰⁰. Additionally, lipids can influence the mid-point potential of the heme b_{585} and to a lesser extent those of hemes b_{595} and d^{36} . The recent study²⁰¹ showed that cardiolipin lipid can form layer on the electrode to which a protein is attached.

Desorption or loss of the activity?

The batch of standard preparation was used. To determine the factor of the current decrease the measurements with a Clark-electrode were conducted. Cyt *bd* from the standard preparation was mixed with 0, 10, 20, 50, and 100 % lipids (PE or PG) and the ability to oxidise DecUQ was monitored.

The catalytic activity in all measurements was 3250 ± 300 (U/mg protein) regardless the presence of the lipids and their concentration.

Thus, it is possible to conclude that the observed current decrease is not associated with loss of catalytic activity of cyt *bd* and is mostly caused with desorption process.

Mutual influence of the surface charge of the SAM and lipid type

The influence of the type and quantity of the lipids on the protein film stability was also examined. The structure of the lipid includes hydrophobic tail and hydrophilic head group (including phosphate group). The PG lipids have a negatively-charged head group whereas PE lipids possess a zwitterionic one (Fig. 26).

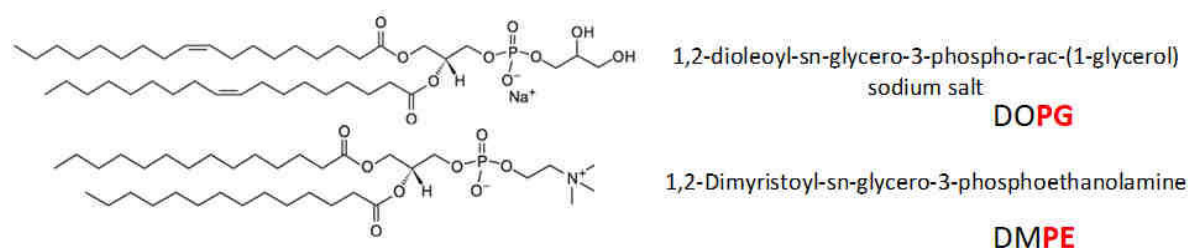


Fig. 26. Structure of the lipids probed for the protein film stability examination. Due to saturation of hydrophobic tails DMPE is a more stable lipid.

The protein purification with residual quantities of lipids (№1) was used. The stability of this batch as compared to almost delipidated one was higher at neutral thiol monolayer (HT/MCH 1/1) on gold electrode modified with GNPs. The catalytic parameters were improved upon addition of 2.5% of PG lipids. The value of E_{cat} increased by 20 mV and the stability rose on 3% (Table 13, Fig. 27A).

Table 13. The characteristics of the voltammograms of *cyt bd* upon addition of different lipid types and variations of the surface properties.

immobilization conditions			E_{cat} ,	di/dE ,	di/i ,
% of lipids	lipid type	thiol type	V (vs SHE)	$\mu A/mV$	%
0	-	HT/MCH (1/1)	+0.11	0.013	9
2.5	PG	HT/MCH (1/1)	+0.13	0.012	6
2.5	PE	HT/MCH (1/1)	+0.08	0.052	15
2.5	PE	HT/MCH/MPA (1/1/1)	+0.16	0.028	4
2.5	PE	HT/MCH/MHA (1/1/1)	+0.11	0.010	7
2.5	PE	HT/MCH/MUA (1/1/1)	-0.01	0.023	10
2.5	PE	HT/MCH/MEA (1/1/1)	+0.20	0.019	8

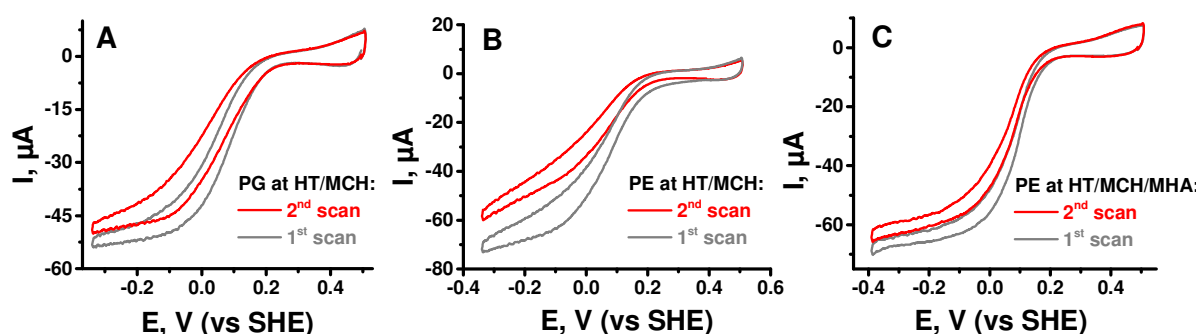


Fig. 27. Successive voltammograms of *cyt bd* with addition of 2.5% lipids of different type (PE or PG) and with immobilisation on different surfaces (polar or negatively-charged).

However, the immobilisation of *cyt bd* mixed with 2.5% PE at uncharged surface led to lower stability, larger slope and lower E_{cat} (Fig. 27B). Incorporation of the charged thiols into the SAM yielded better catalytic parameters. Positively charged MEA, and negatively charged MPA led to signal improvement when *cyt bd* was mixed with 2.5% PE lipids. The highest stability was observed with 4% higher with immobilisation at MPA-containing SAM, but the MEA provided the lowest overpotential.

Hence, a synergetic influence of lipids and SAM type was observed. *Cyt bd* immobilised with negatively charged PG lipids showed better catalytic performance on polar uncharged surface whereas with PE lipids, charged surface was better.

Influence of the thiol spacer length

To understand the influence of the length of the thiols the comparative studies with cyt *bd* with addition of 2.5% PE lipids were conducted on various ω -carboxyl alkanethiols (Fig. 28).

Upon decreasing the spacer length from 11 to 3 carbons the half-wave potential was significantly upshifted. Previously it was shown for soluble model proteins that interfacial electron transfer rate goes down as the distance between metallic surface and the protein rises^{202–205}. Moreover, the loss of the stability also takes place. It is possible that the protein is adsorbed more tightly at the surface with shorter thiols.

The effect of the spacer length on the slope of voltammograms showed optimal-shape dependency. The highest homogeneity of the protein orientations was at the MHA-containing SAM, and it decreased when MPA or MUA were introduced instead. The decrease in the chain length leads to the thiol layer with higher disorder and higher constant of the interfacial electron transfer rate²⁰⁶. Due to this the presence of MPA could raise the slope and decrease overpotential, respectively. Additionally, MPA containing SAM are more permeable for the water since the presence of the COOH-group within the layer, which also decreases the extent of the order and rigidity of the SAM. The long-chain MUA is less soluble and it is more energetically favourable to gather together which can provoke the domain defect formation²⁰⁶ and, hence, higher instability and inhomogeneity of the protein films.

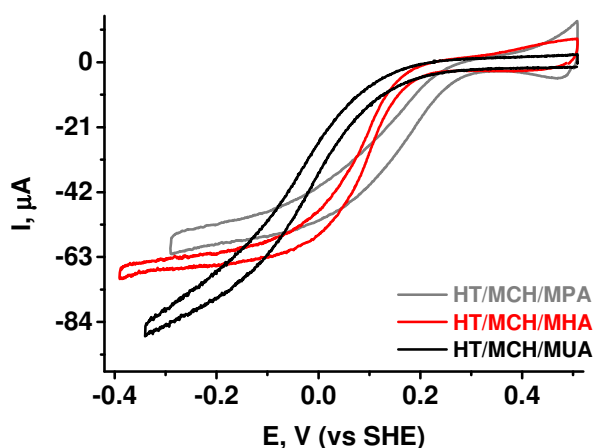


Fig. 28. Voltammogram of cyt *bd* (with 2.5% PE) shape dependence on the length of the ω -carboxyl alkanethiols (MPA, MHA or MUA) introduced in the thiol monolayer.

Detergent variations

The adsorption of the membrane proteins at the SAM is due to hydrophobic and to a lesser extent electrostatic/hydrogen bonding interactions. The same interactions are presented between protein and maintaining its native structure detergent^{207,208,209}. Thus, to remove the excess of the detergent and avoid competition between detergent and SAM for protein bonding, the washing procedure can be varied. For the batch with decreased lipid quantity (purification №2) the variation of the washing buffer and supporting electrolyte buffer revealed the need of the detergent for higher stability: compare the washed in KPi and measured in DDM-devoid buffer ($di/i = 26\%$) vs unwashed and measured in DDM-containing buffer ($di/i = 15\%$). However, the detergent only resembles natural environment of the protein. Thus, the addition of the lipids led much more marked stabilisation effect than DDM.

Additionally, two different detergents were compared. The standard purified batch containing DDM and the batch containing MNG as a detergent were tested (table 14).

*Table 14. Voltammetric parameters of the cyt *bd* oxidase films with fast mode of the modification of the electrode in the presence of the different detergents.*

	di/i, %	E _{cat} , mV (vs SHE)	slope, $\mu\text{A/mV}$
MNG	3	-70	0.031
DDM	4	-50	0.025

The MNG resembles the lipid structure more than DDM (Fig. 29) and is supposed to be a more sufficient detergent maintaining cyt *bd* in the native conformation²¹⁰. The catalytic activity and stability of the protein were shown to be the same if to compare with DDM, however, the melting point in thermal stability assay was higher (group of Pr. Friedrich, unpublished data). The immobilisation of the protein with this preparation did not reveal voltammetric differences, and the optimisation experiment showed that the same pretreatment and immobilisation conditions led to similar results as with DDM as detergent.

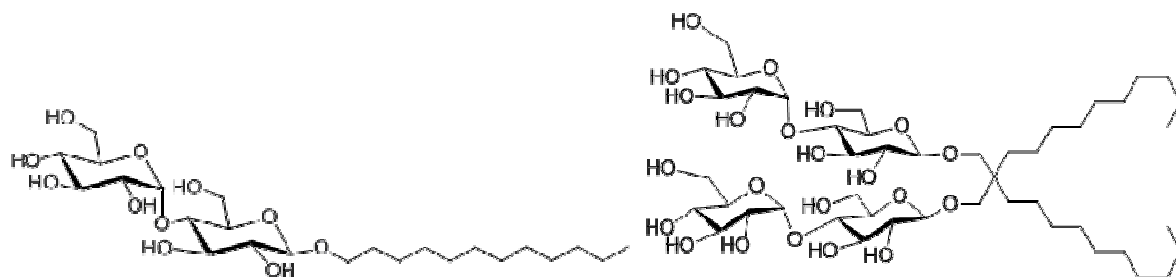


Fig. 29. Structures of the DDM (right) and MNG (left) detergents.

3. Improvement of the preparation procedure

The electrode modification procedure was also changed in order to decrease the time required for preparation of the biosensor

GNPs deposition

Previously, the 7 μ l of GNPs were successively deposited 3 times. To decrease the time for the modification the number of GNPs depositions and the volume deposited at once were altered.

It was shown that it is not the total amount of the deposited GNPs which was crucial for stability but the partial dose (the volume that deposited at once) that influenced the stability of the protein film. For example (table 15), the deposition of the 9 μ M GNPs solution led to stability parameter of 4-5 % regardless of the quantity of the number of depositions.

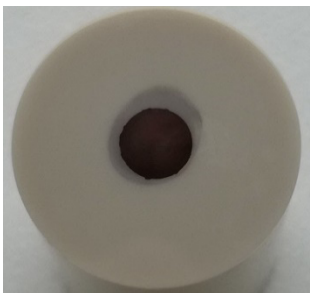
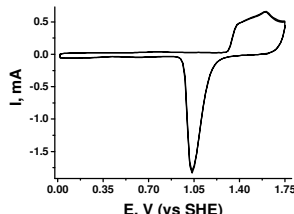

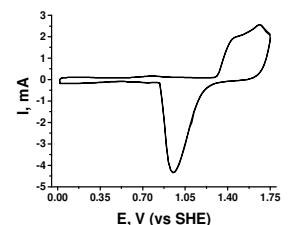
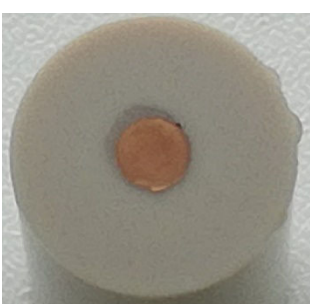
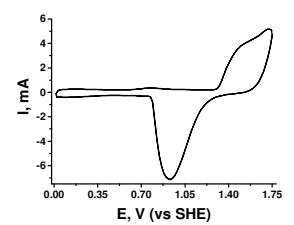
Table 15. The dependence of the cyt bd film stability upon variation of the number of the depositions of GNPs (the total quantity of the GNPs) with fixed single deposited dose (9 μ M).

number of the depositions	di/i, %
1	4
2	5
3	5

However, the one-time deposition of the GNPs but with volume variation in the range 2-20 μ l led to differences in the protein film parameters (table 16). The minimal optimal quantity was 7 μ l with stability of 3%. Decrease in the GNPs volume led to very instable film with drastic slope. The increase of the deposited volume correlates with the rise in homogeneity of the orientation (judged through the signal slope) and the decrease in the overpotential. However, the shortest time of the solvent evaporation was in case of the lowest possible volume of GNPs which is 7 μ l. Moreover, with this condition the highest stability was reached which is one of the most important aspects for the compound screening.

Corresponding voltammograms were not similar. The efficiency of the enhancement of the signal (i at \sim 1 mV) has shown the highest values in the range between 2 and 7 μ l (in 2.6 times with 5 μ l difference) and was of the quite moderate values within the step from 7 to 20 μ l (in 1.4 times with 13 μ l difference). Furthermore, the cathodic peak current corresponding to the reduction of GNPs was upshifted with 2 μ l volume deposition.

Table 16. Influence of GNPs volume utilised for the one deposition on stability parameter. The corresponding electrode surface representation is shown. Incubation in thiols (1/1 HT/MCH) – 15 min, with cyt bd - 15 min.

V(deposited GNPs), μl	visual estimation through the colour of the dried GNPs layer	voltammogram of GNPs (0.1 M H_2SO_4)	di/i, %	slope, $\mu\text{A/mV}$	E_{cat} , mV (vs SHE)
2			32	0.090	-160
7			3	0.033	-100
20			7	0.021	-70

These differences in the protein film voltammogram parameters could be related to the surface microrelief variations. It was shown on the example of iron nanoparticles that the surface roughness and wettability depend on the concentration of the nanoparticle solution and the visual characteristic of the macrosurfaces are, accordingly, varies²¹¹. The different geometric microparameters could determine the curvature of the surface and, thereby, the surface cavities and the order of the SAM.

Thiol incubation

The effect of incubation time of the thiol solution was also examined (table 17). The electrode modified with the GNPs (9 μL , 3 depositions) was incubated in the thiol solution (HT/MCH, 1/1) during 18 min, 2, 5, 8, 14 h or 2 days. The protein with partial delipidation (purification №1) was then deposited without addition of the lipids for overnight adsorption. Additionally, the oxidative adsorption of thiols for SAM formation was conducted at 500 mV (vs SHE) in the presence of oxygen during 20 min.

Table 17. Dependence of the voltammetric parameters of cyt bd on the time of the incubation in thiol solution.

time of incubation	di/i, %	E_{cat} , mV (vs SHE)	slope, $\mu\text{A/mV}$
15-20 min	5	+ 70	0.013
2 h	8	+ 60	0.017
8 h	8	+70	0.015
overnight (app. 14 h)	7	+ 100	0.010
2 days	16	+ 100	0.005
20 min (at +0.5 V vs SHE), O_2	10	+ 70	0.022

A gradual increase in the instability of the protein films with the rise of the incubation time in thiols was observed. After 2 days of incubation the stability fell down by 16% and could also be due to the loss of native conformation of the protein at the electrode surface, and/or due to prevalence of weaker hydrophobic interactions over electrostatic ones that dominate when incubating less. The E_{cat} did not change much showing values between +60 and +100 mV with a slight rise with a time increase of the thiol incubation. Influence on the slope was less straightforward. The values were changing inconsiderably till 14 h incubation, but decreased upon 2 days of incubation. The oxidative thiol attachment during 20 min led to instable and sloppy voltammograms.

The formation of the SAM includes several stages (Fig. 30)^{212,213}. The first steps of the Au-S bond formation takes less than 10 min (physisorption with consequent chemisorption). Around 90% of the thiols are bound after 10 min substituting solvent and impurities that are attached to the gold surface. Then, the removal of the conformational defects continues in the course of 7 h. The last step needs up to 15 h to remove pinhole defects, defects on the edges and to form well-ordered SAM.

Cyt *bd* is a highly hydrophobic protein, and is classified as a “hard”-structure protein. Thus, it could be that for the better adsorption on the surface it is more favourable for *bd*-oxidase to

interact with less rigid SAM (Fig. 31). Shorter incubation times of thiol lead to less ordered and more flexible SAM. In this case the adsorption of the protein would be tighter due to the increased quantity of the contacts protein-surface. Thereby, the decrease in the current could be less prominent.

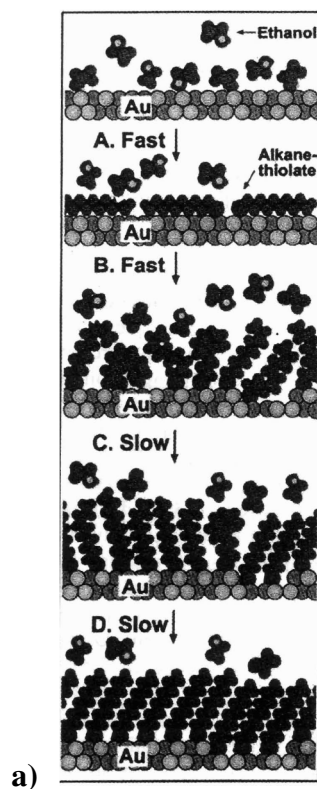


Fig. 30. Formation of the SAM in the course of time²¹².

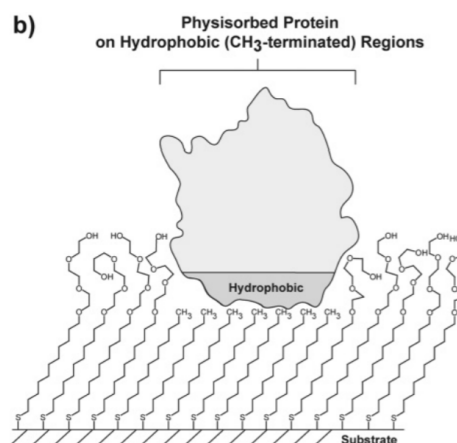


Fig. 31. Adsorption of the hydrophobic protein at SAM¹⁶⁸.

However, the presence of a higher fraction of defects, as compared to prolonged incubation, could lead to higher diversity microenvironments on the electrode and, thus, higher slope of the voltammograms.

The oxidative adsorption of the thiols during 20-30 min could substitute the procedure of 14 h incubation resulting in the ordered SAM as it was reported previously²¹⁴. However, in our studies the current decrease and the slope were of the relatively high values. It might be that the type of the defects of SAM formed during 14h incubation and oxidative adsorption is different which leads to variations of the voltammogram parameters.

The protein incubation at the surface

There were no systematic studies concerning variation of protein incubation on the electrode. It was observed that 15-20 min incubation resulted in the protein films with stability of 3%. Higher times (2 -5 hours) led to almost the same results.

4. Control experiments with HQNO

It would be helpful to know if the immobilised protein molecules are orientated in a way that quinone-binding site is accessible. As a control experiment the inhibition studies with N-oxo-2-heptyl-4-hydroxyquinoline (HQNO) were conducted. Cyt *bd* oxidase from the purification №3 was immobilised at the charged [HT/MCH/MHA] and neutral [HT/MCH] (but with different polarity) surfaces and inhibited with addition of HQNO (DMSO solution) to the final concentration of 10 μ M. Before measurement the electrode was kept 10 min in the solution with the inhibitor. The decrease in the current due to the inhibition was corrected taking into consideration the instability in the absence of HQNO:

$$\left(\frac{di}{i}\right)_c - \left(\frac{di}{i}\right)_0 \quad (12)$$

where $\left(\frac{di}{i}\right)_c$ is the current decrease upon addition of 10 μ M of the HQNO, $\left(\frac{di}{i}\right)_0$ is the current decrease in the control measurements, that is, in the absence of the HQNO. The results are summarised in the table 18.

The decrease in the current upon successive scans and the overpotential had the lowest values when utilising charged thiol mixture HT/MCH/MHA (1/1/1). Thus, the protein film was the most stable, and the most favourable conditions of the DET with the thiol monolayer of this type were provided.

Table 18. Dependency of the voltammetric parameters and HQNO inhibition effectiveness on the type of the thiol monolayer. The inhibition effect was measured for 10 μ M HQNO.

thiol type	(di/i) ₀ , % (in the absence of the HQNO)	(di/i) _c – (di/i) ₀ , % (after addition of 10 μ M HQNO)	slope	E _{cat} , V (vs SHE)
HT/MCH/MHA (1/1/1)	3	19	0.038	-0.01
HT/MCH (2/1)	19	n. d.	n. d.	n. d.
HT/MCH (1.5/1)	12	44	0.038	-0.14
HT/MCH (1/1)	8	28	0.013	-0.09
HT/MCH (1/1.5)	7	26	0.016	-0.07
HT/MCH (1/2)	7	21	0.013	-0.07

Several neutral surfaces with different polarity were studied. The polarity was controlled by mixing HT and MCH in different ratio: 2/1, 1.5/1, 1/1, 1/1.5, and 1/2. The standard modification with HT/MCH (1/1) led to higher current decrease and overpotential in the comparison to the charged surface. However, it was observed that the inhibition effect upon addition of HQNO into solution was more prominent in case of a neutral surface (almost 2 fold).

The most hydrophobic surface (HT/MCH 2/1) led to very instable voltammograms. The introduction of more polar OH-groups into the thiol monolayer allowed the protein to be better immobilised at the ratio HT/MCH $\leq 1.5/1$. However, the stability was low and the slope was quite significant. Since most of the surface of cyt *bd* is hydrophobic there is higher diversity of the sites with hydrophobic properties through which the protein could bind. Thus, it could affect the pluorientation of the protein molecules. The further addition of the MCH (HT/MCH 1/1, 1/1.5, 1/2) led to the similar values of the instability, E_{cat} and slope suggesting that cyt *bd* binding through H-bonding with a surface is accomplished and might be saturated already at HT/MCH 1/1 ratio.

Comparison of the inhibition effect showed that the more hydrophobic surface (HT/MCH 1.5/1) allowed achieving higher drop of the limiting current at - 400 mV (vs SHE). The rise of the polarity decreased the inhibition with HQNO. Thus, the least marked effect of the HQNO addition was shown with HT/MCH 1/2 modification and the value was close to the charged surface.

It is known that HQNO is an unspecific competitive inhibitor that binds in the proximity of the Q-loop^{9,132}. Q-loop is a hydrophilic part of the protein. Therefore, cyt *bd* might interact through Q-loop region with the surface forming H-bonding and leading to the decrease in the accessibility to the Q-site. It could explain the decrease in the HQNO inhibition activity when the surface polarity is raised or the charge is introduced. Hence, the further modification of the surface with HT/MCH 1/1 compromising the effect of the inhibition loss and stability decrease would be the optimal decision.

5. Conclusions

The protein films of cytochrome *bd* oxidase were stabilized at thiol monolayer protected GNPs modified rotating gold electrode. All the steps of the modification were shown to have impact on the final voltammetric characteristics of cyt *bd*.

The pretreatment of the protein with lipids had the most prominent effect confirming that the lipids play important role in the protein function.

Moreover, a synergy between lipids and thiol monolayer surface type was observed. The addition of negatively-charged PG and zwitterionic PE lipids provided the better voltammetric parameters of the cytochrome *bd* films at the neutral and negatively-charged thiol monolayers, respectively. The higher stability, lower overpotential, but higher orientation heterogeneity corresponded to the shorter thiols. Shorter thiols yielded bigger stability, lower overpotential, but higher heterogeneity.

However, the principal issue when working with membrane proteins is that the optimization needs to be made for each new purification and even batch since as it was shown that the voltammetric parameters depend on the quantity of the lipids and detergent.

The immobilized system was shown to be sensitive to all steps of the surface modification. One of the most crucial factors was the quantity of the deposited GNPs. The lower times of thiol incubation were also important for stable protein films of cyt *bd* oxidase from *E. coli*. Additionally, the type of the thiol SAM and the inhibition effectiveness of HQNO were shown to be in correlation. The optimal thiol SAM ratio was chosen for both higher stability and inhibition effect. Preliminary inhibition studies gave insight on the cyt *bd* film properties suggesting that the protein might interact not only hydrophobically but also through hydrogen bonds located near quinol-binding site.

Therefore, the protocol for gold electrode modification was established for further screening of the compounds.

II. The compound examination.

The improved procedure of electrode modification taking around 4 h allowed us to perform fast screening of a large library of compounds. The purpose of the measurements was to examine the compounds that are supposed to bind at or near quinol-binding site since their structure resembles that of the natural substrates: menaquinone or ubiquinone.

1. Aurachin D derivatives examination

The examination of aurachin D derivatives included 6 compounds with different substituent at the 3rd position (Fig. 32, 33). The decrease in the current after addition of a 10 μ M DMSO solution of the compound was measured (Fig. 34). Cyt *bd* with MNG-based preparation was utilised. The control experiments included the HQNO and DMSO influence measurements. The values corresponding to the effectiveness of the compounds are summarised in table 19.

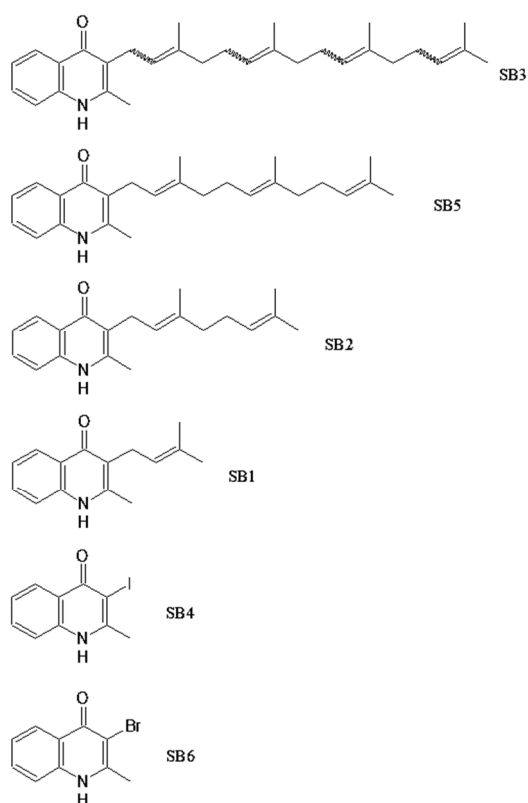


Fig. 32. Structures of the aurachin D derivatives. Substituent in the 3rd position is varied. Aurachin D corresponds to compound SB1.

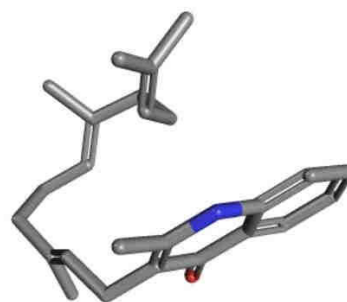


Fig. 33. Crystal structure of aurachin D²¹⁵.

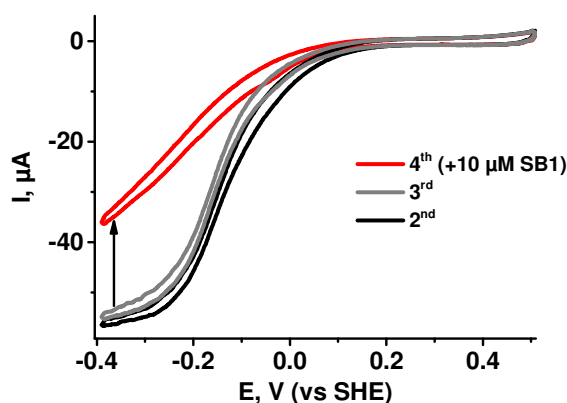


Fig. 34. Example of the inhibition measurement of the compound from the aurachin D derivative group. The 2nd and the 3rd scans are taken for determination of the current decrease in the absence of the inhibitor. The 4th measurement was conducted in the presence of the compound in the solution.

Table 19. Cyt bd catalytic current decrease (at -400 mV (vs SHE)) upon addition of the $10\text{ }\mu\text{M}$ DMSO solution of the compound. $(di/i)_0$ – the current drop in the absence of a compound, $(di/i)_c - (di/i)_0$, % – current decrease due to injection of a compound.

compound	$(di/i)_0$, %	$(di/i)_c - (di/i)_0$, %
SB1	2	32
SB2	2	21
SB3	3	6
SB4	2	9
SB5	3	16
SB6	4	11
DMSO	3	0
DMSO $100\text{ }\mu\text{M}$	3	1
HQNO	3	28

The inhibition effectiveness can be expressed in the following sequence:

$$SB1 (> HQNO) > SB2 > SB5 > SB6 > SB4 > SB3 (>> DMSO)$$

The highest inhibition activity was found for the compound SB1. The compound differs from original aurachin D by a shorter tail (1 isoprenoid unit instead of 3). Beside the size of the substituent the solubility may also contribute to the observed result since a low solubility can prevent the compound to access the binding site. This is in accordance with the sequence of the $SB1 < SB2 < SB5 < SB3$ where the decrease in inhibition activity is coupled with the rise in the isoprenoid chain length and solubility. Additionally, the SB3 compound showed a lower effect due to the presence of diastereoisomeric mixture which suggests decreased

fraction of the active isomer. However, it was shown that type of the aliphatic chain does not play crucial role in the inhibition activity⁹. The compounds with halogen substituents SB4 and SB6 were of the lowest potency. Probably, the presence of the halogen groups leads to a lower effectiveness than the presence of the hydrophobic ones.

In this experiment the intermolecular electron transfer is monitored since the electrons flow from electrode to the oxygen through the protein. Thus, the inhibition in this case could be connected with decrease of electron transfer. In¹³², however, the changes in intermolecular electron flow was not observed. Thereby, the injection of the electrons into protein could be perturbed without intermolecular electron current issues.

The control experiment was conducted to confirm the absence of any effect of the DMSO. Even at high concentration of 100 μ M DMSO did not lead to current decrease.

2. Various compound sets

The further ligand examination studies included various hits of compounds with scaffolds resembling natural electron donors: quinolone, quinone, quinazoline, coumarin, flavanone, flavane, quinoxaline, and pyran/furan derivatives (Fig. 35).

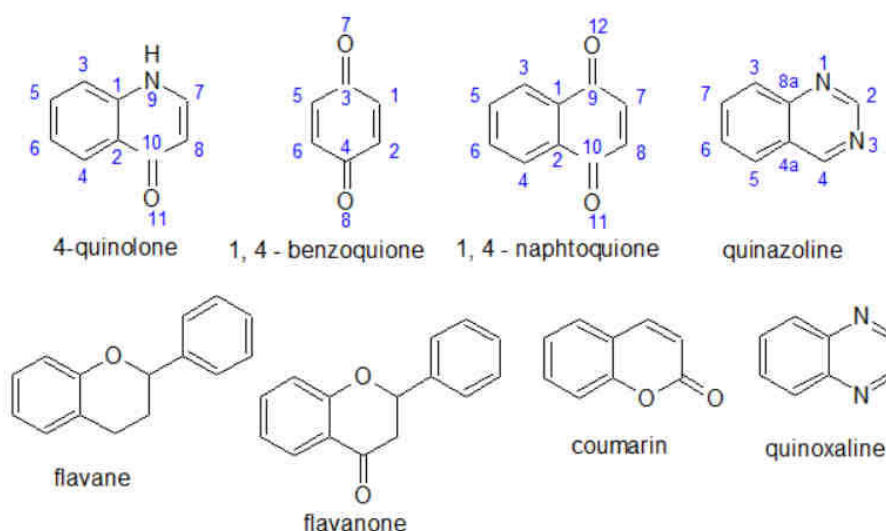


Fig. 35. Basic structures of the potential inhibitors of cyt bd. The compound scaffolds resemble the structures of natural electron donors (MQ and UQ). The locants are mentioned for the compounds concerned in the discussions.

Additionally, some well-known antibiotics were tested as well: minoxidil, tirapazamine, cetilistat, resveratrol, nalidixic acid. The conditions of the experiments were the same as for the previous inhibition studies with aurachin D derivatives. The decrease of the limiting

current at – 300 mV (vs SHE) upon addition of 10 μ M DMSO solution of a compound was monitored (table 20). The analysis is based on experiments as shown in Fig. 34.

Table 20. The limiting current changes (at -300 mV (vs SHE)) upon addition of the 10 μ M DMSO solution of the compounds. The compounds with high inhibition activity are highlighted in red, the compounds with activation or stabilising activity are highlighted in green.

group	N	compound	$(di/di)_c - (di/i)_0, \%$	remark
quinolones	1	Qo-2	0	bad solubility
	2	Qo-3	3	
	3	Qo-4	-2	
	4	Qo-5	23	
	5	Qo-6	0	
	6	Qo-7	43	
	7	Qo-8	2	
quinones	8	S7576	-8	
	9	Q906	0	
	10	STAT	-8	
bromo-naphto-quinones	11	BrN10	-21	strong activation
	12	BrN4c	-10	strong activation
hydroxo-naphto-quinones	13	142905	-2	
	14	S970840	-2	
(bromo)-benzo-quinones	15	19,546-4	2	
	16	TCI D2249	9	catalysis by compound itself
quinazolines	21	QN-1	30	
	22	QN-1Br	37	
	23	QN-2	31	
	24	QN-04	18	
	25	RK01	23	partial inhibitor
	26	CDS004809	0	
	27	CDS013899	2	
	28	31635	4	
coumarins	30	M1381	0	
	31	D87759	0	
	32	Alf10337	-2	
flavanone	33	N5893	3	
	34	Q4951	6	
flavane	35	C1788	-4	
naphtofuran/pyran	36	Q98Cam	-9	“substrate-inhibition”
	37	alpha-Dehydr	-4	
quinoxaline	38	D184977	-2	
diverse set	39	7CITC	0	
	40	B80607	-1	
	41	minoxidil	-2	
	42	tirapazamine	2	changes in the shape of limiting current
	43	cetilistat	2	
	44	resveratrol	10	
	45	nalidixic acid	0	

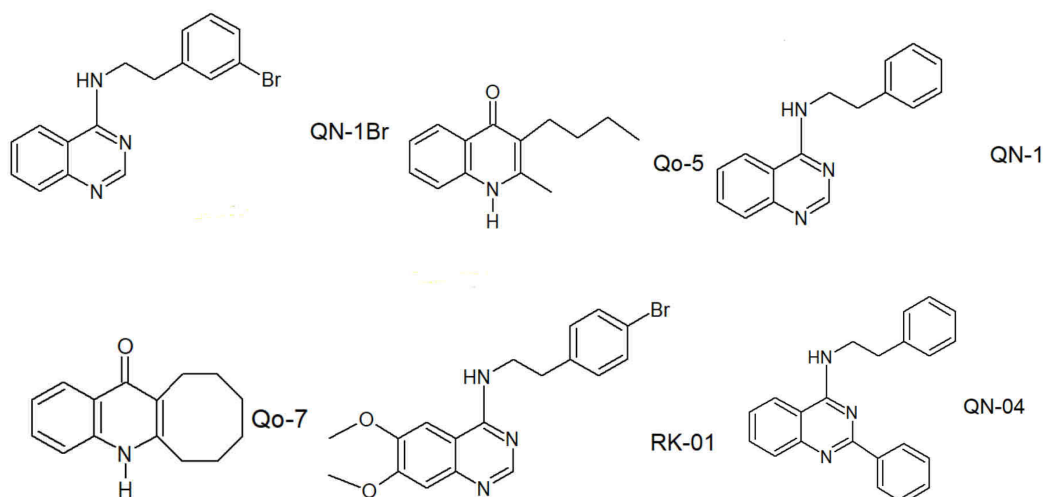


Fig. 36. Structures of the compound with the highest inhibition activity towards *cyt bd*.

QN-1Br > (SB1) > QN-2 > Qo-5 > QN-1 > Qo-7, RK-01 > QN-04

Compounds influenced in three different manners: inhibition (positive values in the table 20), activation (negative values in the table 20) and/or stabilisation (small negative values in the table 20), indifference (near 0 values in the table 21). The highest inhibition activity was found for the compounds in the quinolone (Qo-5, Qo-7) and quinazoline (QN-1, QN-1Br, QN-2, QN-04, RK01) families (Fig. 36). Resveratrol, flavanone Q4951, and quinazoline 31635 did not demonstrate prominent inhibition effect. For the most active compounds the concentration dependent studies were carried out (Fig. 37) and IC_{50} and apparent inhibition constants were determined through Morrison equation (Fig. 38, table 21). Each experiment was conducted once or twice and, thus, the should be reproduce later.

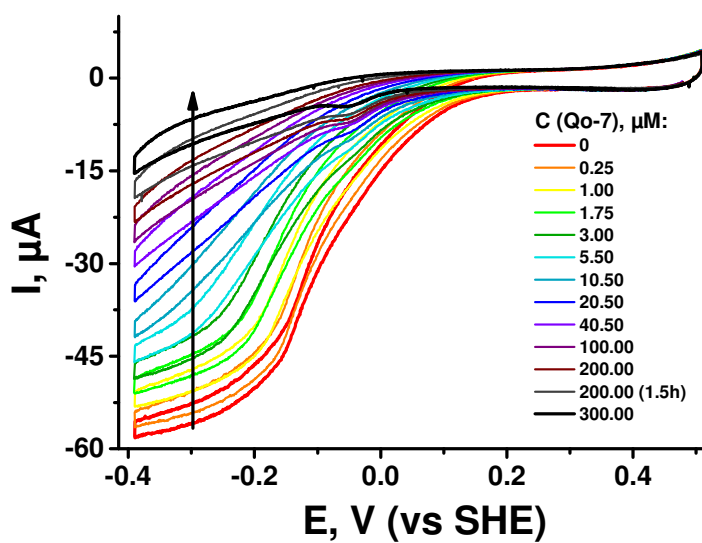


Fig. 37. Example of inhibition experiment. The gradual increase in the Qo-7 concentration leads to the decrease in the current.

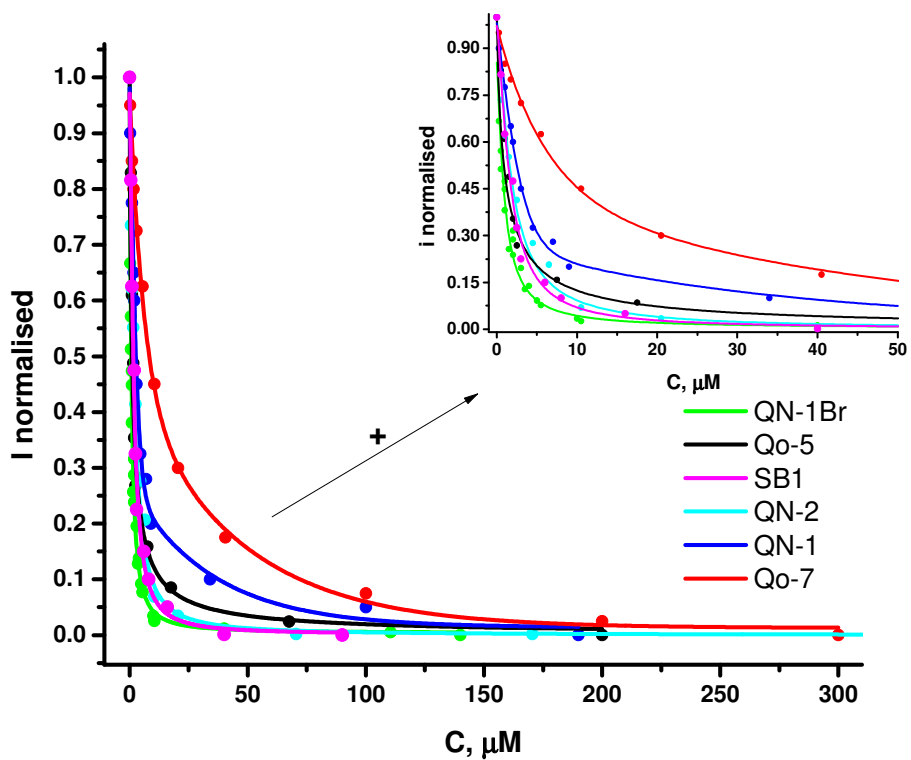


Fig. 38. Fitting with Morrison equation to determine the apparent inhibition constant of the most efficient inhibitors. The initial maximal limiting current at -300 mV (vs SHE) was taken as 1.0, the observed current values were normalised.

Table 21. IC_{50} , apparent inhibition constant and current decrease (upon addition of 10 μM of the compound) values for the most efficient inhibitors.

compound	IC_{50} , μM	compound	$(di/i)_c - (di/i)_0$, %	compound	K_I^{app} , μM
QN-1Br	0.7	Qo-7	43	QN-1Br	0.43
Qo-5	1.0	QN-1Br	37	SB1	0.64
SB1	1.5	SB1	32	QN-2	0.78
QN-2	1.7	QN-2	31	Qo-5	1.32
QN-1	2.5	QN-1	30	QN-1	2.79
Qo-7	8.1	Qo-5	23	Qo-7	8.35
RK01	n. d.	RK01	23	RK01	n. d.
QN-04	n. d.	QN-04	18	QN-04	n. d.
HQNO	1.4	HQNO	28	HQNO	1.40

Judging through the apparent inhibition constant the compound effectiveness is in line with the following sequence: QN-1Br > QN-2 > Qo-5 > QN-1 > Qo-7, RK-01 > QN-04. The comparison of IC_{50} and apparent K_I shows that IC_{50} is 2 fold higher in case of QN-1Br, SB1 and QN-2. These discrepancies ($IC_{50} < K_I$) could come from the tight-binding mode of the inhibition or even irreversible binding in case of quinoxalines. For the compounds that have IC_{50} equal to apparent inhibition constant the classical inhibition mode might be proposed. Additional experiments determining k_{cat} (Koutecky-Levich approach) in the presence of an inhibitor could be helpful for understanding of the inhibition mechanism.

An example of an experiment showing the gradual decrease in the current upon inhibitor addition is shown in Fig.37. Interestingly, almost all the compounds did not lead to the return of the current to the background levels. Some residual current was present in such experiments. This could be explained either through the partial type of inhibition or, the more likely, the pluriorientation of the protein molecules at the surface. Since some protein molecules can be orientated with inhibitor-binding site towards the surface and prevent the access of the inhibitor to this site. Additionally, the interaction between protein molecules could hinder the interaction with the inhibitor. In this case the experiments with variation of *cyt bd* concentration upon inhibitor addition would be interesting.

All effective quinazolines possess the phenylethylamine substituent in the 4th position. The introduction of bromide in the meta-position increased the activity of the compound which could be associated with higher solubility if to compare QN-1Br and QN-1. The decrease in the inhibition effectiveness of the QN-04 could be explained in the same manner since it bears additional phenyl substituent in the 2nd position of the quinazoline skeleton, which decreases its solubility in water solution. On the contrary, the compound RK-01 is also Br-

substituted but the activity is lower than QN-1Br. This could be connected with the presence of two methoxy-groups in the quinazoline ring in the 6th and 7th positions. Thus, for the inhibition not only the substituent in the 2nd position is important but the hydrophobicity of the other parts of the molecule might be necessary. Interestingly, it was shown that two methoxy groups in UQ are involved in the interaction with Glu290 in cyt *bd* from *E. coli*⁹¹, but cyt *bd* can utilise and UQ containing methoxy groups, and PQ devoid of ones⁹⁵. Thus, the importance of the O-atoms in the 6/7-position substituents for binding is under debate. In our studies the presence of the methoxy-groups in these positions was shown to decrease the inhibitor activity of the quinazolines. Additionally, it is quite probable that the distance from substituent to the oxygen atom, that is dimensions of the molecule, is very important for the tighter interaction.

The quinolones Qo-5 and Qo-7 showed also high inhibition effect on cyt *bd*. Qo-5 structurally resembles aurachin D but with saturated and shorter substituent in the 3rd position instead of the isoprenoid chain. It was shown before that the presence of unsaturation is not required for inhibition⁹. Therefore, we can confirm this statement, especially, when comparing apparent inhibition constants of Qo-5 and aurachin D derivative SB1, which are almost alike. Importantly, the methyl-group in the 2nd position is present in the case of Qo-5 and SB1, or hydrophobic cyclooctane fragment - in case of Qo-7, could increase the inhibition activity as it was shown for aurachin C and D derivatives. By comparison the quinazoline and quinolone inhibitor structures we can see that two factors seem to be important for inhibition. First, it is the presence of the heteroatom with one unshared pair of electrons (nitrogen in amine or heteronitrogen in quinazoline, oxygen in ketogroup of quinolones). This fragment could form hydrogen bond with one of the amino acid residues. Secondly, the hydrophobic fragment that should be located in the relative proximity to the aforementioned heteroatom (phenylethyl group is case of quinazoline, or aliphatic chain in case of the quinolones). Probably, the hydrophobic pocket or the patch of cyt *bd* is located near charged amino acid.

The structure of the noneffective compounds cannot be revealed in the thesis for request of the group of Dr. Nasiri (Johann Wolfgang Goethe-University, Frankfurt-am-Main, Germany). In general, the noneffective compounds bear hydrophilic substituents or lack hydrophobic one in the 3rd position or bear bulky ones in the 2nd position in case of the quinolone derivatives (Fig. 39).

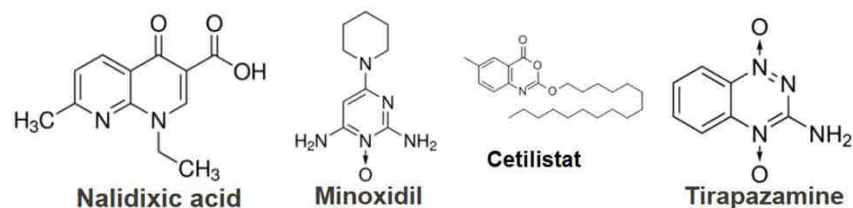


Fig. 39. Some examples of the structures of the compounds with no inhibition effect on *cyt bd*.

To conclude, for the better inhibition of *cyt bd*-oxidase from *E. coli*:

- the quinolone or qunazoline scaffold is required
- the presence of the hydrophobic substituent in the proximity to an heteroatom (O, N) is crucial
- the absence of the substituent in the benzole ring part is desirable
- introduction of unbulky methyl-substituent in the 2nd position might improve the inhibition

Interestingly, several compounds (e. g., *BrN10* > *BrN4c* > *Q98Cam* > *STAT* = *S7576*) were shown to have activation effect coupled with narrowing of the interval of the transition region. Quite frequently the activation effect was coupled with a better stabilisation of the voltammogram (Fig. 40).

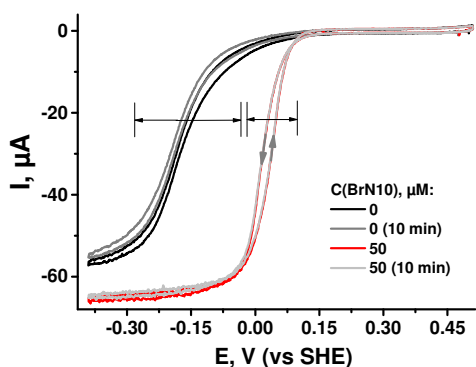


Fig. 40. Activation-stabilisation effect of the *BrN10* on the voltammogram of *cyt bd* from *E. coli*. The transition zone is shown.

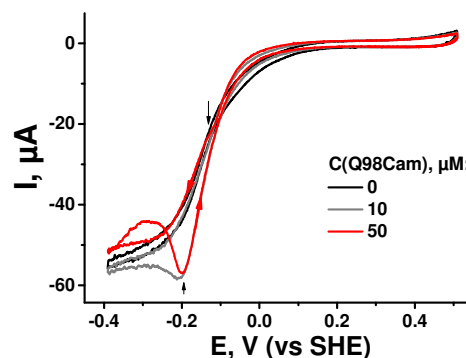


Fig. 41. Substrate-inhibition effect of *Q98Cam*-effector on *cyt bd* from *E. coli*.

The compound-activator seems to behave as redox mediator facilitating the electron transfer between protein and electrode. Additionally, the compound *Q98Cam* (naphthofuran/pyran) led

to activation at 10 μ M concentration. However, at higher concentration the inhibition of cyt *bd*-oxidase was observed (Fig. 41). This type of the behaviour of the effector resembles the substrate-inhibition of nitrate reductase in the presence of high nitrate concentrations²¹⁶.

3. Conclusions

The screening of the compounds has shown that the intermolecular electron transfer in cytochrome *bd*-oxidase was disturbed with quinazoline and quinolone (in particular aurachin D) derivatives in nanomolar range of concentrations. The highest inhibition activity was observed when a hydrophobic substituent was located in the proximity to the electronegative atom (O or N). In particular, the phenylethylamine substituent allowed compound QN-1Br to demonstrate the highest effectiveness with apparent inhibition constant of 430 nM. The determined structure of the most effective inhibitor can serve as a useful template for further derivatization of the compound with potent antibiotic effect.

The inhibition studies elucidated the structure of the quinol binding site. It is probable that the hydrophobic patch of cytochrome *bd* is located near charged residue and interaction with both of them at once is essential for the substrate binding.

III. Cytochrome *bd* from *G. thermodenitrificans*

Cytochrome *bd*-oxidase from thermophilic Gram-positive *Geobacillus thermodenitrificans* (also known as *Bacillus stearothermophilus*²¹⁷) differs from the one extracted from Gram-negative *E. coli* in the Q-loop length: it is twice shorter. Probably, due to this the X-ray structure was successfully obtained for cytochrome *bd* from *G. thermodenitrificans* since the conformational stability of the mostly disordered Q-loop is lower in case of the longer sequence of long Q-loop. Most of the *bd*-oxidases possess short Q-loop and cytochrome *bd* from proteobacteria such as *E. coli* can be regarded as a later evolution acquisition^{20,6} that could allow utilising various quinols. The characterisation of this protein and comparison with the data obtained for already well-studied cytochrome *bd* from the other species is of large interest. Moreover, inhibition studies would elucidate the differences between organisation of short- and long Q-loop types of cytochrome *bd*-oxidases.

1. Comparison with *E. coli* at pH7

UV/Vis-spectroscopy

The absolute absorption spectra were obtained for the air-oxidised and dithionite reduced *cyt bd* from *E. coli* and *G. thermodenitrificans* (Fig. 42). Then, reduced-minus-oxidised spectra were calculated (Fig. 43).

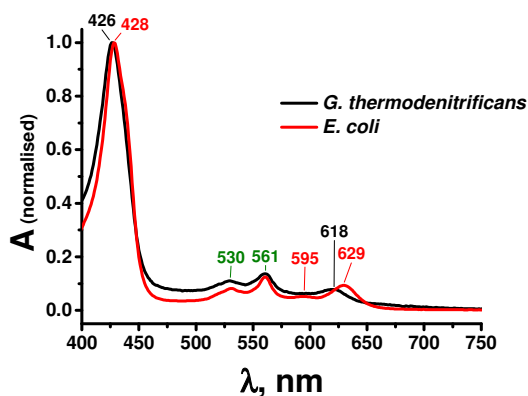


Fig. 42. Absolute absorption spectra of dithionite reduced *bd*-oxidases from *E. coli* and *G. thermodenitrificans* (pH7, RT, spectra are normalized at the Soret band).

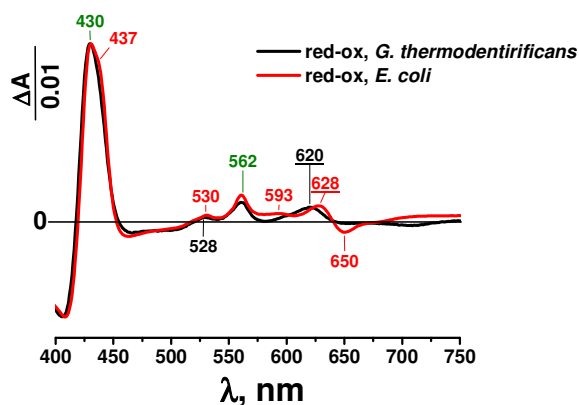


Fig. 43. Differential absorption spectra of *bd*-oxidases from *E. coli* and *G. thermodenitrificans*. Ox-state = air-oxidised, Red-state = dithionite reduced. (pH7, spectra are normalized at the Soret band)

As cyt *bd* from *E. coli*, cyt *bd* from *G. thermodenitrificans* reduced spectrum shows several major bands: 426 nm (Soret band), 561 nm (α -band), 618 nm (α -band), and also 530 nm (β -band). All three hemes contribute to the Soret band with a small relative contribution of the heme *d*⁶. The 560 nm band originates from the protohemes IX, heme *b*, and the 618 nm band is due to heme *d* solely. The main spectral difference between the two proteins is the hypsochromic shift of the *d* heme band in case of cyt *bd* from *G. thermodenitrificans*. The band corresponds to π - π^* transition. Therefore, a more hydrophobic environment is suggested for cyt *bd* from the thermophile: since π^* -orbital is polar and less stable in hydrophobic environment which leads to a higher distance between π and π^* energetic levels. Additionally, the shoulder at 437 nm in the differential red-ox spectra and the band at 595 nm in the absolute spectra were almost absent in case of the *G. thermodenitrificans* enzyme suggesting either a lesser fraction of heme *b*₅₉₅ is present²⁰ or diminished coefficient of molar absorptivity of this heme is in the sample from the thermophile. Similar observations¹⁷ of short Q-loop members of cyt *bd* family are in line with last assumption. Moreover, in some species heme *d* is partially replaced by heme *b*¹⁷. It was shown that despite low intense α -band of heme *b*₅₉₅ the heme stoichiometry is the same⁶.

Spectroelectrochemistry

UV/Vis titration

A spectroelectrochemical titration was conducted (Fig. 44) for cyt *bd* from *G. thermodenitrificans* at pH6, pH7 and pH9.5. Most of the titration experiments for cyt *bd* from other organisms were carried out at pH7 in the literature. At pH6 the protein shows an optimum of catalytic activity²⁰. At pH9.5 the protein demonstrates alterations in catalytic activity at 45°C. The results are summarised in table 22.

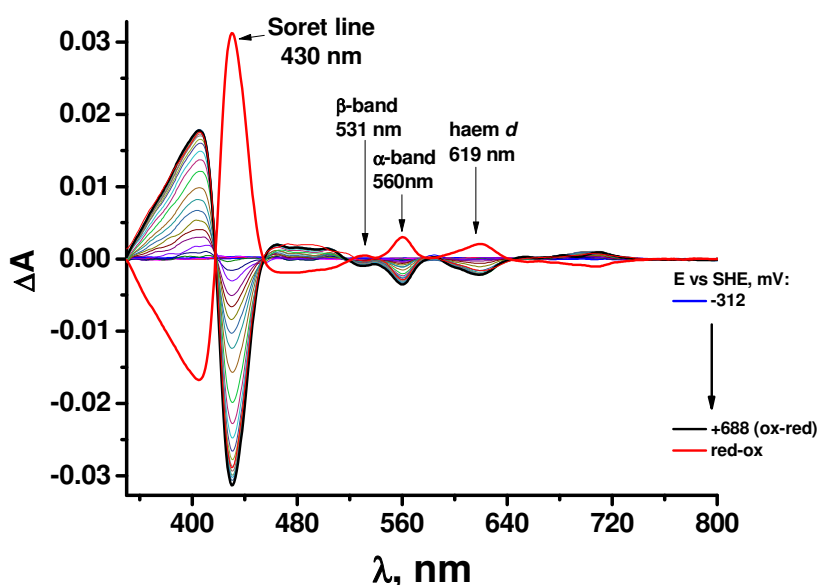


Fig. 44. Example of oxidative titration. One can see full Red-minus-Ox (blue curve) and full Ox-minus-Red (red curve) differential absorption spectra. The step of the titration was varied from 100 mV far from the transition to 25 mV in the region of the redox transitions.

Table 22. Mid-point potentials (vs SHE) of the heme cofactors from *cyt bd* (*G. thermodenitrificans*) at different pH. 13°C, DDM. The hemes *b* were not attributed and were labelled as heme *bN*1 and heme *bN*2. The value errors are mentioned in Annex 3. The $E_{m7} = -43$ mV for heme *d* was calculated based on the hysteresis for heme *d* at pH6 and E_{m7} for heme *d* obtained in oxidative titration.

	619 nm /heme <i>d</i>	heme <i>bN</i> 1	heme <i>bN</i> 2
pH6, oxidative direction	+ 46	+ 79	+ 210
pH6, reductive direction	- 70	+ 59	+ 167
pH6, KCN, oxidative direction	- 43	+ 33	+ 174
pH7, oxidative direction	+ 15	+ 50	+ 155
pH7, reductive direction	- 300 ... - 101	+ 10	+ 119
pH9.5, oxidative direction	- 163	- 18	+ 70
E values with consideration of hysteresis			
pH6	-12	+ 69	+ 189
pH7	- 232 ... -132/-43	+ 30	+137

The set of the experiments at pH6 allowed obtaining the following values of the redox potentials: +46 mV for heme *d* and +79 and +210 for hemes *b* (table 22). The addition of excess of KCN which binds to the high-spin heme *d* led to the following changes: heme *b*

values showed a downshift of the potential of heme *b*N₁ by approximately 40 mV and heme *d* by 90 mV. Thus, we confirmed the attribution of the 618 nm band to heme *d* and demonstrated that the *bd*-oxidase from *G. thermodenitrificans* is sensitive to a nucleophilic ligand such as cyanide. Previously it was observed that cyt *bd* from *G. thermodenitrificans* is more sensitive to cyanide than cyt *bd* from *E. coli* and *A. vinelandii*. For cyt *bd* of long Q-loop type only heme *d* demonstrates potential changes, then hemes *b* do not bind and have the potentials unchanged¹².

The set of the experiments at pH7 yielded the following values: +15 mV for heme *d* and +50 and +155 for hemes *b*. Finally, at pH9.5 all the values were downshifted: -163 mV for heme *d* and - 18 and + 70 for hemes *b*.

From these three pH points we can provide a tentative estimation of the slope of the function $E = f(pH)$ (Fig. 45). The analysis led to dE/dpH values of -30 mV/pH unit for hemes *b*N₁ and *d*, and -40 mV/pH unit for heme *b*N₂. Thus, PCET is a characteristic of all heme reduction.

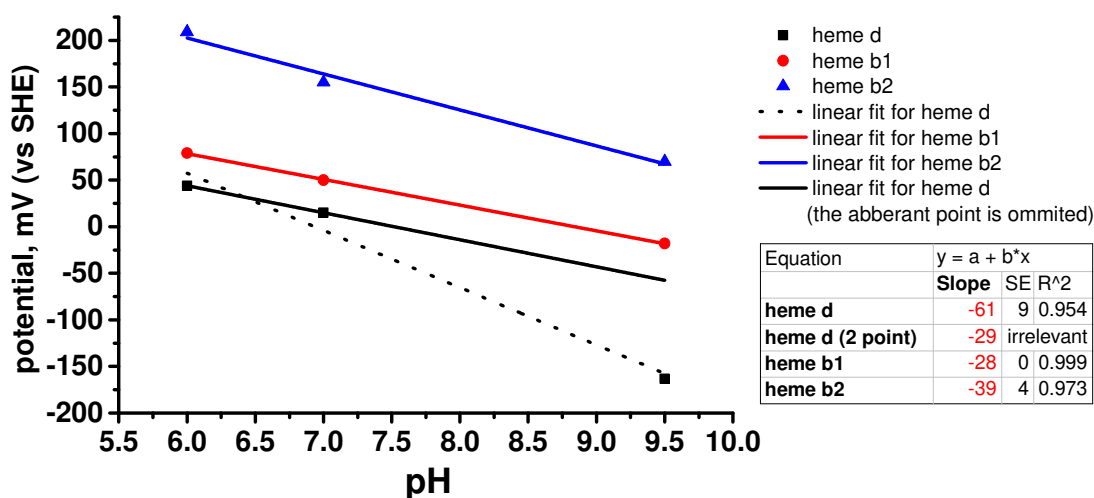


Fig. 45. Dependency of the reductive potentials on pH of cytochrome *bd* cofactors (*G. thermodenitrificans*, in the presence of DDM). The linear fit was utilised for simplicity and on the example of cyt *bd* from *E. coli* that shows this type of $E(pH)$ dependency in this pH region.

Supplementary experiments were conducted at pH6 and pH7 to measure the width of hysteresis. Hysteresis is a difference between potentials measured during reductive and oxidative titration and it could originate from kinetic issues and system not at equilibrium, oxidative protein inactivation, cooperativity that could be revealed only in one titration direction, mediator issues, etc. For both pH6 and pH7 the hysteresis was around 40 mV for

hemes *b* and more than 100 mV for heme *d*. Moreover, we noticed that the E_m of heme *d* determined during reductive titration was in dependency on the initial ox-potential. The higher the initial oxidative potential the more difficult to reduce heme *d* is (hysteresis was higher).

When comparing the obtained results with the data from other species we noticed significant differences for cyt *bd* from *G. thermodenitrificans* (table 23, Fig. 46).

Table 23. The mid-point potentials of the cofactors of cytochrome *bd*-oxidase from different species in the presence of DDM. Tentative attribution of the hemes *b* is based on the further studies with aurachin D and the batch devoid of heme *d*.

species \ E_m , mV (vs SHE)	<i>b</i> ₅₅₈	<i>b</i> ₅₉₅	heme <i>d</i>
<i>E. coli</i>	176	168	258
<i>G. thermodenitrificans</i>	30 (heme <i>b</i> №1)	137 (heme <i>b</i> №2)	- 43
<i>A. vinelandii</i>	166	251	310

As we can see the order of the potential values is distributed from more negative values of heme *d* to the highest values for hemes *b* regardless of pH (pH6, pH7, pH9.5). Cyt *bd* oxidases from *E. coli* and *Azotobacter vinelandii* show a potential distribution in the opposite direction: heme *d* was the highest potential component. Therefore, it was suggested for *E. coli* (due to this E_m distribution) that electrons are passed spontaneously to heme *b*₅₅₈ and then to heme *d* through heme *b*₅₉₅. However, for *G. thermodenitrificans* heme *d* seems to be the lower potential heme, which was an unexpected result because this means that the electron flow from heme *b* to heme *d* could be even inverted. This fact might explain why *G. thermodenitrificans* cyt *bd* demonstrates the lowest O₂-affinity when comparing these three organism⁶. Furthermore, a lower oxidase activity of cyt *bd* from *G. thermodenitrificans* is observed as well²⁰. The differences of the potential in the redox pairs QH₂-*b*₅₅₈ and *d*-O₂ are higher in case of cyt *bd* from *G. thermodenitrificans*, which would facilitate electron exchange between substrates and enzyme; however, the further intramolecular electron transfer in the protein may be hindered. The potential order inversion could be caused with cooperativity (as it was proposed, for example, for *cbb*₃-oxidase¹⁷⁶), but the interaction of the hemes in case of cyt *bd* from *E. coli* was shown as very weak¹⁸⁰. As well as in *cbb*₃-oxidase the electron density is elevated at chlorin heme *d* with Glu as a ligand.

The other difference is that hemes' *b* potentials of cyt *bd* from *E. coli* are very close, which is not the case for the other species. Interestingly, in some studies the heme *b*₅₅₈ from

A. vinelandii was shown to exist in two populations providing two redox components. Finally, the $E = f(\text{pH})$ dependency is different for cyt *bd* from *E. coli* and *G. thermodenitrificans*: the hemes *b* shows a -40 mV/pH unit and heme *d* stands out with -60 mV/pH unit. Importantly, from the electrochemical point of view cytochrome *bd*-oxidases do not form a homogeneous group.

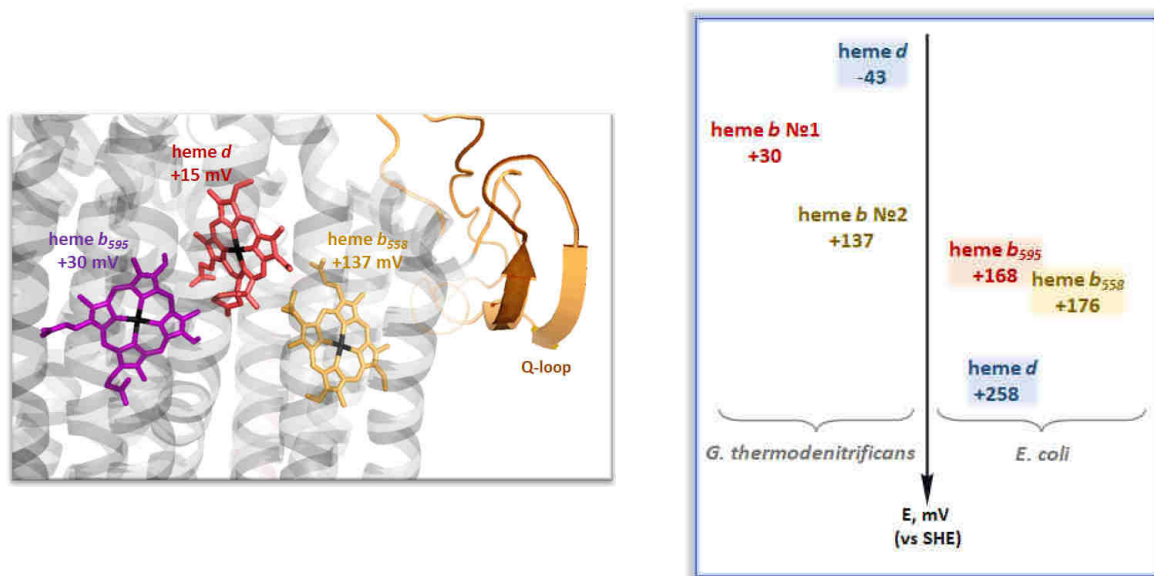


Fig. 46. Probable distribution of potentials E_{m7} within hemes in cyt *bd* from *G. thermodenitrificans*.

Redox-induced differential FTIR spectroscopy

The IR spectroscopic characterisation of cytochrome *bd* from *G. thermodenitrificans* was conducted at 5°C and pH7 for comparison with cyt *bd* from *E. coli* reported before (Fig. 47). In the ox-red spectra the positive bands correspond to the oxidised state, then the negative to reduced state of the protein. The full attribution of the bands can be found in table 24.

A thorough comparison of the two cyt *bd* from different species revealed some additional differences between the species.

The amide I region (1690-1620 cm^{-1}) shows bands at 1685, 1675, 1664, 1631 and 1647 cm^{-1} which can be attributed to mostly C=O vibrations of the polypeptide backbone. The signature at 1664 cm^{-1} was inverted in the spectra of cyt *bd* from thermophile.

The amide II region (1570-1520 cm^{-1}) shows contributions from the CN stretching, NH bending vibrations of the protein backbone, C=C vibrations of the porphyrin ring (e. g., bands at 1552, 1522 cm^{-1}) and -COO^- groups of deprotonated amino acid residues (Asp, Glu) (e. g., 1558 cm^{-1}). Signals from other compounds also can contribute to this spectral region.

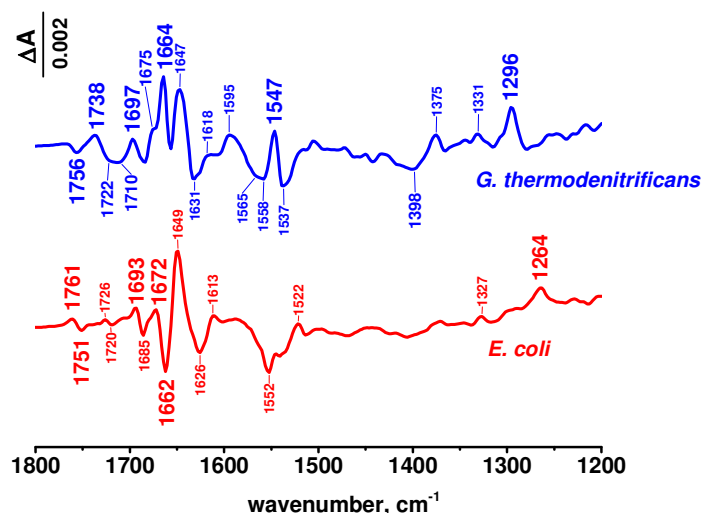


Fig. 47. Ox-red differential spectra of *cyt bd* from *G. thermodenitrificans* and *E. coli* at 5°C and pH7.

The other important spectral region is between 1700 and 1680 cm^{-1} , which contains characteristic bands of protonated heme propionates. Above 1710 cm^{-1} the C=O vibrations of protonated acidic amino acids (Asp, Glu) contribute. Based on H-D exchange experiments²¹⁸, the couple of 1761/1751 cm^{-1} in *E. coli* *cyt bd* spectra is attributed to the protonated Asp or Glu located in hydrophobic environment where the H-bonding is absent. The corresponding bands in case of *G. thermodenitrificans* show very different features. Therefore, different Asp/Glu may be involved here.

One of the principal dissimilarities which should be noted concerns the bands at 1296 and 1264 cm^{-1} that correspond to MQ and UQ, respectively (Fig. 48)^{218,219}. The presence of UQ can be revealed though the presence of the bands at 1264 cm^{-1} corresponding to vibrations of C-O bond in methoxy side chain and 1612 cm^{-1} corresponding to $\nu(\text{C}=\text{C})$ vibrations. The band at 1296 cm^{-1} is attributed to C-C and C=C vibrations in MQ. It is downshifted from 1304 to 1296 cm^{-1} due to interaction with the protein. The vibrations of C=C of aromatic ring in MQ could also contribute to the band at 1595 cm^{-1} . In addition, MQ has bands (1670 and 1632 $\text{cm}^{-1} - \nu(\text{C}=\text{O})$) which overlap with amide I signals (backbone). This may explain the positive peak at 1666 cm^{-1} in the spectra of the samples with excess of MQ. The band at 1738 cm^{-1} of *cyt bd* from *E. coli* containing MQ previously was attributed to the acidic residue that could be protonated upon binding of MQ to the protein. Thus, we can conclude that *E. coli* sample contains UQ, whereas the *G. thermodenitrificans* sample contains MQ. The batches of *cyt bd* from *G. thermodenitrificans* showed various contents of MQ making the data analysis more complicated.

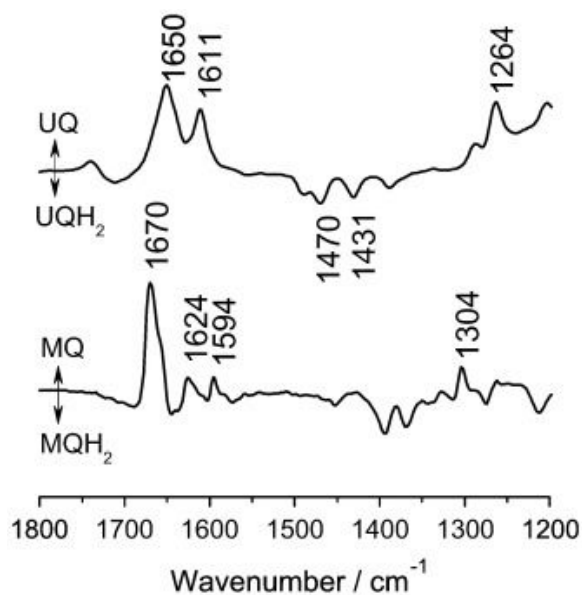


Fig. 48. Ox-red FTIR difference spectra of free MQ and UQ at pH7²¹⁹.

Table 24. Tentative assignments^{218,219} of the bands of ox-red differential FTIR spectra of cyt bd from *E. coli* and *G. thermodenitrificans* (pH7, 5°C). The bands where lipids vibration can contribute are in green.

band position, cm ⁻¹ (positive or negative at ox-red spectrum)	tentative assignment		band position, cm ⁻¹ (positive or negative at ox-red spectrum)
<i>E. coli</i>			<i>G. thermodenitrificans</i>
1264 +	vibrations of C-O bond in C-OCH ₃ side chain of UQ		
1290	vibrations of C-O bond in C-OCH ₃ side chain of UQ	C-C/C=C bonds in MQ	1296 +
1327 +	$\delta(\text{CH})$, $\nu_s(\text{COO}^-)$		1331 +
1336 0/-	Trp		1338 0/-
		$\delta(\text{CH}_3)$	1365 -
1373 +	C=C ring modes of UQ, $\delta(\text{CH}_3)$	$\delta(\text{CH}_3)$	1375 +
		$\nu_s(\text{COO}^-)$	1400 -
1514 -	$\nu(\text{C}=\text{C})$, $\delta(\text{CH})$ of Tyr- OH	$\nu(\text{C}=\text{C})$ of Tyr-O ⁻	1504 +
1522 +	$\nu(\text{C}=\text{N})$ and $\delta(\text{C}=\text{C})$ of backbone, $\nu(\text{C}=\text{C})$ of porphyrin ring, $\delta_{\text{as}}(\text{COO}^-)$ of Asp or Glu		

Continuation of table 24.

1539 -	v(C=N) and δ (C=C) of backbone, v(C=C) of porphyrin ring, δ_{as} (COO ⁻) of Asp or Glu		1537 -
1545 -?			1547 +
1552 -			1558 -
1587 +	ν_{as} (COO ⁻) of Asp or Glu	ν_{as} (COO ⁻) of Asp or Glu, v(C=C) ring vibrations of MQ	1595 +
1600 -	v(C=C) of Tyr-O ⁻		1606 -?
1613 +	v(C=C) vibrations of oxidised UQ, v(C-C) of Tyr-OH		
		ν_s (CN ₃ H ₅ ⁺) of Arg	1618 - ?
1626 -	oxidised UQ	MQ	1631 -
1649 +	v(C=O) backbone, individual amino acids, oxidised UQ	v(C=O) backbone, individual amino acids	1647 +
1662 -	v(C=O) backbone, individual amino acids, oxidised UQ	v(C=O), vibrations of MQ	1656 0
1672 +	v(C=O) backbone, individual amino acids	v(C=O), vibrations of MQ	1664 +
		ν_{as} (CN ₃ H ₅ ⁺) of Arg (without salt bridge)	1676 +
1685 -	v(C=O) of heme propionates		1685 -
1693 +			1697 +
1720 -	v(C=O) of Asp or Glu with H-bonding		1710 -
1726 +			1722 -
		v(C=O) of Asp or Glu with H-bonding	1738 +
1751 -	v(C=O) of Asp or Glu without H-bonding (in hydrophobic environment); heme <i>d</i>		
1761 +			1756 -

Resonance Raman spectroscopy

The Resonance Raman studies were conducted with excitation at 514 nm. The spectra for cyt *bd* from *G. thermodenitrificans* almost coincided with the spectra of cyt *bd* from *E. coli*

(Fig. 49). No shift of the bands was observed (except the undetermined band at 1305-1307 cm^{-1}). The major contributions to the spectra obtained with excitation at 514 nm originate from porphyrin skeletal modes (ν_{10} , ν_{11} , ν_{19} , etc.) of the ferrous hemes *b*, whereas the symmetric vibrations (ν_2 , ν_3 , ν_4 , etc.) are less prominent (table 25). The heme *b* spin-state in cyt *bd* from *G. thermodenitrificans* seems to be the same that in cyt *bd* from *E. coli*.

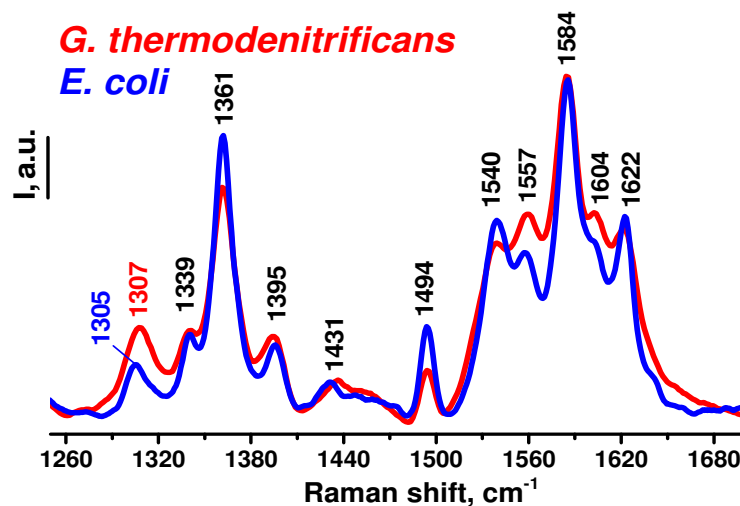


Fig. 49. Resonance Raman spectra of the dried films of cyt *bd* from *E. coli* and *G. thermodenitrificans*. The excitation was conducted at 514 nm.

Heme b_{558} dominates the spectrum of both oxidases due to the excitation wavelength used. The corresponding bands at 1395, 1494, 1540, 1584 and 1622 cm^{-1} are almost of the same intensity. However, the major bands that correspond to heme b_{595} or mixture of *b* hemes are more prominent. For example, the bands at 1557 and 1604 show higher intensity in case of cyt *bd* from *G. thermodenitrificans*. The minor bands are raised mostly due to symmetric vibrations and are less expected to be observed with excitation at 514 nm, thus, the attribution of these bands (1339, 1361, 1494, 1540 cm^{-1}) is less straightforward. Most of these bands are due to heme b_{595} vibrations²²⁰. Nevertheless, according to UV/Vis spectroscopy data the *G. thermodenitrificans* sample contains less heme b_{595} protein or heme b_{595} with lowered coefficient of the absorption, which could explain the lower intensities of the bands.

Both hemes b_{595} and *d* could contribute to the band at 1604 cm^{-1} in case of cyt *bd* from *G. thermodenitrificans*. Since heme *d* α -band is hypsochromically shifted as compared to *E. coli* and, thus, could be more involved in excitation at 514 nm. The other skeletal heme *d*

bands that could overlap with heme *b* spectrum may be found at 1572 and 1575 cm⁻¹. It could explain the different intensity at 1557 cm⁻¹ since the band at 1575 overlaps.

Table 25. Tentative assignment of the Raman bands of cyt *bd* from *E. coli* and *G. thermodenitrificans*. The assignment is based on previous reports^{220,221, 131}. The attribution involves the idea that ferrous (Fe²⁺) heme *b*₅₅₈ is low-spin six-coordinated (axial ligands: His and Met) and ferrous (Fe²⁺) heme *b*₅₉₅ is high-spin pentacoordinated (axial ligand: His). The abbreviations for the band intensity: *s* – strong, *m* – medium, *w* – weak.^{131,220,221}

band position, cm ⁻¹	Tentative attribution	
	vibration type	cofactor
1307/1305	n. d.	n. d.
1339, w	ν_4	<i>b</i> ₅₉₅
1361, s	ν_4 (v (pyr half-ring)sym)	<i>b</i> ₅₉₅ / <i>b</i> ₅₅₈
1395, w	ν_{29}	<i>b</i> ₅₉₅
1431, w	vinyl modes	<i>b</i> hemes
1494, w	ν_3	<i>b</i> ₅₅₈
1540, a	ν_{38}	<i>b</i> ₅₅₈
1557, a	ν_{11} / ν_3	<i>b</i> ₅₅₈ / <i>b</i> ₅₉₅
1584, s	ν_{19} (v (C α -Cm)asym)	<i>b</i> ₅₅₈
1604, a	ν_{10} (v (C α -Cm)asym)	<i>b</i> ₅₉₅ / heme <i>d</i>
1622, a	ν_{10}	<i>b</i> ₅₅₈

In addition, the differences in the intensities of the 1557, 1604 and 1494 cm⁻¹ bands could come from different detergent content which can varies from batch to batch (Annex 4).

With an excitation at 514 nm hemes *b* should be excited but not heme *d*. Thus, the similarity of two spectra suggests that the environment of the hemes *b* in the two proteins is similar.

Previously it was proposed^{220,222} that heme *b*₅₉₅ in cyt *bd* from *E. coli* is coordinated by only one His, but almost coincidence of the Raman spectra of cyt *bd* from the two species allows us to assume that the coordination of the reduced hemes *b*₅₉₅ and *b*₅₅₈ in *E. coli* cyt *bd* is the same as in cyt *bd* from *G. thermodenitrificans*: Glu/His and Glu, respectively (based on the X-ray structure). The pentacoordination in cyt *bd* from *E. coli* was suggested for the reduced protein whereas the X-ray structure was obtained for the air-oxidised state of cyt *bd* from *G. thermodenitrificans*. Upon reduction the Glu acid can dissociate from the iron atom leading to pentacoordinated complex of heme *b*₅₉₅.

Electrochemistry

The modification of the electrode with further immobilisation of cyt *bd* from *G. thermodenitrificans* led to the results shown in Fig. 50.

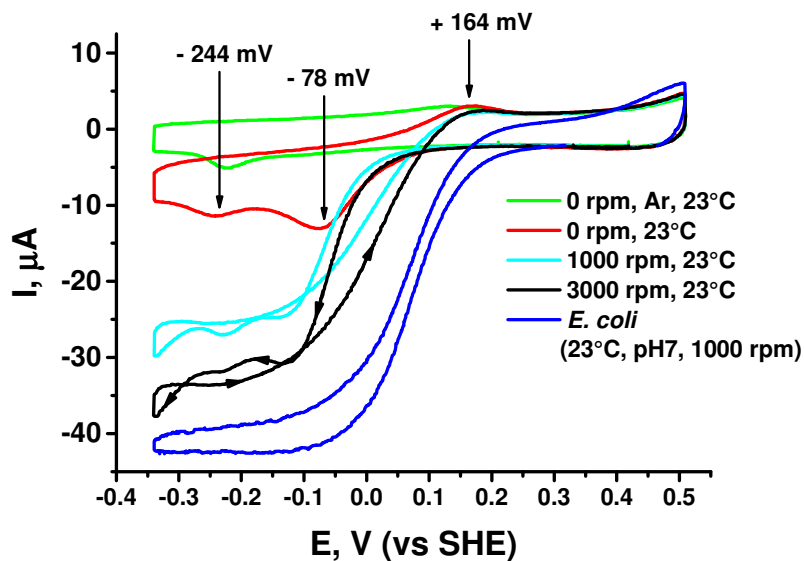


Fig. 50. Cyclic voltammograms for cytochrome *bd* from *G. thermodenitrificans*. Conditions of measurements are demonstrated on the graph. Rate of scanning 0.02 V/s, solution 100 mM KPi, pH7. Cyt *bd* from *E. coli* of the 2nd purification is shown for comparison.

Firstly, in the experiment under argon atmosphere (green curve) a pair of anodic (+164 mV) and cathodic (-244 mV) peaks were observed, which resembles an irreversible redox process. An average of the peaks is -40 mV. In the literature one can find following redox potentials for quinone MQ in standard conditions: - 80 mV MQ-8^{41,44}, - 78 mV vitamin K1⁴⁶, - 75 mV MQ¹³⁸, - 80 mV MQ³⁰. Thus, the E_m of MQ does not coincide exactly with observed values. However, the mid-point potential of MQ is different when quinone is bound to the protein and is not in the propanol solution as standard conditions of the quinone determining measurements.

After introduction of O₂ into the system, the second cathodic peak appears (red curve in Fig. 50) at - 78 mV that we attributed to O₂ reaction. The variation in rotation speed (red, blue and black curves) was performed to determine the turnover number of the protein. However, protein film instability (previous and the next scans show notable decrease in the current values) complicates data interpretation. Interestingly, an unusual curve self-crossing was observed (black and light blue lines in Fig. 50).

Several hypotheses could explain this self-crossing shape of voltammogram.

The first one is connected with protein activation at high reducing conditions as it was observed for nitrate reductase NarGH from *E. coli*¹⁴. For NarGH the presence two fractions,

active and inactive, was shown. However, the mechanism of reductive activation was not revealed. Additionally, NarGH seems to be reductively activated in irreversible manner or at least following oxidative inactivation is slow enough. For cyt *bd* from *G. thermodenitrificans* the activation would be reversible and could be connected with protonation event (e. g., of the heme ligand, amino acid). In the studies with NarGH it was suggested that protonation could be coupled with reductive activation but the hypothesis was not confirmed.

The second hypothesis is based on fumarate reductase studies¹⁵⁵ and predicts the presence of the slow component of the electron transport chain in a protein. The boost of the catalysis starts only after reduction of the slowest component of such chain. In case of cyt *bd* from *G. thermodenitrificans* with possibly inverted electron flow at pH7 and RT this explanation would be suitable. Nonetheless, the variability of the rate of potential sweep (0.02 V/s...0.001 V/s) did not reveal any changes in the self-crossing effect.

Thirdly, the deactivation influence of chloride ions was probed since several proteins^{299,300,301} show sensitivity to the ones. The changes in voltammograms upon immersion of the electrode in chloride containing and devoid of these ions buffers were not observed (Fig. 51).

Finally, the fourth explanation could be based on the other studies with NarGH showing the reversible inhibition effect of high substrate concentration^{216,223}. Cyt *bd* consumes two substrates MQ and oxygen, and, thus, variation in their concentrations would be useful for understanding. 1) a) At 23°C and pH7 oxygen concentration in water is around 270 µM (8.6 mg/l) but at 45°C when the catalysis is more intense it is diminished up to 180 µM (5.9 mg/l). b) Rotation with lower rpm values decreases transport of oxygen to the enzyme. However, the intensity of the signal at lower rpm values was correspondingly declined. Thus, probably the rise of the protein activity at higher temperatures is not associated with oxygen concentration decrease. 2) Addition of MQ-4/DMSO into solution did not lead to changes in voltammogram properties (Fig. 52). On the contrary, the specifically purified batch characterised with lowered MQ content (determined via differential FTIR spectroscopy) had almost removed self-cross of voltammogram (Annex 5). Additionally, to avoid misinterpretation MQ-4 was immobilized alone, but in our experimental conditions in the presence of oxygen MQ-4 did not lead to catalysis by itself. The cathodic peak (-195 mV vs SHE) of MQ-4 resembled the one of the cathodic peak (-226 mV vs SHE) of cyt *bd*. It could be that cyt *bd* from *G. thermodenitrificans* showed substrate-inhibition (high MQ

concentration) behaviour in voltammetric experiments. This type of voltammogram could be modelled²²⁴.

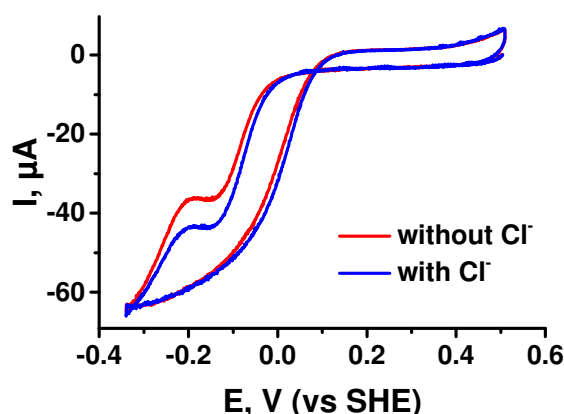


Fig. 51. Influence of the chloride ions on the shape of voltammograms of cyt *bd* from *G. thermodenitrificans*

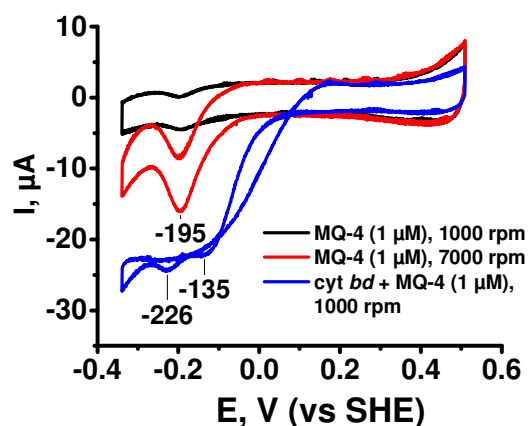


Fig. 52. Voltammograms of cyt *bd* from *G. thermodenitrificans* in MQ-4 excess conditions and control MQ-4 in O_2 presence.

2. The influence of the heme *d* on cyt *bd* properties

A batch that lacked heme *d* was also studied. The absence of the heme *d* was confirmed by UV/Vis spectroscopy (Fig. 53) since the 619 nm band was absent. At the same time, the Soret band was of the same parameters regardless the heme *d* presence. In this sample of cyt *bd* did not show catalytic activity, which confirms that heme *d* is the location of oxygen reduction reaction.

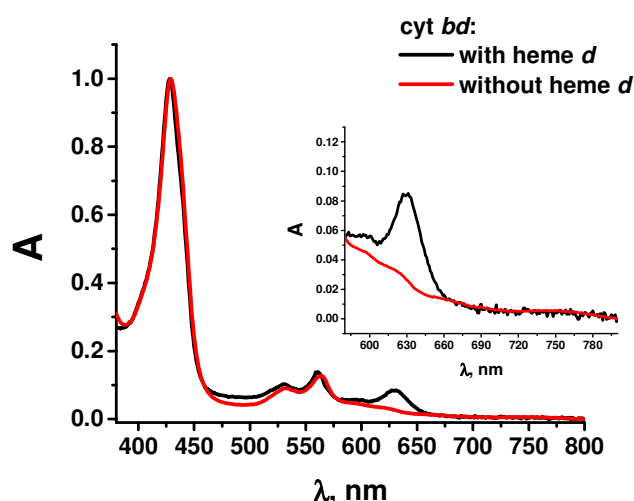


Fig. 53. Normalized UV/Visible-spectra of *G. thermodenitrificans* cyt *bd* from different batches. The spectra were obtained after reductant (sodium dithionite) addition.

Titration experiments were also conducted with this sample (table 26). Heme *b*№2 potential showed a smaller upshift than heme *b*№1 potential. According to X-ray structure heme *b*₅₅₈ is located closer to heme *d*. Hence, heme *b*₅₅₈ probably exhibits the higher redox potential perturbation in the absence of heme *d*. Hence, heme *b*№1 might be attributed to heme *b*₅₉₅ and heme *b*№2 to heme *b*₅₅₈.

The separation between redox potentials of the hemes *b* was decreased by 30 mV in the absence of heme *d*.

Table 26. The influence of the heme d loss on the mid-point potentials of the hemes b in cyt bd oxidase from G. thermodenitrificans at pH6. The values are shown for oxidative titrations.

	619 nm /heme <i>d</i>	heme <i>b</i> №1	heme <i>b</i> №2
cyt <i>bd</i> with heme <i>d</i>	+ 46	+ 79	+ 210
cyt <i>bd</i> without heme <i>d</i>	absent	+ 195	+ 293

Through Raman spectroscopy we did not observe any marked changes in the environment of hemes *b* in the absence of heme *d*. The spectra of the native and cyt *bd* devoid of heme *d* were alike without band shifts (Annex 4).

Differential FTIR spectra were also obtained for the batch devoid of heme *d* (Annex 6). The protein does not seem to be redox stable over several cycles and, thus, the quality of the data is insufficient and not shown here. Interestingly, the FTIR spectra of cyt *bd* lacking heme *d* were quite similar to wild type. The major difference was the removal of the band at 1633 cm⁻¹ in the amide I region which may correspond to vibrations of Arg residues. The slight decrease of the MQ band at 1664 cm⁻¹ was also observed.

3. Dependency on pH and T

Influence of T

The increase in temperature led to partial restoration of the catalytic function (Fig. 54). The thermophile inhabits ecological niches with 65°C, but the protein function was shown to have an optimal activity at 45°C. The catalytic wave (red→ox part of voltammogram) indeed was more prominent at 45°C than at 23°C. However, the self-crossing still remained.

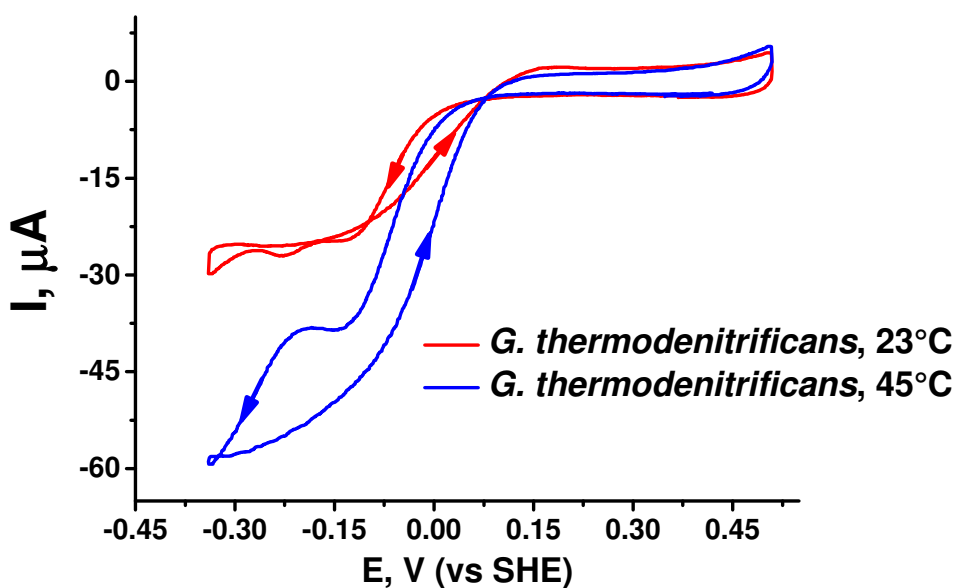


Fig. 54. Influence of temperature on catalytic activity of cyt *bd* from *G. thermodenitrificans*.

Influence of pH

The influence of pH was also studied. No alteration in the voltammograms was observed in acidic medium (pH5-7). At alkali $pH > 9.0$ the self-cross of voltammograms was removed but the catalytic activity was also absent. Firstly, the pH increase could affect potential order of the cofactors but titration experiments did not confirm this hypothesis (vide supra). Secondly, the potential of MQ changes as well with pH. At pH9.5 the $E_{m9.5}$ for MQ-6 is around -215 mV (vs SHE)⁴⁶ which is still lower than the value of the lowest potential cofactor. Finally, at pH9.5 the deprotonation of one of the important for catalysis protonable residue (e. g., heme, amino acid) is possible.

The comparison (Fig. 55) of the redox-induced differential FTIR spectra at pH7 and pH9.5 revealed the disappearance of the band at 1633 cm^{-1} which corresponds to $\nu(\text{C}=\text{C})$ vibrations that can be attributed to the amide I (β -sheets). Arg residue also shows $\nu_s(\text{CN}_3\text{H}_5^+)$ vibrations at this position. Accordingly, the band at 1676 cm^{-1} corresponding to $\nu_{as}(\text{CN}_3\text{H}_5^+)$ is also absent at pH9.5. The Arg99 located in CydB pathway or Arg391 in Q-loop may play the role of a pH sensitive regulator of the catalysis. Interestingly, the same signatures were found for catalytically inactive sample devoid of heme *d*. In particular, changes in heme propionates (band at 1697 cm^{-1}) were almost absent. Raman spectroscopy studies also did not reveal hemes *b* involvement into pH sensitivity (Annex 4).

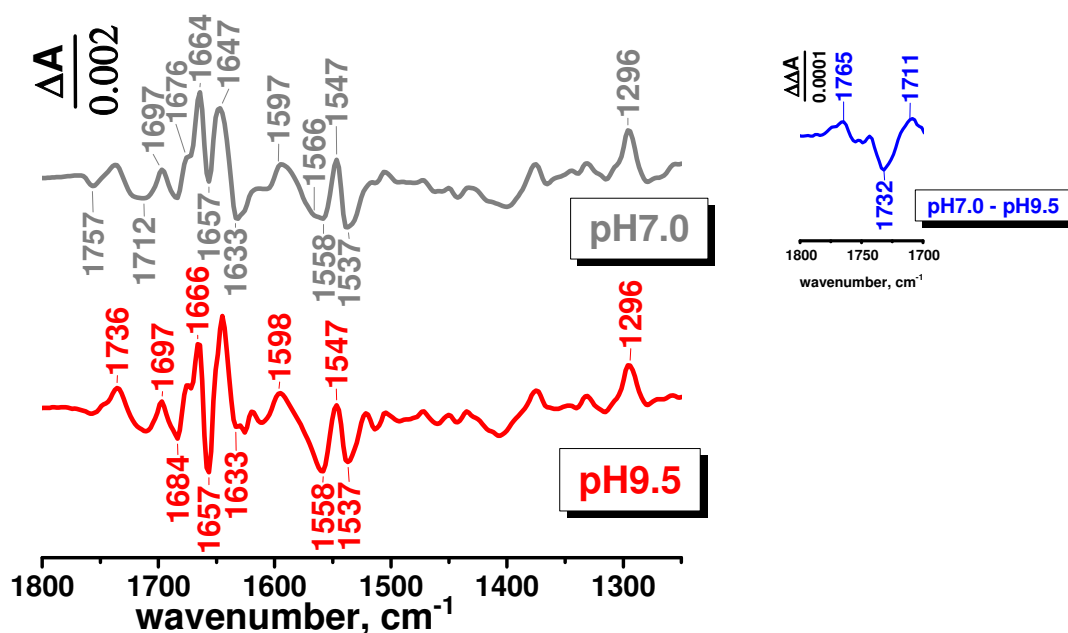


Fig. 55. Influence of the pH on the ox-red differential FTIR spectra of cyt bd from *G. thermodenitrificans* (5°C, KPi pH9.5 vs pH7).

The presence of the strong band at 1406 cm^{-1} (ν_s of COO^-) at FTIR spectra (Fig. 55) may come from the deprotonated acidic residues Glu and Asp. However, the bands corresponding to antisymmetric vibrations ($1574\text{--}1560\text{ cm}^{-1}$) were not altered as well as protonated Asp and Glu residue signatures. Only slight changes could be noticed in the 1722 and 1565 cm^{-1} bands corresponding to protonated Asp or Glu forming H-bonds and $\nu(\text{COO}^-)$ vibrations of deprotonated ones, respectively.

Finally, the MQ contribution was decreased as can be suggested from the intensity of the bands at 1296 and 1664 cm^{-1} .

Mutual influence of pH and T

The most interesting effect was observed when pH and temperature alterations were combined.

First, the optimal temperature of 45°C was taken as an initial condition and the variation of the pH was conducted (Fig. 56).

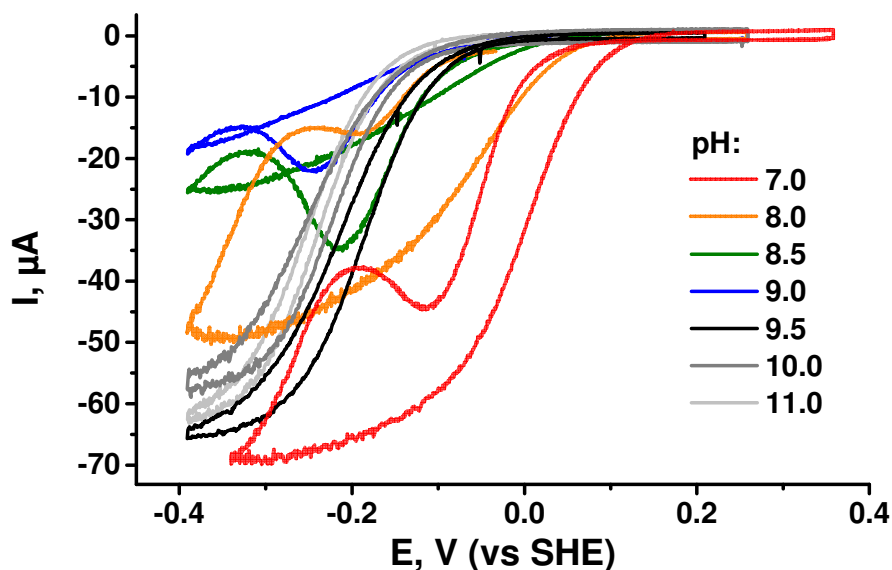


Fig. 56. Influence of the pH on voltammogram shape at 45°C for cyt bd from *G. thermodenitrificans*.

Interestingly, the signal amplitude was gradually decreased when increasing pH from 7.0 to 9.0, but at pH9.5 the current at -400 mV (vs SHE) showed marked restoration of the catalytic activity and transition to a trivial sigmoidal catalytic curve. Further rise in pH up to 11.0 did not show additional effects. The signal amplitude variation in case of pH9.5-11.0 could originate from different protein coverage. The E_{cat} was shifted from pH7.0 to pH10 by approximately 200 mV which corresponds to the -60 mV/pH unit dependency for heme *d*.

The next set of the experiments included variation of the temperature at a fixed value of pH9.5 (Fig. 57). The rise in the temperature already to 30°C provided with sufficient current intensity. However, further temperature increase correlated with burst of the catalytic activity. At 38°C the signal reached its maximal value and had similar amplitude up to 65°C. At 70°C the protein, probably, started to denaturate since the current was lowered at this temperature. Additionally, the better curve shape was observed at $45^\circ\text{C} < t^\circ < 65^\circ\text{C}$.

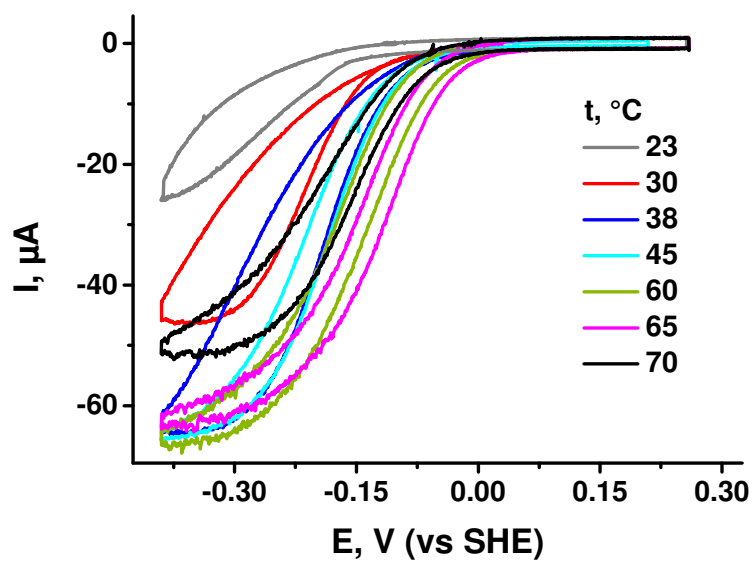


Fig. 57. Influence of the temperature on the voltammetric signal of cyt bd from *G. thermodenitrificans* at pH9.5.

A summary of the mutual pH and T influence is shown in Fig. 58.

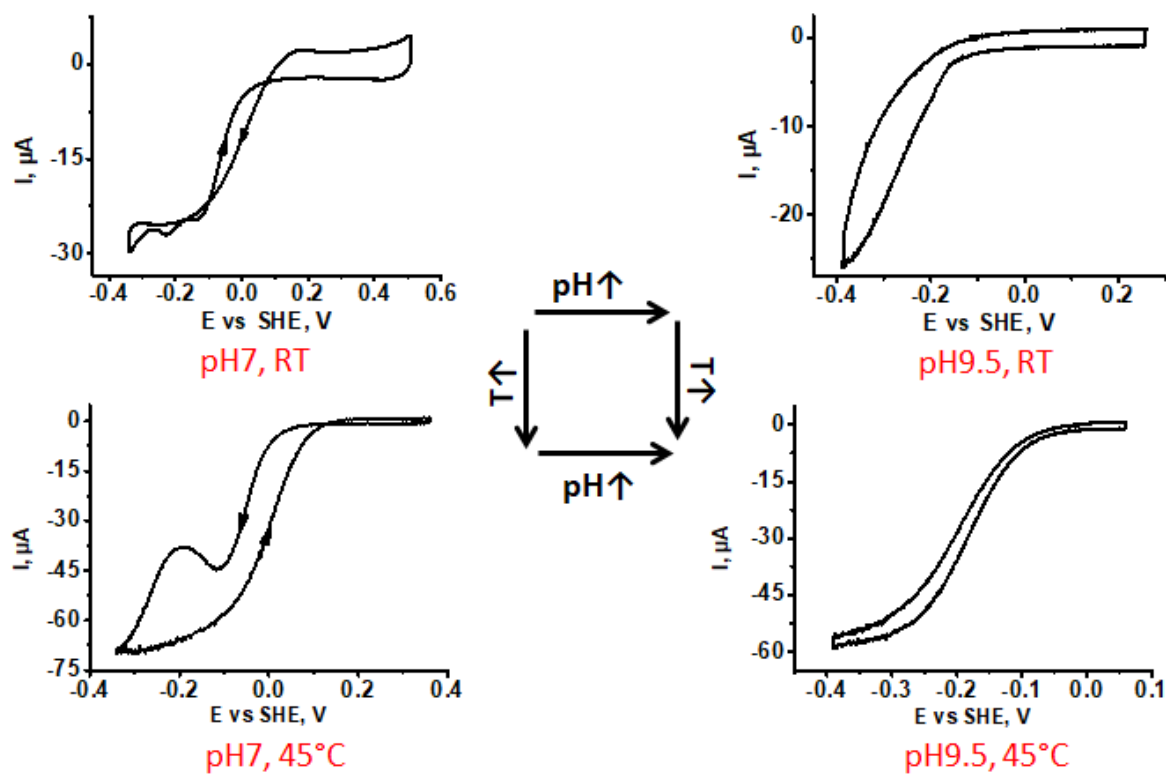


Fig. 58. Mutual influence of temperature and pH on catalytic behaviour of cyt bd from *G. thermodenitrificans*.

To understand if major conformational changes take place upon altering the pH and temperature, IR measurement in transmission mode were carried out. The protein was washed in D₂O based buffer either at pH7 or pH9.5 and the corresponding spectra were obtained at 5 and 45°C. The deconvolution of the amide I band was conducted (Annex 7, table 27).

Table 27. Deconvolution results of the amide I band of the D₂O spectra of cyt *bd* from *G. thermodenitrificans* at 5 and 40°C, pH7 and pH9.5.

attribution	pH7, 5°C		pH7, 45°C		pH9.5, 5°C		pH9.5, 45°C	
	band, cm ⁻¹	%	band, cm ⁻¹	%	band, cm ⁻¹	%	band, cm ⁻¹	%
β-sheet	1623	10	1625	8	1626	13	1625	6
disordered	1637	17	1641	30	1640	26	1639	33
α-helix	1656	66	1659	52	1658	51	1655	48
turns	1679	5	1675	7	1677	9	1672	9
β-sheet	1691	2	1687	3	1691	1	1685	4

The increase in pH from 7 to 9.5 led to higher fraction of the disordered structures and their contribution was even higher with rise in the temperature by 40°C. In contrast, at pH7 the same temperature changes did not result in such a high decrease of the order in the protein conformation. It might be that protein turns into more flexible conformation which allows the catalysis associated with conformational changes. However, the major structure of the protein was quite stable and denaturation did not occur.

4. Preliminary inhibition experiments

The influence of the aurachin D on cyt *bd* from *G. thermodenitrificans* was studied.

The addition of the well-known inhibitor aurachin D did not change the hemes *b* potential dramatically (table 28) and did show influence on heme *d*. Nevertheless, one of the heme *b* (“*b*N₂”) potential was upshifted more than the other one, indicating that it could be heme *b*₅₅₈ which is located near quinone-binding site, where aurachin D is believed to interact. This attribution is in agreement with the one based on the studies of the batch devoid of heme *d*.

Table 28. Influence of aurachin D on reductive potentials (mV, vs SHE) of the cofactors of cyt *bd* from *G. thermodenitrificans* at pH7, 13°C. The results of oxidative titration are shown.

	619 nm/heme <i>d</i>	heme <i>b</i> N ₁	heme <i>b</i> N ₂
without aurachin D	+ 15	+ 50	+ 155
with aurachin D x 30	+ 12	+ 79	+ 221

For cyt *bd* from *E. coli*, in the presence of aurachin D, heme b_{558} potential is shifted (by 65 mV) more than that of heme b_{595} (by -40 mV), while heme d potential is constant¹³². In analogy, in case of *G. thermodenitrificans* more sensitive to aurachin D was heme b_{No2} that may be attributed to heme b_{558} . However, resonance Raman studies did not reveal any alterations in heme b environment. Upon addition of aurachin D coordination and spin states of the hemes b were not altered (Fig. 59).

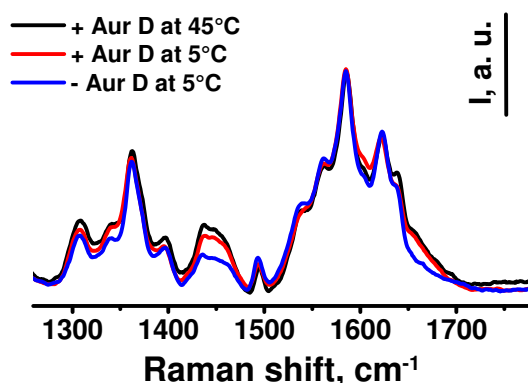


Fig. 59. Resonance Raman spectra of cyt *bd* from *G. thermodenitrificans* in the absence and presence of aurachin D (x30).

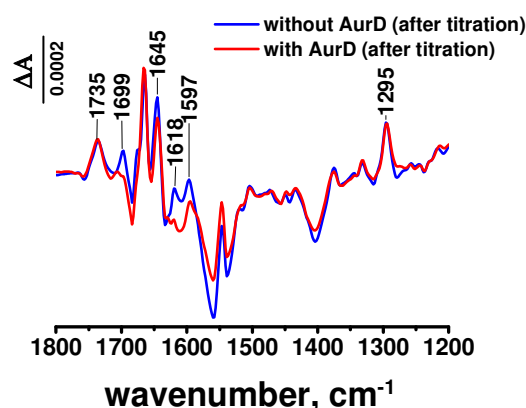


Fig. 60. Ox-red differential FTIR spectra of cyt *bd* from *G. thermodenitrificans* in the absence and presence of aurachin D (x30).

IR differential spectroscopy, however, showed changes in some bands upon addition of aurachin D to cyt *bd* from *G. thermodenitrificans* (Fig. 60). The intensity of the band at 1618 cm^{-1} was significantly decreased when adding aurachin D. The binding of aurachin D could be coupled to MQ displacement from the binding site as it was shown for cyt *bd* from *E. coli*¹⁹. The bands at 1645 , 1618 and 1597 cm^{-1} could involve MQ vibrations. However, the MQ bands were not changed suggesting that it was still bound to the protein. As said before, the 1699 cm^{-1} signal probably originates from vibrations of the protonated propionates of the heme. Importantly, the heme propionate vibrations are located in the amide II region where some bands were altered. It might be that aurachin D interacts with heme b_{558} and only partially displace MQ in cyt *bd* from *G. thermodenitrificans*.

Other inhibitors, such as HQNO, were also tested by means of PFV (Fig. 61). However, the current decrease was not prominent as compared to cyt *bd* from *E. coli*. Additional issue was denaturation of the protein which started already after 3rd/4th scan (Fig. 62). Besides denaturation it could be that thiol monolayer start to degrade at high temperature.

Additionally, at 45°C the adsorption of the protein may be less favourable. Finally, the hydropathic index of cyt *bd* from *G. thermodenitrificans* is higher as compared to *E. coli*²⁰, hence, the adsorption on the surface is probably not exactly the same. Further experiments for optimisation of the conditions for protein film preparation will be required.

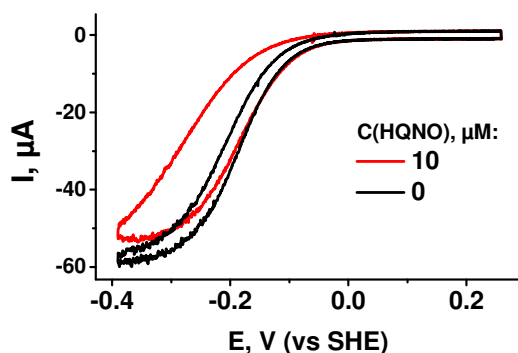


Fig. 61. Influence of 10 μ M HQNO on voltammetric signal of cyt *bd* from *G. thermodenitrificans* (pH9.5, 45°C).

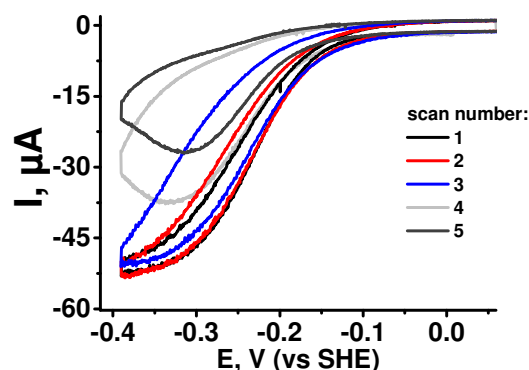


Fig. 62. Evolution of voltammogram of cyt *bd* from *G. thermodenitrificans* upon successive scanning (pH9.5, 45°C).

5. Conclusions

Cyt *bd* from *G. thermodenitrificans* was studied. The observed results showed that this cyt *bd* species is different from cyt *bd* from *E. coli*. The presence of the MQ in the samples was determined. The environment of the heme *d* was proposed to be more hydrophobic, but that of the hemes *b* seemed alike.

The order of the potentials of the cofactors was inverted as compared to cyt *bd* from the other species: heme *d* -43 mV, heme *b*N₁ +30 mV, heme *b*N₂ +137 mV (at pH7). The catalytic behaviour in voltammetric experiment was also outstanding: at pH7 and 23°C the two cathodic peaks and self-crossing of voltammogram were observed. The trivial sigmoidal curve shape was restored with pH increase up to pH9.5 and at 45°. The explanation of mutual influence of the temperature and alkali pH could be connected with deprotonation of amino acid residue without large conformation changes of the entire protein molecule.

Inhibition experiments with aurachin D also showed differences in the mode of action of the ligand. It is probable that aurachin D interacts with heme *b*₅₅₈ without replacement of MQ.

Therefore, wide spread short Q-loop type cyt *bd* from thermophile *G. thermodenitrificans* showed properties which make it clearly distinct from long Q-loop cyt *bd* from *E. coli*.

Part B. mitoNEET

Introduction

I. Structure

mitoNEET (mNT) (13 kDa) is the principal representative of the mNT-like protein family. Its name is due to the Asn-Glu-Glu-Thr (NEET) sequence in the C-terminus. The family encompasses the proteins featuring the following structural properties: CDGSH domain (a specific stretch of 39 amino acids) that includes 4 ligands (3 Cys and 1 His) coordinating the iron-sulfur cluster of 2Fe-2S type. This type of cluster coordination makes this protein family unique (Fig. 63)^{25,225,226}. X-ray studies^{227,228} revealed a homodimer structure (L1-β1-L2-β2-L3-α1-L4-β3) with one iron-sulfur cluster in each monomer. The mNT dimer can be divided into two domains (Fig. 64). The first domain is a so-called β-cap bearing hydrophobic core. The second domain is the more hydrophilic cluster binding domain. C-termini are the functional moieties of mNT, then hydrophobic α-helix N-termini tether the protein into the outer membrane of the mitochondria (OMM). Therefore, mNT is a soluble (Fig. 65) transmembrane protein localised in the cytosol being anchored to OMM²²⁹.

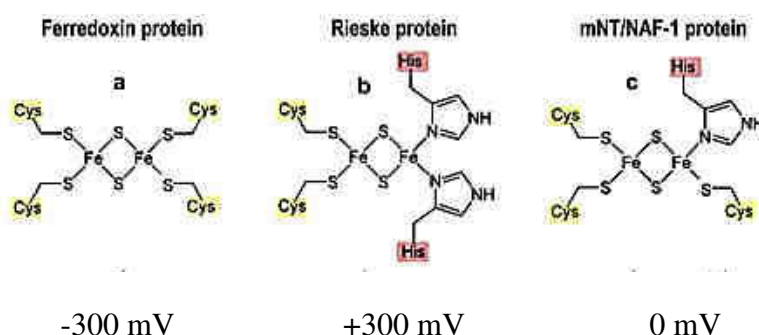


Fig. 63. Schemes of the iron-sulfur cluster variations encountered in nature.²²⁶

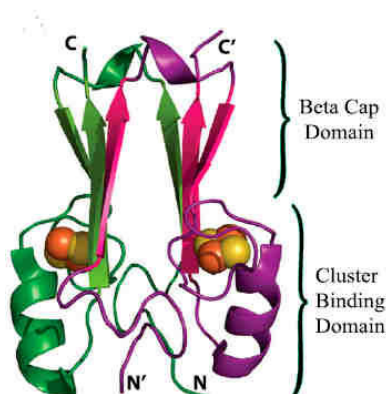


Fig. 64. X-ray structure of homodimeric mNT with two main domains.²³⁰

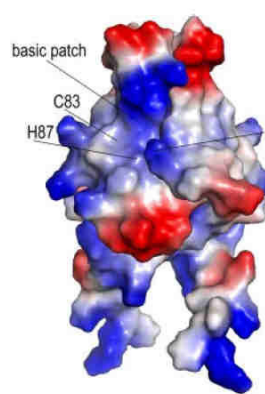


Fig. 65. Charge profile of mNT surface. Positively charged/basic patch is located near FeS-cluster.²²⁷

Several amino acids (Lys55, Ser77, Tyr71, Pro81, Phe82, Arg73) were proposed^{226,228,231} to be involved in the conservative hydrogen network bonding the iron-sulfur cluster with a protein scaffold (Fig. 66). Lys55 and Ser77 interact with a cluster via H-bonds through $\text{H}_2\text{O} \cdots \text{His87}$ ($\text{Fe} \cdots \text{N}_\delta$ bonding) and Asp84 ($\text{COO}^- \cdots \text{S}^{2-}_\mu$), respectively. The other residues are more far away from the cluster¹⁵. Arg73 is localised between two cluster ligands Cys72 and Cys74²²⁶. Tyr71, as well as Val56, Val57, Leu65 and Trp75, are localised at the interface between two monomers providing tight hydrophobic interaction between each other²²⁸.

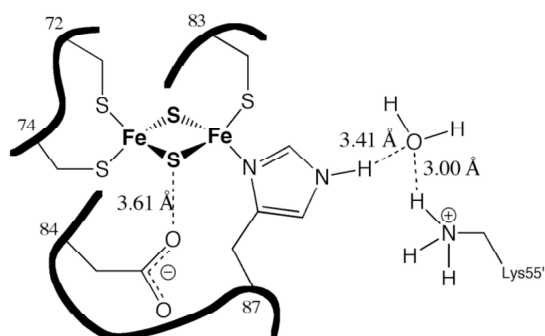


Fig. 66. Some amino acids residues involved in a conservative hydrogen network: His87, Asp84, Lys55. Lys55 and His87 are localised in different monomers, thus, mNT function as a dimer¹⁵.

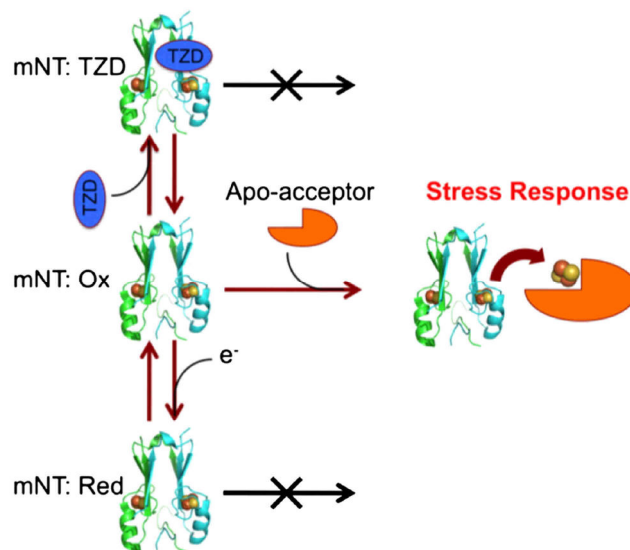


Fig. 67. Cluster release can take place when the protein is in oxidised state. In the reduced or inhibited state (e. g., with TZD) holo-mN does not react with the apoprotein (e. g., Fdx, Adx, aconitase)²³¹.

II. Biophysical properties and mechanism

The protein mNT is sensitive to RedOx state and pH. In the reduced state, the protein is in a resting state: the cluster shows a high stability in a wide range of pH (from pH5.2 up to pH12.5). In the oxidised state the protein starts to release its cluster with decrease in pH (below pH8.0) (Fig. 67)^{15,25,225,226}. Thus, the cluster becomes labile only when two conditions are fulfilled: oxidised state and acidic pH. It was assumed before²³² that cluster release at acidic pH could take place during the protonation of the iron ligand His87. The protonation of His87 was suggested to be at the origin of the pH dependence. Mutants of this residue point towards a more complex pH dependency. The studies on H87C variant²²⁹ demonstrated that the pH dependent lability of the cluster stays the same regardless of the ligand type. The

substitution of His by Cys raises the stability of the cluster in all pH range in general which is also reflected in electrochemical properties. Due to unique 3Cys/1His coordination the cluster in this protein family demonstrates a mid-point potential around $E_{m,7}=0$ mV²³³, while for Rieske type protein (2Cys, 2His) and Fdx type proteins (4Cys) the mid-point potentials are around + 300 mV and – 300 mV, respectively²²⁵. Additionally, PCET modelling²³⁴ and studies on the pH dependency of the redox potential, which is - 50 mV/pH unit^{15,233}, have shown that the one-electron process is coupled with two protonation events. It was concluded that the function of mNT does not only involve cluster but also electron transfer^{22,226}.

III. Biological role

The cluster donation in the form Fe/FeS by mitoNEET holoprotein was demonstrated towards apoferredoxin, IRP-1/aconitase, and anamorsin^{22,25}. The S^0 atom was shown to be stuck to the polypeptide after cluster release²⁵. Additionally, unspecific cluster release can be provoked by ROS and mitochondrial membrane potential^{225,226}. Therefore, mNT is regarded as a protein maintaining iron/ROS homeostasis. Furthermore, the protein could be a sensor to oxidative stress: at physiological conditions resting cytosolic potential is – 290 mV so the cluster is in reduced state, while during oxidative conditions the resting potential rises up to + 200 mV, which can lead to oxidation of the cluster and its release¹⁵. mNT is also involved in the mitochondrial junction formation and mitophagy²³⁵. The malfunction of mNT leads to diseases such as diabetes, obesity, cystic fibrosis, neuronal development issues, neurodegenerative diseases, and cancer^{225,226,236}.

IV. Influence of addition of compounds

So-called low-weight ligands can influence the stability of the cluster. It was assumed that the basic patch (Fig. 65) at the molecule surface, in the proximity to the iron/cluster, could be the interaction site for the ligands inducing redox potential changes of mNT²²⁷. Later on it was shown that pioglitazone (next pio), resveratrol-3-sulfate (next rsv3S) (Fig. 68), but not resveratrol itself²³⁷, rosiglitazone^{233,238} and NADPH²³⁹ can increase stability of the cluster and prevent Fe/Fe-S release in order to donate it to apoferredoxin. The rational design led to the development of the efficient cluster stabiliser NL-1²²⁵, destabiliser MAD-28²³⁶ and others^{238,240} which were supposed to interact tightly with mNT. A mid-point potential shift of – 100 mV was observed upon addition of pioglitazone²³³. It was suggested that pioglitazone

binds to the protein in oxidised state²³³ and prevents cluster release²³³ and/or dedimerisation²³⁸. The ligand binding is made through His48, Ile49, Arg76, Lys78, Ala86, Lys89, and His90 via van der Waals interactions and through Gln50 forming hydrogen bonds with TZD rings²³⁸. The interaction of phosphate ions with His87 was also discussed^{232,241}. The NADPH affects the protein via Asp84²³⁹. The crystal structure showed the localisation of phosphate ions in the vicinity of iron-sulfur cluster²⁴¹.

mNT can be reduced partially or fully when interacting with natural monothiols (e. g., glutathione, L-cysteine) or dithiothreitol, thioredoxin/thioredoxin reductase. At the same time H₂O₂ can reversibly oxidize mNT avoiding protein damage²⁴². Interestingly, the pioglitazone inhibits the effect of the natural thiols^{242,243}. Thus, it also shows that mNT could be a regulator of the cell response towards oxidative stress.

The redox state is also regulated by small ubiquitous ligands. mNT can be reduced by FADH₂²⁴⁴ and FMNH₂ and oxidised by UQ or O₂²⁴⁵. Oxygen is less efficient than UQ²⁴⁵. Additional studies revealed that oxygen does not affect iron-sulfur cluster transfer rate and is not necessary for this process²⁵.

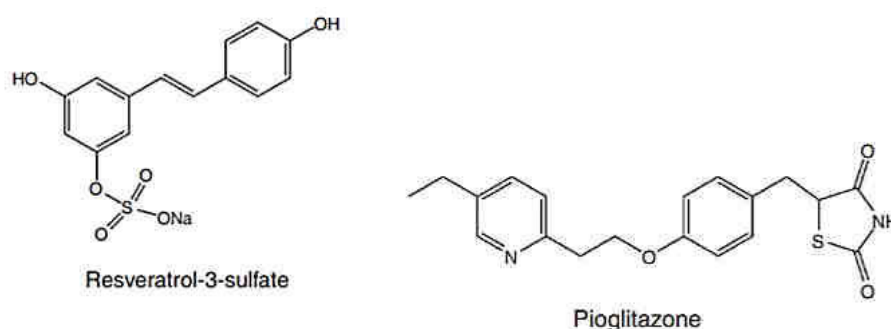


Fig. 68. Compounds which are supposed to stabilise the mNT cluster²²⁵.

Aim of the PhD project

It is still unclear why mNT is so stable in the reduced state and how exactly low-weight ligands can affect the structure of mNT preventing Fe/FeS release. Additionally, albeit the role of His87 ligand for pH sensitivity was excluded, an explanation why the oxidised protein loses its cluster at acidic pH is still missing. The spectroscopy combined with electrochemistry and ligand-protein interaction studies could allow us to better understand underlying processes.

Part B. mitoNEET

Results and discussion

I. Preliminary studies

1. Cyclic voltammetry

First, we optimised the procedure of protein immobilisation on the surface of the electrode. The glassy carbon electrode was modified with carbon nanomaterials. The gold electrode was modified with various thiols: HT/MCH, MPA, MEA, MHA, and MCH/MPA.

No signal from the protein was observed at carbon electrode. The same results were obtained for the neutral thiol surface HT/MCH (table 29). At the positively charged surfaces (MEA) the cathodic and anodic peak currents were presented. However, a decrease in the peak current was observed. With negatively charged thiols the signals were more stable in case of MPA and very stable in case of MHA (Fig. 69). The E_{m7} were determined in all experiments.

The observed current peaks could be probably attributed to “[Fe₂-S₂]²⁺ (ferric form) ↔ [Fe₂-S₂]¹⁺ (ferric/ferrous form)” process since super-reduced ferrous form [Fe₂-S₂]⁰ is a quite rare species in FeS-cluster protein family²⁴⁶. Since the protein surface is mostly charged (Fig. 65) it was not surprising that no signal was obtained when utilising uncharged polar surfaces (PGE or HT/MCH). Electrostatic interactions favoured attachment of mNT than charge was presented. The instability of the signal in case of MEA modification might be explained through the direct cluster interaction with the gold surface upon successive cycling or interaction with monothiols²⁴². In both cases the degradation of the cluster may take place. The higher signal stability at negatively charged thiols (MPA and MHA) could originate from different protein orientation. It may be that at negative surface cluster patch is more distant from electrode surface. The higher stability at MHA than at MPA surface could be also explained through increased distance between cluster and gold due to larger spacer length. Additionally, the results obtained with MHA modification are the closest to the ones already reported¹⁵: $E_{m,7}$ is around 0 mV (vs SHE).

Therefore, the modification of the gold electrode with mercaptohexanoic acid allowed anchoring the protein to the surface and to carry out cyclic voltammetry experiments.

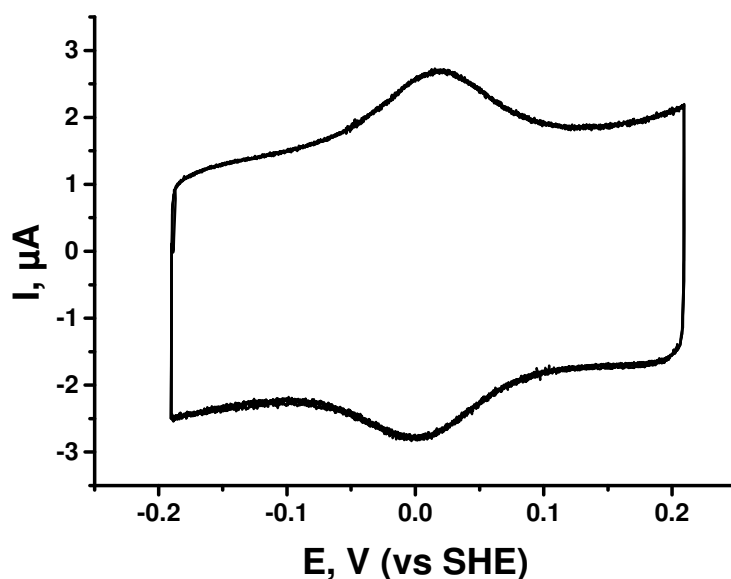


Fig. 69. CV of mNT at MHA modified gold electrode. O_2 , pH7, Tris 50 mM, 100 mM NaCl. 0.02 V/s.

Table 29. The influence of the surface type on the quality of voltammetric signal of immobilised mNT. Tris 50 mM, NaCl 100 mM, pH7, 0.02 V/s, under argon.

type of thiols	E_{m7} , mV (vs SHE)	remark
HT, MCH	n. d.	no signal
MEA	-30	evolution (decrease) of the redox peaks
MPA	-55	stable prominent signal, MPA desorption at low potentials
MHA	+10	stable prominent signal
MPA, MCH	-10	peak separation (slow ET kinetics)

2. Resonance Raman spectroscopy

Resonance Raman spectroscopy in the spectral region $200 - 450 \text{ cm}^{-1}$ can provide information concerning the structure of iron-sulfur cluster and its surrounding^{232,246}. The excitation wavelength used here was 457 nm which corresponds to the maximum (S→Fe MLCT transition) of the mNT-holoprotein absorption (458 nm) and 514 nm.

One can discriminate three regions in the spectrum²³² (Fig. 70): 250-300, 300-360, 360-420 cm^{-1} . Due to the laser excitation the spectra of the proteins are photoreduced²⁵. However, in the presence of natural oxidant UQ-2 and defocalisation we managed to obtain Raman spectra of oxidised state at 514 nm. Bands were observed at 321, 307, 371, 390 and 262 cm^{-1} (table 30). The same type of cluster coordination was found in transcriptional factor IscR

(3Cys/1His)²⁴⁷, D39A mutant of IscU²⁴⁸, H→C mutant of Rieske protein (unstable in reduced state)²⁴⁹ and complex Fra2-Grx3 (X/Cys/1His/glutathione)^{249,250}. However, the studies involved different experimental conditions including wavelength of incident radiation and vibrational assignment cannot be performed rigorously.

The region I may bear the bands corresponding to Fe-N_{imid}^t vibrations^{232,251}. Nevertheless, there is contribution from Fe-S^t stretching vibrations, and the contribution of Fe-O (e. g. Asp, Ser) vibrations also cannot be easily excluded^{247,249,251}. The band at 262 cm⁻¹ is localised in an anomalously low frequency region (if to compare to Rieske-type proteins) and it is quite possible that it corresponds to the B_{3u}^t mode which, together with 307 cm⁻¹, could be connected with Fe-N vibration^{246,247}. However, in²³² it was shown that the bands of the region I are pH-sensitive, but at the same time assumed that the protonation of the His is not the first step before cluster release²⁵¹.

The predominant band at 321 cm⁻¹ may be attributed to Fe(III)-S^t symmetrical stretching vibration^{25,246,252} A_g^t band²⁴⁸. In ferredoxin the band A_g^t is coupled with the band B_{1g}^b, which may be localised at the position 307 cm⁻¹ in the present studies. The Raman spectra of reduced state of the protein are less intense than the ones of the oxidised form²⁴⁶ that could explain the lowered intensity of the band 390 cm⁻¹ which may correspond to A_g^b mode, Fe-S bridging vibration²⁵². Also the attribution is possible to B_{3u}^b mode since the band was enhanced with excitation with higher wavelength laser 514 nm (Fig. 70)²⁵³. In general, Fe-S terminal modes are at lower frequencies as compared to bridging ones²⁵⁴. The assignment of the band at 371 cm⁻¹ is more difficult, and, for instance, in adrenoxin studies it was proposed to be a spurious band²⁵².

Table 30. Tentative assignment of the resonance Raman spectrum of reduced mNT spectrum [Fe2-S2]^{I+}, λ_{ex}=457 nm.

band, cm ⁻¹	tentative attribution	mode
262	Fe-N (Fe-O less probable) and Fe-S ^t	B _{3u} ^t
307	Fe-N (Fe-O less probable) and Fe-S ^t	B _{1g} ^b
321	Fe(II)-S terminal symmetric stretching	B _{1u} ^t /A _g ^t
371	unknown	
390	Fe-S bridging	A _g ^b

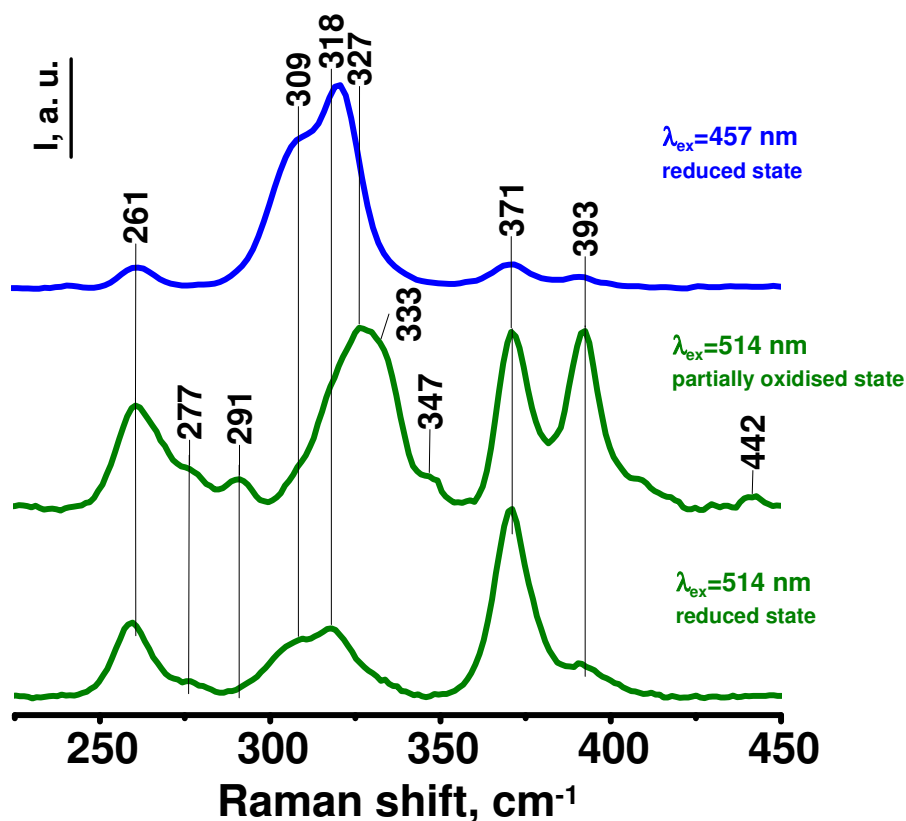


Fig. 70. RR spectra of mNT with excitation at 457 and 514 nm, pH8, Tris buffer. To obtain partially oxidised spectrum UQ-2 and defocalisation were employed; the time between each single spectrum 10 s (50 spectra were averaged).

3. Redox-induced differential FTIR spectroscopy

In order to determine redox-induced amino acid rearrangement differential FTIR experiments were conducted. The spectrum of mNT (Fig. 71) resembles the spectra of the other iron-sulfur cluster containing proteins²⁵⁵. The protein was very stable in the course of the experiment (for more than 80 redox cycles).

In order to identify the contribution to amide region experiments in D_2O were also conducted. In the differential spectra in H_2O the major bands at 1682, 1662, 1628, 1556 cm^{-1} can be attributed to amide I (1690-1620 cm^{-1}) and amide II (1570-1520 cm^{-1}). No signal in the 1740-1700 cm^{-1} range can be observed, hence, the protonated acidic residues are not involved in redox conformational changes^{256,257}. In particular, the band at 1500 cm^{-1} which is attributed to $\nu(\text{CC})$ and $\delta(\text{CH})$ of TyrO^- and does not undergo shift in D_2O is almost absent, which allows

excluding deprotonated Tyr from redox structure changes. Moreover, the band of protonated TyrOH 1517 cm^{-1} is also not present neither in H_2O nor in D_2O .

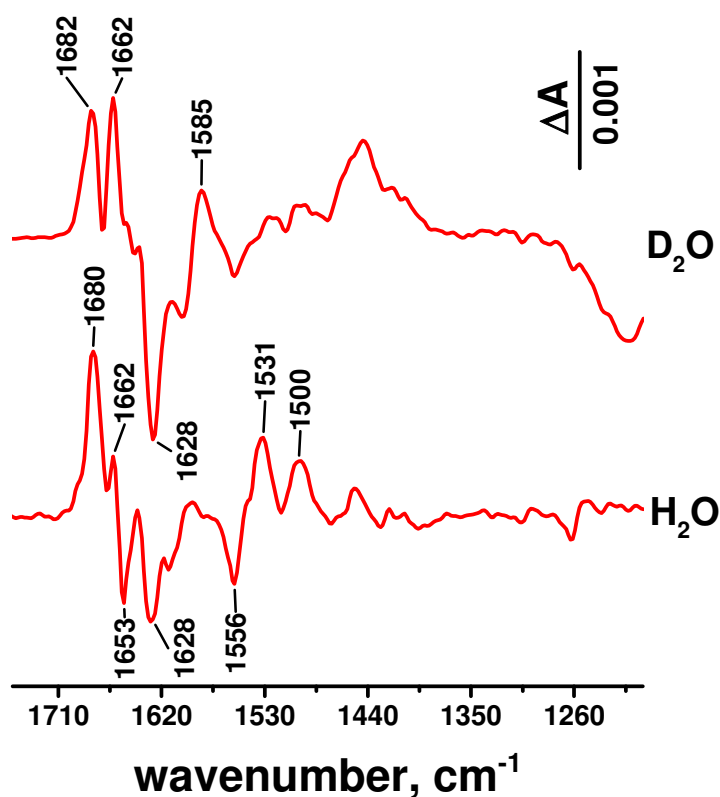


Fig. 71. Comparison of ox-red differential spectra of mNT in H_2O and D_2O .

II. Influence of phosphate ions

1. Cyclic voltammetry

In the next step, we compared the influence of the phosphate ions on the redox potential of mNT (table 31). The rate of the interfacial electron transfer was measured through the Laviron method (Annex 9). The comparison of the protein film properties in the presence and absence of the phosphate ion revealed that no noteworthy effect was seen.

Table 31. The influence of the phosphate ions on the quality of voltammetric signal of immobilised mNT. pH8, 0.02 V/s, under argon, at MHA.

type of the buffer	$k_{\text{ET}}, \text{s}^{-1}$	$E_{\text{m8}}, \text{mV (vs SHE)}$
KPi	9.8	-12
Tris	11.2	+10

2. Resonance Raman spectroscopy

The experiments were conducted in order to determine the influence of the phosphate ions on the spectra at different pH. On the Fig. 72 data for pH8 and pH6.2 are shown.

In²³² it was shown that the phosphate influences the Fe-N band of the oxidised state. In the more stable^{15,25} reduced state shown here no effect was found.

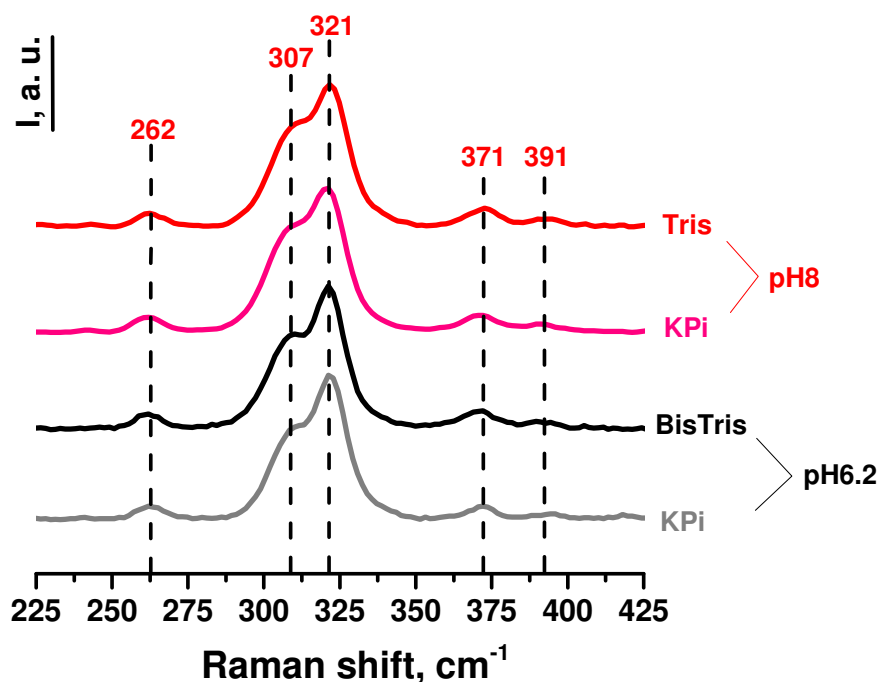


Fig. 72. RR spectra of mNT in the presence and absence of the phosphate ions.

III. Influence of pH

1. Resonance Rama spectroscopy

The next set of the experiments dealt with pH variation of the media from pH8.5 up to pH4.6 (Fig. 73). In the whole range from pH8.5 to pH5.8 the reduced cluster demonstrated high stability. The symmetry and coordination of the cluster started to change at pH lower than pH5.6. At pH4.8 the 262 cm⁻¹ band disappeared and bands at 239 and 283 cm⁻¹ were observed. The 328 cm⁻¹ band is probably a result of 321 cm⁻¹ band shift with additional shoulders at 339 and 354 cm⁻¹. Finally, the intensity of the 390 cm⁻¹ band rose. The spectrum at pH4.6 resembles the one obtained for mNT in the oxidised state in the region 300-400 cm⁻¹

and for H87C mutant/ferredoxin-type protein in the whole range of the spectrum^{232,250}. The new band at 283 cm⁻¹ and band 390 cm⁻¹ in the H87C could be attributed to Fe-S bridging vibrations of the oxidised form.

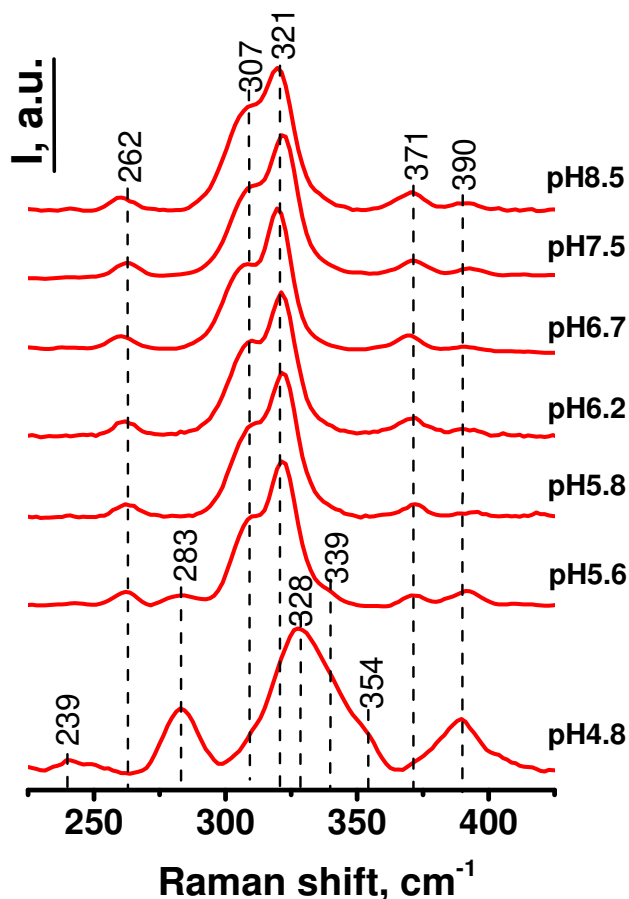


Fig. 73. Alterations of the RR spectrum of mNT with pH decrease. The buffer used: pH8.5, 7.5 – Tris, pH6.7, 6.2 – BisTris, pH5.8, 5.6, 4.8 – MES; $\lambda_{ex}=457$ nm.

Most likely that His residues are protonated at this pH and it cannot function as a ligand for the cluster. Interestingly that during washing of the protein the released cluster should not stay in the sample being filtered out. The presence of the FeS signatures in the spectra suggests that we see either mixed reduced/oxidised state of mNT or only one cluster from the homodimer was released.

2. Redox-induced differential FTIR spectroscopy

In differential redox-induced FTIR spectra the changes in pH (Fig. 74) revealed alterations of the bands at 1662 and 1653 cm⁻¹, and slight perturbation of the bands 1593, 1585 and

1531 cm^{-1} indicating that protein undergoes some alteration in structure upon pH variation. This observation is in line with a previously obtained data²⁵ suggesting that mNT does not undergo global conformational changes during functioning. We propose a tentative assignment of the 1531 cm^{-1} band to Lys δ_s -vibrations of NH_3^+ -group (pK8.95 in solution) but amide II or buffer (NH-group in Tris molecule) can also contribute to this signal.

After buffer exchange from pH8.0 to pH4.6 one can notice an alteration of the colour of the solution from red to brown regardless to the presence/absence of PO_4^{3-} . The intensity of the spectra is considerably diminished starting from pH 6.2 to pH5.6. Probably, the decrease in pH leads to conformational changes and concomitant partial FeS-cluster release. The differential spectra at pH4.6 are flat, which suggests the complete loss of the FeS-cluster at this pH. It is not clear from these experiments whether it is denaturation of the protein that caused the Fe/FeS-cluster release or native conformational changes. At low pH the apo-form of mNT turns into molten globule state that is characteristic of the denaturated form at 80°C¹⁵.

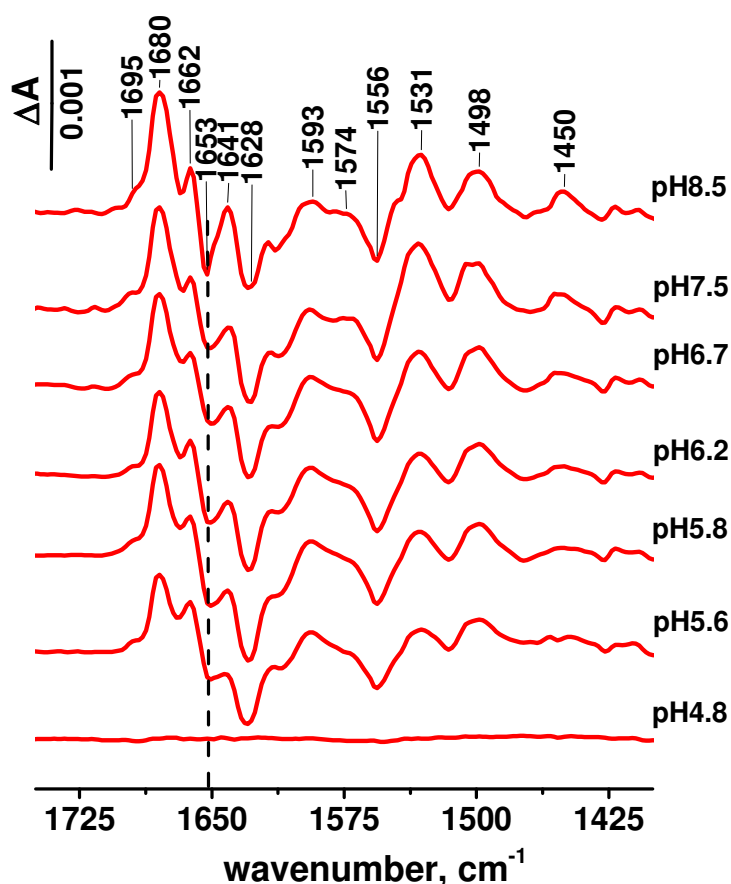


Fig. 74. Changes in the ox-red differential FTIR spectra of mNT in dependence on pH. Conditions: pH8.5, 7.5 – Tris, pH 6.7, 6.2 – BisTris, pH 5.8, 5.6, 4.8 – MES.

IV. Influence of the ligands

1. Cyclic voltammetry

Finally, several ligands that were suggested to interact with the protein were examined. Comparison of the ligands influence on the mNT electrochemical properties is shown in table 32. The control experiment with DMSO was additionally conducted.

Table 32. Electrochemical properties of mNT in the presence of the ligands. Scan rate 0.1 V/s, pH8, Tris 50 mM, 100 mM NaCl.

mNT+	conditions	E cathodic, mV (vs SHE)	E anodic, mV (vs SHE)	peak separation, mV	E _{m8} , mV (vs SHE)
DMSO 20% (incubation)	Ar	-112	0	112	-56
rsv3S x68 (incubation)	Ar	-96	-42	54	-69
pio, DMSO (addition into solution 187 µM, 10 min with 1000 rpm rotation)	Ar	-95	-4	91	-50
nothing (control at MHA)	Ar	-91	-26	65	-58
pio x5, DMSO 20% (incubation)	O ₂	-113	+5	118	-54
nothing (control at MHA)	O ₂	-137	-41	96	-89

The observations were as follows:

- midpoint potentials are almost the same in anaerobic conditions;
- separation of the peaks is higher in case of the DMSO and DMSO+pio;
- anodic peak is upshifted in case of DMSO and DMSO+pio;
- cathodic peak is slightly downshifted in case of DMSO.

It should be noted that the reduction of mitoNEET is more hindered in the presence of oxygen (see E cathodic for control Ar vs control O₂).

To conclude, DMSO induced the decrease of the electron transfer kinetics; while rsv3S does not show a strong influence on the electrochemical properties of mNT. The changes caused by the addition of pioglitazone into solution with DMSO resemble the ones caused by DMSO only, excluding an effect of pioglitazone.

2. Resonance Raman spectroscopy

Resonance Raman spectroscopy did not reveal significant differences between control sample (mitoNEET at pH8, Tris buffer) and the samples with addition of the ligands (DMSO, pio, rsv3S) (Fig. 75). In all experiments the bands at 262, 307, 321, 370, 391 cm^{-1} were observed. Nevertheless, the relative intensity of the bands at 307 and 321 cm^{-1} is different. Additionally, slight changes in the intensity were noticed in the band 370 cm^{-1} . The deconvolution (table 33) of the major peaks at 307 and 321 cm^{-1} did not show considerable differences as well between the samples. Thus, the coordination of the cluster stays the same upon addition of the ligands. However, some small changes are seen in the reduced state.

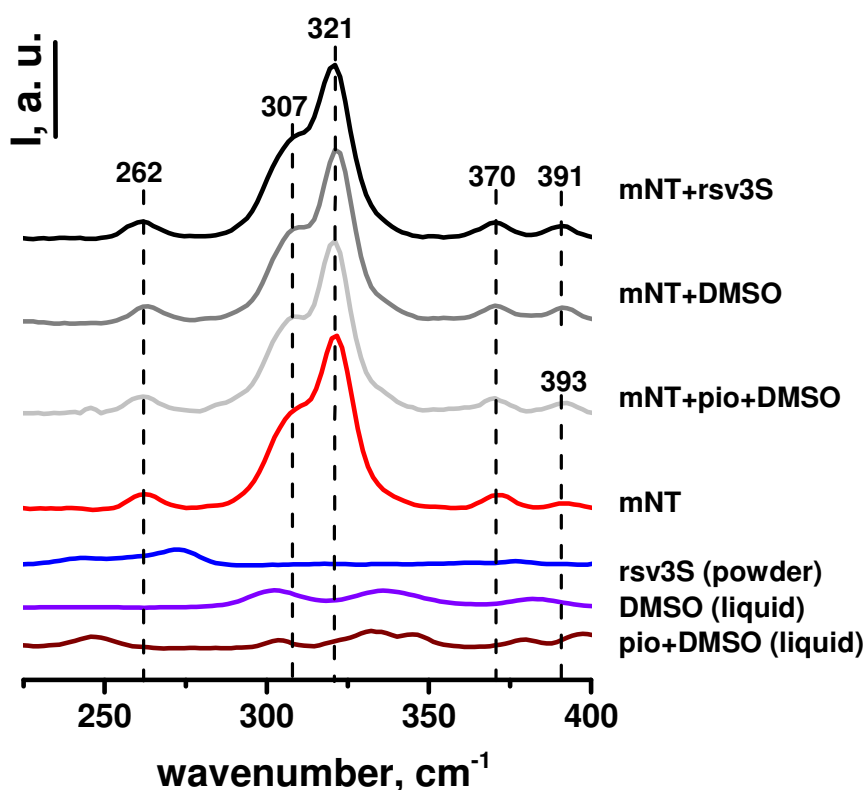


Fig. 75. RR spectra of the dried films of mitoNEET with addition of the ligands. Experimental conditions: Tris, pH8, $\lambda_{\text{ex}}=457 \text{ nm}$.

It was supposed that the cluster is stabilised indirectly through lability decrease of His¹⁵. In this case the cluster would not be perturbed itself and the Raman spectra would stay unchanged.

Table 33. Deconvolution results of the major Raman peaks at 307 and 321 cm^{-1} (Annex 8). Relative contribution surface under central peak is shown.

	307 cm^{-1}	321 cm^{-1}	ratio 321/307
mNT + rsv3S	36%	64%	1.78
mNT + DMSO	37%	63%	1.70
mNT + pio + DMSO	35%	65%	1.86
mNT	38%	62%	1.63

Moreover, Raman spectroscopy studies for protein-ligand interaction were not conducted elsewhere yet. It could be that these ligands do interact but do not induce the alterations in the cluster properties. Additionally, we remind, that in our studies we probed reduced state which is high-stable^{25,225,226} and maybe does not favour interaction of the protein with ligand: for instance, pioglitazone prefers the oxidised state to interact with²³³.

3. Redox-induced differential FTIR spectroscopy

In differential FTIR studies it was necessary to increase the equilibrium time in the redox experiments. This could be due to the decreased electron transfer when ligand is added. The obtained spectra are almost identical to that of wild type (Fig. 76); the differences in the amide II region could come from baseline drift and decrease of Tris quantity when mixing with DMSO. Slight changes in the band at 1593/1574 cm^{-1} were observed in the presence of pioglitazone and resemble the changes at more acidic pH. Previously it was proposed²⁵⁸ that pioglitazone interacts with the protein in the cluster vicinity preventing His87 to be protonated and thus to block Fe/FeS-cluster release. In contrast, the protonated form of the His possesses the signature doublet 1594/1575 cm^{-1} ²⁵⁷. However, we cannot attribute these spectral changes to His since it shows very low absorption coefficient²⁵⁷ which is not sufficient for being presented in the spectra even if to consider His-tag. It was also claimed that not His by itself could have influence on the cluster lability, but the other amino acids involved in conservative hydrogen network¹⁵. Thus, it is even more probable that the $\nu_{\text{as}}(\text{COO}^-)$ vibrations of Asp contribute to the band 1573 cm^{-1} . In the same time the contribution of $\nu_{\text{s}}(\text{COO}^-)$ of Asp at 1404 cm^{-1} is negligibly small. To sum up, the addition of the ligands did not reveal marked changes in the protein differential FTIR spectra.

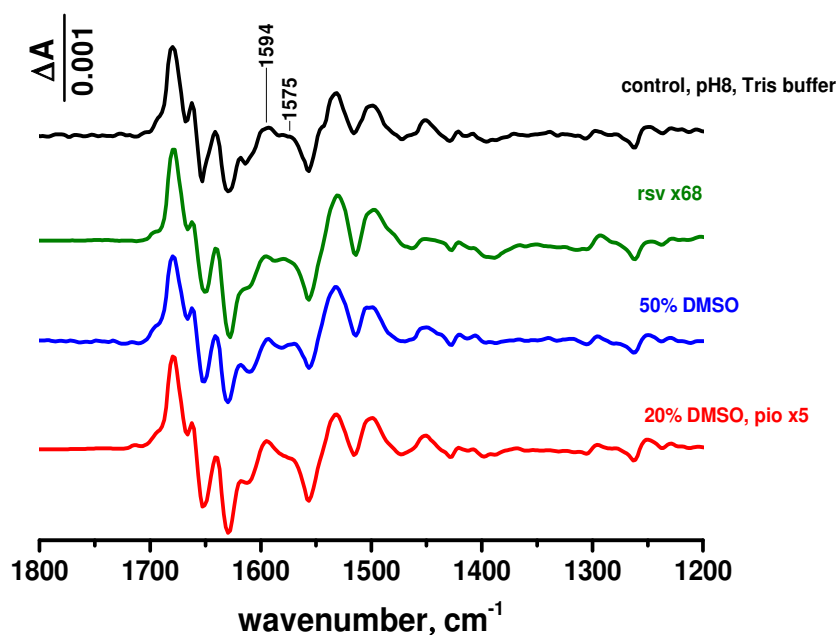


Fig. 76. Influence of the ligand on the protein redox-induced rearrangements detected by FTIR. Ox-red spectra are shown.

Conclusions

mitoNEET showed very high stability in electrochemical and spectroscopic experiments. Only at low pH ($\text{pH} < 6$) the iron-sulfur cluster was lost. No influence of phosphate ions was observed. Neither amino acid reorganisation nor the cluster itself was perturbed upon addition of ligands, and only slight influence of pioglitazone was shown in case of FTIR measurements. However, these alterations are more probably connected with DMSO which is supposed to denature the protein at high concentrations. It is probable that the effect of cluster release is a consequence of dedimerisation event that is diminished in the presence of the ligands. Finally, the reduced state was shown to be very stable in a wide range of pH regardless different ligand presence.

General conclusions and perspectives

1. The development of the biosensor for ligand examination for cytochrome *bd* oxidase from *E. coli* was successfully achieved. It was found that lipids are crucial for protein immobilisation and that lipids and thiols demonstrated a mutual influence on stability of protein films. The other important observed parameters were the deposited quantity of gold nanoparticles and the time of incubation with thiols.

It would be interesting to characterise the surface at every step of modification (e. g., AFM and STEM for gold nanoparticle layer, determine the protein orientation at the surface by SEIRAS).

2. The optimised method of cytochrome *bd* immobilisation gave the opportunity to conduct the screening of a wide range of potential inhibitors of cytochrome *bd* oxidase. The groups of quinazoline and quinolone derivatives including aurachin D showed the highest inhibition effectiveness. The most potent inhibitors were characterised with inhibition constant in the nanomolar range. This property was conferred with hydrophobic substituent located in the position next to the heteroatom.

The most effective quinazoline can serve as a template for further derivatisation of the structure and design of new antibiotics.

3. Cytochrome *bd* from the thermophile *G. thermodenitrificans* was also studied. Electrochemical and spectroscopic properties showed that cytochrome *bd* oxidases from both organisms are not alike even if they constitute one protein family. Moreover, cytochrome *bd* from *G. thermodenitrificans* revealed an unusual pH and temperature dependent electrochemical behaviour and an inverted potential order of the cofactors.

It would be interesting to conduct a mathematical analysis of the voltammograms and to understand the mechanism of the catalysis. Cytochrome *bd* oxidases from other species would be interesting to study as well for comparison purposes. Additionally, it is intriguing to compare the influence of the inhibitors on the other *bd*-oxidases. Understanding of the observed phenomena demands additional experiments and could be very helpful since the thermophile proteins are important for industry purposes³⁰².

4. Finally, mitoNEET protein was studied. It showed a high stability of the reduced state at various pH values and in the presence of different ligands. Only at pH4.6 the protein released one of its clusters. It would be interesting to investigate the oxidised state. In the next step, mutants and different ligands (e. g., natural thiols) will be studied.

Experimental part

Methods

I. Electrochemistry

1. Cyclic voltammetry of adsorbed species

Protein film voltammetry deals with immobilised protein at the electrode surface^{155,169,259,260}, thus, the diffusion of the analyte is avoided (Fig. 77). In the absence of the substrate the pair of the oxidation and reduction peaks of the cofactors is observed in the voltammogram. The total registered current sums Faradic current i_f and capacitive/charging current i_c which originate from redox transformations of electroactive species and charging of the electrical double layer, respectively:

$$i = i_f + i_c = \frac{dQ_f}{dt} + \frac{dQ_c}{dt} = \frac{dQ_f}{dt} + C * \frac{dE}{dt} \quad (13)$$

where i – total current, i_f – faradic current, i_c – capacitive current, t – time, E – potential, C – capacitance of the electrical double layer, Q – charge quantity required to charge the electrical double layer. The value of the capacitive current depends on scan rate and capacitance. It is determined by several parameters: the area of the electrode, type and concentration of the electrolyte, potential of the electrode.

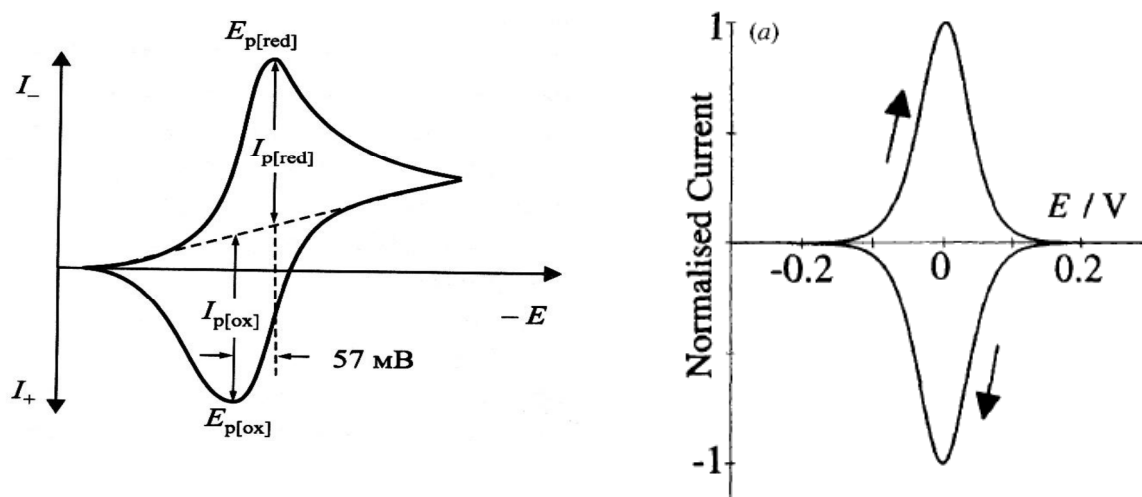


Fig. 77. Typical cyclic voltammogram of a reversible redox system in the solution (left)²⁶¹ and adsorbed on the electrode surface (right).²⁶²

In these experimental conditions it is possible to characterise several parameters of the system. First of all, the value of the peak separation and intensity of the peak currents can

provide the information about reversibility of the redox processes. For example, for reversible systems the separation of the peaks does not depend on scan rate and its value is:

$$\Delta E_p = E_{p,a} - E_{p,c} = 2.20 * \left(\frac{RT}{nF} \right) = \frac{57}{n} mV \text{ at } 298K \quad (14)$$

However, the high-weight membrane proteins typically show irreversible or quasi-reversible behaviour. The Laviron's method²⁶³ can be helpful in characterisation of these system (*vide infra*).

It is possible to measure the quantity of electroactive species absorbed at the electrode surface. The integration of the area under one of the peaks is connected with total charge as follows:

$$\Gamma = \frac{Q_f}{nAF} \quad (15)$$

where Γ – surface concentration of the electroactive species, Q_f – obtained total charge through peak integration, n – quantity of electrons, F – Faraday constant, A – area of the electrode.

The half-width of the peak could give an idea about the number of electrons participating in the redox process, but for a complex system such as protein it also depends on the homogeneity of the adsorbates. For a reaction involving n electrons the half-width of the peak is $90/n$ mV. However, due to possible inhomogeneity of adsorbed species at the surface the width can be larger.

The interfacial electron transfer rate constant k_{ET} can be determined using Laviron's theory of immobilised species. The principal idea of the method is to measure the separation of the peaks ΔE_p as a function of the scan rate v . For each ΔE_p value the theory attributes a parameter m (table 34) which depends on the scan rate v :

$$m = \frac{RTk_{ET}}{Fnv} \quad (16)$$

Table 34. The $1/m$ values depending on peak separation and electron quantity considering $\alpha=0.5$.

$\Delta E_p * n$	18.8	27	34.8	48.8	61.2	722	82.4	91.8	100.6
m^{-1}	0.5	0.75	1.0	1.5	2.0	2.5	3.0	3.5	4

$\Delta E_p * n$	116.2	130	142.4	153.8	164	173.4	182	190	197.6
m^{-1}	5	6	7	8	9	10	11	12	13

In bioelectrochemical measurements the linear part of the plot $\frac{1}{m} = f(v)$ ($\Delta E_p < 200/n$ mV) provides us with slope α (transfer coefficient) which in its turn allows us to determine rate of electron transfer k_{ET} :

$$k_{ET} = \frac{Fn}{RT\alpha} \quad (17)$$

The value of k_{ET} depends on the protein orientation and the distance between cofactor and electrode surface.

2. Stationary electrochemistry

The introduction of the substrate in solution induces the transformation of the voltammogram into sigmoidal catalytic curve. The electrons are transferred from electrode through the protein to the substrate. The diluted substrate in the supporting electrolyte should reach the adsorbed protein, thus, the mass transport (diffusion and convection) influences the observed signal. Charge migration is avoided by increasing the supporting electrolyte concentration up to 0.1 M. The convection is ensured by the rotation of the electrode. A stationary state is reached which is characterised by a constant thickness of the diffusional layer. However, not only mass transport influences magnitude of the measured current. Other factors such as substrate diffusion in the protein, its binding and modification in the active centre, and product release are important. The principal factor is the rate of the catalysis by the protein and, thus, it is interesting to measure the turnover number of the protein.

The limiting diffusion current i_{MT} , that is, the current which depends on mass transport effect, is related to the rotation speed ω of the electrode according to Levich equation:

$$i_{MT} = 0.62 * n * F * A * D^{\frac{2}{3}} * \omega^{\frac{1}{2}} * C * \nu^{-\frac{1}{6}} = B_L * \omega^{\frac{1}{2}} \quad (18)$$

where C – electroactive specie concentration, ν – kinetical viscosity, n – quantity of the electrons, F – Faraday constant, A – area of the electrode, d – coefficient of diffusion, B_L – Levich constant.

However, mass transport is not present anymore when the rotation speed of the electrode is high enough. The limiting current is then a measure of the catalytic current i_K . The catalytical current is the kinetical current which rises after charge transfer to electroactive species (EC mechanism in the case of a simple system). The Koutecký–Levich equation takes in consideration both parameters of the measured current i_m : diffusion current i_{MT} and catalytic current i_K :

$$\frac{1}{i_m} = \frac{1}{i_{MT}} + \frac{1}{i_K} = \frac{1}{B_L * \omega^{\frac{1}{2}}} + \frac{1}{i_K} \quad (19)$$

It is possible to separate the catalytic current and mass transport current within data processing. For this, the plot of $\frac{1}{i_m} = f(\frac{1}{\sqrt{\omega}})$ is traced. The slope of the plot corresponds to the Levich constant. At the point of the cross-section of the curve with Y-axis the rotation speed is supposed to be infinite, thus, mass transport is completely avoided, which provides the finite value of i_K^{-1} (Fig. 78). Finally, this parameter allows us to obtain the k_{cat} value of the protein:

$$\frac{1}{i_k} = \frac{C + K_M}{nFA\Gamma C k_{cat}} \quad (20)$$

where C - concentration of the substrate, K_M – Michaelis-Menten constant. The $A \times \Gamma$ is taken from integration of the cathodic peak in the absence of substrate (*vide supra*). In our case the concentration of the substrate is the concentration of the oxygen in solution under 1 (250 μ M) atmosphere and room temperature. Thus, for instance, for *bd*-oxidases the condition $C \gg K_M$ is fulfilled since this family of complex IV operates in nanomolar range of substrate concentration.

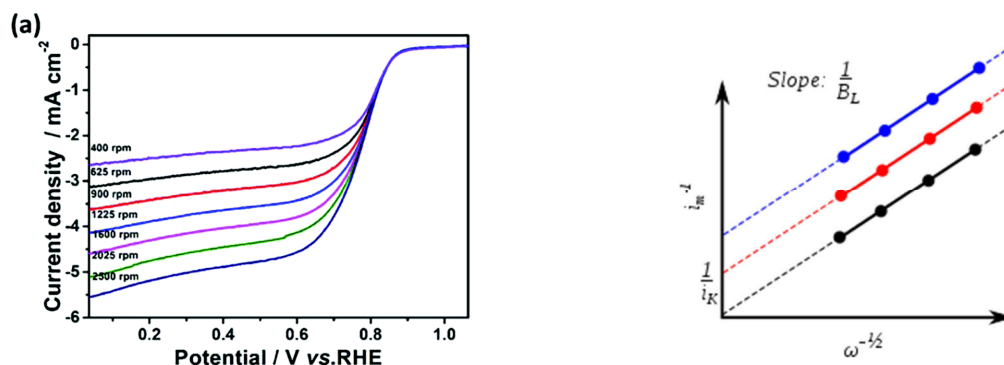


Fig. 78. Left²⁶⁴: raw data obtained in CV experiment: voltammogram at different electrode rotation speed. Right: Koutecky-Levich plot which leads to calculation of i_K^{-1} .

In conclusion, it is useful to compare k_{ET} and k_{cat} . In good experimental conditions the interfacial electron transfer should not be the limiting parameter. In other words, $k_{ET} \gg k_{cat}$.

II. Spectroscopy

1. Absorption spectroscopy

The interaction of the light with matter includes absorption/transmission, scattering, reflection, refraction, polarization, diffraction and luminescence²⁶⁵.

Absorption is a decrease in the intensity of incident light after traversing a sample. This process is described by Beer–Lambert–Bouguer law:

$$A_\lambda = -\lg T_\lambda = \lg\left(\frac{I_0}{I}\right) = \varepsilon l C \quad (21)$$

where A_λ – absorption at particular wavelength λ , T_λ – transmission, I – intensity of passed light, I_0 – intensity of incident light, ε – molar extinction coefficient, l – path length, C – molar concentration.

The quantum mechanical interpretation of the absorption can be expressed through Jablonski diagram (Fig. 79) or Morse curves (Fig. 80).

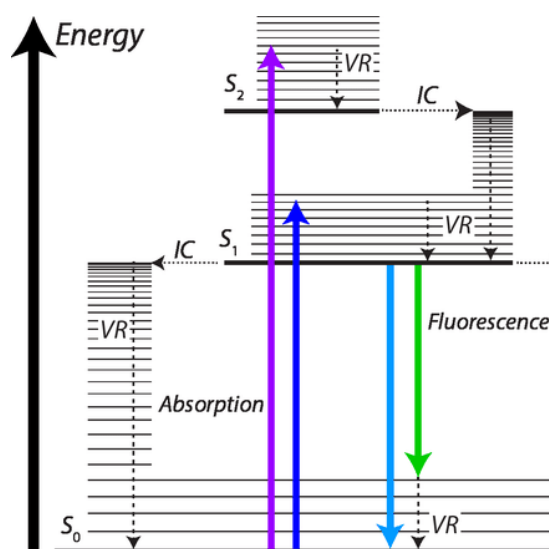


Fig. 79. Jablonski diagram for molecular transitions. Only singlet states are shown²⁶⁶. IC – internal conversion, VR – vibrational relaxation.

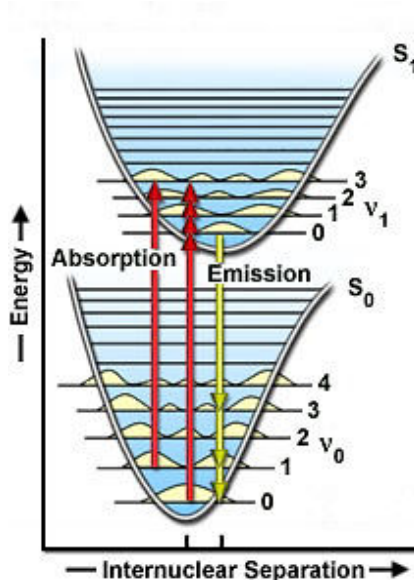


Fig. 80. Morse potential energy curves. The rotation levels situated between rotational levels are omitted²⁶⁷.

The absorption induces transitions from the lower energy state E_1 to the upper one E_2 . The difference in the energies between the states $\Delta E = E_2 - E_1$ is equal to the energy of the absorbed electromagnetic irradiation $h\nu$. The energy is inversely proportional to wavelength. Thereby, for easier interpretation of the spectrum in energy units, the wavenumber, which is directly proportional to frequency and energy, is used:

$$\Delta E = h\nu = \frac{hc}{\lambda} = hck = 1.25 * 10^{-4} * k \text{ (eV * cm}^{-1}\text{)} \quad (22)$$

where ΔE – the energy difference between the energetic level/states, λ – wavelength, $k = 1/\lambda$ – wavenumber, h – Plank constant, c – light velocity in vacuum.

The energy of the molecule consists of three major components considering electron energy E_e , energy of the bond vibrations E_v and rotation of the molecule as an entirety E_r . Hence, the total molecule energy can be approximately expressed as:

$$E = E_e + E_v + E_r \quad (23)$$

The molecule, consequently, can undergo three types of transitions. Each type of transition is for a specific spectral region and corresponding spectroscopic approach (Fig. 81):

- $\Delta E_v + \Delta E_r$ – IR spectroscopy, which can be classified into three regions:
 - far IR spectroscopy ($800..10 \text{ cm}^{-1}$) /FAR/
 - middle IR spectroscopy ($800...4000 \text{ cm}^{-1}$) /MIR/
 - near IR spectroscopy ($125000...4000 \text{ cm}^{-1}$) /NIR/
- ΔE_e – UV/Vis spectroscopy (100 nm – 800 nm) and NIR

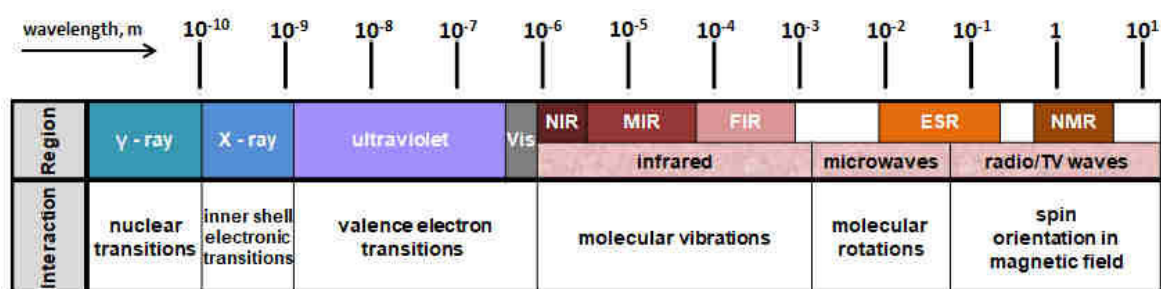


Fig. 81. Gradation of the spectral scale and the corresponding transitions in molecules.

UV/Vis spectroscopy and its application towards proteins and cofactors

UV/Vis spectroscopy allows detecting electron transition between molecular orbitals (Fig. 82). The most intense spectroscopic bands correspond to $\pi \rightarrow \pi^*$ transitions in conjugated system and metal-to-ligand charge transfer MLCT transitions in coordination complexes. Hence, heme cofactors in proteins are good chromophores (Fig. 83) and several characteristic $\pi \rightarrow \pi^*$ bands are seen: B-band (Soret/ γ -line) ($S_0 \rightarrow S_2$) and Q-bands (α and β) ($S_0 \rightarrow S_1$) (table 35).

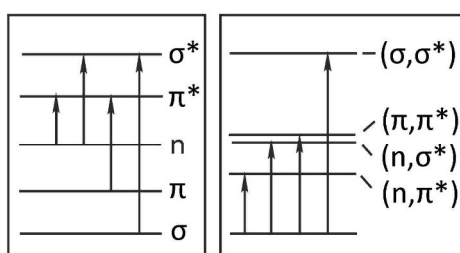


Fig. 82. Transitions in the molecule shown through Jablonski-type (left) and molecular orbital (right) representation. The MO theory considers the energy of the transition.

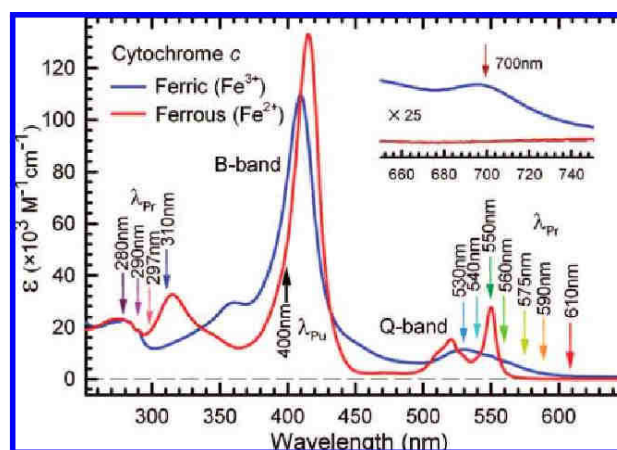


Fig. 83. Absorption spectra of heme c. Red-state vs ox-state.²⁶⁸

Table 35. Position and attribution of the most characteristic heme bands^{269,270}.

band	approximate position, nm	attribution (MO classification)
α	550	$\pi \rightarrow \pi^*/S_0-S_1$
β	520	$\pi \rightarrow \pi^*/S_0-S_1$
γ	430	$\pi \rightarrow \pi^*/S_0-S_2$
δ	310	$n \rightarrow \pi^*$
ϵ	280	$n \rightarrow \sigma^*$

These transitions are sensitive to a redox-state of the cofactor (Fig. 83) and, thus, allow conducting electrochemical titrations utilising a custom-made electrochemical cell (Fig. 93 at p. 140). The experiment is carried out by monitoring the absorption alterations in the differential spectrum when gradually changing the potential in the system. The differential spectrum is more sensitive to small alterations than absolute spectra (1% fraction). First of

all, the fully differential spectra (red-ox and ox-red) are obtained to determine that the system is reversible and stable. Afterwards, the titration is launched. At regions of the titration curve, which are far from the redox transition, the step of the potential shift is high and varied from 150 to 50 mV. At the titration point the step is decreased to 25 mV. The series of differential spectra obtained during the titration are shown in Fig. 84.

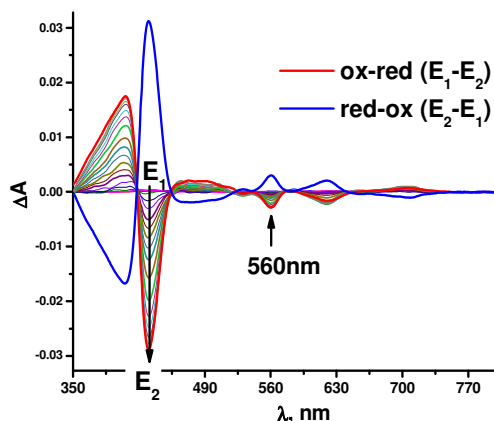


Fig. 84. Differential redox-induced UV/Vis spectra with several titration points.

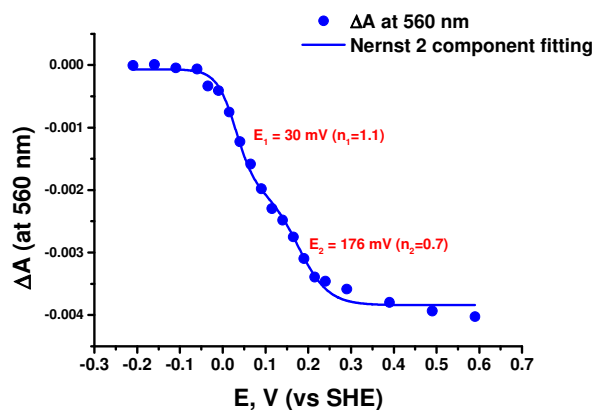


Fig. 85. Fitting with modified Nernst equation in order to determine the mid-point potentials of the redox active protein cofactors.

The analysis of the data includes the plotting of the changes of differential absorption at particular wavelength versus applied potential and following fitting with modified Nernst equation (Fig. 85):

$$y = y_0 + \sum_{i=1}^n \frac{A_i}{\exp\left(-\left(\frac{nF}{RT}\right) * (x - E_i)\right) + 1} \quad (24)$$

where y – differential absorption ΔA , y_0 – baseline, A_i – total differential absorption, n – quantity of electrons involved in the redox transition ($n \in [0.8; 1.1]$), F – Faraday constant, R – universal gas constant, T – temperature of the experiment, x – applied potential, E_i – mid-point potential. For the derivation of modified Nernst equation please see to Annex 10.

In titration experiments the system is at equilibrium. It is necessary to prevent protein adsorption on the surface of the gold working electrode which is, thereby, modified with corresponding thiols. The time of equilibration is controlled by recording consecutive spectra until stabilisation. Moreover, to decrease equilibrating time, the redox mediators are added

into solution to provide mediated electron transport. Thus, the studies include direct (immobilisation via GNPs-SAM at RDE) and indirect electrochemistry (UV/Vis and MIR spectroelectrochemistry with utilisation of the cell in Fig. 93, p. 140) (table 36).

Table 36. Comparison of the direct and indirect electrochemistry of proteins.

electrochemistry type	direct	indirect/mediated
equilibrium	not reached	reached
attachment to working electrode	through weak bonds to modified surface	should be avoided
usage of mediators	no	yes
thiol type (for hydrophobic protein)	uncharged	charged

Mid-infrared spectroscopy of proteins

MIR spectroscopy allows determining transitions between molecular vibrational levels. The vibrations of a molecule are described through the model of harmonic and enharmonic oscillators. Within the harmonic model the two atoms are regarded as two masses m_1 and m_2 which are bound through weightless spring with elastic constant K . The frequency ν of the vibration is given as:

$$\nu = \frac{1}{2\pi} \sqrt{\frac{K}{\mu}}, \mu = \frac{m_1 * m_2}{m_1 + m_2} \quad (25)$$

Thus, the frequency is a function of atomic masses and rigidity of the bond. This dependency is useful for the data analysis and the experiments with isotope atom exchange (for example, D₂O exchange experiment). The vibrational levels in the harmonic model are equidistant. The anharmonic oscillator model is based on the idea that the dipole momentum is not in linear dependency of atom movement and leads to conclusion that the distance between vibrational energetic levels is decreased with number of energetic levels.

In nonlinear molecule there are $3N - 6$ normal (independent) vibrations modes which can be classified as stretching (the length of the bond changes) or deformation (the angle of the bond changes) vibrations (Fig. 86).

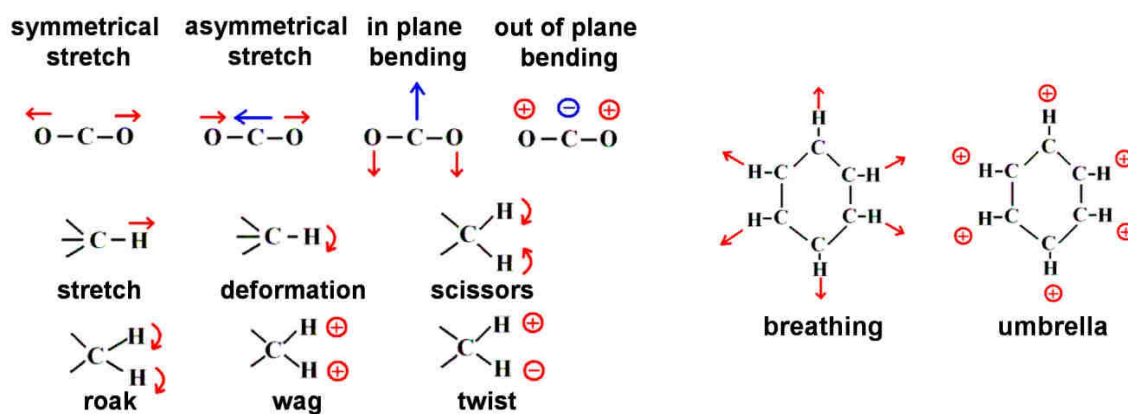


Fig. 86. Classification of the normal vibrations modes.²⁷¹

MIR spectroscopy when is applied to proteins elucidates various conformational changes and allows determination of the involved residues. The protein spectrum includes several characteristic regions (table 37) with corresponding vibrations of the protein scaffold (based on amide bond). In particular, amide I region is informative concerning secondary structure of protein (table 38). The spectra are obtained in transmission mode with corresponding cell (see p. 140, Fig. 93 and p. 142, Fig. 95). However, the drawbacks of IR spectroscopy is the water contribution to the spectra which results in sensitivity to humidity, instabilities of the source of IR light and detector, overinformation due to overlapping of wide range of the compounds (amino acid side chains, cofactors, small biological molecules, and components of the buffer). The error in the method is up to 10% and the precise attribution of the signals is somewhat hindered. The solutions facilitating spectrum interpretation include isotope exchange, introduction of the mutation in the protein molecule, solvent exchange (e. g., D₂O instead of H₂O), etc.

Table 37. Useful spectral regions for study of protein in MIR spectral region²⁵⁶.

amide	wavenumber, cm ⁻¹	attribution
A	3300	v(N-H)
B	3100	v(N-H)
I	1610-1695	v(C=O) (70%), v(C-N), δ(CCN), δ(N-H)
II	1480-1575	v(C-N), δ(N-H) (60%), δ(C=O), v(C-C), v(C-N) (40%)
III	1220-1320	v(C-N), δ(C=O), v(C-C), δ(N-H),

Table 38. Amide I components in the protein spectrum (the average maxima are shown)²⁵⁶

	band position (in H ₂ O), cm ⁻¹	band position (in D ₂ O), cm ⁻¹
α-helix	1654	1652
β-sheet	1633	1630
β-sheet	1684	1679
turn	1672	1671
disorder	1654	1645

Redox active proteins have different absorption spectra depending on the redox state. However, the intensity alterations of the absolute spectra upon applied potential variation are only 0.1% of the amide I absolute intensity. Again differential redox-induced spectroscopy is very helpful here. The electrochemical cell is the same as the one used for UV/Vis titration (p. 140, Fig. 93). The regular spectrum contains contributions from amino acids presented in reduced or oxidised state (Fig. 87). It is important to control the absolute absorption ($Abs < 1$ of amide I) before the experiment to have a correct subtraction of the solvent contribution. Additionally, the stability of the humidity should be verified before the measurements. Due to low intensity of the spectra several cycles (usually 60) should be conducted to obtain well resolved spectrum with high signal-to-noise ratio. The attribution of the bands can be conducted based on the literature^{256,257,272} and supplementary experiments (e. g., with isotope exchange, protein mutants, labelling).

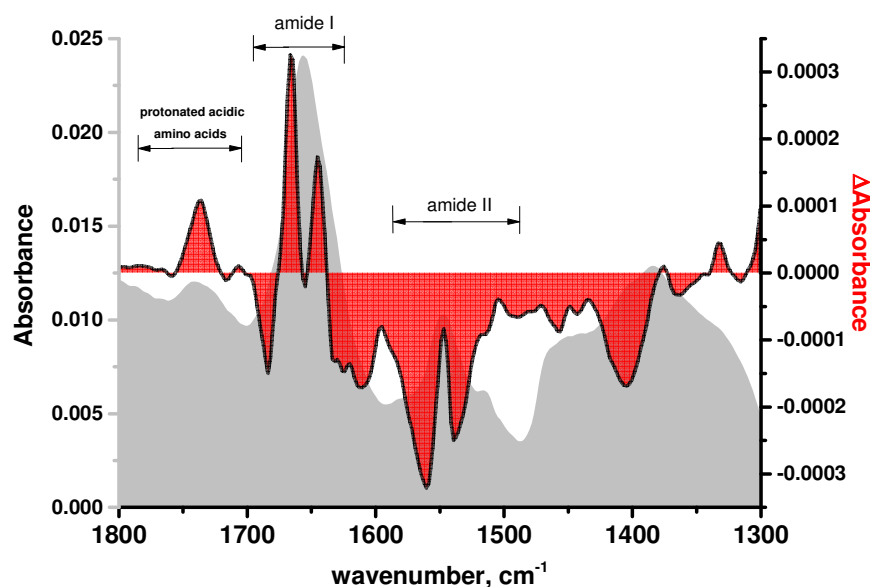


Fig. 87. Ox-red absorption IR spectrum of a protein (red). The negative bands come from reduced state, then the positive bands come from oxidised state. The absolute spectrum is in grey colour.

2. Raman spectroscopy. Application for the study of protein cofactors

The Raman effect is based on inelastic scattering, which means that the wavelength of the diffused light is different from that of the incident irradiation. Upon elastic Rayleigh scattering the system is excited and returns to the same energetic level, whereas upon Raman scattering the system comes back to a vibrational level different from the initial one (Fig. 88). The difference between energy levels is described as Raman shift $\bar{\nu}$ in cm^{-1} :

$$\bar{\nu} = \left(\frac{1}{\lambda_{\text{excitation}}} - \frac{1}{\lambda_{\text{emission}}} \right) * 10^7 \quad (26)$$

where $\lambda_{\text{excitation}}$ – wavelength of the incident laser irradiation, $\lambda_{\text{emission}}$ – wavelength of the scattered irradiation in nm.

The intensity of the Raman scattering is very low. One of the possibilities to enhance the signal is to excite the system with a coherent light at the absorption maximum of the samples which leads to the signal increase in 10^6 times (resonance Raman RR). Resonance Raman can compete with fluorescence. The main difference is that fluorescence live times are longer than that of the scattering processes. Additional issues that can be faced include sample photodegradation or photoreduction. To avoid this, one can use defocalisation of the laser, work in solution, and rotate the sample. Both fluorescence and photodegradation can be decreased with a choice of higher wavelength of the excitation laser. Additionally, it is sometimes useful to work with a diluted sample to diminish the effect of autoabsorption by the sample of the emitted Raman irradiation^{273–275}.

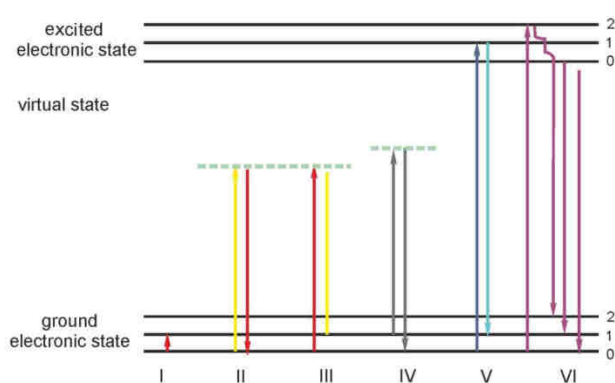


Fig. 88. Schematic representations of (I) infrared absorption, (II) Rayleigh scattering, (III) Stokes Raman scattering, (IV) anti-Stokes Raman scattering, (V) resonance Raman scattering, (VI) fluorescence (adapted from²⁷⁶).

Resonance Raman (RR) spectroscopy is a complementary method to IR absorption spectroscopy due to different selection rules. IR spectrum gives mostly information about the protein backbone; the RR approach provides data concerning cofactors buried in protein. This difference is based on the underlying physical phenomena. The absorption is connected with changes in the dipole momentum P which depends on charges Q and the distance L between them: $P = QL$. The scattering is a process of electron cloud distortion and is connected with the changes in the polarizability. Thus, the polar bonds (widely present in protein scaffold) are more IR active than nonpolar bonds (widely present in heme cofactors). Moreover, in RR studies the resonant laser specifically excites heme groups of the protein allowing us to see the only cofactor signatures in the spectra.

The absorption spectrum of proteins in UV/Vis region is mainly due to its cofactors. In the framework of the thesis, FeS-clusters and heme groups are studied^{277,278}.

The heme group contains iron surrounded with porphyrin ring. The skeletal and group modes of the organic ring include nonpolar C-C and C=C bonds (Fig. 89) which produce quite intense RR signal. The vibrations in the porphyrin ligand are sensitive to redox state and coordination (ligand quantity and types) of the central iron atom which allows conducting the characterisation of the heme cofactor in a protein. The classification of vibrations in the porphyrin was developed by Spiro^{279–281} (Fig. 89) and the approximate attribution is illustrated in table 39. The high-frequency porphyrin modes are located in 1000-1650 cm⁻¹. The bands of the high-spin complex are more downshifted than those of the low-spin. The reduction of the iron Fe(III)→Fe(II) leads to a decrease in the Raman shift, but the redox state is not the main aspect that determines band position. If spectral sensitivity to redox state is connected with size of the porphyrin cycle (based on the size of the bonds), then the spin-state is connected with structural alterations connected with changes in the symmetry of the heme²⁸².

Table 39. Assignment of the RR spectra bands of the hemes in dependence on spin, coordination and redox-state^{279–281}.

vibration type	parameter	position, cm ⁻¹	coordination
$\nu_2(\text{C}_b\text{C}_b)$	high-spin	1565	
	low-spin	1585	
$\nu_3(\text{C}_a\text{C}_m)$	Fe(II), high-spin	1472	5
	Fe(II), low-spin	1490	6
	Fe(III), high-spin	1480	6
	Fe(III), low-spin	1505	6
$\nu_4(\text{C}_a\text{N})$	Fe(III)	1370	
	Fe(II)	1360	
$\nu_{10}(\text{C}_a\text{C}_m, \text{C}=\text{C})$	high-spin	1610	6
	high-spin	1630	5
	low-spin	1640	6

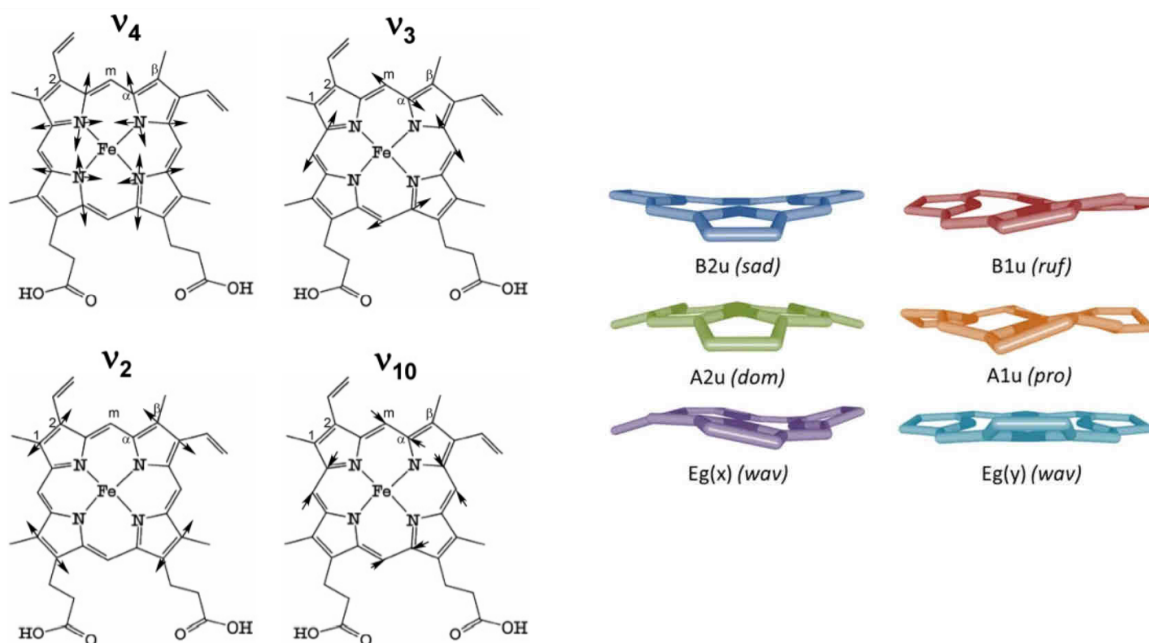


Fig. 89. Some examples of skeletal²⁸³ and in-plane¹¹⁶ heme vibrations. The locants of the atoms in the heme group are shown (left).

FeS-cluster containing proteins show MLCT S→Fe transition in the 450 nm region and, thus, can be studied by RR approach. The enhancement of the signal is around 10^3 - 10^5 . However, FeS-cluster excitation coefficient is typically low and, due to this, high concentrations of sample are required. The clusters can be of various structures FeS₄, Fe₂S₂, Fe₃S₄, Fe₄S₄ (Fig. 90).

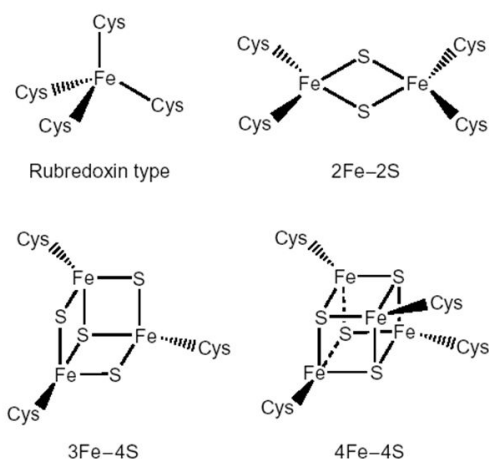


Fig. 90. Types of the FeS-cluster the most encountering in the nature²⁸⁴.

The major RR bands are located in the low-frequency 200-450 cm^{-1} region and their positions are sensitive to cluster type, structure and nature of the ligands, symmetry, and redox-state. The reduced state is usually a low-absorptive state and, thus, in some cases it is more difficult to detect it by RR in comparison to oxidised state. Moreover, the different excitation wavelength can probe different states and the type of the iron-sulfur cluster within one protein. The more iron atoms are presented in the cluster the more oxidation states it is possible to detect^{246,278}.

Instrumentation

I. Electrochemical equipment

In all experiments a three electrode cell was used (Fig. 91). The role of the auxiliary/counter electrode is to prevent the polarisation of the reference electrode. Unless otherwise stated, the ion strength of the supporting electrolyte was 0.1 M.

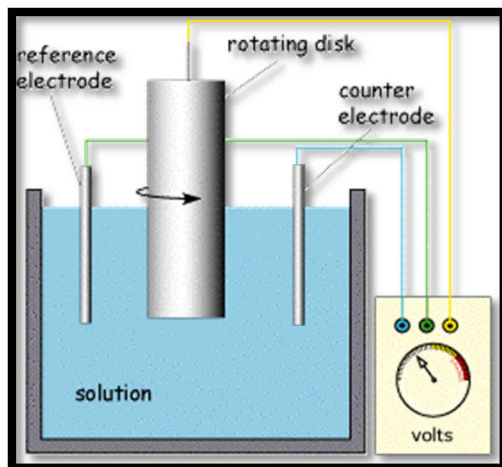


Fig. 91. Scheme of the three electrode electrochemical cell.²⁸⁵

The working electrode (WE) was either a gold disk rotating electrode RDE or a glassy carbon electrode GCE. The reference electrode (RE) was a commercial Ag/AgCl (3M KCl) electrode (+208 mV vs SHE). The counter electrode (CE) was a platinum wire. The potential at WE was maintained between WE and RE, and the current is measured in the circuit between WE and CE.

The voltammetric measurements were performed with a Princeton Applied Research VERSASTAT 4 potentiostat.

II. UV/Vis spectrometer

A dual-beam spectrometer VARIAN Cary 300 in single beam mode was used during the experiments. The source was a deuterium lamp for UV part of the spectra and xenon lamp for the visible part of the spectrum. The slit width was 1 nm. This spectrometer is based on scanning monochromator (Fig. 92). All the measurements were conducted in a single beam mode. The measurements were conducted either in a quartz cell (1 cm pathlength, 700 μ l volume) or with a thin-layer cell (described below).

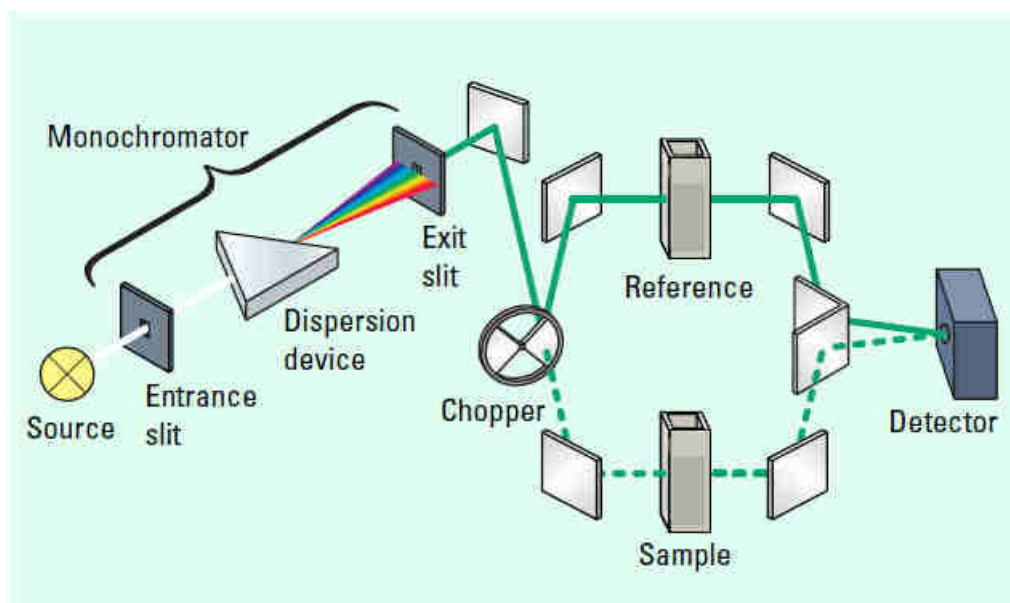


Fig. 92. Optical path in the UV/Vis spectrometer. Only one channel was used during single beam mode (dashed line).²⁸⁶

Thin-layer electrochemical cell

For the titration experiments an optically transparent thin-layer electrochemical cell¹¹ was used (Fig. 93). The cell possesses a pathlength $< 10 \mu\text{m}$ which is comparable to diffusion layer and which is very advantageous as it does not require stirring. It is a standard three electrode cell. The gold grid is used as a working electrode, a platinum contact (the square plate with 3 mm edge) as counter electrode, and home-made Ag/AgCl (3M KCl) as reference electrode. The protein solution is deposited on the gold grid (70% transparent, $6 \mu\text{m}$ thick, modified with thiols to prevent protein to adsorb), and then the cell is closed with CaF_2 windows, which are transparent in both UV/Vis and MIR region of the spectrum. Afterwards, the cell is filled with buffer. The loss of protein in 24 h is as low as 5% and it is due to capillary forces and small contact area with the buffer. Then, the cell is set up into spectrometer and connected to homemade potentiostat. Since the cell is a thin-layer cell, it allows decreasing water signal which shows strong absorption bands in MIR spectral region. On the other hand, the protein solution should be concentrated enough to reach satisfying signal-to-noise ratio.

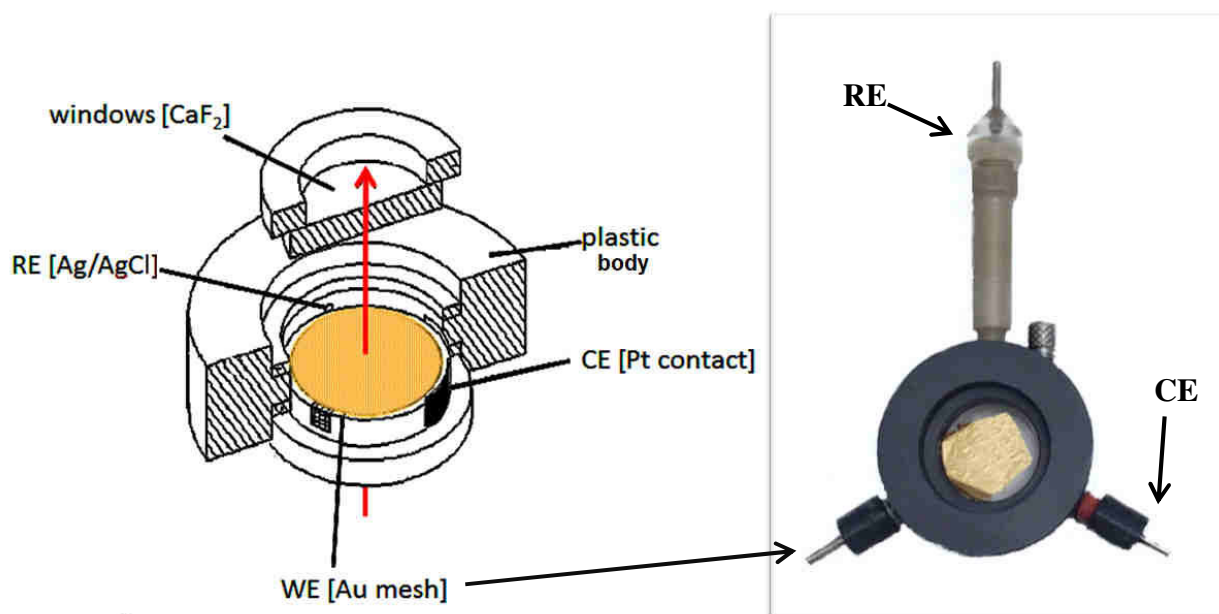


Fig. 93. Construction of the thin-layer electrochemical cell¹¹.

III. FTIR spectrometer

The MIR spectra were collected with a Vertex 70 Spectrometer from Brucker Optiks (Karlsruhe). The light source is a globar (CSi) heated up to 1300 K. The optical system includes (Fig. 94) the Michelson interferometer (*vide infra*) with KBr beam splitter and He-Ne calibrating laser (632 nm). The detector is a MCT (mercury cadmium telluride HgCdTe) which is cooled down with liquid nitrogen. The optical materials include: thin-layer electrochemical cell (*vide supra*) and transmission cell (*vide infra*). Each spectrum included accumulation of 256 scans with 40 kHz scan rate and 4 cm⁻¹ resolution.

Interferometer

The light emitted with a light source reaches semi-transparent mirror (“beam splitter”) and is split into two coherent beams. One beam goes to the fixed mirror then the second one is directed to the movable mirror with position $x \in [-L; L]$. The reflected beams meet again and interfere. The interferogram is registered with the detector. The resulted interferogram is a sum of the interferograms at all wavelengths except the ones that were absorbed.

The interferogram is the result of either one-side scan (the mirror change position from 0 to L) or two-side scan (mirror changes position from $-L$ to L). The Fourier transformation allows obtaining the restored spectrum.

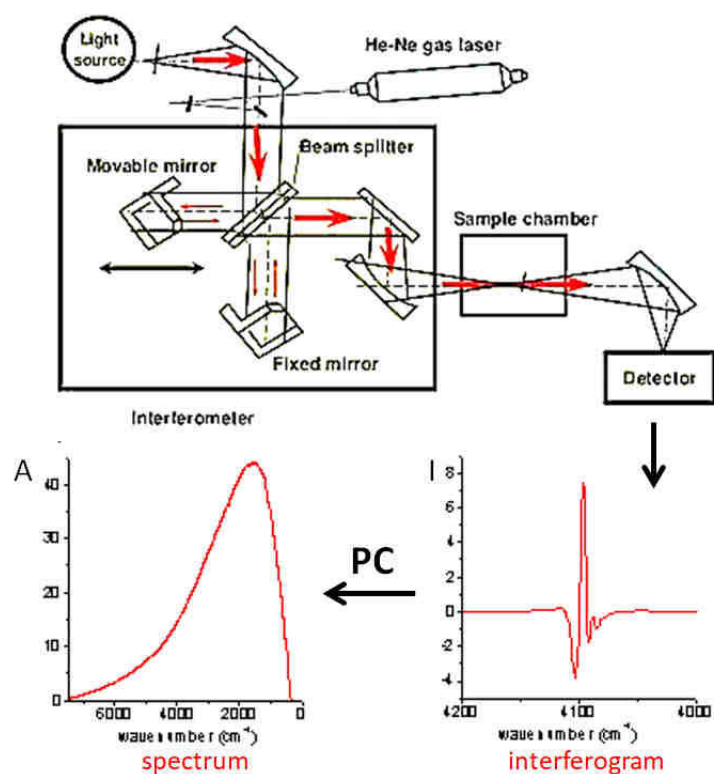


Fig. 94. Scheme of the FTIR spectrometer and the data obtained during the experiment.²⁸⁷

The interferometer measurements are connected with several advantages leading to the increase in the signal-to-noise ratio due to: the possibility to scan all wavelengths simultaneously (Fellgett's advantage), and the use of a collimating aperture and not a regular slit allowing more light to pass in the system (Jacquinot's advantage), and the avoidance of the mechanical movements of the calibrating laser (Connes' advantage).

The resolution $\Delta\kappa$ of the spectra is in dependence of retardation δ (maximal difference of the pathlength) as follows: $\Delta\kappa = 1/\delta$. For the standard spectrometer, the maximal amplitude of the movable mirror is 0.25 cm which leads to the 4cm^{-1} resolution.

Transmission cell

The used cell (Fig. 95) includes CaF_2 windows (case of the MIR measurements) enclosed in the metallic body with teflon buffering spacers. The cell is connected to the thermal bath. The experiment does not demand a big quantity of the sample: the interwindow space is filled with 1-2 μl of solution with average protein concentration of 30-100 μM . The experiments are carried out in D_2O to avoid contribution of H_2O in amide I region.

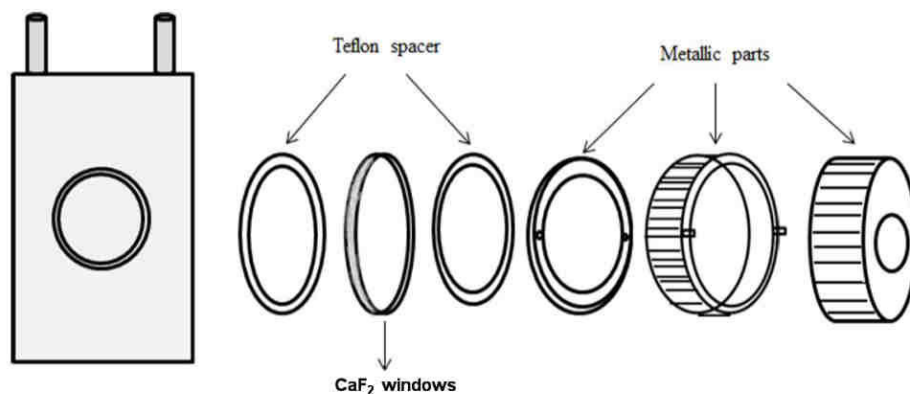


Fig. 95. Transmission cell used for secondary protein structure determination.²⁸⁸

The analysis of the secondary protein structure is conducted through FTT filter smoothing of the amide I band, baseline subtraction, peak determination by taking 2nd derivative (negative peaks), and deconvolution with Gaussian function with correlation coefficient of $R^2=0.999$.

IV. Raman spectrometer

A Renishaw InVia Reflex Raman spectrometer was used in the experiments.

The optical system of the dispersive type spectrometer includes (Fig. 96): an argon ion laser with excitation wavelengths at 457 (9 mW) and 514 nm (12.5mW), Leica focalising optics, 4 notch filters (for Rayleigh scattering cut off), the slit, dispersive monochromator (grating: 2400 /cm) with a charge coupled device (CCD) detector.

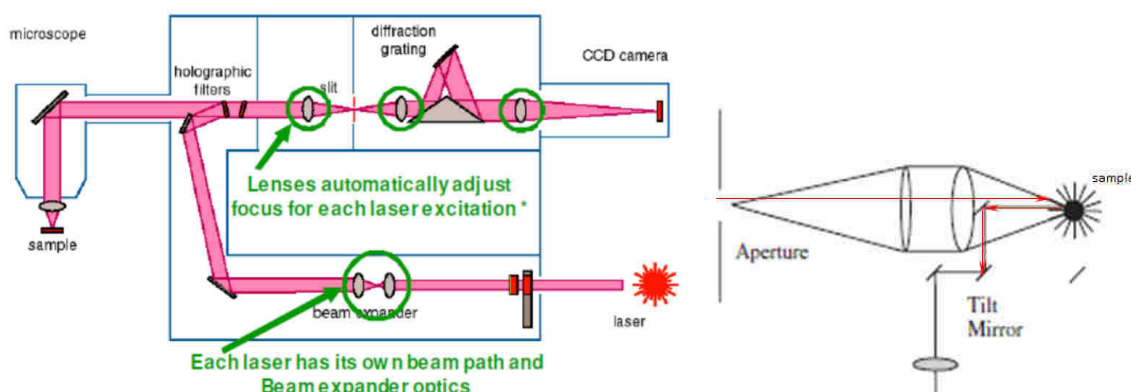


Fig. 96. Optical scheme of Raman spectrometer²⁸⁹ (left) and scheme of backscattering collection of the Raman emission from the sample (right).²⁹⁰

The collection of the Raman scattering emission is conducted under 180° (backscattering). Resolution is 1 cm⁻¹.

For the measurements of the dried films two types of supports were used depending on the region of interest:

- high-density polyethylene windows: transparency in 500-50 cm^{-1} , sustainable to a big variety of the solvents;
- CaF_2 windows: transparency in 83333-1111 cm^{-1} , insoluble in water, sensitive to NH_4^+ .

V. Clark-electrode

Auxiliary measurements of the ubiquinoloxidase activity were conducted with chemical sensor Clark-electrode. The construction of the system is shown in Fig. 97. The sensor is a Pt disk cathode (WE) and Ag ring anode (CE). The electrodes are immersed in the supporting electrolyte and separated from the buffer with sample through a thin gas-permeable membrane. Albeit various gases can penetrate the membrane (e. g., O_2 , N_2 , CO_2), only oxygen is reduced at the cathode. The sensor is enclosed in the plastic vessel filled with a buffer with a sample. The continuous stirring of the solution is provided. The result signal of chronoamperometric experiment is a steady-state current that is proportional to the dissolved oxygen concentration. Depending on the protein oxygen consumption activity the quantity of oxygen in the closed system can be measured.

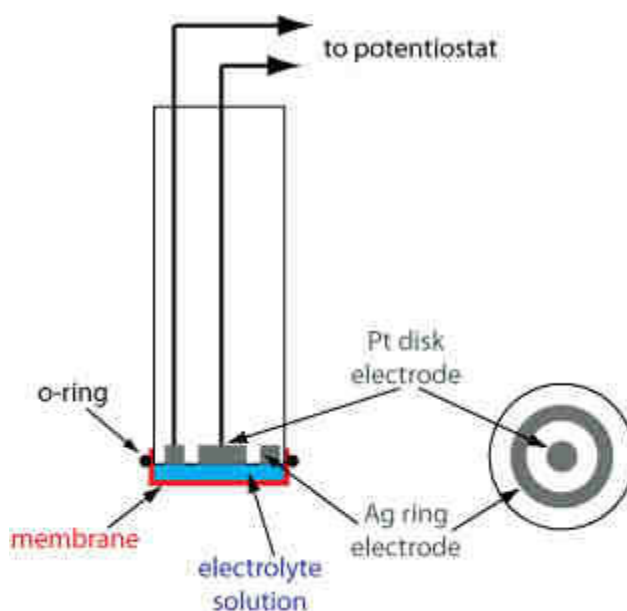


Fig. 97. Principal scheme of construction of a Clark-electrode²⁹¹.

Experimental protocols

I. Protein preparations

1. Purification

bd-oxidase from E. coli

The protein (pI5.3²⁹⁸) was extracted and purified by the group of Pr. Friedrich (University of Freiburg, Germany). The purification protocol includes metal affinity chromatography IMAC (His-tag). The precise protocol was published previously⁵⁴. We worked with the protein samples from three various purification which differed by the number of chromatographic columns and type of detergent used:

- №1: DDM 0.05%, 20 mM MOPS, 20 mM NaCl, pH7 (“regular preparation”);
- №2: DDM 0.05%, 20 mM MOPS, 20 mM NaCl, pH7 (more columns – less lipids);
- №3: MNG 0.05%, 20 mM MOPS, 20 mM NaCl, pH7.

bd-oxidase from G. thermodenitrificans

Cyt *bd* from *G. thermodenitrificans* was purified by the group of Pr. Michel (M. Planck Institute of Biophysics, Frankfurt-am-Main, Germany) following reference⁵. 200 μ M cyt *bd*, DDM 0.02%, 50 mM KCl, 20 mM NaPi, pH6 has been used.

mitoNEET

The soluble part of the protein mN44-108 bearing additionally His-tag (8.58 kDa, pI7.15) was expressed in *E. coli* and purified according to previous report²⁹².

2. Pretreatment of the samples

PFV

The filter (Amicon) was prewashed with water and corresponding (table 40) exchange buffer (10 min, 7500-9000 rpm, 500 μ l). The protein was washed at 4°C in the corresponding conditions.

Table 40. Protein washing procedures for PFV experiments.

	cyt <i>bd</i> (<i>E. coli</i>)	cyt <i>bd</i> (<i>G. thermodenitrificans</i>)	mitoNEET
washed solution	5 μ l, 250 μ M	8 μ l, 200 μ M	40 μ l, 1 mM
exchange buffer	KPi 0.1 M, pH7	KPi 0.1 M, pH7	KPi 0.1 M or Tris 50 mM, KCl 0.1 M, pH8
filter cutoff, kDa	50	50	3
rotation speed, rpm	7500	4000	9000
number of centrifugation cycles	1	2-3	2
time of centrifugation cycle	45 min	10 min	30 min
final filtrate volume, μl	17-21	17-21	35

Then the protein was incubated with lipids and/or UQ (cyt *bd*), or a ligand (mitoNEET), if needed. Finally, the solution was diluted with exchange buffer to the final concentration.

In some experiments the washing procedure was repeated twice or thrice until stable protein films were obtained at RDE.

Procedure of lipid addition for cyt *bd* from *E. coli*

The lipids were separately diluted in an ethanol-chloroform (1/3) solution of 36 μ M concentration. The needed quantity of the lipids (table 41) was deposited on the bottom of a cone-like glass vessel and dried under weak argon stream. At the same time the ethanol solution of ubiquinone was added, if needed. On the next step, the protein solution was added to the lipids and incubated in the course of \geq 1h.

The lipid percentage mentioned in protocols is a fraction of the lipids relative to the protein concentration, which is taken as 100%.

Table 41. Cyt *bd* from *E. coli* sample preparation for PFV experiments.

experiment type	protein purification	lipid/quinol addition
concentration variation	№1	no
influence of the lipids	№2	PE/PG 1/1 in concentration 0, 5, 15, 22, 30, 44%
influence of the thiol type	№1	2.5% PE or PG, 3xUQ ₁
influence of the polarity of the surface on HQNO inhibition	№3	2.5% PG, 3xUQ ₁
inhibition experiments	№3	2.5% PE, 3xUQ ₁ .

Differential FTIR spectroscopy

Table 42. Conditions of the protein preparation for differential redox-induced FTIR experiments.

	cyt <i>bd</i> (<i>E. coli</i>)	cyt <i>bd</i> (<i>G. thermodenitrificans</i>)	mitoNEET
exchange buffer	DDM 0.05%, 0.1 M KCl, 20 mM KPi		KPi 0.1 M or Tris 50 mM, KCl 0.1 M
each mediator concentration, μM	50		25
time of incubation with mediators, min	40		20
protein studied concentration, μM	300		1200

Raman spectroscopy

The samples used for RR were treated in the same way as for FTIR experiments.

Electrochemical titrations

Cyt *bd* from *G. thermodenitrificans* was concentrated up to app. 400 μ M. with DDM 0.05%, 100 mM KCl, 20 mM KPi buffer; parameters of the washing were as for pretreatment for PFV. The mediator concentration was 50 μ M (each).

FTIR transmission measurements

Cyt *bd* from *G. thermodenitrificans* was washed with phosphate buffer in D₂O.

Catalytic activity measurements in solution

The regular purification (№1) of cyt *bd* from *E. coli* was utilised. The protein was buffer exchanged in the same manner as described before in case of direct electrochemistry measurements. Cyt *bd* was mixed with PE or PG lipids with the concentrations: 0, 10, 20, 50, and 100 %.

II. Electrode pretreatment and modification

The electrode (4.5 mm in diameter) was mechanically polished with 0.3 μ m aluminium oxide powder (without sonication in screening) and electrochemically pretreated in 0.1 M H₂SO₄: 1) + 2V, 5 s; 2) -0.35 V, 10 s, 100 points; 3) CV: 100 (25 in screening) cycles, 4 V/s, -0.35...1.5 V; 4) verification CV: 2 cycles, 0.1 V/s, -0.35...1.5 V.

Then centrifuged gold NPs were deposited on the gold electrode surface. After drying 20 (10 in screening) control cycles, 0.1 V/s, -0.2...1.55 V were performed. Then, the electrode was immersed in an ethanolic thiol solution with a concentration 1 mM of each thiol and incubated. The measurements of the background were conducted in buffer with 100 mM ion strength: CV with 20 (10 for screening) cycles at 0.1 V/s and 2 cycles at 0.02 V/s. The protein solution was then drop casted and left on the electrode at 4°C. For the precise parameters of the experiments see table 43.

Table 43. Conditions of the electrode modification procedure.

experiment type	GNPs volume (deposition number)	thiol mixture	time of thiol incubation	time of protein incubation	final deposited protein concentration, μM
concentration variation	9 μl (x3)	HT/MCH 1/1	overnight	overnight	200, 20, 10, 6, 3, and 2
influence of the lipids	9 μl (x3)	HT/MCH 1/1	overnight	overnight	10-15
influence of the thiol type	9 μl (x3)	varied	overnight	1-5 h	10-15
influence of the polarity of the surface on HQNO inhibition	9 μl (x3)	HT/MCH (ratio varied)	overnight	1-3 h	10-15
inhibition experiments	7 μl (x1)	HT/MCH 1/1	15-20 min	15-30 min	10-15
cyt <i>bd</i> (<i>G. thermodenitrificans</i>)	9 μl (x3)	HT/MCH 1/1	overnight	overnight	10-15
optimisation mitoNEET	7 μl (x3)	varied	overnight	overnight	200
ligand interaction with mitoNEET	7 μl (x3)	MHA	overnight	overnight	200

III. FTIR parameters

All the experiments were conducted at 5°C. The protein and gold grid pretreatment conditions are discussed in the corresponding sections. 256 spectra were accumulated in each cycle and averaged. More than 60 averaged spectra were utilised to obtain ox-red differential spectrum. The resolution of the spectra was 4 cm^{-1} . The conditions of measurement are described in table 44.

Table 44. Conditions of the redox-induced differential FTIR experiments.

experimental parameter	cyt <i>bd</i> (<i>E. coli</i>), “purification №1”	cyt <i>bd</i> (<i>G. thermodenitrificans</i>)	mitoNEET
potential range, mV (vs Ag/AgCl)	[-500, 500]		[-600, 0]
equilibration time, s	300		120-240

IV. Raman spectroscopy measurements

Sample conditions were the same for RR and FTIR experiments. Dried films of a protein solution (2 μ l) were used. A x50 magnification was applied for all experiments. Several spectrum accumulations from 3 different spots were collected. The resolution of the spectra was 1 cm^{-1} . For additional conditions of the experiments see table 45.

Table 45. Conditions of the RR measurements.

experimental parameters	cyt <i>bd</i> (<i>E. coli</i>)	cyt <i>bd</i> (<i>G. thermodenitrificans</i>)	mitoNEET
window material	CaF ₂		polyethylene
studied concentration, μ M	15		1200
excitation wavelength, nm	514		457
number of spectrum accumulations	~60		~300

V. Redox titration experiments

Before each titration experiment the heme content of each batch of cyt *bd* protein was verified using chemical reduction. The air-oxidised protein solution 2 μ l was diluted in 900 μ l buffer solution in the quartz-cuvette and reduced with dithionite. The presence of the bands at 560 and 620 nm allowed us to conclude the presence of all three heme cofactors in the protein. The concentration was then calculated based on $\Delta\epsilon$ values determined for specific wavelengths⁴. The calculations employed the formula:

$$C = \frac{(A_{\lambda 1}^{red} - A_{\lambda 2}^{red}) - (A_{\lambda 1}^{ox} - A_{\lambda 2}^{ox})}{\Delta\epsilon_{\lambda 1, \lambda 2}^{red-ox}} = \frac{(A_{\lambda 1}^{red} - A_{\lambda 1}^{ox}) - (A_{\lambda 2}^{red} - A_{\lambda 2}^{ox})}{\Delta\epsilon_{\lambda 1, \lambda 2}^{red-ox}} \quad (27)$$

where C – protein concentration, A – absorption at specific wavelength λ and for specific state: reduced or oxidised.

The temperature of the titration experiment was 13°C. The resolution of the spectra was 1 nm.

VI. IR transmission

2.5 μ l of 10 μ M protein solution were deposited between CaF₂ windows. The background of corresponding buffer at corresponding temperature was measured and subtracted from the sample spectra.

VII. Catalytic activity in solution

10 μ l of 20 μ M *bd* were injected into 2 ml of the DDM 0.05% buffer in Clark electrode (0.1 μ M cyt *bd*). The background was measured. Further, to determine catalytic activity 2 μ l of 100 mM DecQH₂ were added (DecQH₂/*bd*=1000/1). The buffer solution filled into Clark electrode was 50 mM KCl, 50 mM KPi, pH7, 0.05% DDM, heated up to 30°C and stirred.

DecQH₂ was reduced before the mixing by adding NaBH₄ in 20 μ l of 100 μ M DecQH₂ ethanol solution. To neutralise excess of NaBH₄ a drop of 1M HCl was added in order to reach pH7.

The data treatment was performed with kind help of Alexander Thesseling (group of Pr. Friedrich, Freiburg University, Germany).

Materials

I. Compounds

Sodium citrate, hydrogen tetrachloroaurate trihydrate, sulfuric acid, ubiquinone-1, 1-mercaptohexanol (MCH), 1-hexanethiol (HT), mercaptohexanoic acid (MHA) and mercaptoundecanoic acid (MUA) were purchased from Sigma; potassium phosphate dibasic trihydrate from Fischer BioReagents; mercaptopropionic acid and cysteamine (MEA) from Tokio Chemical Industry. 1,2-dioleoyl-sn-glycero-3-phospho-(1'-rac-glycerol) (sodium salt) (PG) and 1,2-dimyristoyl-sn-glycero-3-phosphoethanolamine (PE) were provided by Avanti Polar Lipids. H₂O₂ (33%) and H₂SO₄ (96%) were purchased from Sigma-Aldrich, HNO₃ (65%) - from Fluka, aluminum oxide powder – from Buehler.

The compounds for inhibition studies were provided by Dr. Nasiri (Johann Wolfgang Goethe-University, Frankfurt-am-Main, Germany), the aurachin D derivatives were synthesized by the group of Dr. Speicher (Saarland University, Saarbrücken, Germany)²⁹³. Pioglitazone and resveratrole-3-sulfate were received as a gift from the group of Dr. Golinelli-Cohen. HQNO was purchased from Enzo Life Sciences Inc.

II. Gold nanoparticles preparation and validation

The gold nanoparticles GNPs were prepared according to the method developed by Turkevich et al.²⁹⁴, Frens⁸. The HAuCl₄ solution (49 mg) in 125 ml of water was boiled, and subsequently a solution of sodium citrate (143 mg in 13 ml of water) was added. The solution was kept under boiling for 15 minutes, cooled down to room temperature and concentrated by centrifugation at 10 krpm during 30 min. 95% of the supernatant was removed. The size of GNPs was measured by UV/Vis spectroscopy from the ratio of the plasmon resonance band to the background absorption at 450 nm: $GNPs\ diameter = f\left(\frac{A_{spr}}{A_{450}}\right)^{295}$.

III. Gold grid modification

The gold grid was modified with thiols. For cytochrome *bd* oxidase the thiol solution was 1/1 MPA/MEA (1 mM each) and 1/1 HT/MCH (1 mM each) for mitoNEET. The modification was conducted at least overnight. After each experiment the gold grid was sonicated (10 min, 2 times). After each 4th experiment due to passivation of the protein the grid was washed with piranha / aqua regia solution (300 µl HNO₃ (65%), 3000 µl H₂O₂ (33%) and 3x600 µl H₂SO₄ (96%)).

IV. Mediators

The mediator solutions (table 46) were prepared by two successive dilutions. The weighted mass was diluted with 1.25 ml of corresponding solvent ($C_1 = 0.01 \text{ mM}$) and well-mixed in shaker. Then, the 20 μl of the C_1 solution were then diluted more with 780 μl solvent and were shaken during 15 min ($C_2 = 0.25 \text{ mM}$). Finally, all mediators were mixed together by taking 1 μl of each solution, thus, with final concentration of 25 μl of each compound. With this concentration the contribution of the mediators to the spectra is negligible. The mediators were chosen to cover the whole potential range from -600 to +600 mV (vs Ag/AgCl) (modified from ²⁹⁶).

Table 46. List of 19 mediators used in the differential redox-induced spectroscopy measurements. All mediators are low-weight redox active compounds.

compound	E^0 , mV (vs Ag/AgCl)	solvent	producer
ferrocenylmethyltrimethylammoniumiodide	607	ethanol	Strem chemicals
1,1' - ferrocenedicarboxylic acid	436	ethanol	Fluka
potassiumhexacyanoferrate(II) trihydrate	212	water	Riedel-de-Haen
1,1' - dimethylferrogene	133	ethanol	Aldrich
quinhydrone	70	ethanol	Fluka
tetrachloro — 1,4 -benzoquinone (<i>p</i> -Chloranil)	72	acetone	Aldrich
N,N,N',N' — tetramethyl- <i>p</i> -phenylenediamine dihydrochloride	62	water	Fluka
2,6-dichlorophenolindophenol sodium salt hydrate	9	ethanol	Biochemika
hexaammineruthenium(III)chloride	-8	water	Aldrich
anthraquinone-2-sulfonic acid sodium salt	-23	water	Aldrich
1,4 naphthoquinone hydrate	-63	ethanol	Aldrich
anthraquinone	-108	ethanol	Aldrich
5-hydroxy-1,4-naphthoquinone	-158	ethanol	Aldrich
duroquinone	-198	ethanol	Sigma
menadione	-220	acetone	Sigma
2-hydroxyl-1,4-naphthoquinone	-333	ethanol	Sigma
9,10-antraquinone-2,6-dizulfonic acid disodium salt	-433	ethanol	Sigma
Neutral Red	-515	ethanol	Sigma-Aldrich
methyl viologen dichloride hydrate	-628	water	Aldrich

V. Inhibitor addition

Cyt *bd*

In PFV experiments a solution of inhibitor in DMSO (20 mM) was injected into 20 ml buffer (KPi 100 mM, pH7) solution in which rotating disk electrode was immersed.

For the RR and differential FTIR measurements the protein was preincubated 1 h at 4°C or 1 h at 45°C with aurachin D, and overnight at 4°C with KCN. The excess was x30 for aurachin D and x100 for KCN.

mitoNEET

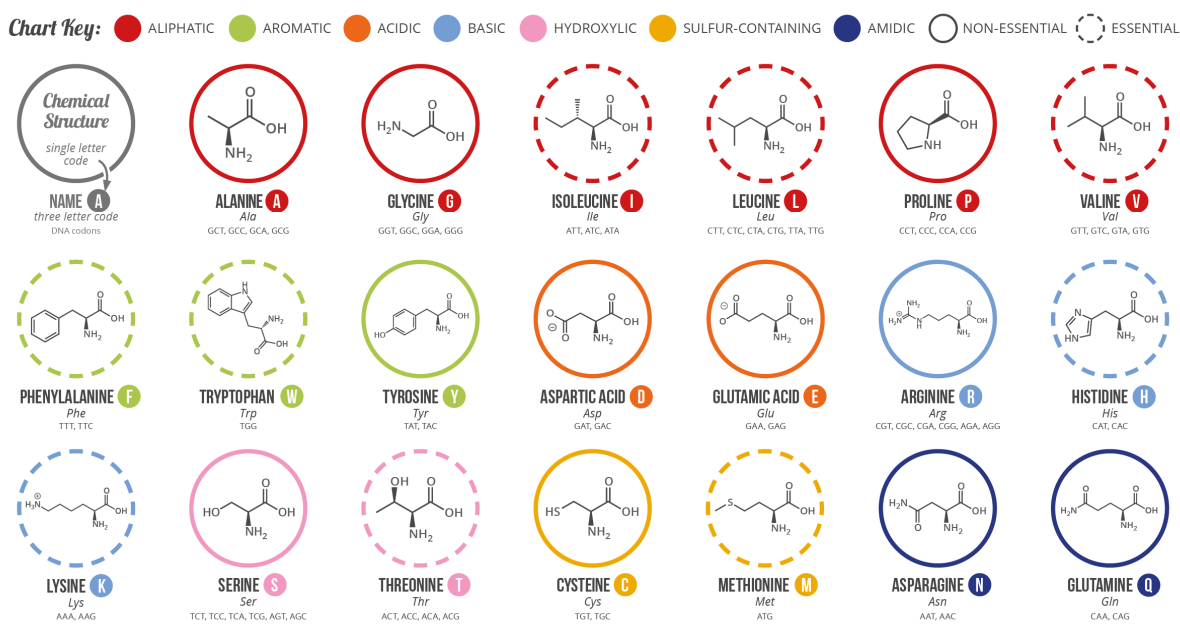
The protein was preincubated overnight with a ligand at 4°C in all types of the experiments, unless otherwise stated.

Software

The data was processed by means of Origin Lab Pro 9.5, VersaStudio, Microsoft Office, and Opus Brucker.

Annexes

A1. List of the essential amino acids²⁹⁷ and table of their properties²⁷.



Amino acid	pK ₁	pK ₂	pK _R	pI	Hydropathy index
	-COOH	-NH ₃ ⁺	R group		
Ala	2.34	9.69	-	6.00	1.8
Arg	2.17	9.04	12.48	10.76	-4.5
Asn	2.02	8.80	-	5.41	-3.5
Asp	1.88	9.60	3.65	2.77	-3.5
Cys	1.96	10.13	8.18	5.07	2.5
Glu	2.19	9.67	4.25	3.22	-3.5
Gln	2.17	9.13	-	5.65	-3.5
Gly	2.34	9.60	-	5.97	-0.4
His	1.82	9.17	6.00	7.59	-3.2
Ile	2.36	9.60	-	6.02	4.5
Leu	2.36	9.60	-	5.98	3.8
Lys	2.18	8.95	10.53	9.74	-3.9
Met	2.28	9.21	-	5.74	1.9
Phe	1.83	9.13	-	5.48	2.8
Pro	1.99	10.60	-	6.30	1.6
Ser	2.21	9.15	-	5.58	-0.8
Thr	2.09	9.10	-	5.60	-0.7
Trp	2.83	9.39	-	5.89	-0.9
Tyr	2.20	9.11	10.07	5.66	-1.3
Val	2.32	9.62	-	5.96	4.2

A2. Amino acid sequence alignment of subunits *CydA* and *CydB* of *cyt bd* from *G. thermodenitrificans* and *E. coli*⁵. Conserved residues involved in: heme coordination – yellow, quinol binding – purple, *CydA* proton pathway – blue, *CydB* proton pathway – red, charge compensation – green⁵. Sequence identity is less than 30%.⁵

CydA alignment

<i>E. coli</i>	1	--MLDVELSRQLQFALTAMYHFLFVPLTLGMAFLLAIMETVYVLSGKQIYKDMTKFWGKL	58
<i>Geobacillus thermodenitrificans</i>	1	MNGYDPVLLSRILTELTLTVHIIYATIGVGVPLMIAIAQWGI RKNDMHYILLARRWTRG	60
<i>E. coli</i>	59	FGINFALGVATGLTMEFQFGTNWSYSHYVGDIFGAPLAIHGLMAFFLESTFVGLFFFGW	118
<i>Geobacillus thermodenitrificans</i>	61	FVITVAVGVVGTGAIGLQLSLLWPNFMQLAGQVLSLPLFME-TFAFFFEAIFLGIYLYTW	119
<i>E. coli</i>	119	DRLGKVGQ-HMCVTWLVALGSNLSALWILVANGWMQNPIASDFNFETMRMEMVSFSELVLN	177
<i>Geobacillus thermodenitrificans</i>	120	DRFENQKKHLLLLIPVAIGSSASAMFI TMVNAFMNTPQGFEKNG--ELVNI DP I VAMFN	177
<i>E. coli</i>	178	PVAQVKFVHTVASGYVTGAMF LGISAWMLKGRDFAFAKRSFAIAASFGMAAVLSVIVL	237
<i>Geobacillus thermodenitrificans</i>	178	PAMPTKVAHVLATSYM TSAFVLASIAAWHLWKGNRHIYHRKALHLMKTA FIFSVASALV	237
<i>E. coli</i>	238	GDESGYEMGDVQKTKLAAIEAEWE TQAPAAFTLFGIPDQEEETNKFAIQIPYALGIIAT	297
<i>Geobacillus thermodenitrificans</i>	238	GDLSGKFLAEYQPEKLAAAWHFETSS-HAPLILFGTLE-EDNEVKYALEIPYALSILAH	295
<i>E. coli</i>	298	RSVDTPVIGLKELMVQHEERIRNGMKAYS LLEQLRSGSDQAVRDQFNSMKKDLGYGLLL	357
<i>Geobacillus thermodenitrificans</i>	296	NHPAAVVTGLNDIPED-----	311
<i>E. coli</i>	358	KRYTPNVADATEAQIQATKDSIPRVAPLY--FAFRIMVACGFLLLAIIALSFW--SVIR	413
<i>Geobacillus thermodenitrificans</i>	312	-----E--RPPLYIHYLFDVMVTIGVFLMVAA-VYWLGSIFR	346
<i>E. coli</i>	414	NRIGKKWL LRAALYGIPLPWI AVEAGWFAEYGRQPWAGEVLP TAVANSSLTAGDLIF	473
<i>Geobacillus thermodenitrificans</i>	347	WKWTAKNWFGLLVAGGPLAMIAIEAGWLA EYGRQPWILRGYMKTAEGATTS--AHVDT	404
<i>E. coli</i>	474	SMVLICGLYTLFLVAELFLMFKFARLGPSSLKTGRYHFEQSSTTTQPAR	522
<i>Geobacillus thermodenitrificans</i>	405	MLVLFCLLYIVLVIASATVLRMFRRNPVERELEERA---NRGEVAP--	448

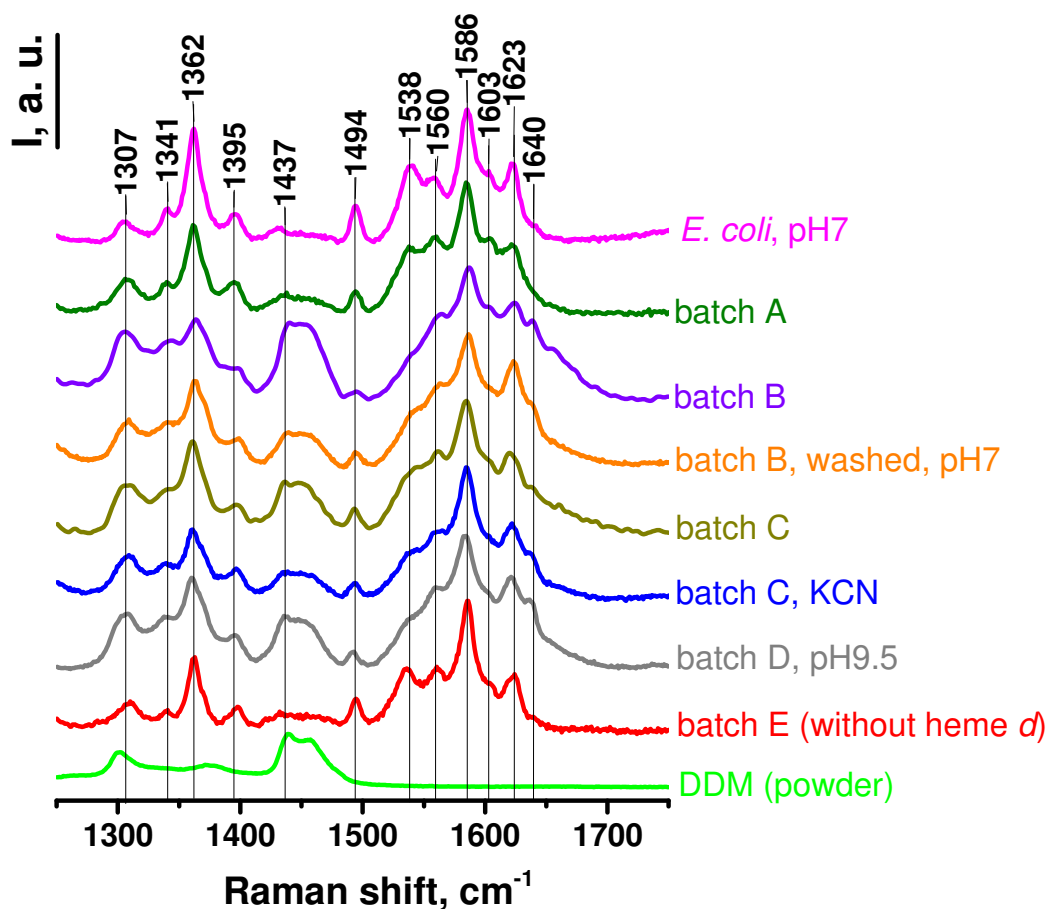
CydB alignment

<i>E. coli</i>	1	-MIDYEVLRFIWMLLVGVLLIGFAVTDGFMGVGMLTRFL---GRNDTERRIMINSIAPH	56
<i>Geobacillus thermodenitrificans</i>	1	MTLEVIGISVLWLF---LFGYIIVASIDFGAGFFSVYSHWANQQHILHRIQRYLSPV	55
<i>E. coli</i>	57	WDGNQVWLITAGGALFAAWPMVYAAAFSGFYVAMI LVLASLF-----FIPVGFDRSKIE	111
<i>Geobacillus thermodenitrificans</i>	56	WEVTNVFLVFFVVGIVGFFPKT-----AYYYSILLVPASIAIVLLAIGSYAFHTYGE	110
<i>E. coli</i>	112	-ETWRNMWDWGI F I GSFVPLP---VIGVAFGNLLQGVPFNVDEYLRLYYTGNFFQLLNP	167
<i>Geobacillus thermodenitrificans</i>	111	TERNWY-LLAYGL-TGLFIPASLSIVLTI SEGGFVEENAAGV---ALDY-GKLF A--SP	161
<i>E. coli</i>	168	FGLLAGVVSVMII TOGATY LQMRTV GELHLRTRATAQVAALVTLVCFALAGVWWMY GID	227
<i>Geobacillus thermodenitrificans</i>	162	LSWSVVLLSVTSVLYISAVFLTYYADA-----AGDEQARALLRRY---ALLWSGP TML	211
<i>E. coli</i>	228	GYVVKSTMDHYAASNPLNKEVVREAGAWLVNFNNTPI LWAIPALGV---VLP L L T I L T A	283
<i>Geobacillus thermodenitrificans</i>	212	SALL--IIYQLRYHNP-----EHYDNLWNVAWMLVIFLFFVITVWLLG	253
<i>E. coli</i>	284	RMDKAAWAFVSSSLTLCII ILTAGIAMFPFVMPSS TMMNASLT MWDATSSQL-TLN-VMT	341
<i>Geobacillus thermodenitrificans</i>	254	RQRRFGWAFIALLFQYAFAYAGISHYPYLLYPYL-----TIYDGFNETMAMALIVA	307
<i>E. coli</i>	342	WAV--VLVP I I L-LYTAWCYWKFGRITKEDIERNTHSLY	379
<i>Geobacillus thermodenitrificans</i>	308	F I AGLLLL IPSLYLLMRLFLFNKAYV---KGKWEKGK---	342

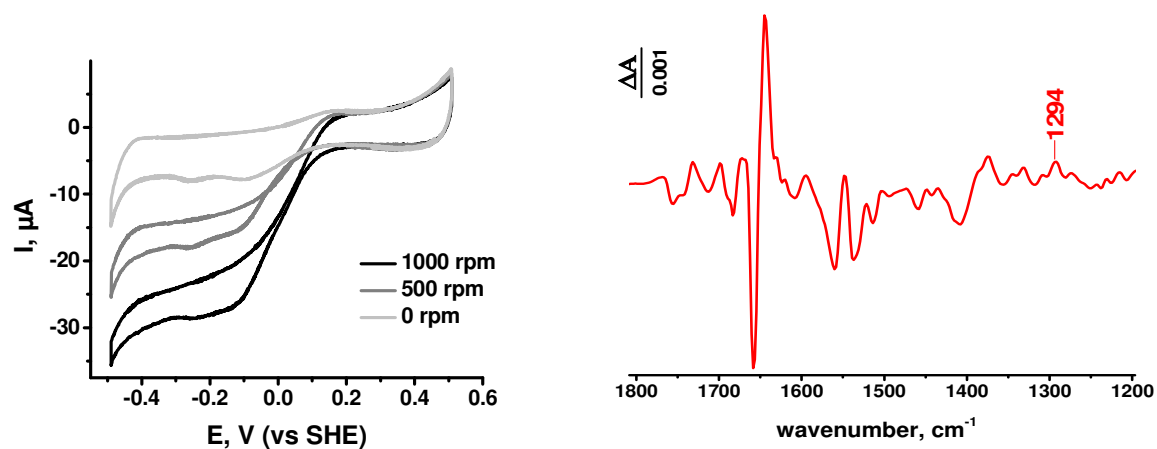
A3. Corresponding descriptive statistics for midpoint potential values (see table 22) in mV (vs SHE) for the cofactor of bd-oxidase from *G. thermodenitrificans* obtained in different conditions: standard deviation SD is in red and the random error ϵ (t-distribution with $p=0.95$) is in black.

	619 nm /heme d		heme b№1		heme b№2	
	SD	ϵ	SD	ϵ	SD	ϵ
pH6, oxidative direction	9	8	11	7	27	17
pH6, reductive direction	4	32	11	95	6	51
pH6, KCN, oxidative direction	6	51	6	10	4	6
pH7, oxidative direction	6	5	41	35	53	45
pH7, reductive direction	n. d.		14	8	25	40
pH7, AurD x 30, oxidative direction	3	6	8	20	12	19
pH9.5, oxidative direction	29	260	1	13	1	13
pH6, without heme d, oxidative direction	absent		13	114	23	210

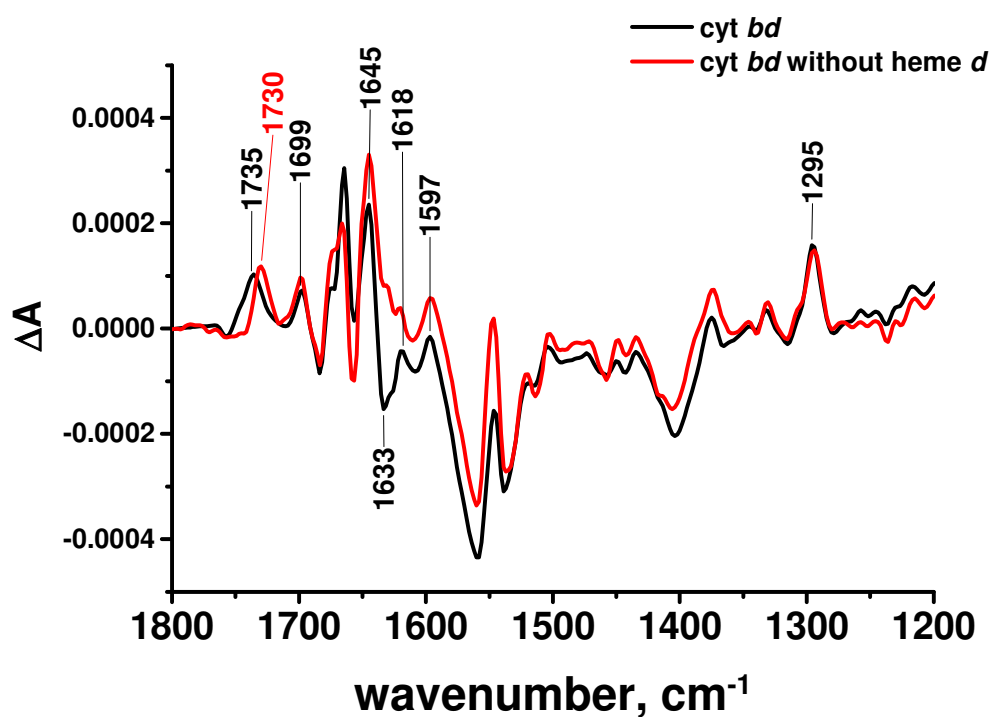
A4. Raman spectra of cyt bd from *G. thermodenitrificans* and *E. coli*, and background (DDM). Comparison of various batches (A, B, C) of cyt bd from *G. thermodenitrificans* with different DDM content. Influence of the heme d (batch E), pH9.5 (batch D), KCN (batch C) and washing (batch B) on RR spectra is shown. Unless otherwise stated, the conditions are pH6, unwashed sample, *G. thermodenitrificans*.



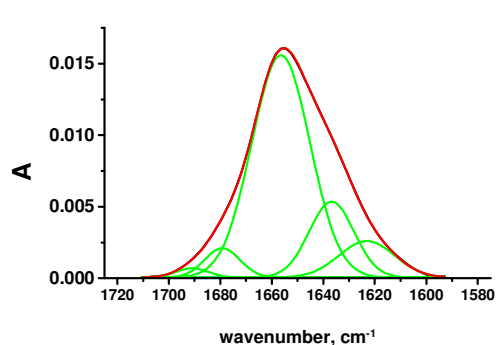
A5. Voltammograms of the cyt *bd* from *G. thermodenitrificans* and corresponding difference FTIR spectra (the batch with decreased MQ content).



A6. Ox-red differential FTIR spectrum of cyt *bd* from *G. thermodenitrificans* devoid of heme *d*.



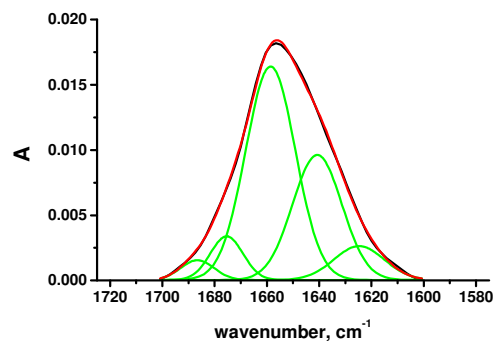
A7. Deconvolution of amide I of cyt bd from *G. thermodenitrificans* at pH7 and pH9.5 and 5° and 45°C. Spectra were obtained in D₂O, 30 spectra were averaged. Smoothing of amide I were conducted with FTT 3 pts filter. The deconvolution with Gaussian function provided the fit with $R^2=0.9995$.



Fitting Results

Peak	Peak Type	Area Intg	FWHM	Max Height	Center Grvty	Area IntgP
1.	Gaussian	0.06826	25.29318	0.00254	1623.11007	10.20507
2.	Gaussian	0.11558	20.53219	0.00529	1636.77999	17.28053
3.	Gaussian	0.44	26.63605	0.01552	1656.47102	65.78531
4.	Gaussian	0.03502	16.11944	0.00204	1679.23948	5.23525
5.	Gaussian	0.00999	14.68799	6.4E-4	1690.93125	1.49384

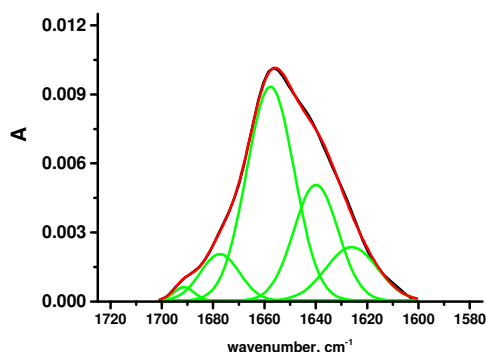
pH7, 5°C



Fitting Results

Peak	Peak Type	Area Intg	FWHM	Max Height	Center Grvty	Area IntgP
1.	Gaussian	0.06222	22.64351	0.0026	1624.7305	8.24328
2.	Gaussian	0.38986	22.39028	0.01636	1658.56995	51.64728
3.	Gaussian	0.02391	15.01208	0.00152	1686.58479	3.16784
4.	Gaussian	0.2265	22.20668	0.00958	1640.69711	30.00627
5.	Gaussian	0.05235	14.69884	0.00335	1675.38076	6.93534

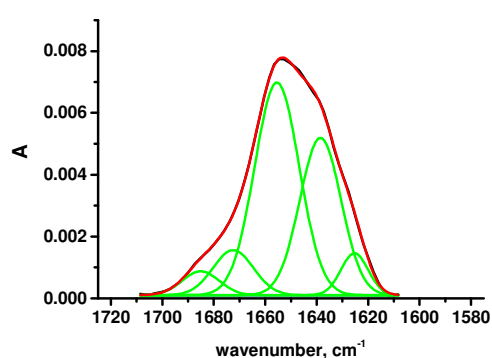
pH7, 45°C



Fitting Results

Peak	Peak Type	Area Intg	FWHM	Max Height	Center Grvty	Area IntgP
1.	Gaussian	0.05837	23.67898	0.00233	1625.99319	13.61708
2.	Gaussian	0.00585	9.39824	5.9E-4	1691.38459	1.36444
3.	Gaussian	0.10935	20.40221	0.00504	1639.91213	25.51165
4.	Gaussian	0.21642	21.86496	0.0093	1657.63351	50.49
5.	Gaussian	0.03865	17.93729	0.00203	1677.35327	9.01683

pH9.5, 5°C

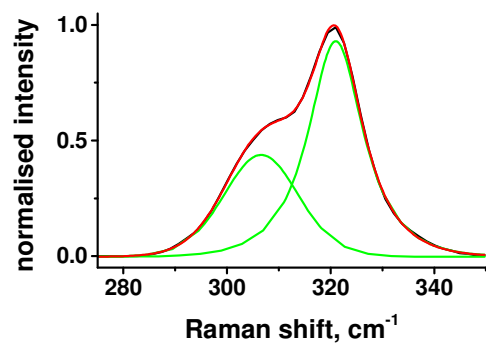


Fitting Results

Peak	Peak Type	Area Intg	FWHM	Max Height	Center Grvty	Area IntgP
1.	Gaussian	0.01394	16.93774	7.7E-4	1685.08843	4.46115
2.	Gaussian	0.02872	18.50572	0.00146	1672.44527	9.18886
3.	Gaussian	0.14937	20.4022	0.00688	1655.44113	47.79674
4.	Gaussian	0.10253	18.92403	0.00509	1638.5422	32.80747
5.	Gaussian	0.01796	12.44719	0.00136	1625.27266	5.74578

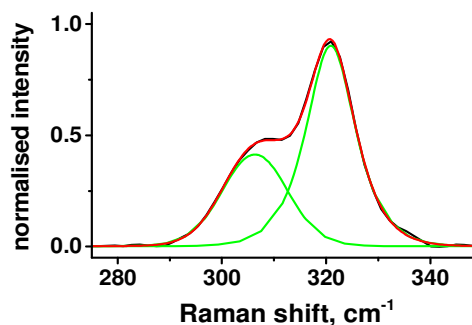
pH9.5, 45°C

A8. Deconvolution of the major band (307-321 cm^{-1}) of the resonance Raman spectra of mitoNEET.



Fitting Results

Peak	Peak Type	Area Intg	FWHM	Max Height	Center Grvty	Area IntgP
1. 307	GaussLoren	8.12551	269.97978	0.44054	-289.63843	36.22053
2. 321	GaussLoren	14.30793	92.53099	0.93246	-289.64151	63.77947

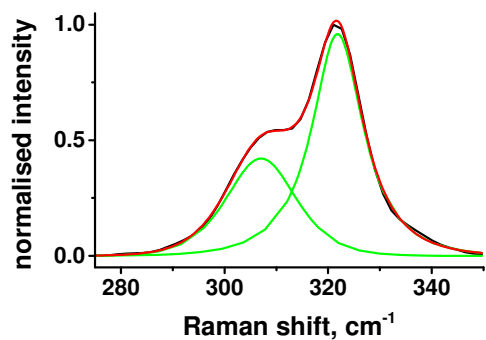


Fitting Results

Peak	Peak Type	Area Intg	FWHM	Max Height	Center Grvty	Area IntgP
1.	GaussLorenz	6.4857	251.58982	0.41102	-289.63731	35.63116
2.	GaussLorenz	11.71663	173.11109	0.89987	-289.63849	64.36884

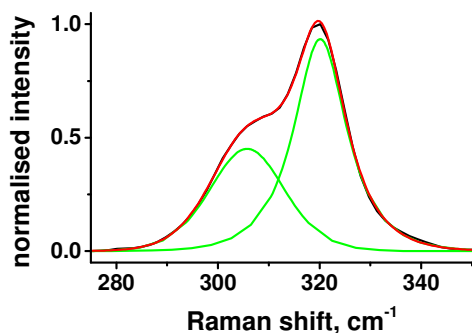
mitoNEET + rsv3S

mitoNEET + pio + DMSO



Fitting Results

Peak	Peak Type	Area Intg	FWHM	Max Height	Center Grvty	Area IntgP
1. 307	GaussLoren	7.48086	226.43507	0.42076	-289.63923	34.41047
2. 322	GaussLoren	14.25922	17.43033	0.95918	-289.64287	65.58953



Fitting Results

Peak	Peak Type	Area Intg	FWHM	Max Height	Center Grvty	Area IntgP
1. 306	GaussLoren	14.05061	93.43927	0.93416	-289.64123	62.12439
2. 320	GaussLoren	8.56629	259.33043	0.45048	-289.63884	37.87561

mitoNEET + DMSO

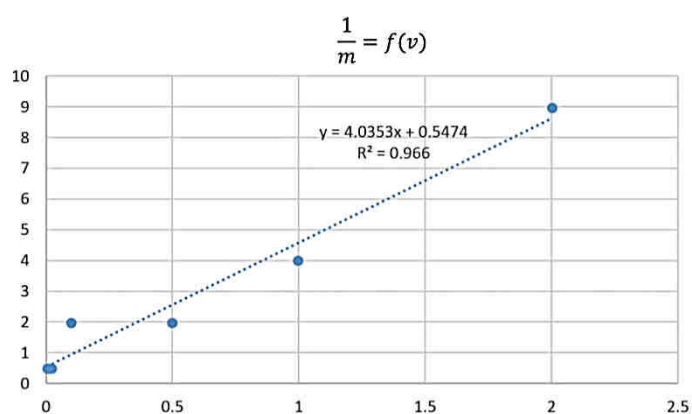
mitoNEET

A9. Example of Laviron method calculation of electron transfer constant.

Attribution of the peak separation to $1/m$ value (for $\alpha = 0.5$):

Potential sweeping rate (v), V/s	E_c , mV	E_a , mV	Peak separation ($E_c - E_a$), mV	$1/m$, V/s
0.005	-283	-272	11	0.5
0.01	-291	-287	4	0.5
0.02	-293	-287	6	0.5
0.1	-323	-261	62	2
0.5	-324	-255	69	2
1.0	-344	-241	103	4
2.0	-372	-204	168	9

Plot for the $1/m$ dependency on the velocity of the potential sweep v :



The plot was fitted with the equation:

$$\frac{1}{m} = 4.03 * v + 0.55$$

The slope of the fitted curve allows us to determine constant of electron transfer k_{ET} :

$$4.03 = \frac{Fn}{RTk_{ET}}$$

For one electron $n=1$:

$$k_{ET} = \frac{96485}{4.04 * 8.31 * 293.15} = 9.8 \text{ s}^{-1}$$

A10. Deduction of modified Nernst equation.

- 1) The Nernst equation relates the redox potential to the activities of the Red and Ox forms of the electroactive species. The approximation allows us to substitute activities with concentrations (for reaction: $O + n \bar{e} = R$):

$$E = E^0 + \frac{RT}{nF} * \ln\left(\frac{a_{ox}}{a_{red}}\right) \approx E^0 + \frac{RT}{nF} * \ln\left(\frac{[O]}{[R]}\right)$$

- 2) To obtain the concentration values from absorption the Beer-Lambert-Buger law is used. For fully reduced/oxidised solution we have:

$$A_{red} = \varepsilon_{red} * l * C$$

$$A_{ox} = \varepsilon_{ox} * l * C$$

where C is total concentration and for partly reduced/oxidised solution can be noted as:

$$C = [O] + [R]$$

Total absorption for partly reduced/oxidised system is:

$$A = \varepsilon_{ox} * l * [O] + \varepsilon_{red} * l * [R]$$

- 3) The measured differential absorption can be expressed through total absorptions of reduced/oxidised form and total absorption of partly reduced/oxidised system:

$$\Delta A = A - A_{red} \Rightarrow A_{ox} - A = A_{ox} - A_{red} - \Delta A$$

- 4) This leads to possibly to express concentration of Ox-form and Red-form through total absorption A:

- for Ox-form:

$$\begin{aligned} A &= \varepsilon_{ox} * l * [O] + \varepsilon_{red} * l * (C - [O]) = \varepsilon_{red} * l * C + l * [O] * (\varepsilon_{ox} - \varepsilon_{red}) \\ &= A_{red} + l * [O] * (\varepsilon_{ox} - \varepsilon_{red}) \\ [O] &= \frac{A - A_{red}}{l * (\varepsilon_{ox} - \varepsilon_{red})} \end{aligned}$$

- for Red-form:

$$\begin{aligned} A &= \varepsilon_{ox} * l * (C - [R]) + \varepsilon_{red} * l * [R] = \varepsilon_{ox} * l * C + l * [R] * (\varepsilon_{red} - \varepsilon_{ox}) \\ &= A_{ox} + l * [R] * (\varepsilon_{red} - \varepsilon_{ox}) \\ [R] &= \frac{A - A_{ox}}{l * (\varepsilon_{red} - \varepsilon_{ox})} = \frac{A_{ox} - A}{l * (\varepsilon_{ox} - \varepsilon_{red})} \end{aligned}$$

- 5) From now on we can use the ratio of Ox and Red form concentrations for Nernst equation:

$$\frac{[O]}{[R]} = \frac{A - A_{red}}{A_{ox} - A} = \frac{\Delta A}{A_{ox} - A_{red} - \Delta A}$$

$$E = E^0 + \left(\frac{RT}{nF}\right) \ln \left(\frac{\Delta A}{A_{ox} - A_{red} - \Delta A} \right)$$

$$\frac{\Delta A}{A_{ox} - A_{red} - \Delta A} = \exp \left[\left(\frac{nF}{RT} \right) * (E - E^0) \right]$$

And finally, the observed differential absorption show the dependency on the applied potential as follows:

$$\Delta A = \frac{A_{ox} - A_{red}}{\exp \left[\left(-\frac{nF}{RT} \right) * (E - E^0) + 1 \right]}$$

The fitting in the Origin Lab Pro 9.5 was conducted through non-sigmoidal user defined peak-functions with the code:

$$y = y_0 + \frac{A_1}{\exp \left[\left(-\frac{nF}{1000RT} \right) * (x - E_1) + 1 \right]}$$

where

- n – quantity of electrons for transition, can be varied from 0.8 till 1.1 for the experiment devoid kinetical issues /slope of the transition/half-height width/
- R=8.31 – universal gas constant, J·mol⁻¹·K⁻¹ /constant/
- F= 96485.33 – Faraday constant, C mol⁻¹ /constant/
- T – temperature of the experiment, K /constant/
- A₁ – maximal differential absorption/amplitude/
- x – applied potential, mV /x/
- E₁ – mid-point potential, mV /centre of the transition/
- y₀ – /baseline/

The coefficient “1000” is added in order to obtain the potential values in mV. For the several transitions the additional component should be added: y=y₀+component 1+...+component N.

References

1. Melin, F. & Hellwig, P. Recent advances in the electrochemistry and spectroelectrochemistry of membrane proteins. *Biol. Chem.* **394**, 593–609 (2013).
2. Skulachev, V. P., Bogachev, A. V. & Kasparinsky, F. O. *Principles of bioenergetics*. (Springer-Verlag Berlin Heidelberg, 2013-).
3. Sousa, F. L. *et al.* The superfamily of heme–copper oxygen reductases: Types and evolutionary considerations. *Biochim. Biophys. Acta - Bioenerg.* **1817**, 629–637 (2012).
4. Borisov, V. B., Gennis, R. B., Hemp, J. & Verkhovsky, M. I. The cytochrome *bd* respiratory oxygen reductases. *Biochim. Biophys. Acta - Bioenerg.* **1807**, 1398–1413 (2011).
5. Safarian, S. *et al.* Structure of a *bd* oxidase indicates similar mechanisms for membrane-integrated oxygen reductases. *Science*. **352**, 583–586 (2016).
6. Arutyunyan, A. M., Sakamoto, J., Inadome, M., Kabashima, Y. & Borisov, V. B. Optical and magneto-optical activity of cytochrome *bd* from *Geobacillus thermodenitrificans*. *Biochim. Biophys. Acta - Bioenerg.* **1817**, 2087–2094 (2012).
7. Melin, F. *et al.* Direct electrochemistry of cytochrome *bo*₃ oxidase at a series of gold nanoparticles-modified electrodes. *Electrochem. commun.* **26**, 105–108 (2013).
8. Frens, G. Controlled Nucleation for the Regulation of the Particle Size in Monodisperse Gold Suspensions. *Nat. Phys. Sci.* **241**, 20–22 (1973).
9. Meunier, B., Madgwick, S. A., Reil, E., Oettmeier, W. & Rich, P. R. New Inhibitors of the Quinol Oxidation Sites of Bacterial Cytochromes *bo* and *bd*. *Biochemistry* **34**, 1076–1083 (1995).
10. Li, X. W. *et al.* Synthesis and biological activities of the respirator chain inhibitor aurachin D and new ring versus chain analogues. *Beilstein J. Org. Chem.* **9**, 1551–1558 (2013).
11. Moss, D., Navedryk, E., Breton, J. & Mäntele, W. Redox-linked conformational changes in proteins detected by a combination of infrared spectroscopy and protein electrochemistry. Evaluation of the technique with cytochrome *c*. *Eur. J. Biochem.* **187**, 565–572 (1990).
12. Jünemann, S. Cytochrome *bd* terminal oxidase. *Biochim. Biophys. Acta - Bioenerg.* **1321**, 107–127 (1997).
13. Arutyunyan, A. M. *et al.* Strong excitonic interactions in the oxygen-reducing site of *bd*-type oxidase: The Fe-to-Fe distance between hemes *d* and *b*₅₉₅ is 10 Å. *Biochemistry* **47**, 1752–1759 (2008).
14. Ceccaldi, P. *et al.* Reductive activation of *E. coli* respiratory nitrate reductase. *Biochim. Biophys. Acta - Bioenerg.* **1847**, 1055–1063 (2015).
15. Bak, D. W. & Elliott, S. J. Conserved hydrogen bonding networks of mitoNEET tune Fe-S cluster binding and structural stability. *Biochemistry* **52**, 4687–4696 (2013).
16. Geldenhuys, W. J., Funk, M. O., Barnes, K. F. & Carroll, R. T. Structure-based design of a thiazolidinedione which targets the mitochondrial protein mitoNEET. *Bioorganic Med. Chem. Lett.* **20**, 819–823 (2010).
17. Forte, E., Borisov, V. B., Vicente, J. B. & Giuffrè, A. Cytochrome *bd* and Gaseous Ligands in Bacterial Physiology. *Adv. Microb. Physiol.* **71**, 171–234 (2017).
18. Zhang, J. *et al.* Site-directed mutation of the highly conserved region near the Q-loop of the cytochrome *bd* quinol oxidase from *Escherichia coli* specifically perturbs heme *b*₅₉₅. *Biochemistry* **40**, 8548–8556 (2001).

19. Yang, K. *et al.* Glutamate 107 in subunit I of the cytochrome *bd* quinol oxidase from *Escherichia coli* is protonated and near the heme *d*/heme *b*₅₉₅ binuclear center. *Biochemistry* **46**, 3270–3278 (2007).
20. Sakamoto, J. *et al.* Gene structure and quinol oxidase activity of a cytochrome *bd*-type oxidase from *Bacillus stearothermophilus*. *Biochim. Biophys. Acta - Bioenerg.* **1411**, 147–158 (1999).
21. Hards, K. & Cook, G. M. Targeting bacterial energetics to produce new antimicrobials. *Drug Resist. Updat.* **36**, 1–12 (2018).
22. Paddock, M. L. *et al.* MitoNEET is a uniquely folded 2Fe–2S outer mitochondrial membrane protein stabilized by pioglitazone. *Proc. Natl. Acad. Sci.* **104**, 14342–14347 (2007).
23. Lipper, C. H. *et al.* Cancer-related NEET proteins transfer 2Fe-2S clusters to anamorsin, a protein required for cytosolic iron-sulfur cluster biogenesis. *PLoS One* **10**, 1–15 (2015).
24. Kusminski, C. M. *et al.* MitoNEET-Parkin Effects in Pancreatic α - and β -Cells , Cellular Survival , and Intrinsular Cross Talk. *Diabetes* **65**, 1534–1555 (2016)..
25. Golinelli-Cohen, M. P. *et al.* Redox control of the human iron-sulfur repair protein MitoNEET activity via its iron-sulfur cluster. *J. Biol. Chem.* **291**, 7583–7593 (2016).
26. Mons, C. *et al.* The H₂O₂ -Resistant Fe–S Redox Switch MitoNEET Acts as a pH Sensor To Repair Stress-Damaged Fe–S Protein. *Biochemistry* acs.biochem.8b00777 (2018).
27. Lehninger, J. *Principles of biochemistry* (4th ed.): Nelson, D., and Cox, M. *Biochem. Mol. Biol. Educ.* **33**, 74–75 (2005).
28. Rich, P. R. & Maréchal, A. The mitochondrial respiratory chain. *Essays Biochem.* **47**, 1–23 (2010).
29. Takusagawa. Lecture notes. Chapter 17 : Electron Transport and Oxidative Phosphorylation. pp. 1–29, www.coursehero.com
30. Sharma, P., Teixeira De Mattos, M. J., Hellingwerf, K. J. & Bekker, M. On the function of the various quinone species in *Escherichia coli*. *FEBS J.* **279**, 3364–3373 (2012).
31. Harris, R. & Boekema, E. Membrane protein complexes: structure and function. *Springer Nature* **87**, (2018).
32. Guo, R., Gu, J., Zong, S., Wu, M. & Yang, M. Structure and mechanism of mitochondrial electron transport chain. *Biomed. J.* **41**, 9–20 (2018).
33. Nomenclature Committee of the International Union of Biochemistry (NC-IUB). Nomenclature of Electron-Transfer Proteins. www.sbcs.qmul.ac.uk/iubmb
34. Kadish, K. M., Smith, K. M. & Guillard, R. *Handbook of Porphyrin Science with applications to chemistry, physics, materials science, engineering, biology and medicine: NMR and EPR Techniques.* (World Scientific Publishing Co. Pte. Ltd., 2010).
35. Site, O. *et al.* pH Dependence of Proton Translocation in the Oxidative and Reductive Phases of the Catalytic Cycle of Cytochrome *c* Oxidase. The role of H₂O produced at the oxygen-reduction site. *Biochemistry*. **45**, 1930–1937 (2006).
36. Lorence, R. M., Miller, M. J., Borochoy, A., Faiman-Weinberg, R. & Gennis, R. B. Effects of pH and detergent on the kinetic and electrochemical properties of the purified cytochrome *d* terminal oxidase complex of *Escherichia coli*. *Biochim. Biophys. Acta* **790**, 148–153 (1984).
37. Kita, K., Konishi, K. & Anraku, Y. Terminal Oxidases of *Escherichia coli* Aerobic Respiratory Chain. *J. Biol. Chem.* **259**, 3368–3374 (1984).
38. Koch, H.-G. & Schneider, D. Folding, assembly, and stability of transmembrane cytochromes. *Curr. Chem. Biol.* **1**, 59–74 (2007).

39. King, Z. a. *et al.* The respiratory chains of *Escherichia coli*. *Microbiol. Rev.* **6**, 748–766 (1984).
40. Sarewicz, M. & Osyczka, A. Electronic Connection Between the Quinone and Cytochrome *c* Redox Pools and Its Role in Regulation of Mitochondrial Electron Transport and Redox Signaling. *Physiol. Rev.* **95**, 219–243 (2015).
41. Unden, G. & Bongaerts, J. Alternative respiratory pathways of *Escherichia coli*: Energetics and transcriptional regulation in response to electron acceptors. *Biochim. Biophys. Acta - Bioenerg.* **1320**, 217–234 (1997).
42. Cook, G. M., Greening, C., Hards, K. & Berney, M. Energetics of Pathogenic Bacteria and Opportunities for Drug Development. *Advances in Microbial Physiology* **65**, 1-62 (2014).
43. Chen, Y.-R. & Zweier, J. L. Cardiac Mitochondria and Reactive Oxygen Species Generation. *Circ. Res.* **114**, 524–537 (2014).
44. Fujimoto, N., Kosaka, T. & Yam, M. Menaquinone as Well as Ubiquinone as a Crucial Component in the *Escherichia coli* Respiratory Chain. *Chem. Biol.* **1**, 187-208 (2012).
45. Marchal, D., Boireau, W., Laval, J. M., Moiroux, J. & Bourdillon, C. An electrochemical approach of the redox behavior of water insoluble ubiquinones or plastoquinones incorporated in supported phospholipid layers. *Biophys. J.* **72**, 2679–2687 (1997).
46. Wagner, G. C., Kassner, R. J. & Kamen, M. D. Redox potentials of certain vitamins K: implications for a role in sulfite reduction by obligately anaerobic bacteria. *Proc. Natl. Acad. Sci. U. S. A.* **71**, 253–6 (1974).
47. Mulikdjanian, A. Y. Ubiquinol oxidation in the cytochrome *bc_L* complex: Reaction mechanism and prevention of short-circuiting. *Biochim. Biophys. Acta - Bioenerg.* **1709**, 5–34 (2005).
48. Tran, Q. M., Rothery, R. A., Maklashina, E., Cecchini, G. & Weiner, J. H. The quinone binding site in *Escherichia coli* succinate dehydrogenase is required for electron transfer to the heme b. *J. Biol. Chem.* **281**, 32310–32317 (2006).
49. Weiss, S. A. *et al.* Characterization of cytochrome *bo₃* activity in a native-like surface-tethered membrane. *Biochem. J.* **417**, 555–60 (2009).
50. Ferguson-Miller, S. & Babcock, G. T. Heme/Copper Terminal Oxidases. *Chem. Rev.* **96**, 2889–2908 (1996).
51. Shiba, T. *et al.* Structure of the trypanosome cyanide-insensitive alternative oxidase. *Proc. Natl. Acad. Sci.* **110**, 4580–4585 (2013).
52. Albury, M. S., Elliott, C. & Moore, A. L. Ubiquinol-binding site in the alternative oxidase: Mutagenesis reveals features important for substrate binding and inhibition. *Biochim. Biophys. Acta - Bioenerg.* **1797**, 1933–1939 (2010).
53. Maréchal, A., Kido, Y., Kita, K., Moore, A. L. & Rich, P. R. Three redox states of *Trypanosoma brucei* alternative oxidase identified by infrared spectroscopy and electrochemistry. *J. Biol. Chem.* **284**, 31827–31833 (2009).
54. Hoeser, J., Hong, S., Gehmann, G., Gennis, R. B. & Friedrich, T. Subunit CydX of *Escherichia coli* cytochrome *bd* ubiquinol oxidase is essential for assembly and stability of the di-heme active site. *FEBS Lett.* **588**, 1537–1541 (2014).
55. Sun, Y.-H. *et al.* The small protein CydX is required for function of cytochrome *bd* oxidase in *Brucella abortus*. *Front. Cell. Infect. Microbiol.* **2**, 1–15 (2012).
56. Iwata, S., Ostermeier, C., Ludwig, B. & Michel, H. Structure at 2.8 Å resolution of cytochrome *c* oxidase from *Paracoccus denitrificans*. *Nature* **376**, 660–669 (1995).

57. Varanasi, L. *et al.* Altering conserved lipid binding sites in cytochrome *c* oxidase of *Rhodobacter sphaeroides* perturbs the interaction between subunits I and III and promotes suicide inactivation of the enzyme. *Biochemistry* **45**, 14896–14907 (2006).
58. Qin, L., Hiser, C., Mulichak, A., Garavito, R. M. & Ferguson-Miller, S. Identification of conserved lipid/detergent-binding sites in a high-resolution structure of the membrane protein cytochrome *c* oxidase. *Proc. Natl. Acad. Sci. U. S. A.* **103**, 16117–22 (2006).
59. Qin, L., Sharpe, M. A., Garavito, R. M. & Ferguson-Miller, S. Conserved lipid-binding sites in membrane proteins: a focus on cytochrome *c* oxidase. *Curr. Opin. Struct. Biol.* **17**, 444–450 (2007).
60. Yap, L. L. *et al.* The quinone-binding sites of the cytochrome *bo*₃ ubiquinol oxidase from *Escherichia coli*. *Biochim. Biophys. Acta - Bioenerg.* **1797**, 1924–1932 (2010).
61. Abramson, J. *et al.* The structure of the ubiquinol oxidase from *Escherichia coli* and its ubiquinone binding site. *Nat. Struct. Mol. Biol.* **7**, 910 (2000).
62. Choi, S. K., Lin, M. T., Ouyang, H. & Gennis, R. B. Searching for the low affinity ubiquinone binding site in cytochrome *bo*₃ from *Escherichia coli*. *Biochim. Biophys. Acta - Bioenerg.* **1858**, 366–370 (2017).
63. Noor, M. R. & Soulimane, T. Structure of *caa*₃ cytochrome *c* oxidase - A nature-made enzyme-substrate complex. *Biol. Chem.* **394**, 579–591 (2013).
64. Lyons, J. *et al.* Structural insights into electron transfer in *caa*₃-type cytochrome oxidase. *Nature Letters* **487**, 514–518 (2012).
65. Yoshikawa, S. & Shimada, A. Reaction mechanism of cytochrome *c* oxidase. *Chem. Rev.* **115**, 1936–1989 (2015).
66. Yoshikawa, S. *et al.* Redox-coupled crystal structural changes in bovine heart cytochrome *c* oxidase. *Science*. **280**, 1723–1729 (1998).
67. Richter, O. M. H. & Ludwig, B. Electron transfer and energy transduction in the terminal part of the respiratory chain - Lessons from bacterial model systems. *Biochim. Biophys. Acta - Bioenerg.* **1787**, 626–634 (2009).
68. Tiefenbrunn, T. *et al.* High resolution structure of the *ba*₃ cytochrome *c* oxidase from *Thermus thermophilus* in a lipidic environment. *PLoS One* **6**, 1–11 (2011).
69. Soulimane, T., Than, M. E., Dewor, M., Huber, R. & Buse, G. Primary structure of a novel subunit in *ba*₃-cytochrome oxidase from *Thermus thermophilus*. *Protein Sci.* **9**, 2068–73 (2000).
70. Soulimane, T. Structure and mechanism of the aberrant *ba*₃-cytochrome *c* oxidase from *Thermus thermophilus*. *EMBO J.* **19**, 1766–1776 (2000).
71. Kohlstaedt, M. *et al.* Identification and Characterization of the Novel Subunit CcoM in the *cbb*₃ -Cytochrome *c* Oxidase from *Pseudomonas stutzeri* ZoBell. *MBio* **7**, 1–9 (2016).
72. Hino, T., Nagano, S., Sugimoto, H., Tosha, T. & Shiro, Y. Molecular structure and function of bacterial nitric oxide reductase. *Biochim. Biophys. Acta - Bioenerg.* **1817**, 680–687 (2012).
73. Flock, U., Lachmann, P., Reimann, J., Watmough, N. J. & Ädelroth, P. Exploring the terminal region of the proton pathway in the bacterial nitric oxide reductase. *J. Inorg. Biochem.* **103**, 845–850 (2009).
74. Hellwig, P., Soulimane, T., Buse, G. & Mäntele, W. Electrochemical, FTIR, and UV/VIS spectroscopic properties of the *ba*₃ oxidase from *Thermus thermophilus*. *Biochemistry* **38**, 9648–9658 (1999).

75. Von Ballmoos, C., Ädelroth, P., Gennis, R. B. & Brzezinski, P. Proton transfer in *ba₃* cytochrome *c* oxidase from *Thermus thermophilus*. *Biochim. Biophys. Acta - Bioenerg.* **1817**, 650–657 (2012).
76. Veríssimo, A. F. *et al.* A *ba₃* oxygen reductase from the thermohalophilic bacterium *Rhodothermus marinus*. *FEMS Microbiol. Lett.* **269**, 41–47 (2007).
77. Muresanu, L. *et al.* The Electron Transfer Complex between Cytochrome *c₅₅₂* and the *Cu_A* Domain of the *Thermus thermophilus ba₃* Oxidase. **281**, 14503–14513 (2006).
78. Pitcher, R. S. & Watmough, N. J. The bacterial cytochrome *cbb₃* oxidases. *Biochim. Biophys. Acta - Bioenerg.* **1655**, 388–399 (2004).
79. Buschmann, S. *et al.* The Structure of *cbb₃* Cytochrome Oxidase Provides Insights into Proton Pumping. *Science*. **329**, 327–330 (2010).
80. Shiro, Y. Structure and function of bacterial nitric oxide reductases: Nitric oxide reductase, anaerobic enzymes. *Biochim. Biophys. Acta - Bioenerg.* **1817**, 1907–1913 (2012).
81. Rice, C. W. & Hempfling, W. P. Oxygen-limited continuous culture and respiratory energy conservation in *Escherichia coli*. *J. Bacteriol.* **134**, 115–24 (1978).
82. Morris, R. L. & Schmidt, T. M. Shallow breathing: Bacterial life at low O₂. *Nat. Rev. Microbiol.* **11**, 205–212 (2013).
83. Preisig, O., Zufferey, R., Thony-Meyer, L., Appleby, C. & Hennecke, H. A high-affinity *cbb₃*-type cytochrome oxidase terminates the symbiosis- specific respiratory chain of *Bradyrhizobium japonicum*. *J. Bacteriol.* **178**, 1532–1538 (1996).
84. De Gier, J. W. L. *et al.* Structural and functional analysis of *aa₃*-type and *cbb₃*-type cytochrome *c* oxidases of *Paracoccus denitrificans* reveals significant differences in proton-pump design. *Mol. Microbiol.* **20**, 1247–1260 (1996).
85. Chen, H., Luo, Q., Yin, J., Gao, T. & Gao, H. Evidence for the requirement of CydX in function but not assembly of the cytochrome *bd* oxidase in *Shewanella oneidensis*. *Biochim. Biophys. Acta - Gen. Subj.* **1850**, 318–328 (2015).
86. Vanorsdel, C. E. *et al.* The escherichia coli CydX protein is a member of the CydAB cytochrome *bd* oxidase complex and is required for cytochrome *bd* oxidase activity. *J. Bacteriol.* **195**, 3640–3650 (2013).
87. Ransac, S. & Mazat, J.-P. Mechanism of complex II. *19ème Congrès du Groupe Français Bioénergétique, Lacanau, 20-24 Sept. 2017* p. 112 (2017).
88. Zhang, J., Hellwig, P., Osborne, J. P. & Gennis, R. B. Arginine 391 in subunit I of the cytochrome *bd* quinol oxidase from *Escherichia coli* stabilizes the reduced form of the hemes and is essential for quinol oxidase activity. *J. Biol. Chem.* **279**, 53980–53987 (2004).
89. Osborne, J. P. & Gennis, R. B. Sequence analysis of cytochrome *bd* oxidase suggests a revised topology for subunit I. *Biochim. Biophys. Acta - Bioenerg.* **1410**, 32–50 (1999).
90. Mogi, T. *et al.* Probing the ubiquinol-binding site in cytochrome *bd* by site-directed mutagenesis. *Biochemistry* **45**, 7924–7930 (2006).
91. Matsumoto, Y. *et al.* Mass spectrometric analysis of the ubiquinol-binding site in cytochrome *bd* from *Escherichia coli*. *J. Biol. Chem.* **281**, 1905–1912 (2006).
92. Hastings, S. F. *et al.* Identification of a stable semiquinone intermediate in the purified and membrane bound ubiquinol oxidase-cytochrome *bd* from *Escherichia coli*. **323**, 0–6 (1998)

93. Jünemann, S. & Wrigglesworth, J. M. Antimycin inhibition of the cytochrome *bd* complex from *Azotobacter vinelandii* indicates the presence of a branched electron transfer pathway for the oxidation of ubiquinol. *FEBS Lett.* **345**, 198–202 (1994).
94. Matsumoto, Y. *et al.* Kinetic mechanism of quinol oxidation by cytochrome *bd* studied with ubiquinone-2 analogs. *J. Biochem.* **139**, 779–788 (2006).
95. Mogi, T. & Miyoshi, H. Properties of cytochrome *bd* plastoquinol oxidase from the cyanobacterium *Synechocystis* sp. PCC 6803. *J. Biochem.* **145**, 395–401 (2009).
96. Popović, D. M. & Stuchebrukhov, A. a. Electrostatic study of the proton pumping mechanism in bovine heart cytochrome *c* oxidase. *J. Am. Chem. Soc.* **126**, 1858–71 (2004).
97. Nyquist, R. M., Heitbrink, D., Bolwien, C., Gennis, R. B. & Heberle, J. Direct observation of protonation reactions during the catalytic cycle of cytochrome *c* oxidase. *Proc. Natl. Acad. Sci. U. S. A.* **100**, 8715–8720 (2003).
98. Wikström, M. & Verkhovsky, M. I. Towards the mechanism of proton pumping by the haem-copper oxidases. *Biochim. Biophys. Acta - Bioenerg.* **1757**, 1047–1051 (2006).
99. Verkhovsky, M. I., Belevich, I., Bloch, D. A. & Wikström, M. Elementary steps of proton translocation in the catalytic cycle of cytochrome oxidase. *Biochim. Biophys. Acta - Bioenerg.* **1757**, 401–407 (2006).
100. Konstantinov, A. A. Cytochrome *c* oxidase: Intermediates of the catalytic cycle and their energy-coupled interconversion. *FEBS Lett.* **586**, 630–639 (2012).
101. Siletsky, S. A. & Konstantinov, A. A. Cytochrome *c* oxidase: Charge translocation coupled to single-electron partial steps of the catalytic cycle. *Biochim. Biophys. Acta - Bioenerg.* **1817**, 476–488 (2012).
102. Sharma, V., Enkavi, G., Vattulainen, I., Róg, T. & Wikström, M. Proton-coupled electron transfer and the role of water molecules in proton pumping by cytochrome *c* oxidase. *Proc. Natl. Acad. Sci.* **112**, 2040–2045 (2015).
103. Brändén, G., Gennis, R. B. & Brzezinski, P. Transmembrane proton translocation by cytochrome *c* oxidase. *Biochim. Biophys. Acta - Bioenerg.* **1757**, 1052–1063 (2006).
104. Paulus, A., Werner, C., Ludwig, B. & De Vries, S. The cytochrome *ba₃* oxidase from *Thermus thermophilus* does not generate a tryptophan radical during turnover: Implications for the mechanism of proton pumping. *Biochim. Biophys. Acta - Bioenerg.* **1847**, 1093–1100 (2015).
105. Lee, H. J., Gennis, R. B. & Adeloeth, P. Entrance of the proton pathway in *cbb₃*-type heme-copper oxidases. *Proc. Natl. Acad. Sci.* **108**, 17661–17666 (2011).
106. Borisov, V. B., Forte, E., Sarti, P. & Giuffrè, A. Catalytic intermediates of cytochrome *bd* terminal oxidase at steady-state: ferryl and oxy-ferrous species dominate. *Biochim. Biophys. Acta - Bioenerg.* **1807**, 503–509 (2011).
107. Jasaitis, A. *et al.* Electrogenic reactions of cytochrome *bd*. *Biochemistry* **39**, 13800–13809 (2000).
108. Giuffrè, A., Borisov, V. B., Arese, M., Sarti, P. & Forte, E. Cytochrome *bd* oxidase and bacterial tolerance to oxidative and nitrosative stress. *Biochim. Biophys. Acta - Bioenerg.* **1837**, 1178–1187 (2014).
109. Lee, H. J., Reimann, J., Huang, Y. & Adeloeth, P. Functional proton transfer pathways in the heme-copper oxidase superfamily. *Biochim. Biophys. Acta - Bioenerg.* **1817**, 537–544 (2012).
110. Belevich, I., Borisov, V. B. & Verkhovsky, M. I. Discovery of the true peroxy intermediate in the catalytic cycle of terminal oxidases by real-time measurement. *J. Biol. Chem.* **282**, 28514–28519 (2007).

111. Borisov, V. B. & Verkhovsky, M. I. Oxygen as Acceptor. *EcoSal Plus* **6**, 1-32 (2015).
112. Al-Attar, S. *et al.* Cytochrome *bd* Displays Significant Quinol Peroxidase Activity. *Sci. Rep.* **6**, 1–12 (2016).
113. Forte, E. *et al.* The Terminal Oxidase Cytochrome *bd* Promotes Sulfide-resistant Bacterial Respiration and Growth. *Sci. Rep.* **6**, 1–8 (2016).
114. Voet, D., Voet, J. G. Rates of Enzymatic Reactions. *Biochemistry* 482–505 (2011).
115. Chang, R. Enzyme Kinetics. *Phys. Chem. Biosci.* 363–400 (2005).
116. Yang, X. *et al.* Classification of difference between inhibition constants of an inhibitor to facilitate identifying the inhibition type. *J. Enzyme Inhib. Med. Chem.* **28**, 205–213 (2013).
117. Hold, C. & Panke, S. Towards the engineering of *in vitro* systems. *J. R. Soc. Interface* **6**, S507–S521 (2009).
118. Sharma, R. *Enzyme inhibition and bioapplications. Enzyme Inhibition and Bioapplications* (InTech, 2012).
119. Copeland, R. *Enzymes: A Practical Introduction to Structure, Mechanism, and Data Analysis.* (Wiley-VCH, 2000)
120. Copeland, R. A. *Evaluation of Enzyme Inhibitors in Drug Discovery: A Guide for Medicinal Chemists and Pharmacologists.* (John Wiley & Sons, Inc., 2013).
121. Williams, J. W. & Morrison, J. F. *The Kinetics of Reversible Tight-Binding Inhibition. Methods in Enzymology* **63**, (1979).
122. Kuzmič, P. *et al.* High-throughput screening of enzyme inhibitors: Automatic determination of tight-binding inhibition constants. *Anal. Biochem.* **281**, 62–67 (2000).
123. Whiteley, C. Enzyme kinetics: partial and complete competitive inhibitor. *Biochem. edu.* **4412**, 144–146 (1997).
124. Brodbeck, U. *Enzyme Inhibitors* (Verlag Chemie: Proceedings of a Meeting held in Basel, 1980).
125. Yung-Chi, C. & Prusoff, W. H. Relationship between the inhibition constant (K_i) and the concentration of inhibitor which causes 50 per cent inhibition (I_{50}) of an enzymatic reaction. *Biochem. Pharmacol.* **22**, 3099–3108 (1973).
126. Kuzmic, P., Hill, C., Kirtley, M. P. & Janc, J. W. Kinetic determination of tight-binding impurities in enzyme inhibitors. *Anal. Biochem.* **319**, 272–279 (2003).
127. Cha, S. Tight-binding inhibitors-kinetic behavior. *Biochem. Pharmacol.* **24**, 2177–2185 (1975).
128. Kuzmic, P. *Why IC 50 's Are Bad for You And Other Surprises.* (BioKin, Ltd., 2004)
129. Dixon, M. The graphical determination of K_m and K_i . *Biochem. J.* **129**, 197–202 (1972).
130. Tsubaki, M., Hori, H., Mogi, T. & Anraku, Y. Cyanide-binding site of *bd*-type ubiquinol oxidase from *Escherichia coli*. *J. Biol. Chem.* **270**, 28565–28569 (1995).
131. Sun, J. *et al.* Resonance Raman Studies of *Escherichia coli* Cytochrome *bd* Oxidase. Selective Enhancement of the Three Heme Chromophores of the “As-Isolated” Enzyme and Characterization of the Cyanide Adduct. *Biochemistry* **34**, 12144–12151 (1995).
132. Jünemann, S., Wrigglesworth, J. M. & Rich, P. R. Effects of Decyl -aurachin D and Reversed Electron Transfer in Cytochrome *bd*. *Biochemistry* **36**, 9323–9331 (1997).

133. Kita, K. K. and Y. A. Terminal Oxidases of *Escherichia coli* Aerobic Respiratory Chain. *J. Biol. Chem.* **259**, 3368–3374 (1984).
134. Ben Best (1990) <https://www.benbest.com/nutrceut/CoEnzymeQ.html>.
135. Miyoshi, H., Takegami, K., Sakamoto, K., Mogi, T. & Iwamura, H. Characterization of the ubiquinol oxidation sites in cytochromes *bo* and *bd* from *Escherichia coli* using aurachin C analogues. *J. Biochem.* **125**, 138–142 (1999).
136. Huse, H. & Whiteley, M. 4-Quinolones: Smart phones of the microbial world. *Chem. Rev.* **111**, 152–159 (2011).
137. Heeb, S. *et al.* Quinolones: From antibiotics to autoinducers. *FEMS Microbiol. Rev.* **35**, 247–274 (2011).
138. Kroger, A. & Dadak, V. On the Role of Quinones in Bacterial Electron Transport The Respiratory System of *Bacillus megateriurn*. *Eur. J. Biochem* **11**, 328–340 (1969).
139. Wakai, S., Kikumoto, M., Kanao, T. & Kamimura, K. Involvement of Sulfide:Quinone Oxidoreductase in Sulfur Oxidation of an Acidophilic Iron-Oxidizing Bacterium, *Acidithiobacillus ferrooxidans* NASF-1. *Biosci. Biotechnol. Biochem.* **68**, 2519–2528 (2004).
140. Kim, M. S. & Kim, Y. J. Enzymatic properties of the membrane-bound NADH oxidase system in the aerobic respiratory chain of *Bacillus cereus*. *J. Biochem. Mol. Biol.* **37**, 753–756 (2004).
141. Kurokawa, T. & Sakamoto, J. Purification and characterization of succinate:menaquinone oxidoreductase from *Corynebacterium glutamicum*. *Arch. Microbiol.* **183**, 317–324 (2005).
142. Pistorius, D., Li, Y., Sandmann, A. & Müller, R. Completing the puzzle of aurachin biosynthesis in *Stigmatella aurantiaca* Sg a15. *Mol. Biosyst.* **7**, 3308 (2011).
143. Nakayama, Y., Hayashi, M., Yoshikawa, K., Mochida, K. & Unemoto, T. Inhibitor studies of a new antibiotic, korormicin, 2-n-heptyl-4-hydroxyquinoline N-oxide and Ag⁺ toward the Na⁺-translocating NADH-quinone reductase from the marine *Vibrio alginolyticus*. *Biol. Pharm. Bull.* **22**, 1064–7 (1999).
144. Hoefnagel, M. H. N. *et al.* New Inhibitors of the Ubiquinol Oxidase of Higher Plant Mitochondria. *Eur. J. Biochem.* **233**, 531–537 (1995).
145. Pessarakli, M. *Handbook of Photosynthesis*. (Boca Raton: CRC Press, 2005).
146. Shirude, P. S. *et al.* Quinolinylnyl pyrimidines: Potent inhibitors of NDH-2 as a novel class of anti-TB agents. *ACS Med. Chem. Lett.* **3**, 736–740 (2012).
147. Faxén, K., Salomonsson, L., Ädelroth, P. & Brzezinski, P. Inhibition of proton pumping by zinc ions during specific reaction steps in cytochrome c oxidase. *Biochim. Biophys. Acta - Bioenerg.* **1757**, 388–394 (2006).
148. Kuznetsova, S. S., Azarkina, N. V., Vygodina, T. V., Siletsky, S. a & Konstantinov, A. Zinc ions as cytochrome C oxidase inhibitors: two sites of action. *Biochemistry. (Mosc).* **70**, 128–136 (2005).
149. Ferguson-Miller, S., Hiser, C. & Liu, J. Gating and regulation of the cytochrome c oxidase proton pump. *Biochim. Biophys. Acta - Bioenerg.* **1817**, 489–494 (2012).
150. Mogi, T., Ui, H., Shiomi, K., Omura, S. & Kita, K. Gramicidin S identified as a potent inhibitor for cytochrome *bd*-type quinol oxidase. *FEBS Lett.* **582**, 2299–2302 (2008).
151. Grieshaber, D., MacKenzie, R., Vörös, J. & Reimhult, E. Electrochemical Biosensors - Sensor Principles and Architectures. *Sensors* **8**, 1400–1458 (2008).
152. Koyun, A., Ahlatcioğlu, E. & İpek, Y. K. *Biosensors and Their Principles*. A Roadmap Biomed. Eng. Milestones pp. 117–142 (IntechOpen, 2012).

153. Touhami, A. *Biosensors and Nanobiosensors: Design and Applications*. Nanomedicine (One Central Press, 2015).
154. Willner, I. & Katz, E. *Bioelectronics: from theory to application* (Willey-VCH, 2005).
155. Léger, C. & Bertrand, P. Direct Electrochemistry of Redox Enzymes as a Tool for Mechanistic Studies. *Chem. Rev.* **108**, 2379–2438 (2008).
156. Armstrong, F. A. Protein film voltammetry: Revealing the mechanisms of biological oxidation and reduction. *Russ. J. Electrochem.* **38**, 49–62 (2002).
157. Sassolas, A., Blum, L. J. & Leca-Bouvier, B. D. Immobilization strategies to develop enzymatic biosensors. *Biotechnol. Adv.* **30**, 489–511 (2012).
158. Takeda, K. *et al.* Real-time dynamic adsorption processes of cytochrome *c* on an electrode observed through electrochemical high-speed atomic force microscopy. *PLoS One* **10**, 1–10 (2015).
159. Chen, P. & McCreery, R. L. Control of Electron Transfer Kinetics at Glassy Carbon Electrodes by Specific Surface Modification. *Anal. Chem.* **68**, 3958–3965 (1996).
160. Yamini Satyawali, S. S. Enzymatic Electrosynthesis: An Overview on the Progress in Enzyme Electrodes for the Production of Electricity, Fuels and Chemicals. *J. Microb. Biochem. Technol.* **7**, 1-20 (2013)
161. Jeuken, L. J. C. *et al.* Redox enzymes in tethered membranes. *J. Am. Chem. Soc.* **128**, 1711–1716 (2006).
162. Ataka, K. *et al.* Oriented attachment and membrane reconstitution of His-tagged cytochrome *c* oxidase to a gold electrode: In situ monitoring by surface-enhanced infrared absorption spectroscopy. *J. Am. Chem. Soc.* **126**, 16199–16206 (2004).
163. Bostick, C. D. *et al.* Protein bioelectronics: A review of what we do and do not know. *Reports Prog. Phys.* **81**, 1–158 (2018).
164. Dai, J. *et al.* Some thoughts on the existence of ion and water channels in highly dense and well-ordered CH₃-terminated alkanethiol self-assembled monolayers on gold. *Biosens. Bioelectron.* **24**, 1074–1082 (2009).
165. Abdullin, T. I. *et al.* Effect of size and protein environment on electrochemical properties of gold nanoparticles on carbon electrodes. *Bioelectrochemistry* **77**, 37–42 (2009).
166. Wang, Q., Wang, C., Zhang, M., Jian, M. & Zhang, Y. Feeding Single-Walled Carbon Nanotubes or Graphene to Silkworms for Reinforced Silk Fibers. *Nano Lett.* **16**, 6695–6700 (2016).
167. Nagaraju, K., Reddy, R. & Reddy, N. A review on protein functionalized carbon nanotubes. *J. Appl. Biomater. Funct. Mater.* **13**, 1-12 (2015).
168. Love, J. C., Estroff, L. A., Kriebel, J. K., Nuzzo, R. G. & Whitesides, G. M. Self-assembled monolayers of thiolates on metals as a form of nanotechnology. *Chemical Reviews* **105**, 1103-1170 (2005).
169. Leger, C. & Fourmond, V. *Protein Electrochemistry: Questions and Answers*. (Springer Int. Publishing Basel) (2017).
170. Jin, R., Zeng, C., Zhou, M. & Chen, Y. Atomically Precise Colloidal Metal Nanoclusters and Nanoparticles: Fundamentals and Opportunities. *Chem. Rev.* **116**, 10346–10413 (2016).
171. Saha, K., Agasti, S. S., Kim, C., Li, X. & Rotello, V. M. Gold nanoparticles in chemical and biological sensing. *Chem. Rev.* **112**, 2739–2779 (2012).

172. Meyer, T. *et al.* Evidence for distinct electron transfer processes in terminal oxidases from different origin by means of protein film voltammetry. *J. Am. Chem. Soc.* **136**, 10854–10857 (2014).
173. Meyer, T. *et al.* Electrochemistry of cytochrome c_1 , cytochrome c_{552} , and Cu_A from the respiratory chain of *Thermus thermophilus* immobilized on gold nanoparticles. *J. Phys. Chem. B* **115**, 7165–70 (2011).
174. Zeng, T. *et al.* Transient Catalytic Voltammetry of Sulfite Oxidase Reveals Rate Limiting Conformational Changes. *J. Am. Chem. Soc.* **139**, 11559–11567 (2017).
175. Witt, H., Zickermann, V. & Ludwig, B. Site-directed mutagenesis of cytochrome c oxidase reveals two acidic residues involved in the binding of cytochrome c . *Analyzer* **1230**, 74–76 (1995).
176. Melin, F. *et al.* The unusual redox properties of C-type oxidases. *Biochim. Biophys. Acta - Bioenerg.* **1857**, 1892–1899 (2016).
177. Chang, H.-Y., Hemp, J., Chen, Y., Fee, J. A. & Gennis, R. B. The cytochrome ba_3 oxygen reductase from *Thermus thermophilus* uses a single input channel for proton delivery to the active site and for proton pumping. *Proc. Natl. Acad. Sci. U. S. A.* **106**, 16169–16173 (2009).
178. Pitcher, R. S., Cheesman, M. R. & Watmough, N. J. Molecular and spectroscopic analysis of the cytochrome cbb_3 oxidase from *Pseudomonas stutzeri*. *J. Biol. Chem.* **277**, 31474–31483 (2002).
179. Fournier, E. *et al.* Creation of a gold nanoparticle based electrochemical assay for the detection of inhibitors of bacterial cytochrome bd oxidases. *Bioelectrochemistry* **111**, 109–114 (2016).
180. Bloch, D. A., Borisov, V., B., Mogi, T., Verkhovsky, M. I. Heme/heme redox interaction and resolution of individual optical absorption spectra of the hemes in cytochrome bd from *Escherichia coli*. *Biochim. Biophys. Acta* **1787**, 1246–1253 (2009).
181. Li, W. F., Zhou, X. X. & Lu, P. Structural features of thermozymes. *Biotechnol. Adv.* **23**, 271–281 (2005).
182. Sterner, R. & Liebl, W. Thermophilic adaptation of proteins. *Crit. Rev. Biochem. Mol. Biol.* **36**, 39–106 (2001).
183. Razvi, A. & Scholtz, J. M. Lessons in stability from thermophilic proteins. *Protein Sci.* **15**, 1569–1578 (2006).
184. Luke, K. A., Higgins, C. L. & Wittung-Stafshede, P. Thermodynamic stability and folding of proteins from hyperthermophilic organisms. *FEBS J.* **274**, 4023–4033 (2007).
185. Somero, G. N. Proteins and Temperature. **57**, 43–68 (1995).
186. Medda, L., Salis, A. & Magner, E. Specific ion effects on the electrochemical properties of cytochrome c . *Phys. Chem. Chem. Phys.* **14**, 2875–2883 (2012).
187. Pasche, S., Vörös, J., Griesser, H. J., Spencer, N. D. & Textor, M. Effects of Ionic Strength and Surface Charge on Protein Adsorption at PEGylated Surfaces Effects of Ionic Strength and Surface Charge on Protein Adsorption at PEGylated Surfaces. *J. Phys. Chem. B* **109**, 17545–52 (2005).
188. Capitanio, G., Martino, P. L., Capitanio, N. & Papa, S. Redox Bohr effects and the role of heme a in the proton pump of bovine heart cytochrome c oxidase. *Biochim. Biophys. Acta - Bioenerg.* **1807**, 1287–1294 (2011).
189. Papa, S. *et al.* Cooperative coupling and role of heme a in the proton pump of heme-copper oxidases. *Biochimie* **80**, 821–836 (1998).

190. Papa, S., Capitanio, N., Capitanio, G. & Palese, L. L. Protonmotive cooperativity in cytochrome *c* oxidase. *Biochim. Biophys. Acta - Bioenerg.* **1658**, 95–105 (2004).
191. Mason, M. G., Nicholls, P. & Cooper, C. E. The steady-state mechanism of cytochrome *c* oxidase: redox interactions between metal centres. *Biochem. J.* **422**, 237–46 (2009).
192. Meyer, T. *et al.* Electrochemistry suggests proton access from the exit site to the binuclear center in *Paracoccus denitrificans* cytochrome *c* oxidase pathway variants. *FEBS Lett.* **589**, 565–568 (2015).
193. Jeuken, L. J. C. *Biophotoelectrochemistry: From Bioelectrochemistry to Biophotovoltaics*. (Springer International Publishing AG, 2016).
194. Léger, C. An Introduction to Electrochemical Methods for the Functional Analysis of Metalloproteins. *Pract. Approaches to Biol. Inorg. Chem.* 179–216 (2013).
195. Krejci, J. *et al.* Monolayers of photosystem II on gold electrodes with enhanced sensor response — effect of porosity and protein layer arrangement. *Anal. Bioanal. Chem.* **381**, 1558–1567 (2005).
196. Shokri, A. & Larsson, G. Characterisation of the *Escherichia coli* membrane structure and function during fedbatch cultivation. *Microb. Cell Fact.* **3**, 1–12 (2004).
197. Denning, E. J. & Beckstein, O. Influence of lipids on protein-mediated transmembrane transport. *Chem. Phys. Lipids* **169**, 57–71 (2013).
198. Lee, A. G. How lipids affect the activities of integral membrane proteins. *Biochim. Biophys. Acta - Biomembr.* **1666**, 62–87 (2004).
199. Brown, M. F. Soft Matter in Lipid – Protein Interactions. *Annu. Rev. Biophys.* **46**, 379–410 (2017).
200. Kolonay, J. F., Moshiri, F., Gennis, R. B., Kaysser, T. M. & Maier, R. J. Purification and characterization of the cytochrome *bd* complex from *Azotobacter vinelandii* - Comparison to the complex from *Escherichia coli*. *J. Bacteriol.* **176**, 4177–4181 (1994).
201. Lebègue, E. *et al.* An optimal surface concentration of pure cardiolipin deposited onto glassy carbon electrode promoting the direct electron transfer of cytochrome-*c*. *J. Electroanal. Chem.* **808**, 286–292 (2018).
202. Chi, Q., Zhang, J., Andersen, J. E. T. & Ulstrup, J. Ordered assembly and controlled electron transfer of the blue copper protein azurin at gold (111) single-crystal substrates. *J. Phys. Chem. B* **105**, 4669–4679 (2001).
203. Murgida, D. H. & Hildebrandt, P. Proton-Coupled Electron Transfer of Cytochrome *c*. *J. Am. Chem. Soc.* **123**, 4062–4068 (2001).
204. Wei, J. *et al.* Electron-transfer dynamics of cytochrome *c*: A change in the reaction mechanism with distance. *Angew. Chemie - Int. Ed.* **41**, 4700–4703 (2002).
205. Fujita, K. *et al.* Mimicking protein-protein electron transfer: Voltammetry of *Pseudomonas aeruginosa* azurin and the *Thermus thermophilus* Cu_A domain at ω -derivatized self-assembled-monolayer gold electrodes. *J. Am. Chem. Soc.* **126**, 13954–13961 (2004).
206. Eckermann, A. L., Feld, D. J., Shaw, J. & Meade, T. J. Electrochemistry of redox-active self-assembled monolayers.. *Coord Chem Rev* **254**, 1769–1802 (2010).
207. Maire, L. M., Champeil, P. & Møller, J. V. Interaction of membrane proteins and lipids with solubilising detergents. *Biochim. Biophys. Acta* **1508**, 86–111 (2000).

208. Rigaud, J.-L., Lévy, D., G, M. & Lambert, O. Detergent removal by Bio-Beads. Application to membrane protein reconstitution and two-dimensional crystallisation. *Eur J. Biophys.* **27**, 305–319 (1998).
209. Seddon, A. M., Curnow, P. & Booth, P. J. Membrane proteins, lipids and detergents: Not just a soap opera. *Biochim. Biophys. Acta - Biomembr.* **1666**, 105–117 (2004).
210. Chae, P. S. *et al.* Maltose-neopentyl glycol (MNG) amphiphiles for solubilization, stabilization and crystallization of membrane proteins. *Nat. Methods* **7**, 1003–1008 (2010).
211. Kiyomura, I. S., Nascimento, F. J., Cunha, A. P. & Cardoso, E. M. Analysis of the Influence of Surface Roughness and Nanoparticle Concentration on the Contact Angle. *Conf. ABCM* **106**, 666-674 (2017).
212. Whitesides, G. M., Kriebel, J. K. & Love, J. C. Molecular engineering of surfaces using self-assembled monolayers. *Sci. Prog.* **88**, 17–48 (2005).
213. Vericat, C., Vela, M. E., Benitez, G., Carro, P. & Salvarezza, R. C. Self-assembled monolayers of thiols and dithiols on gold: new challenges for a well-known system. *Chem. Soc. Rev.* **39**, 1805 (2010).
214. Liu, Y., Yang, Y. & Lee, Y. Assembly Behavior and Monolayer Characteristics of OH-Terminated Alkanethiol on Au (111): in situ STM and Electrochemical Studies. *Assembly* **7**, 1–8 (2007).
215. PubHem (NCBI, 2018)
https://pubchem.ncbi.nlm.nih.gov/compound/Aurachin_D#section=3D-Conformer.
216. Jacques, J. G. J. *et al.* Kinetics of substrate inhibition of periplasmic nitrate reductase. *Biochim. Biophys. Acta - Bioenerg.* **1837**, 1801–1809 (2014).
217. Nazina, T. N. *et al.* Taxonomic study of aerobic thermophilic bacilli: Descriptions of *Geobacillus subterraneus* gen. nov., sp. nov. and *Geobacillus uzenensis* sp. nov. from petroleum reservoirs and transfer of *Bacillus stearotherophilus*, *Bacillus thermocatenulatus*, *Bacillus th.* *Int. J. Syst. Evol. Microbiol.* **51**, 433–446 (2001).
218. Zhang, J., Oettmeier, W., Gennis, R. B. & Hellwig, P. FTIR spectroscopic evidence for the involvement of an acidic residue in quinone binding in cytochrome bd from *Escherichia coli*. *Biochemistry* **41**, 4612–4617 (2002).
219. Hellwig, P. Infrared spectroscopic markers of quinones in proteins from the respiratory chain. *Biochim. Biophys. Acta - Bioenerg.* **1847**, 126–133 (2015).
220. Sun, J. *et al.* Resonance Raman Spectroscopic Identification of a Histidine Ligand of b 595 and the Nature of the Ligation of Chlorin d in the Fully Reduced *Escherichia coli* Cytochrome bd Oxidase. *Biochemistry* **35**, 2403–2412 (1996).
221. Rygula, A. *et al.* Raman spectroscopy of proteins: A review. *J. Raman Spectrosc.* **44**, 1061–1076 (2013).
222. Hirota, S., Mogi, T., Anraku, Y., Gennis, R. B. & Kitagawa, T. Resonance Raman study on axial ligands of heme irons in cytochrome bd-type ubiquinol oxidase from *Escherichia coli*. *Biospectroscopy* **1**, 305–311 (1995).
223. Jacques, J. G. J. *et al.* Reductive activation in periplasmic nitrate reductase involves chemical modifications of the Mo-cofactor beyond the first coordination sphere of the metal ion. *Biochim. Biophys. Acta - Bioenerg.* **1837**, 277–286 (2014).
224. Limoges, B. & Savéant, J. M. Catalysis by immobilized redox enzymes. Diagnosis of inactivation and reactivation effects through odd cyclic voltammetric responses. *J. Electroanal. Chem.* **562**, 43–52 (2004).

225. Geldenhuys, W. J., Leeper, T. C. & Carroll, R. T. mitoNEET as a novel drug target for mitochondrial dysfunction. *Drug Discov. Today* **19**, 1601–1606 (2014).
226. Tamir, S. *et al.* Structure-function analysis of NEET proteins uncovers their role as key regulators of iron and ROS homeostasis in health and disease. *Biochim. Biophys. Acta - Mol. Cell Res.* **1853**, 1294–1315 (2015).
227. Hou, X. *et al.* Crystallographic studies of human MitoNEET. *J. Biol. Chem.* **282**, 33242–33246 (2007).
228. Lin, J., Zhou, T., Ye, K. & Wang, J. Crystal structure of human mitoNEET reveals distinct groups of iron sulfur proteins. *Proc. Natl. Acad. Sci. U. S. A.* **104**, 14640–14645 (2007).
229. Conlan, A. R. *et al.* The novel 2Fe-2S outer mitochondrial protein mitoNEET displays conformational flexibility in its N-terminal cytoplasmic tethering domain. *Acta Crystallogr. Sect. F Struct. Biol. Cryst. Commun.* **65**, 554–559 (2009).
230. Baxter, E. L., Jennings, P. A. & Onuchic, J. N. Strand swapping regulates the iron-sulfur cluster in the diabetes drug target mitoNEET. *Proc. Natl. Acad. Sci.* **109**, 1955–1960 (2012).
231. Zuris, J. A. *et al.* Facile transfer of [2Fe-2S] clusters from the diabetes drug target mitoNEET to an apo-acceptor protein. *Proc. Natl. Acad. Sci.* **108**, 13047–13052 (2011).
232. Tirrell, T. F. *et al.* Resonance Raman studies of the (His)(Cys)₃ 2Fe-2S cluster of mitoNEET: Comparison to the (Cys)₄ mutant and implications of the effects of pH on the labile metal center. *Biochemistry* **48**, 4747–4752 (2009).
233. Bak, D. W., Zuris, J. A., Paddock, M. L., Jennings, P. A. & Elliott, S. J. Redox characterization of the FeS protein MitoNEET and impact of thiazolidinedione drug binding. *Biochemistry* **48**, 10193–10195 (2009).
234. Bergner, M. *et al.* Model of the MitoNEET [2Fe-2S] cluster shows proton coupled electron transfer. *J. Am. Chem. Soc.* **139**, 701–707 (2017).
235. Vernay, A. *et al.* MitoNEET-dependent formation of intermitochondrial junctions. *Proc. Natl. Acad. Sci.* **114**, 201706643 (2017).
236. Bai, F. *et al.* The Fe-S cluster-containing NEET proteins mitoNEET and NAF-1 as chemotherapeutic targets in breast cancer. *Proc. Natl. Acad. Sci.* **112**, 3698–3703 (2015).
237. Waqar, A., Shu, X. *et al.* Complexes of the Outer Mitochondrial Membrane Protein MitoNEET with Resveratrol-3-Sulfate.. *Biochemistry*; **50**, 5806–5811 (2011)
238. Bieganski, R. M. & Yarmush, M. L. Novel ligands that target the mitochondrial membrane protein mitoNEET. *J. Mol. Graph. Model.* **29**, 965–973 (2011).
239. Zuris, J. A. *et al.* NADPH inhibits [2Fe-2S] cluster protein transfer from diabetes drug target MitoNEET to an Apo-acceptor protein. *J. Biol. Chem.* **287**, 11649–11655 (2012).
240. Geldenhuysa, W. J., Heather M., Yonutasb, B, Daniel, L., Morris, P. G., Sullivan, C. & Altaf S. D. Identification of small molecules that bind to the mitochondrial protein mitoNEET. *Bioorg. Med. Chem. Lett.* **26**, 5350–5353 (2016).
241. Conlan, A. R. *et al.* Mutation of the His ligand in mitoNEET stabilizes the 2Fe-2S cluster despite conformational heterogeneity in the ligand environment. *Acta Crystallogr. Sect. D Biol. Crystallogr.* **67**, 516–523 (2011).
242. Landry, A. P. & Ding, H. Redox control of human mitochondrial outer membrane protein mitoneet [2FE-2S] clusters by biological thiols and hydrogen peroxide. *J. Biol. Chem.* **289**, 4307–4315 (2014).

243. Landry, A. P., Cheng, Z. & Ding, H. Reduction of mitochondrial protein mitoNEET [2Fe-2S] clusters by human glutathione reductase. *Free Radic. Biol. Med.* **81**, 119–127 (2015).
244. Landry, A. P. *et al.* Flavin nucleotides act as electron shuttles mediating reduction of the [2Fe-2S] clusters in mitochondrial outer membrane protein mitoNEET. *Free Radic. Biol. Med.* **102**, 240–247 (2017).
245. Wang, Y., Landry, A. P. & Ding, H. The mitochondrial outer membrane protein mitoNEET is a redox enzyme catalyzing electron transfer from FMNH₂ to oxygen or ubiquinone. *J. Biol. Chem.* **292**, 10061–10067 (2017).
246. Todorovic, S. & Teixeira, M. Resonance Raman spectroscopy of Fe–S proteins and their redox properties. *J. Biol. Inorg. Chem.* **23**, 1–15 (2018).
247. Fleischhacker, A. S. *et al.* Characterization of the [2Fe-2S] cluster of Escherichia coli transcription factor IscR. *Biochemistry* **51**, 4453–4462 (2012).
248. Adrover, M., Howes, B. D., Iannuzzi, C., Smulevich, G. & Pastore, A. Anatomy of an iron-sulfur cluster scaffold protein: Understanding the determinants of [2Fe-2S] cluster stability on IscU. *Biochim. Biophys. Acta - Mol. Cell Res.* **1853**, 1448–1456 (2015).
249. Li, H. *et al.* The yeast iron regulatory proteins Grx3/4 and Fra2 form heterodimeric complexes containing a [2Fe-2S] cluster with cysteinyl and histidyl ligation. *Biochemistry* **48**, 9569–9581 (2009).
250. Li, H. *et al.* Histidine 103 in Fra2 is an iron-sulfur cluster ligand in the [2Fe-2S] Fra2-Grx3 complex and is required for in vivo iron signaling in yeast. *J. Biol. Chem.* **286**, 867–876 (2011).
251. Kounosu, A. *et al.* Engineering a Three-cysteine, One-histidine Ligand Environment into a New Hyperthermophilic Archaeal Rieske-type [2Fe-2S] Ferredoxin from Sulfolobus solfataricus. *J. Biol. Chem.* **279**, 12519–12528 (2004).
252. Fu, W., Drozdowski, P. M., Davies, M. D., Sligar, S. G. & Johnson, M. K. Resonance Raman and magnetic circular dichroism studies of reduced [2Fe-2S] proteins. *J. Biol. Chem.* **267**, 15502–15510 (1992).
253. Cutone, A. *et al.* Pichia pastoris Fep1 is a [2Fe-2S] protein with a Zn finger that displays an unusual oxygen-dependent role in cluster binding. *Sci. Rep.* **6**, 1–12 (2016).
254. Xiao, Y. *et al.* Dynamics of *Rhodobacter capsulatus* [2Fe-2S] ferredoxin VI and *Aquifex aeolicus* ferredoxin 5 via nuclear resonance vibrational spectroscopy (NRVS) and resonance Raman spectroscopy. *Biochemistry* **47**, 6612–6627 (2008).
255. Friedrich, T. & Hellwig, P. Redox-induced conformational changes within the *Escherichia coli* NADH ubiquinone oxidoreductase (complex I): An analysis by mutagenesis and FT-IR spectroscopy. *Biochim. Biophys. Acta - Bioenerg.* **1797**, 659–663 (2010).
256. Barth, A. Infrared spectroscopy of proteins. *Biochim. Biophys. Acta - Bioenerg.* **1767**, 1073–1101 (2007).
257. Wolpert, M. & Hellwig, P. Infrared spectra and molar absorption coefficients of the 20 amino acids in aqueous solutions in the spectral range from 1800 to 500 cm⁻¹. *Spectrochim. Acta - Part A Mol. Biomol. Spectrosc.* **64**, 987–1001 (2006).
258. García-Ruiz, I., Solís-Muñoz, P., Fernández-Moreira, D., Muñoz-Yagüe, T. & Solís-Herruzo, J. A. Pioglitazone leads to an inactivation and disassembly of complex I of the mitochondrial respiratory chain. *BMC Biol.* **11**, 1–15 (2013).
259. Baymann, F. *et al.* Voltammetry of a ‘protein on a rope’. *FEBS Lett.* **539**, 91–94 (2003).

260. Armstrong, F. A., Hill, H. A. O., Walton, N. J., Hill, H. A. & Walton, J. Direct electrochemistry of redox proteins. *Accounts of Chemical Research* **21**, 407–413 (1988).
261. Henze, G. *Polarographie und Voltammetrie*. (Springer-Verlag Berlin Heidelberg, 2001).
262. Armstrong, F. A., Heering, H. A. & Hirst, J. Reaction of complex metalloproteins studied by protein-film voltammetry. *Chem. Soc. Rev.* **26**, 169 (1997).
263. Laviron, E. General expression of the linear potential sweep voltammogram in the case of diffusionless electrochemical systems. *J. Electroanal. Chem.* **101**, 19–28 (1979).
264. Bin, D. *et al.* Crab-shell induced synthesis of ordered macroporous carbon nanofiber arrays coupled with MnCo₂O₄ nanoparticles as bifunctional oxygen catalysts for rechargeable Zn-air batteries. *Nanoscale* **9**, 11148–11157 (2017).
265. Owen, T. Fundamentals of modern UV-visible spectroscopy. (*Hewlett-Packard Co.* 1996).
266. Dzebo, D. PhD thesis: Photon Upconversion through Triplet-Triplet Annihilation Towards Higher Efficiency and Solid State Applications. Goteborg, Sweden (2016).
267. Microscopy resource center (Olympus-America 2004-2009)
<http://fluoview.magnet.fsu.edu/theory/fluoroexciteemit.html>.
268. Zang, C. *et al.* Ultrafast proteinquake dynamics in cytochrome *c*. *J. Am. Chem. Soc.* **131**, 2846–2852 (2009).
269. Gouterman, M. Study of the effects of substitution on the absorption spectra of porphin. *J. Chem. Phys.* **30**, 1139–1161 (1959).
270. Eaton, W. A., Hanson, L. K., Stephens, P. J., Sutherl, J. C. & Dunn, J. B. R. Optical Spectra of Oxy- and Deoxyhemoglobin. *J. Am. Chem. Soc.* **100**, 4991–5003 (1978).
271. Péter Maróti (Lasers in Biophysics, 2011) www.tankonyvtar.hu/hu/tartalom/tamop412A/2011-0013_maroti_lasers_in_biophysics/adatok.html
272. Barth, A. The infrared absorption of amino acid side chains. *Prog. Biophys. Mol. Biol.* **74**, 141–173 (2000).
273. Long, D. A. *The Raman effect: a unified treatment of the theory of Raman scattering by molecules*. (John Wiley & Sons Ltd, 2002).
274. Wartewig, S., Schorn, C. & Bigler, P. *IR and Raman Spectroscopy*. (2003).
275. Schmid, W. *Optical Spectroscopy in Chemistry and Life Sciences. An Introduction*, (WILEY-VCH Verlag GmbH & Co. KGaA, 2005).
276. Bunaciu, A. A., Aboul-Enein, H. Y. & Fleschin, Ș. Vibrational spectroscopy in clinical analysis. *Appl. Spectrosc. Rev.* **50**, 176–191 (2015).
277. David, C. Raman Spectroscopy for proteins. *Raman Spectrosc.* **36**, 1–53 (2012).
278. Nakamoto, K. *Infrared and Raman Spectra of Inorganic and Coordination Compounds Part A : Theory and Applications*. (John Wiley & Sons, Inc., 2009).
279. Spiro, T. G. & Editor. Biological Applications of Raman Spectroscopy , Vol. 3: Resonance Raman Spectra of Heme and Metalloproteins. **1988**, 565 (1988).
280. Spiro, T. G. & Strekas, T. C. Resonance Raman spectra of heme proteins. Effects of oxidation and spin state. *J. Am. Chem. Soc.* **96**, 338–345 (1974).
281. Spiro, T. G., Czernuszewicz, R. S. & Li, X.-Y. Metalloporphyrin structure and dynamics from resonance Raman spectroscopy. *Coord. Chem. Rev.* **100**, 541–571 (1990).

282. Hu, S., Morris, I. & Singh, J. Complete assignment of cytochrome c resonance Raman spectra via enzymic reconstitution with isotopically labeled hemes. *J. Am. Chem. Soc.* **115**, 12446–12458 (1993).
283. Biju, V. *et al.* Combined spectroscopic and topographic characterization of nanoscale domains and their distributions of a redox protein on bacterial cell surfaces. *Langmuir* **23**, 1333–1338 (2007).
284. Lu, Y. Assembly and Transfer of FeS Clusters in the Plastid. *Front. Plant Sci.* **9**, 1–17 (2018).
285. University of Cambridge (2017) <https://www.ceb.cam.ac.uk/research/groups/rg-eme/teaching-notes/hydrodynamic-voltammetry>.
286. Agilent Technologies (2018) <https://www.agilent.com>.
287. Tüm Hakları Saklıdır (2018, LabServis). <http://www.labservis.net/cihaz-periyodik-bakim/ft-ir/>
288. Srour, B. PhD thesis: Emerging roles for natural and artificial lipids in shaping the catalytic function, stability and oligomeric state of membrane proteins. Strasbourg, France (2015).
289. Soutter, W. What is Raman Spectroscopy? *Renishaw Raman Support* (2012).
290. Smith, E. & Dent, G. *Modern Raman Spectroscopy: A Practical Approach*. **5**, 1-224 (2005).
291. Image and Video Exchange Forum (ASDL Community, 2018) <http://community.asdlib.org>.
292. Ferecatu, I. *et al.* The diabetes drug target MitoNEET governs a novel trafficking pathway to rebuild an Fe-S cluster into cytosolic aconitase/iron regulatory protein 1. *J. Biol. Chem.* **289**, 28070–28086 (2014).
293. Dejon, L. & Speicher, A. Synthesis of aurachin D and isoprenoid analogues from the myxobacterium *Stigmatella aurantiaca*. *Tetrahedron Lett.* **54**, 6700–6702 (2013).
294. Turkevich, J., Stevenson, P. C. & Hiller, J. a Study of the Nucleation and Growth Processes In the Synthesis of Colloidal Gold. *Discuss. Faraday Soc.* **11**, 55–75 (1951).
295. Haiss, W., Thanh, N. T. K., Aveyard, J. & Fernig, D. G. Determination of size and concentration of gold nanoparticles from UV-Vis spectra. *Anal. Chem.* **79**, 4215–4221 (2007).
296. Hellwig, P., Scheide, D., Bungert, S., Mantele, W. & Friedrich, T. FT-IR spectroscopic characterization of NADH:Ubiquinone oxidoreductase (complex I) from *Escherichia coli*: Oxidation of FeS cluster N2 is coupled with the protonation of an aspartate or glutamate side chain. *Biochemistry* **39**, 10884–10891 (2000).
297. Brunning A. (Compound Interest, 2017) Compound Interest <https://www.compoundchem.com>.
298. Miller, M. J. & Genniss, B. The Purification and Characterization of the Cytochrome *d* Terminal Oxidase Complex of the *Escherichia coli* Aerobic Respiratory Chain. *J. Biol. Chem.* **258**, 9159–9165 (1983).
299. Ralle, M. *et al.* Coordination of Cu(B) in reduced and CO-liganded states of cytochrome *bo*₃ from *Escherichia coli*. Is chloride ion a cofactor. *Biochemistry* **38**, 7185–7194 (1999).
300. Solomon, E. I., Mano, N. & Lojou, E. Mechanism of Chloride Inhibition of Bilirubin Oxidases and Its Dependence on Potential and pH. *ACS Catal.* 3916–3923 (2017).
301. Katayama, K. *et al.* “*In situ*” observation of the role of chloride ion binding to monkey green sensitive visual pigment by ATR-FTIR spectroscopy. *Phys. Chem. Chem. Phys.* **20**, 3381–3387 (2018).
302. Cihan, A. C., Ozcan, B., Tekin, N. & Cokmus, C. *Geobacillus thermodenitrificans* subsp. *calidus*, subsp. nov., a thermophilic and α -glucosidase producing bacterium isolated from Kizilcahamam, Turkey. *J. Gen. Appl. Microbiol.* **57**, 83–92 (2011).

List of figures

Fig. 1. Effet de la quantité de lipides sur la stabilité des voltammogrammes cycliques du cytochrome bd immobilisé sur l'électrode d'or modifiée avec HT/MCH (1/1).	11
Fig. 2. Dépendance des voltammogrammes cycliques du cytochrome bd en la longueur du thiol : MPA vs MHA vs MUA.....	11
conditions d'immobilisation	12
Fig. 3. Spectre FTIR différentiel induit par la réaction redox du cytochrome bd provenant de <i>G. thermodenitrificans</i> et d' <i>E. coli</i> . 5°C, pH7.....	14
Fig. 4. Spectre de Raman de résonance du cytochrome bd de <i>G. thermodenitrificans</i> et d' <i>E. coli</i> . Films secs. Excitation laser de 514 nm.....	14
Fig. 5. Spectres d'absorption UV/Vis pour les bd-oxydases de <i>G. thermodenitrificans</i> et d' <i>E. coli</i>	14
Fig. 6. Exemple de la détermination des potentiels médians des cofacteurs par le fit avec l'équation de Nernst modifiée. Les transitions à 560 nm sont montrés.	14
Fig. 7. Voltammogrammes cycliques du cytochrome bd de <i>G. thermodenitrificans</i> dans différentes conditions.	15
Fig. 8. Spectres FTIR différentiels induits par la réaction redox du mitoNEET dépendant du pH dans le tampon dépourvu des ions phosphates.	17
Fig. 9. Spectres de résonance Raman de mitoNEET dépendant de la présence d'ions phosphates et du pH. Films secs. Excitation laser de 514 nm.	17
Fig. 10. Electron transport chain in inner mitochondria membrane (IMM) ²⁸	22
Fig. 11. Left: natural heme structures (A) and a scheme of biosynthesis (B) ³⁸ . Right: possible heme covalent bonding with protein scaffold encountering in the nature.....	24
Fig. 12. Comparison of the pH dependency of the midpoint potential of the prokaryotic cyt c ₂ - , mitochondrial cyt c - and Q-pools ⁴⁰	27
Fig. 13. Stages of the quinone core reduction to quinol. The process involves two protonation and two reduction events: $Q + 2e^- + 2H^+ \rightarrow QH_2$ ²	27
Fig. 14. Probable organisation of the electron transport in cyt bd (from <i>G. thermodenitrificans</i>) ¹⁷	32
Fig. 15. Cristal structure of cyt bd from <i>G. thermodenitrificans</i> with resolution 3.6 Å. The charges at the surface are shown (red – negative, blue – positive, navy blue – polar). [pdb 5IR6] ⁵	33
Fig. 16. Relative localisation of the hemes in cyt bd from <i>G. thermodenitrificans</i> . The distances Fe-to-Fe (15.2 vs 19.4 Å) and edge-to-edge (5.9 vs 8.5 Å) are provided. Trp residue between hemes d and b ₅₅₈ is shown. [pdb 5IR6] ⁵	33
Fig. 17. Proposed catalytic cycle of aa ₃ cytochrome c oxidase. In the frame there is a schematic drawing of BNC of the enzyme. To simplify, the heme a ₃ is depicted as Fe ³⁺ and aromatic (Tyr) residue as Y. The changes in the BNC during catalysis are highlighted in red.....	36
Fig. 18. Catalytic cycle of cyt bd. The superscripts of the state labels correspond to electron quantity injected in the system. R ³ →A ³ : 1.4 μs for 365 μM O ₂ ; 0.9: 0.6-1.1.	37
Fig. 19. Diagram of the two substrate and two product (bi-bi) catalysis. a) ordered mechanism, b) random mechanism, c) ping-pong mechanism. The A is a leading substrate, B is following substrate ¹¹⁷	40
Fig. 20. Difference in the substrate (UQH ₂) and product (UQ) structures utilised by cyt bd ¹³⁴	46
Fig. 21. Structures of the natural electron donors of cyt bd (UQ, MQ, DMQ), TMPD and the structures of the several inhibitors (HQNO, Piericidin A, aurachin C (aurachin D lacks 1-OH group); Antimycin A, UHDBT).	48
Fig. 22. Schematic representation of some immobilisation approaches (adapted from ¹⁶⁰).	51

Fig. 23. Defects found in SAM formed on gold surface. Moreover, the tightly attached impurities can cause additional disorder. ¹⁶⁴	53
Fig. 24. Catalytic voltammograms of cyt bd in presence of O ₂ . 1000 rpm, 0.02 V/s, pH7, KPi 0.1 M.	59
Fig. 25. Stabilisation of the cyt bd protein films upon addition of the PE/PG (1/1) lipid mixture. The 22% lipid concentration (grey line) led to the optimal results.	60
Fig. 26. Structure of the lipids probed for the protein film stability examination. Due to saturation of hydrophobic tails DMPE is a more stable lipid.	61
Fig. 27. Successive voltammograms of cyt bd with addition of 2.5% lipids of different type (PE or PG) and with immobilisation on different surfaces (polar or negatively-charged).	62
Fig. 28. Voltammogram of cyt bd (with 2.5% PE) shape dependence on the length of the ω -carboxyl alkanethiols (MPA, MHA or MUA) introduced in the thiol monolayer.	63
Fig. 29. Structures of the DDM (right) and MNG (left) detergents.	64
Fig. 30. Formation of the SAM in the course of time ²¹²	68
Fig. 31. Adsorption of the hydrophobic protein at SAM ¹⁶⁸	68
Fig. 32. Structures of the aurachin D derivatives. Substituent in the 3 rd position is varied. Aurachin D corresponds to compound SB1.	72
Fig. 33. Crystal structure of aurachin D ²¹⁵	72
Fig. 34. Example of the inhibition measurement of the compound from the aurachin D derivative group. The 2 nd and the 3 rd scans are taken for determination of the current decrease in the absence of the inhibitor. The 4 th measurement was conducted in the presence of the compound in the solution.	73
Fig. 35. Basic structures of the potential inhibitors of cyt bd. The compound scaffolds resemble the structures of natural electron donors (MQ and UQ). The locants are mentioned for the compounds concerned in the discussions.	74
Fig. 36. Structures of the compound with the highest inhibition activity towards cyt bd.	76
QN-1Br > (SB1) > QN-2 > Qo-5 > QN-1 > Qo-7, RK-01 > QN-04.	76
Fig. 37. Example of inhibition experiment. The gradual increase in the Qo-7 concentration leads to the decrease in the current.	77
Fig. 38. Fitting with Morrison equation to determine the apparent inhibition constant of the most efficient inhibitors. The initial maximal limiting current at – 300 mV (vs SHE) was taken as 1.0, the observed current values were normalised.	77
Fig. 39. Some examples of the structures of the compounds with no inhibition effect on cyt bd.	80
Fig. 40. Activation-stabilisation effect of the BrN10 on the voltammogram of cyt bd from E. coli. The transition zone is shown.	80
Fig. 41. Substrate-inhibition effect of Q98Cam-effector on cyt bd from E. coli.	80
Fig. 42. Absolute absorption spectra of dithionite reduced bd-oxidases from E. coli and G. thermodenitrificans (pH7, RT, spectra are normalized at the Soret band).	82
Fig. 43. Differential absorption spectra of bd-oxidases from E. coli and G. thermodenitrificans. Ox-state = air-oxidised, Red-state = dithionite reduced. (pH7, spectra are normalized at the Soret band)	82
Fig. 44. Example of oxidative titration. One can see full Red-minus-Ox (blue curve) and full Ox-minus-Red (red curve) differential absorption spectra. The step of the titration was varied from 100 mV far from the transition to 25 mV in the region of the redox transitions.	84
Fig. 45. Dependency of the reductive potentials on pH of cytochrome bd cofactors (G. thermodenitrificans, in the presence of DDM). The linear fit was utilised for simplicity and on the example of cyt bd from E. coli that shows this type of E(pH) dependency in this pH region.	85
Fig. 46. Probable distribution of potentials E _{m7} within hemes in cyt bd from G. thermodenitrificans.	87

Fig. 47. Ox-red differential spectra of cyt bd from <i>G. thermodenitrificans</i> and <i>E. coli</i> at 5°C and pH7.....	88
Fig. 48. Ox-red FTIR difference spectra of free MQ and UQ at pH7 ²¹⁹	89
Fig. 49. Resonance Raman spectra of the dried films of cyt bd from <i>E. coli</i> and <i>G. thermodenitrificans</i> . The excitation was conducted at 514 nm.....	91
Fig. 50. Cyclic voltammograms for cytochrome bd from <i>G. thermodenitrificans</i> . Conditions of measurements are demonstrated on the graph. Rate of scanning 0.02 V/s, solution 100 mM KPi, pH7. Cyt bd from <i>E. coli</i> of the 2 nd purification is shown for comparison.	93
Fig. 51. Influence of the chloride ions on the shape of voltammograms of cyt bd from <i>G. thermodenitrificans</i>	95
Fig. 52. Voltammograms of cyt bd from <i>G. thermodenitrificans</i> in MQ-4 excess conditions and control MQ-4 in O ₂ presence.	95
Fig. 53. Normalized UV/Visible-spectra of <i>G. thermodenitrificans</i> cyt bd from different batches. The spectra were obtained after reductant (sodium dithionite) addition.....	95
Fig. 54. Influence of temperature on catalytic activity of cyt bd from <i>G. thermodenitrificans</i>	97
Fig. 55. Influence of the pH on the ox-red differential FTIR spectra of cyt bd from <i>G. thermodenitrificans</i> (5°C, KPi pH9.5 vs pH7).....	98
Fig. 56. Influence of the pH on voltammogram shape at 45°C for cyt bd from <i>G. thermodenitrificans</i>	99
Fig. 57. Influence of the temperature on the voltammetric signal of cyt bd from <i>G. thermodenitrificans</i> at pH9.5.....	100
Fig. 58. Mutual influence of temperature and pH on catalytic behaviour of cyt bd from <i>G. thermodenitrificans</i>	100
Fig. 59. Resonance Raman spectra of cyt bd from <i>G. thermodenitrificans</i> in the absence and presence of aurachin D (x30).	102
Fig. 60. Ox-red differential FTIR spectra of cyt bd from <i>G. thermodenitrificans</i> in the absence and presence of aurachin D (x30).	102
Fig. 61. Influence of 10µM HQNO on voltammetric signal of cyt bd from <i>G. thermodenitrificans</i> (pH9.5, 45°C).	103
Fig. 62. Evolution of voltammogram of cyt bd from <i>G. thermodenitrificans</i> upon successive scanning (pH9.5, 45°C).	103
Fig. 63. Schemes of the iron-sulfur cluster variations encountered in nature. ²²⁶	105
Fig. 64. X-ray structure of homodimeric mNT with two main domains. ²³⁰	105
Fig. 65. Charge profile of mNT surface. Positively charged/basic patch is located near FeS-cluster. ²²⁷	105
Fig. 66. Some amino acids residues involved in a conservative hydrogen network: His87, Asp84, Lys55. Lys55 and His87 are localised in different monomers, thus, mNT function as a dimer ¹⁵	106
Fig. 67. Cluster release can take place when the protein is in oxidised state. In the reduced or inhibited state (e. g., with TZD) holo-mN does not react with the apoprotein (e. g., Fdx, Adx, aconitase) ²³¹	106
Fig. 68. Compounds which are supposed to stabilise the mNT cluster ²²⁵	108
Fig. 69. CV of mNT at MHA modified gold electrode. O ₂ , pH7, Tris 50 mM, 100 mM NaCl. 0.02 V/s.	111
Fig. 70. RR spectra of mNT with excitation at 457 and 514 nm, pH8, Tris buffer. To obtain partially oxidised spectrum UQ-2 and defocalisation were employed; the time between each single spectrum 10 s (50 spectra were averaged).	113
Fig. 71. Comparison of ox-red differential spectra of mNT in H ₂ O and D ₂ O.	114
Fig. 72. RR spectra of mNT in the presence and absence of the phosphate ions.	115

Fig. 73. Alterations of the RR spectrum of mNT with pH decrease. The buffer used: pH8.5, 7.5 – Tris, pH6.7, 6.2 – BisTris, pH5.8, 5.6, 4.8 – MES; $\lambda_{\text{ex}}=457$ nm.	116
Fig. 74. Changes in the ox-red differential FTIR spectra of mNT in dependence on pH. Conditions: pH8.5, 7.5 – Tris, pH 6.7, 6.2 – BisTris, pH 5.8, 5.6, 4.8 – MES.	117
Fig. 75. RR spectra of the dried films of mitoNEET with addition of the ligands. Experimental conditions: Tris, pH8, $\lambda_{\text{ex}}=457$ nm.	119
Fig. 76. Influence of the ligand on the protein redox-induced rearrangements detected by FTIR. Ox-red spectra are shown.	121
Fig. 77. Typical cyclic voltammogram of a reversible redox system in the solution (left) ²⁶¹ and adsorbed on the electrode surface (right). ²⁶²	124
Fig. 78. Left ²⁶⁴ : raw data obtained in CV experiment: voltammogram at different electrode rotation speed. Right: Koutecky-Levich plot which leads to calculation of $iK - 1$	127
Fig. 79. Jablonski diagram for molecular transitions. Only singlet states are shown ²⁶⁶ . IC – internal conversion, VR – vibrational relaxation.	128
Fig. 80. Morse potential energy curves. The rotation levels situated between rotational levels are omitted ²⁶⁷	128
Fig. 81. Gradation of the spectral scale and the corresponding transitions in molecules.	129
Fig. 82. Transitions in the molecule shown through Jablonski-type (left) and molecular orbital (right) representation. The MO theory considers the energy of the transition.	130
Fig. 83. Absorption spectra of heme c. Red-state vs ox-state. ²⁶⁸	130
Fig. 84. Differential redox-induced UV/Vis spectra with several titration points.	131
Fig. 85. Fitting with modified Nernst equation in order to determine the mid-point potentials of the redox active protein cofactors.	131
Fig. 86. Classification of the normal vibrations modes. ²⁷¹	133
Fig. 87. Ox-red absorption IR spectrum of a protein (red). The negative bands come from reduced state, then the positive bands come from oxidised state. The absolute spectrum is in grey colour.	134
Fig. 88. Schematic representations of (I) infrared absorption, (II) Rayleigh scattering, (III) Stokes Raman scattering, (IV) anti-Stokes Raman scattering, (V) resonance Raman scattering, (VI) fluorescence (adapted from ²⁷⁶).	135
Fig. 89. Some examples of skeletal ²⁸³ and in-plane ¹¹⁶ heme vibrations. The locants of the atoms in the heme group are shown (left).	137
Fig. 90. Types of the FeS-cluster the most encountering in the nature ²⁸⁴	138
Fig. 91. Scheme of the three electrode electrochemical cell. ²⁸⁵	139
Fig. 92. Optical path in the UV/Vis spectrometer. Only one channel was used during single beam mode (dashed line). ²⁸⁶	140
Fig. 93. Construction of the thin-layer electrochemical cell ¹¹	141
Fig. 94. Scheme of the FTIR spectrometer and the data obtained during the experiment. ²⁸⁷	142
Fig. 95. Transmission cell used for secondary protein structure determination. ²⁸⁸	143
Fig. 96. Optical scheme of Raman spectrometer ²⁸⁹ (left) and scheme of backscattering collection of the Raman emission from the sample (right). ²⁹⁰	143
Fig. 97. Principal scheme of construction of a Clark-electrode ²⁹¹	144

List of tables

Tableau 1. Influence de la quantité de lipides sur la stabilité des films de protéine. i_1 - courant mesuré au 1 ^{er} balayage, i_2 - courant mesuré au 2 ^{ème} balayage. La surface est non chargée (HT / MCH, 1/1).	11
Tableau 2. Influence du type de lipide et du type de surface sur les paramètres des voltammogrammes de la bd-oxydase.....	12
Tableau 3. Diminution du courant (di/i) mesuré pour les composés ayant une activité d'inhibition la plus marquée (concentration finale de 10 μ M).	13
Table 4. Characteristics of the redox processes occurring in the complexes (c.) of mitochondrial respiratory chain. The route of electron flow within the protein and quantity of pumped proton per electron are also mentioned ^{2,28}	23
Table 5. Reductive potentials of the some quinole/quinone pairs in water/ethanol solution ^{45,46}	26
Table 6. Structural characteristics of the terminal oxidases and the description of electron pathways. BNC – binuclear centre or its analogue (catalytic site); hs or ls – high or low spin; Nc – coordinated with N ligands.	30
Table 7. Comparison of the efficiency of the terminal oxidases and affinity to the oxygen.	31
Table 8. Intermediates of the catalytic cycle of the aa ₃ -oxidase with precision of the oxidation state and ligation of the redox active cofactors.	36
Table 9. Kinetic parameter changes in the dependence on the inhibition type ¹¹⁶	42
Table 10. Inhibition and Michaelis constants for the discussed compounds. For KCN, NO, CO the UQH ₂ -oxidation reaction was monitored.	46
Table 11. Electrochemical and catalytical properties of terminal oxidases from various organisms.....	55
Table 12. Parameters of the voltammograms of cyt bd oxidase in dependence on the concentration of added lipid mixture (PE/PG 1/1).	60
Table 13. The characteristics of the voltammograms of cyt bd upon addition of different lipid types and variations of the surface properties.....	62
Table 14. Voltammetric parameters of the cyt bd oxidase films with fast mode of the modification of the electrode in the presence of the different detergents.....	64
Table 15. The dependence of the cyt bd film stability upon variation of the number of the depositions of GNPs (the total quantity of the GNPs) with fixed single deposited dose (9 μ M).	65
Table 16. Influence of GNPs volume utilised for the one deposition on stability parameter. The corresponding electrode surface representation is shown. Incubation in thiols (1/1 HT/MCH) – 15 min, with cyt bd - 15 min.	66
Table 17. Dependence of the voltammetric parameters of cyt bd on the time of the incubation in thiol solution.....	67
Table 18. Dependency of the voltammetric parameters and HQNO inhibition effectiveness on the type of the thiol monolayer. The inhibition effect was measured for 10 μ M HQNO.	69
Table 19. Cyt bd catalytic current decrease (at – 400 mV (vs SHE)) upon addition of the 10 μ M DMSO solution of the compound. (di/i) ₀ – the current drop in the absence of a compound, (di/i) _c – (di/i) ₀ , %– current decrease due to injection of a compound.	73
Table 20. The limiting current changes (at -300 mV (vs SHE)) upon addition of the 10 μ M DMSO solution of the compounds. The compounds with high inhibition activity are highlighted in red, the compounds with activation or stabilising activity are highlighted in green.....	75
Table 21. IC ₅₀ , apparent inhibition constant and current decrease (upon addition of 10 μ M of the compound) values for the most efficient inhibitors.	78

Table 22. Mid-point potentials (vs SHE) of the heme cofactors from cyt bd (<i>G. thermodenitrificans</i>) at different pH. 13°C, DDM. The hemes b were not attributed and were labelled as heme bN ₁ and heme bN ₂ . The value errors are mentioned in Annex 3. The $E_{m7} = -43$ mV for heme d was calculated based on the hysteresis for heme d at pH6 and E_{m7} for heme d obtained in oxidative titration.	84
Table 23. The mid-point potentials of the cofactors of cytochrome bd-oxidase from different species in the presence of DDM. Tentative attribution of the hemes b is based on the further studies with aurachin D and the batch devoid of heme d.	86
Table 24. Tentative assignments ^{218,219} of the bands of ox-red differential FTIR spectra of cyt bd from <i>E. coli</i> and <i>G. thermodenitrificans</i> (pH7, 5°C). The bands where lipids vibration can contribute are in green.	89
Table 25. Tentative assignment of the Raman bands of cyt bd from <i>E. coli</i> and <i>G. thermodenitrificans</i> . The assignment is based on previous reports ^{220,221} , ¹³¹ . The attribution involves the idea that ferrous (Fe^{2+}) heme b ₅₅₈ is low-spin six-coordinated (axial ligands: His and Met) and ferrous (Fe^{2+}) heme b ₅₉₅ is high-spin pentacoordinated (axial ligand: His). The abbreviations for the band intensity: s – strong, m – medium, w – weak. ^{131,220,221}	92
Table 26. The influence of the heme d loss on the mid-point potentials of the hemes b in cyt bd oxidase from <i>G. thermodenitrificans</i> at pH6. The values are shown for oxidative titrations.	96
Table 27. Deconvolution results of the amide I band of the D ₂ O spectra of cyt bd from <i>G. thermodenitrificans</i> at 5 and 40°C, pH7 and pH9.5.	101
Table 28. Influence of aurachin D on reductive potentials (mV, vs SHE) of the cofactors of cyt bd from <i>G. thermodenitrificans</i> at pH7, 13°C. The results of oxidative titration are shown.	101
Table 29. The influence of the surface type on the quality of voltammetric signal of immobilised mNT. Tris 50 mM, NaCl 100 mM, pH7, 0.02 V/s, under argon.	111
Table 30. Tentative assignment of the resonance Raman spectrum of reduced mNT spectrum $[Fe2-S2]^{I+}$, $\lambda_{ex} = 457$ nm.	112
Table 31. The influence of the phosphate ions on the quality of voltammetric signal of immobilised mNT. pH8, 0.02 V/s, under argon, at MHA.	114
Table 32. Electrochemical properties of mNT in the presence of the ligands. Scan rate 0.1 V/s, pH8, Tris 50 mM, 100 mM NaCl.	118
Table 33. Deconvolution results of the major Raman peaks at 307 and 321 cm^{-1} (Annex 8). Relative contribution surface under central peak is shown.	120
Table 34. The 1/m values depending on peak separation and electron quantity considering $\alpha = 0.5$	126
Table 35. Position and attribution of the most characteristic heme bands ^{269,270}	130
Table 36. Comparison of the direct and indirect electrochemistry of proteins.	132
Table 37. Useful spectral regions for study of protein in MIR spectral region ²⁵⁶	133
Table 38. Amide I components in the protein spectrum (the average maxima are shown) ²⁵⁶	134
Table 39. Assignment of the RR spectra bands of the hemes in dependence on spin, coordination and redox-state ^{279–281}	137
Table 40. Protein washing procedures for PFV experiments.	146
Table 41. Cyt bd from <i>E. coli</i> sample preparation for PFV experiments.	146
Table 42. Conditions of the protein preparation for differential redox-induced FTIR experiments.	147
Table 43. Conditions of the electrode modification procedure.	148
Table 44. Conditions of the redox-induced differential FTIR experiments.	148
Table 45. Conditions of the RR measurements.	149
Table 46. List of 19 mediators used in the differential redox-induced spectroscopy measurements. All mediators are low-weight redox active compounds.	152

List of annexes

A1. List of the essential amino acids ²⁹⁷ and table of their properties ²⁷	154
A2. Amino acid sequence alignment of subunits CydA and CydB of cyt bd from <i>G. thermodenitrificans</i> and <i>E. coli</i> ⁵ . Conserved residues involved in: heme coordination – yellow, quinol binding – purple, CydA proton pathway – blue, CydB proton pathway – red, charge compensation – green ⁵ . Sequence identity is less than 30%. ⁵	155
A3. Corresponding descriptive statistics for midpoint potential values (see table 22) in mV (vs SHE) for the cofactor of bd-oxidase from <i>G. thermodenitrificans</i> obtained in different conditions: standard deviation SD is in red and the random error ε (t-distribution with $p=0.95$) is in black.....	156
A4. Raman spectra of cyt bd from <i>G. thermodenitrificans</i> and <i>E. coli</i> , and background (DDM). Comparison of various batches (A, B, C) of cyt bd from <i>G. thermodenitrificans</i> with different DDM content. Influence of the heme d (batch E), pH9.5 (batch D), KCN (batch C) and washing (batch B) on RR spectra is shown. Unless otherwise stated, the conditions are pH6, unwashed sample, <i>G. thermodenitrificans</i>	156
A5. Voltammograms of the cyt bd from <i>G. thermodenitrificans</i> and corresponding difference FTIR spectra (the batch with decreased MQ content).....	157
A6. Ox-red differential FTIR spectrum of cyt bd from <i>G. thermodenitrificans</i> devoid of heme d.	157
A7. Deconvolution of amide I of cyt bd from <i>G. thermodenitrificans</i> at pH7 and pH9.5 and 5° and 45°C. Spectra were obtained in D ₂ O, 30 spectra were averaged. Smoothing of amide I were conducted with FTT 3 pts filter. The deconvolution with Gaussian function provided the fit with $R^2=0.9995$	158
A8. Deconvolution of the major band (307-321 cm ⁻¹) of the resonance Raman spectra of mitoNEET.....	159
A9. Example of Laviron method calculation of electron transfer constant.	160
A10. Deduction of modified Nernst equation.	161

Anton NIKOLAEV

Etudes d'inhibition de métalloprotéines par électrochimie et spectroscopie

Résumé

Les études d'interaction protéine-ligand aident à mieux comprendre la structure et la fonction des protéines. Dans la première partie de la thèse, la cyt *bd* oxydase a été étudiée. La protéine d'*E. coli* a été immobilisée avec succès sur des électrodes modifiées par des nanoparticules d'or. Ainsi, un biocapteur électrochimique a été créé, permettant de tester certains inhibiteurs potentiels de cyt *bd* provenant d'*E. coli*. Le cyt *bd* issue de *G. thermodenitrificans* thermophile a également été étudié. En faisant appel aux spectroscopies IR et Raman ainsi que l'électrochimie, il a été démontré que la protéine est distincte du cyt *bd* d'*E. coli*. Une influence mutuelle du pH et de la température sur la catalyse a été aussi démontrée. La deuxième partie de la thèse portait sur la protéine mitochondriale mitoNEET. L'influence du pH et de divers ligands (pioglitazone, resvératrol, ions phosphates) a été examinée.

Mots-clés: cytochrome *bd*, complexe IV, quinol oxydase, mitoNEET, bioélectrochimie, résonance Raman, spectroscopie IR, criblage à haut débit, biocapteur, aurachin D, quinazoline, quinolone.

Résumé en anglais

Protein-ligand interaction studies help to better understand the structure and function of proteins. In the first part of the thesis cyt *bd* oxidase was studied. The protein from *E. coli* was successfully immobilised at gold nanoparticles modified electrodes. Thus, an electrochemical biosensor was created allowing testing some potential inhibitors of cyt *bd* from *E. coli*. The cyt *bd* from thermophilic *G. thermodenitrificans* was also studied. By means of IR, Raman spectroscopy and electrochemistry the protein was shown to be distinct from cyt *bd* from *E. coli*. A mutual influence of pH and temperature was demonstrated on the electrochemical and catalytical properties. The second part of the thesis focused on mitochondrial mitoNEET protein. The influence of the pH and various ligands was studied.

Keywords: cytochrome *bd*, complex IV, quinol oxidase, mitoNEET, bioelectrochemistry, resonance Raman, IR spectroscopy, high-throughput screening, biosensor, aurachin D, quinazoline, quinolone